Theses and Dissertations   Graduate School

2020

Strategies and Devices for Improving Respiratory Drug Delivery to Infants and Children with Cystic Fibrosis

Karl Bass
Virginia Commonwealth University

Strategies and Devices for Improving Respiratory Drug Delivery to Infants and

Children with Cystic Fibrosis

A dissertation submitted in partial fulfillment of the requirements for the degree of Doctor

of Philosophy at Virginia Commonwealth University.

by

KARL BASS

Bachelor of Engineering, University of West England, UK, 2009

Director: Dr. P. WORTH LONGEST

Professor, Department of Mechanical and Nuclear Engineering and

Department of Pharmaceutics

Virginia Commonwealth University

Richmond, Virginia

May 2020

Acknowledgements

Table of Contents

List of Tables

4

List of Figures

11

Abstract

Strategies and Devices for Improving Respiratory Drug Delivery to Infants and Children with Cystic Fibrosis

by Karl Bass

A dissertation submitted in partial fulfillment of the requirements for the degree of Doctor of Philosophy at Virginia Commonwealth University.

Virginia Commonwealth University

Director: Dr. P. Worth Longest
Professor, Department of Mechanical and Nuclear Engineering and
Department of Pharmaceutics

Cystic Fibrosis (CF) is a degenerative disease, which causes thickening of the airway surface liquid and reduced mucociliary clearance, which provides an ideal habitat for bacterial infections. Early treatment of CF in children can prevent chronic infection, improve quality of life, and increase life expectancy. The most predominant bacteria found in CF-diseased lungs is Pseudomonas aeruginosa (Pa), which can be treated with inhaled tobramycin. Excipient enhanced growth (EEG) powder formulations are well suited for administering tobramycin to children, as the EEG approach provides minimal upper airway loss and targeted drug delivery. This method uses an initially small aerosol for high extrathroacic transmission, and includes hygroscopic excipients within the formulation that absorb moisture from the humid airways and increase lung retention of the aerosol. The overarching goal of this work was to develop delivery systems and strategies for improving respiratory drug delivery to children with CF, which was based on insights from computational fluid dynamics (CFD) simulations and *in vitro* models. The studies presented in this dissertation have three distinct and sequential phases: (i) CFD methods

development; (ii) respiratory device design and optimization; and (iii) complete-airway modeling for aerosol delivery strategy development.

The methods development phase produced meshing and solution guidelines that were computationally-efficient, accurate, and validated based on *in vitro* data. Results showed that the two-equation k-ω model, with near-wall corrections, was capable of matching experimental data across a range of Reynolds numbers and particle sizes that are specific to respiratory drug delivery. The guidelines also provided comparable accuracy to the more complex Large Eddy Simulation (LES) model, while providing multiple order-of-magnitude savings in computational time. The device optimization phase developed a highly efficient delivery system for tobramycin administration to pediatric CF patients. Correlations were developed, based on flow field quantities, that were predictive of aerosolization performance and depositional loss. Successful a priori validation with experimental testing highlighted the predictive capabilities of the correlations and CFD model accuracy. The best-case delivery system demonstrated an aerosol size of approximately 1.5 μm and expected lung dose of greater than 75% of loaded dose, which is a marked improvement compared to commercial devices. The delivery strategy development phase identified optimal EEG aerosol properties that better unify drug surface concentration. These studies present numerical models of a tobramycin EEG powder formulation for the first time, and provide the first instance of a complete-airway CFD model evaluating pediatric CF lungs. Results show that EEG aerosols are capable of delivering the drug above the minimum inhibitory concentration in all airway regions, reducing regional dose variability, and targeting the lower airways where infection is more predominant. In conclusion, results from this dissertation

demonstrate: (i) accurate and efficient CFD models of respiratory drug delivery; (ii) optimized designs for respiratory delivery systems; and (iii) optimal delivery strategies for inhaled tobramycin to pediatric patients with CF.

Chapter 1: Specific Aims

Respiratory drug delivery with pharmaceutical aerosols offers a number of advantages compared with other delivery routes and for many medications is the most logical approach in the treatment of lung diseases and conditions. While potentially beneficial, challenges associated with respiratory drug delivery include aerosolizing the powder at a respirable size with limited flow energy, penetrating the extrathoracic airways, which are intended to filter foreign objects, and depositing the aerosol at the intended location within the lungs to achieve the desired biological effect. Additional challenges after the medication is deposited in the lungs include dissolution within the limited airway lining fluid, avoidance of clearance mechanisms, and absorption in the mucus and airway tissue.

Of the various patient groups that may benefit from respiratory drug delivery, administration of pharmaceutical aerosols to infants and children is especially difficult. Their relatively small extrathoracic airways are an obstacle to delivering drugs to the lungs. Furthermore, infants and children often do not comply with receiving inhaled or other forms of medication. Even with good patient compliance, only approximately 1% to 10% of the initial aerosol is typically delivered to the lungs, and inter-subject variability is expected to be high. Further reductions in lung delivery efficiency and increases in inter-subject variability are expected with diseased lungs.

To improve respiratory drug delivery for infants and children, innovations are needed in pharmaceutical delivery strategies, devices, and formulations. The overarching **goal** of this work is to develop and optimize strategies and devices for improving respiratory drug delivery to infants and children using computational fluid dynamics (CFD)

and *in vitro* models. To accomplish this goal, objectives are targeted in three key areas: (i) model development, (ii) device development, and (iii) delivery strategy development. As described in more detail below, each of these key objectives is intended to move the field of respiratory drug delivery forward. In particular, the primary application of this work is to quantitatively analyze and optimize the delivery of inhaled antibiotics to children with cystic fibrosis (CF).

The validation of a CFD model is often an iterative process of defining and adjusting numerous meshing and solution parameters until good agreement is made with experimental data. The first objective of this dissertation intends to streamline the **model development** process by defining a set of meshing and solution guidelines that are validated for the micro-particle size range and under flow conditions that are consistent with respiratory airways. Naturally, each project is unique and requires its own considerations, but these guidelines strive to reduce the effort taken to develop a CFD model by providing a baseline set-up that is known to give accurate results.

With sound numerical methods, one can apply CFD to obtain detailed physical insight into the performance and behavior of aerosol-delivery devices. The second objective of this dissertation uses CFD to provide insight into dry powder inhaler (DPI) and cannula **device development**, which improve aerosol delivery efficiency. Specifically, delivery systems aim to provide a relatively small particle size, for increased lung penetration, and a high emitted dose (ED), for reduced device losses.

The third objective of this work applies the developed nasal and lung models (with validated CFD methods) and optimized aerosolization device in the development of a **delivery strategy** for the administration of inhaled antibiotics to children with CF. The

delivery strategies employed, and developed by our group, include enhanced excipient growth (EEG) and nose-to-lung (N2L) administration with correctly-sized aerosols. As a first step, the delivery strategy will be assessed and optimized with regional CFD simulations of the patient interface, nasal cavity, and upper tracheobronchial (TB) airways. Thereafter, complete-airway CFD simulations will be used to optimize aerosol delivery throughout the lungs with the goal of uniform antibiotic concentrations. There are numerous CFD models of particle transport through the lungs in the literature and by our group, but there has been little work to date specific to drug delivery in pediatric lungs as well as in diseased lungs.

The objectives stated above build upon one another, and all focus on providing a CFD-based analysis of the treatment of pediatric CF lung infections with inhaled antibiotics. The most recent data from the Cystic Fibrosis Foundation Patient Registry (2016) states approximately 30,000 people are living with the disease, with the median age of diagnosis being 4 months old. CF is a debilitating disease, which greatly reduces quality of life, with a mean survival of 48 years (Cystic Fibrosis Foundation Patient Registry, 2016). The disease primarily affects lung function, but also affects the pancreas, liver, sweat glands, and vas deferens (Elborn, 2016). In fact, the name of the disease originates from the pancreatic fibrosis and cysts that were described when CF was first identified (Andersen, 1938).

CF is caused by a genetic mutation in the Cystic Fibrosis transmembrane conductance regulator (CTFR) gene (Cheng et al., 1990), which causes poor transport of Na^+ (increased absorption) and Cl^- (reduced secretion) ions through the epithelial cells (Matsui et al., 1998; Tarran et al., 2001), and effectively dehydrates the lungs. This

dehydration leads to thicker mucus and decreased mucociliary clearance (Stoltz, Meyerholz, & Welsh, 2015), which causes bacterial infections to reside in the lungs for much of the patient's life (Boucher, 2007). The most dominant bacterium found in CF lungs is *Pseudomonas aeruginosa* (*Pa*) (Elborn, 2016), which typically forms a biofilm in the thick mucus. Biofilms are colonies of cells encased in a sticky substance (Donlan, 2002) that attach to the lung surfaces, which makes it difficult for the patient's mucociliary clearance to remove the bacteria (Boucher, 2007). The combined effects of bacterial infection and thick mucus leads to the three main types of lung damage in CF: bronchiectasis (irreversible thickening of airway walls), mucus obstructions, and inflammation, which all drastically reduce lung function. Key spirometry tests to evaluate the extent of CF lung damage are the percent of predicted forced expiratory volume in one second (%FEV_1) and forced vital capacity (%FVC), with percentages compared to the baseline given for the patient's age. Reported functional performance for CF patients from 11-13 years of age are a %FEV_1 and %FVC of approximately 75% and 85%, respectively (de Jong et al., 2004), which demonstrates how severely the lungs can be damaged at a young age with early disease progression.

CF mortality rates have improved in recent years and are expected to continue to improve (Burgel et al., 2015), with the increased survival attributed to advances in treatment methods (Elborn, 2016). The low median age of CF diagnosis (4 months) is due to the screening of newborns in many developed countries (Mayell et al., 2009), which allows parents and clinicians to begin treating lung infections early in the patient's life. Approximately one-third of children have signs of lung damage in computed tomography (CT) scans by the age of three (Elborn, 2016), so starting treatment methods early is of

paramount importance. The methods known to improve quality of life and survival are the use of techniques to aid mucus clearance in the lungs (physiotherapy, vibrating respiratory devices, and breathing exercises), inhaled and oral antibiotics to treat infection (Geller & Rubin, 2009), and improvements in nutrition (Elborn, 2016). Early treatment of *Pa* can prevent patients developing a chronic lung infection during childhood (C. R. Hansen, Pressler, & Hoiby, 2008; Hoiby, 2011), hence the need to improve the pediatric administration of antibiotics.

Tobramycin was the first commercially available inhaled antibiotic, as it has high activity, low toxicity, and is easily radiolabeled (A. L. Smith, 2002). A key trial that demonstrated the efficacy of tobramycin for treating CF was conducted by Ramsey et al. (1999) who demonstrated an average 12% increase in FEV_1, 26% decrease in pulmonary exacerbations, less hospitalization, and a 1.1 $\log_{10}$ CFU/g reduction in *Pa* infection. Inhaled tobramycin is available in two forms: tobramycin inhaled solution (TIS), which is loaded into a nebulizer, and tobramycin inhaled power (TIP), which is loaded into a DPI. TIP is the focus of this work as DPIs require less cleaning and sterilization than nebulizers, and can deliver antibiotics faster (Somayaji & Parkins, 2015). An important consideration when treating any bacterial infection with antibiotics is to minimize the possibility of resistant forms of the bacterium. If the concentration of tobramycin delivered to the airway surface liquid (ASL) is below the minimum inhibitory concentration (MIC), then strains of *Pa* develop that cannot be treated with the antibiotic (Dalhoff, 2014). Therefore, it is imperative that the respiratory delivery of inhaled tobramycin is highly efficient and provides consistent dosage in order to minimize the possibility of antibiotics resistance.

Numerous studies from our group have demonstrated that the EEG method is a very efficient approach for delivering pharmaceutical aerosols to the respiratory airways (Hindle & Longest, 2012; Longest et al., 2015; Longest & Hindle, 2009b, 2012; Longest, Tian, Li, Son, & Hindle, 2012; Tian, Hindle, & Longest, 2014; Tian, Longest, Li, & Hindle, 2013). EEG utilizes a spray-dried formulation of a drug that produces an aerosol with a mass-median aerodynamic diameter (MMAD) of less than approximately 1.5 μm (Son, Longest, & Hindle, 2012; Son, Longest, Tian, & Hindle, 2013), when sufficiently aerosolized by a DPI. These small particles have low inertia, which leads to increased penetration fractions, and reduced losses in the delivery system and extrathoracic region. The formulation includes a hygroscopic excipient that causes particle or droplet growth, once inside the lungs, by absorbing moisture from the humid airways. The aerosol size can increase to an MMAD of 3-6 μm (Tian et al., 2014; Tian et al., 2013), which increases its inertia and improves lung retention once it has penetrated deep in the conducting airways. EEG is expected to be a viable method for delivering tobramycin to pediatric patients with CF and diseased airways. The high delivery efficiency of the EEG method offers a targeted approach of providing high dose concentrations in the ASL of the conducting airways. Combined with N2L administration via a streamlined nasal cannula, losses in the patient interface and extrathoracic region are expected to be low (Longest et al., 2015). Using a nasal cannula also has the expected benefit of reducing patient distress, especially for infants and young children, when compared to a facemask (Amirav, 2011; Everard, 2003).

Previous work from our group has also demonstrated the importance of using a concurrent experimental and CFD approach when developing aerosol delivery systems

(Behara, Farkas, Hindle, & Longest, 2014; Behara, Longest, Farkas, & Hindle, 2014a, 2014b; Hindle & Longest, 2013; Longest, Azimi, Golshahi, & Hindle, 2014; Longest, Azimi, & Hindle, 2014; Son, Longest, Tian, et al., 2013) and evaluating particle transport through the lungs, with validation against *in vitro* (Longest & Hindle, 2009a; Longest, Hindle, Das Choudhuri, & Byron, 2007; Longest, Tian, Delvadia, & Hindle, 2012; Longest, Tian, Walenga, & Hindle, 2012; Longest & Vinchurkar, 2007b; Tian, Longest, Su, Walenga, & Hindle, 2011) and *in vivo* (Longest et al., 2015; Walenga & Longest, 2016) data. CFD models provide a high degree of engineering insight, such as localized deposition patterns, flow field characteristics, and predictions of turbulence behavior. For optimization of a system, changes to design parameters can be made and quickly evaluated via CFD (once the baseline model is developed), without running a large number of experiments. However, the numerical model must be validated against experimental data to ensure the conclusions drawn from the CFD results are accurate. Therefore, much of the work for this dissertation relies on collaboration with Dr. Michael Hindle at the VCU School of Pharmacy, and this joint effort combines the numerical and experimental sides of the investigation, in order to improve device design and evaluate deposition in the airways.

The expected contributions to the field of respiratory drug delivery from this dissertation are summarized as follows:

- An experimental and CFD model of a 6-month-old infant for the evaluation of N2L delivery methods

- A set of CFD meshing and solution guidelines, which are validated against suitable experimental data, and will form the basis of future numerical work

- An optimized DPI and nasal cannula interface, using CFD insight, which provides highly efficient tobramycin delivery to children

- Three characteristic experimental and CFD models of the diseased upper airways from patients with CF aged from 2-3, 5-6, and 9-10 years old

- A CFD-based proof of concept for the application of EEG formulation tobramycin to treat pediatric CF lung infections

- Preliminary delivery parameter recommendations for use with EEG and N2L aerosol administration that maximize lung delivery of the aerosol and improved dose uniformity across multiple lung levels based on an initial complete-airway CFD model of a child with CF

Objective 1: Accurate CFD Simulations of Aerosol Delivery in Infants and Children

Rationale

From the perspective of developing a skill set, Objective 1 provides a fundamental understanding and working knowledge of modeling aerosol transport through pediatric airways via CFD. The breathing infant lung (BIL) model has been used previously for *in vitro* evaluation of surfactant administration in a representative complete-airway model (Holbrook, 2015). However, questions remain related to how accurately the BIL model approximates deposition in infant lungs, especially in terms of regional deposition. Insight from CFD models can be used to investigate deposition patterns in the packed bed and determine how that compares with an anatomically accurate model.

Flow and particle behavior in the nasal passage is very different compared to the distal airways considered in the BIL model. Airflow conditions are usually transitional or

turbulent, and impaction is the primary deposition mechanism in the extrathoracic airways. As such, CFD models require different methods and considerations. There is limited material available in the literature for a validated methodology for applying CFD to nasal passage geometries. Such guidelines are available for the aerospace, oil and gas, and automotive industries, but these recommendations may not be applicable to extrathoracic airways. Therefore, Objective 1 also aims to define a set of validated meshing and solution guidelines that can help guide CFD model set-up, and streamline the development stage of an investigation. This also develops a broad set of CFD skills and a foundation to aid in the completion of subsequent objectives.

Methods

For the BIL model evaluation, a stochastic individual path (SIP) model for infant airways will be developed and validated against well-defined algebraic correlations. A SIP model separates the airways into three distinct regions and models each of them individually to account for changes in flow regimes through the distal airways (Longest, Tian, Delvadia, et al., 2012; Tian et al., 2011). The model starts with an anatomically accurate geometry of the extrathoracic airways to Bifurcation 3 (B3), which was developed from CT scan data. In this region, flow is turbulent and highly transient, and as such a turbulence model and transient formulation of the transport equations are applied. The second region covers B4-B7 with physically realistic bifurcation geometries (Heistracher & Hofmann, 1995), where the flow is laminar and can be modelled with a steady-state formulation. The third region encompasses B8-B15, and has the same flow conditions as B4-B7, but a new sample of particles are introduced into the domain to account for possible particle convergence issues as larger particles deposit upstream.

The infant SIP model will be based on the original adult version, but scaled to match infant dimensions. The CFD model of the packed bed will be compared against various bifurcation regions in the infant SIP model to evaluate regional and total deposition characteristics.

To develop CFD meshing and solution guidelines for the airways, an initial validation study of a simplified geometry will be conducted using the two-equation k-ω model. A CFD model will be developed and validated against the experimental data from Pui et al. (1987), who evaluated particle deposition in a 90° bend test geometry across a range of Reynolds and Stokes numbers that are consistent with microparticle deposition in the upper airways. Once the guidelines are validated for the representative 90° bend geometry, they will be applied to an anatomically accurate model of an infant nasal passage, and validated against *in vitro* data provided by the VCU School of Pharmacy. This requires development of experimental and numerical infant N2L models, which are obtained via the segmentation of CT scans. Segmentation is a process whereby one selects pixels in the CT images that define the airways through the nasal passage. Selecting pixels for each slice defines voxels, which build up the 3D model, and smoothing algorithms in the software package provide a realistic representation of the nasal cavity. The geometry can then be converted to CAD data and used to build the required experimental and numerical models.

Tasks

Task 1.1: Evaluate Deposition Realism of In Vitro Packed-Bed Breathing Infant Lung Model (BIL)

- Status: Complete and published (Bass & Longest, 2018a)

Task 1.2: Recommendations for Simulation of Microparticle Transport and Deposition Using Two-Equation Turbulence Models

- Status: Complete and published (Bass & Longest, 2018b)

Task 1.3: Validating CFD Predictions of N2L Aerosol Delivery in a 6-Month-Old Infant Airway Model

- Status: Complete and published (Bass, Boc, Hindle, Dodson, & Longest, 2019)

Outcomes

The work completed by Objective 1 provides a thorough evaluation of an *in vitro* method for modelling whole-lung aerosol delivery using CFD insight, a set of meshing and solution guidelines for the numerical modelling of microparticles in the upper airways, and an experimental and CFD model of a 6-month-old nasal passage. The CFD-based evaluation of packed bed lung models will determine whether such models are accurate in their predictions of total and regional deposition. The solution guidelines provide a foundation for future CFD work in all areas of respiratory drug delivery, and aim to streamline the CFD model development process. The 6-month-old nasal model will be used in future work by our group to assess N2L delivery methods to infants, both numerically and experimentally. Objective 1 also provides the fundamental knowledge and skill sets required to model aerosol transport, through delivery systems and the airways, which are required for successfully completing Objective 2 and 3.

Objective 2: Quantitative Analysis and Design of High Efficiency Pediatric DPIs

Rationale

Commercial DPIs are generally inefficient due to high device and extrathoracic losses, which typically arise from relatively large particle diameters (>2 μm) and high

velocity flows used to disperse the powder. Delivery efficiency of devices can be improved with highly dispersible powders and improvements in aerosolization performance. Previous work from our group has shown how turbulence characteristics of the flow deaggregates the powder and reduces particle size (Longest, Son, Holbrook, & Hindle, 2013). Recent work has also shown that non-dimensional turbulence parameters, derived from CFD models, correlate well with the aerosol MMAD and ED for DPIs that utilize dose aerosolization and containment (DAC) units (Longest & Farkas, 2018). The DAC unit comprises a capsule that holds the powder, with inlet and outlet capillaries that introduce an air jet to aerosolize the powder. These DPIs are designed to be used with a low volume (LV) of actuation air, and are referred to as LV-DPIs. This objective uses DAC units with a higher flow rate (HF), which are referred to as HF-DPIs. It is expected that numerous changes to the HF-DPI design parameters can be explored via CFD, and predictive correlations can be used to estimate device performance, with a focus on minimizing MMAD and maximizing ED. Once the DAC unit is optimized, improvements will be sought in the design of the cannula that delivers the aerosol to the nasal airways, which provides a thorough and complete optimization of multiple elements of the delivery system.

Methods

Initial work will begin by applying the same non-dimensionalization and correlation methods to the HF-DPIs as developed for the LV-DPIs presented by Longest and Farkas (2018). Initial correlations will be developed using a number of prototype devices for which the MMAD and ED have been experimentally determined. Other flow field and turbulence characteristics will be explored via the CFD model, to determine what aspects of the device design drives performance at high flow rates, which will lead to additional non-

dimensional parameters and correlations. Once a predictive correlation is found, numerous CFD models of DAC unit designs will be evaluated in terms of aerosolization performance. The best designs will then be tested experimentally to verify the CFD predictions and ensure the predicted performance of the DAC unit is achieved. A similar quantitative approach to design evaluation will be applied to the nasal cannula in order to reduce deposition losses in the patient interface. This method demonstrates the benefits of leveraging the strengths of experimental and numerical models, and combining them to drive the optimization of the delivery system.

Tasks

Task 2.1: CFD Optimization of an Inline DPI for EEG Tobramycin Formulations

- Status: Complete and published (Bass, Farkas, & Longest, 2019)

Task 2.2: Develop DPI Patient Interfaces for Improved Aerosol Delivery to Children

- Status: Complete and in press (Bass & Longest, 2020)

Outcomes

Meeting the requirements of Objective 2 provides CFD-driven optimization of a delivery system for administering inhaled antibiotics to pediatric CF patients. The methods used to determine design optimizations are also beneficial for future work that aims to improve device performance. Once the performance of the delivery system meets a pre-determined level of efficiency, the transport of aerosol through the airways and deposition patterns will then be evaluated by Objective 3.

Objective 3: CFD Predictions of EEG Aerosol Antibiotic Delivery to Children with Cystic Fibrosis

Rationale

To date, few studies have developed CFD models for the diseased airways of patients with CF. Damage to the lungs from CF is known to affect airway morphometry with bronchiectasis (thickening of bronchi walls), general inflammation from infection, and mucus obstructions. Therefore, the geometry of an airway CFD model for CF patients would be very different to healthy lungs, which is expected to affect the flow field and particle trajectories. The first such study in this field was conducted by Awadalla et al. (2014) who developed a Large Eddy Simulation (LES) model of porcine lungs with CF that replicate human CF lungs. Results showed that reduced airway diameters lead to higher flow velocities, which in turn caused an increase in deposition due to impaction. They also concluded that submicron particles may be critical in treating disease in the narrow airways. The first CFD investigation into aerosol administration in human CF lungs was conducted by Bos et al. (2015). They developed CFD models from CT scans of 40 adult patients and evaluated whether delivered concentrations of Aztreonam lysine (AZLI) were sufficient in the ASL to treat infections. Results showed that concentrations were adequate in the majority of cases considered, though there was a large amount of inter-subject variability. Interestingly, they also showed that the lung lobes with the most amount of disease had less ventilation, and hence less aerosol delivery. Primary limitations to this study include a number of assumptions regarding particle size and the ASL thickness, and CFD results were not directly validated against *in vitro* or *in vivo* data. Bos et al. (2017) extended this work with a second study comparing two nebulizers and

their efficiency at delivering TIP. Again, the CFD deposition results from this study were not validated against an experimental model. Objective 3 aims to build upon these studies by validating and evaluating EEG N2L administration of tobramycin to pediatric lungs with CF lung damage.

Methods

Three CF diseased lung models will be developed that are representative of patients aged 2-3, 5-6, and 9-10 years old from CT scans. This objective requires collaboration with Dr. Harm Tiddens' group at Erasmus Medical Centre (Rotterdam, Netherlands), as they will be providing the CT scans, and conducted the human CFD investigations into CF lung deposition mentioned previously (Bos et al., 2017; Bos et al., 2015). If the CF lung scans do not include the extrathoracic region, nasal models will be developed from our own in-house database of CT scans and combined with the diseased airway model. Generating experimental and numerical models from CT data requires segmentation of the scans as described in Objective 1. The fidelity of the scan resolution limits how accurately distal regions of the lung can be extracted from the CT images, and models of pediatric CF lungs typically terminate when the airway diameter is 1-2 mm (which is approximately Bifurcation 6) (Bos et al., 2015). SIP geometries will be used to determine deposition in each lung lobe, with dimensions that are consistent with CF lungs. The SIP geometries will also be modified to account for the bronchiectasis and other forms of lung damage associated with CF. Deposition data from the experimental and numerical CF SIP lung models will be used to determine whether sufficient concentrations of tobramycin are delivered to the ASL, via the optimized delivery devices.

Tasks

Task 3.1: Develop In Vitro Upper Airway Geometries of CF Patients in Age Ranges of 2-3, 5-6, And 9-10 Years

- Status: Complete and *in vitro* testing complete

Task 3.2: Develop CFD Models of Upper Airway Geometries for Pediatric Patients and Evaluate Delivery Efficiency and Aerosol Growth with Comparisons to In Vitro Experiments

- Status: Complete and manuscript in preparation

Task 3.3: Extend and Develop CFD Lung Models to Predict Regional Lung Deposition and Tobramycin ASL Concentrations in Healthy and CF Complete-Airway Lung Models

- Status: Complete and manuscript in preparation

Outcomes

Objective 3 provides a proof of concept for applying the EEG approach, via N2L administration, for the treatment of bacterial infections in CF lungs with inhaled tobramycin. Specifically, three upper airway geometries are developed from CT scans of individuals with CF in the age ranges of 2-3, 5-6, and 9-10 years old. These geometries enable experimental and numerical models of aerosol deposition after inhalation of antibiotics from the optimized delivery system. The models will also be beneficial for future studies, by our group and others, in the field of CF treatment. Extending the lung model into distal regions provides insight into regional deposition patterns, and determines whether tobramycin is delivered in sufficient quantities to provide an ASL concentration that is high enough to eradicate the bacteria.

Chapter 2: Evaluate Deposition Realism of *In Vitro* Packed-Bed Breathing Infant Lung Model (BIL)

2.1 Objective

The objective of this study was to determine whether packed bed *in vitro* models, which contain spheres as the primary repeating unit, provide a realistic representation of aerosol deposition in the tracheobronchial region of infant lungs based on computational fluid dynamics (CFD) predictions. To focus on impaction deposition in the tracheobronchial airways, particles in the size range of 0.5 to 10 µm are evaluated. Systems considered are the packed bed arrangement with an inlet jet generated by outlets of the upper airway model and a realistic bifurcating airway anatomy. To understand the deposition in each of these systems, CFD simulations are implemented. Numerous studies from our group have validated the accuracy of CFD models for predicting aerosol deposition in comparison with *in vitro* lung experiments (Longest & Hindle, 2009a; Longest et al., 2007; Longest, Tian, Delvadia, et al., 2012; Longest, Tian, Walenga, et al., 2012; Longest & Vinchurkar, 2007b; Tian et al., 2011) and *in vivo* data (Longest et al., 2015; Walenga & Longest, 2016).

2.2 Introduction

In vitro airway models provide a convenient and scientifically useful testing platform for determining aerosol delivery to and deposition within the lungs (Byron et al., 2010; Carrigy, Ruzycki, Golshahi, & Finlay, 2014; R. Delvadia, Longest, & Byron, 2012; Warren H. Finlay & Martin, 2008). These models can be used to determine inhaled dose of airborne pollutants and bioaerosols arising from environmental exposures. *In vitro* airway models are also useful in determining the lung delivery efficiency of inhaled

medications and developing more efficient respiratory drug delivery systems. Specific advantages of *in vitro* airway models include the avoidance of human subject testing with the associated safety and ethical concerns, a reproducible and controllable platform with well-defined physical attributes, and the ability to instrument the system as needed. Disadvantages include limited establishment of *in vivo-in vitro* correlations (IV-IVC) and difficulty in reproducing the highly complex and dynamic airway system (Byron et al., 2010).

Considering infants, a number of studies have implemented *in vitro* models to evaluate aerosol deposition in a portion of the airways. Widely used infant nasal models based on a single subject scan have been reported for pre-term (Minocchieri et al., 2008) and 9-month-old (Janssens et al., 2001) infants. Javaheri et al. (2013) developed a characteristic infant nasal model based on 10 previously published geometries in the age range of 3-18 months. Xi et al. (2012) developed a set of pediatric nasal models across an age range from infant to 5-years-old. The studies of Storey-Bishoff et al. (2008) and Golshahi et al. (2010) provide examples of implementing *in vitro* infant nasal models to determine the lung delivery efficiency of inhaled aerosols. Carrigy et al. (2014) further reviews the development of infant and pediatric extrathoracic models with applications to determine lung delivered dose from inhaled pollutants and inhaled pharmaceutical aerosols.

A hybrid-style *in vitro* lung model can be defined as containing a geometrically realistic upper airway structure and an approximation of the remaining lung anatomy. As reported by Carrigy et al. (2014), pediatric extrathoracic models typically connect to a filter or aerosol impactor to evaluate total lung delivery and particle size distributions (PSD) of

the lung delivered dose. More detailed hybrid-style *in vitro* lung models also contain some of the upper tracheobronchial bifurcating airways. For example, Delvadia et al. (2012) report small, medium, and large adult upper airway geometries through the third respiratory bifurcation with the airway outlets contained in a lung Plexiglas chamber with a filtered outlet. Pulmonary deposition was calculated as the dose deposited on the chamber walls and filter at the chamber exit, which assumes that no dose is exhaled due to the presence of a breath-hold period. A mixing inlet style system was used to reproduce accurate inhalation profiles. Delvadia et al. (2012; 2013) report very good agreement between *in vitro* predictions of lung deposition and *in vivo* studies across multiple inhalation waveforms and devices, and the ability of *in vitro* models to capture intersubject variability. Verbanck et al. (2016) developed an adult *in vitro* airway model extending to approximately the fifth airway generation and connected each outlet to a separate collection filter. Studies by Longest et al. (2015; 2012) have implemented a hybrid-style *in vitro* model and sized the lung chamber prior to an impactor to reproduce realistic lung aerosol residence times in order to study hygroscopic aerosol growth during a respiration cycle. While providing additional information about respiratory aerosol transport, these hybrid-style lung models have not attempted to capture the mechanisms of particle deposition in the lower lung and, therefore, are not capable of capturing exhaled aerosol dose and regional aerosol deposition.

Packed beds, also known as glass bead media or granular beds, are a form of porous media composed of spheres or beads in a tightly packed arrangement (Nield & Bejan, 1999). Fluids can move between the spheres and the spherical surfaces providing a high surface-area to volume ratio. Packed beds are traditionally used for gas or liquid

40

flows with surface reactions, as with component extraction or purification applications, but have also been characterized for aerosol filtration. Gebhart et al. (1973) initially characterized diffusional and sedimentation deposition in a packed bed structure. Subsequent studies characterized aerosol deposition by interception (K. W. Lee & Gieseke, 1979) and impaction (D'Ottavio & Goren, 1982) in packed beds.

Both packed beds and the alveolar region of the lung have a high surface-area to volume ratio, which in the case of a packed bed can be tuned to equal that of the lung (Gebhart & Heyder, 1985). As a result, several studies have used simple packed bed models as an approximate surrogate of the human lung for deposition in the sedimentation and diffusion regimes. Brand et al. (1994) used a packed bed model as a test case to evaluate the sensitivity of the aerosol derived airway morphometry approach. It was assumed that aerosol bolus dispersion was identical in the lung and packed bed tube filled with 0.8 mm beads. Rosenthal et al. (1992) compared aerosol dispersion in a packed bed tube and in human subject studies. Aerosol dispersion in the human lungs was largely influenced by the larynx and breath-pause period, which were not captured in the packed bed media. Hence, inclusion of the upper airways and laryngeal jet were shown to be important. Rosati et al. (2003) used a packed bed model as an "approximate surrogate to the human lung" to compare the difference in the deposition of polydisperse and monodisperse aerosols.

Very few studies have previously generated a hybrid *in vitro* airway model by combining a realistic extrathoracic airway model with a packed bed model of the lower lungs. This interesting idea was originally suggested by Gebhart and Heyder (1985). As shown in Figure 1 of their study, they approximated the mouth-throat as a 90-degree bend

41

and reproduced the first several bronchi leading to a packed bed. Modifications to the packed bed length and bead size allowed the model to capture deposition by diffusion and sedimentation consistent with *in vivo* experiments. In a short conference paper by Saini et al. (2002), a hybrid model is reported consisting of a larynx cast and glass bead model in a triangular geometry containing three different glass bead sizes. This model could theoretically capture impaction, sedimentation and diffusion deposition mechanisms similar to lung airways. However, comparisons to *in vivo* data of lung aerosol deposition are not provided.

Similar to Gebhart and Heyder (1985), an appealing approach for creating a complete airway *in vitro* model is to combine a realistic 3D printed upper airway geometry with a packed bed structure. Realistic upper airway geometries have been shown to predict delivery efficiency of aerosols to the lungs consistent with *in vivo* data (R. Delvadia et al., 2012; R. R. Delvadia, Hindle, et al., 2013; Yu Zhang, Gilbertson, & Finlay, 2007). Packed bed arrangements can capture correct surface area to volume ratios of the lung as well as correct sedimentation and diffusion properties of submicrometer particles (Gebhart & Heyder, 1985). However, it is not currently known if packed beds can capture impaction similar to airway bifurcations in the mid- and lower-level bronchi. Introducing a jet of airflow to a packed bed will spread through the bed in a manner that may be similar to a bifurcating network. Furthermore, the intersections of packed spheres form flow dividers that will serve as aerosol deposition points potentially similar to the branching airways.

The envisioned hybrid-style complete-airway model for an infant consists of a realistic upper airway geometry derived from a CT scan together with a shell of the plural

region. The plural cavity is filled with monodisperse beads. Of interest is whether the packed bed region can capture correct total deposition similar to the lung airways and if the model can capture regional (spatial) deposition distributions. Matching both total and regional deposition will require correctly capturing impaction, sedimentation and diffusion mechanisms at the appropriate time scales and flow rates of respiration. More advanced complete-airway models will implement multiple bead sizes, as with Saini et al. (2002). However, the first challenge is to determine if a packed bed of spheres can capture impaction similar to the bronchi and bronchioles of the respiratory airways.

2.3   Methods

An overview of the systems considered in this study is shown in Figure 2.1. The infant complete-airway *in vitro* model integrates a CT-scan-based upper airway geometry through B3 with a packed bed structure to represent the remainder of the lungs (Figure 2.1a). The realistic model is truncated at approximately B3 based on resolution of the CT scan and structural integrity of the model. The TB airways extend beyond B3 through bifurcation B15, which contains the terminal bronchioles and leads to the respiratory bronchioles containing alveoli. A stochastic individual pathway model, as developed by Longest et al. (Longest, Tian, Delvadia, et al., 2012; Longest, Tian, Walenga, et al., 2012; Tian et al., 2011), is shown in Figure 2.1b extended from B3 exits through B15. The respiratory airways contain approximately 300,000 bronchi/bronchioles (including the respiratory bronchioles) and 480 million alveoli (Ochs et al., 2004), which is not practical to reproduce with current 3D printing technologies. To represent the conducting airways, this study implements a packed bed (PB) model as shown in Figure 2.1c. The tube shown in the PB model is the transition between the outlet of B3 to the sphere array. It is expected

that this transition region will have an important impact on performance of the PB model. This study focuses on deposition comparisons between the SIP and PB models, using CFD simulations. These systems, as well as the complete-airway model, are described in more detail in the following sections.

Infant Complete-Airway Model

The infant complete-airway *in vitro* model (Holbrook, 2015) was originally developed to evaluate the improved compliance of the lung while administering surfactants to infants. The upper airways (MT-B3) of the infant complete-airway model were based on an adult model (Walenga, Tian, & Longest, 2013) referred to as Model D, and scaled to match infant morphometric data (Phalen, Oldham, Beaucage, Crocker, & Mortensen, 1985). The lower airways (B4 onwards) are represented by a pleural cavity shell, constructed from an infant computed tomography (CT) scan that was completely filled with 6 mm diameter spheres. The pleural cavity was scaled so that the Functional Residual Capacity (FRC) was 150 mL of airspace after the spheres were added. The 6 mm spheres were initially selected for the infant complete-airway model because the hydraulic diameter of the triangular void between three connected spheres (0.62 mm) is a reasonable approximation of the number average diameter of the remaining infant tracheobronchial airways from B4 to B15 (0.45 mm). However, this sphere diameter may not be ideal, and the current study intends to determine whether alternative sphere sizes may be more suitable for matching deposition in the infant lung. To represent the airway surface liquid, 12 mL of water was added to the pleural cavity to form liquid bridges between the connected spheres. Administration of surfactant to the model reduced the

surface tension of these liquid bridges and improved lung compliance in a realistic way (Holbrook, 2015).

CFD-Packed Bed (PB) Model

A CFD model was constructed to represent the PB region of the complete-airway model with a focus on the junction between the B3 outlet and surrounding spheres (CFD-PB model; Figure 2.1c). The sphere arrangement is a hexagonal close packed formation, which gives the maximum packing density for equal diameter spheres. To account for the water added to the infant complete-airway model, filleted surfaces represent the liquid bridges between each connected sphere. The 0.29 mm radius of these fillets (see Figure 2.1) determines the added volume of the liquid bridges, which matches the 12 mL of water used in the infant complete-airway model.

The inlet duct of the CFD-PB model is equivalent to the outlet of the upper airways in the infant complete-airway model. That is, the CFD-PB inlet represents the transition from the infant complete-airway upper airways to the pleural cavity filled with spheres. The results evaluate two examples of CFD-PB models: one that replicates the infant complete-airway model with the spheres representing the lung from B4 onwards (CFD-PB B4+), and another where the spheres represent the lung from B7 onwards (CFD-PB B7+). The intention of the CFD-PB B7+ case is to determine whether the spheres should only model the smaller tracheobronchial airways, with inclusion of more of the bifurcating lung geometry upstream of the packed bed.

The inlet duct points toward the center of what this study refers to as the *first sphere.* The distance from the inlet duct to the first sphere is the same as the length from the inlet to the carina for the first bifurcation that the CFD-PB model represents. For

example, the CFD-PB B4+ case uses a distance from the inlet to the first sphere that matches the carinal length of B4. Imposing this distance on the CFD-PB configuration aims to capture impaction on the surface of the first sphere similar to the first bifurcation that this sphere replaces. Other cases are evaluated that consider the packed bed after the inlet duct, thereby looking at a cross-section (CS) of the sphere array, which are referred to as CFD-PB CS models. These models do not use an inlet duct and instead introduce flow into the domain through the entire CFD-PB model rear inlet surface (Figure 2.3a).

The CFD-PB models (Figure 2.3) extend three sphere diameters laterally both above and below the tubular inlet, with respect to gravity, to capture spreading of the airflow in the packed bed. Symmetry is present along the center of the inlet duct, so the domain extends three sphere diameters away from this symmetry plane. In the axial (downstream) direction, each case has an adjusted domain length so that particles do not escape through the outlet during a realistic transport time. At most, the domain extends 16 sphere diameters.

ICEM CFD 14.5 meshing software (ANSYS, Inc., Canonsburg, PA, USA) generated the tetrahedral, Delaunay mesh for the domain (Figure 2.3b). There is a conformal mesh interface between the inlet mesh and remaining domain, with a one-to-one match between vertices and cell faces (Figure 2.3c). This ensures there is no interpolation of variables across the interface when solving the flow field. The mesh accurately resolves the shape of the filleted surfaces between spheres with appropriately aligned mesh lines (Figure 2.3c). The two near-wall prism layers included in the mesh are

sufficient to resolve the boundary layer under low-speed, laminar flow conditions. The volume mesh quality has a minimum value of 0.1.

To minimize the numerical error in the CFD results, a mesh dependency study was performed to identify the most efficient and accurate cell size for the models. The deposition profiles for a coarse (1.6 million cells), and fine (12.9 million cells) mesh for the CFD-PB B4+ geometry were compared to determine if results converge to the same solution as the cell size is decreased. The deposition fraction for the coarse and fine mesh had an absolute difference of 0.2% for the 5.0 µm particles. Reducing the refinement level lower than the course mesh made it difficult to resolve the curvature of the fillets between sphere contacts. As these meshes give similar results, the coarse mesh was used for all simulations. At most, the cell count for the largest evaluated domain (CFD-PB CS) is approximately four million cells.

CFD-Stochastic Individual Path (SIP) Model

Previous studies by our group have documented the details and development of the SIP approach for CFD modeling of the complete airways (Longest et al., 2015; Longest, Tian, Delvadia, et al., 2012; Longest, Tian, Walenga, et al., 2012; Tian et al., 2011). Briefly, a SIP geometry is a randomly determined individual pathway through the lung from B4 to B15, where at each bifurcation, one branch is continued and one is not. Previous work by our group has shown that following a pathway through the lower left lobe of the lung provides deposition characteristics that are representative of the average of all lobes (Longest, Tian, Delvadia, et al., 2012). CFD simulations of the SIP geometry begin with the B4 inlet and assume steady laminar flow. Velocity and particle profile inlet conditions are generated from simulations in upstream airways. While it is known that

turbulence is generated in the laryngeal jet and extends often past B4 based on CFD simulations (Xi, Longest, & Martonen, 2008) our previous results indicate that the best agreement with human *in vivo* data for pharmaceutical aerosols is achieved assuming turbulence occurs above B4 and laminar flow occurs below B4 (Longest et al., 2015; Walenga & Longest, 2016). To allow for the injection of additional particles to best resolve deposition, the SIP model simulations were divided into B4-B7 and B8-B15 sections.

The bifurcations used in the previously developed adult SIP models are based on a physically realistic geometry (Heistracher & Hofmann, 1995) and adult morphometric data (Yeh & Schum, 1980), which provide anatomically accurate models. Simulating the lung bifurcations with the SIP method greatly reduces computational processing times, and studies have validated the results against experimental *in vitro* (Longest, Tian, Delvadia, et al., 2012; Longest, Tian, Walenga, et al., 2012; Tian et al., 2011) and *in vivo* (Longest et al., 2015; Walenga & Longest, 2016) data.

To create the infant CFD-SIP model, available morphometric data must be scaled to match infant dimensions. A review of the literature (Dunnill, 1962; Herring, Putney, Wyatt, Finkbeiner, & Hyde, 2014; Hislop, Wigglesworth, & Desai, 1986; Langston, Kida, Reed, & Thurlbeck, 1984; Thurlbeck, 1982) shows large variation in measurements of infant FRC and volume fractions of the bronchial, bronchiolar, and alveolar-interstitial regions, which are the morphometric data required to scale from adult to infant dimensions. As an alternative approach, the scale factor used to convert from adult to infant dimensions was taken as the ratio of the average B3 outlet diameter from the infant complete-airway model and the adult morphometric data (Yeh & Schum, 1980), which gives a value of approximately 0.29.

Applying this dimensional scale factor to the adult morphometric lung data (Yeh & Schum, 1980) results in an FRC of approximately 145 mL. This value is within the span of lung volumes found in the literature for infants, which range from 127 mL (Hislop et al., 1986) to 222 mL (Herring et al., 2014), and matches well with the 150 mL FRC used in the infant complete-airway model. Furthermore, the World Health Organization (WHO) Growth Charts (WHO, 2006) indicate that the 50th percentile female and male has a height of 49 cm and 50 cm respectively at birth, which applied to infant airway dimension correlations (Phalen et al., 1985) gives a B3 outlet diameter of approximately 2.55 mm with a standard error of 0.37 mm. This compares favorably with the average B3 outlet diameter from the infant complete-airway model, which is 2.30 mm.

Transport Equations and Numerical Methods

The ANSYS FLUENT 14.5 software package (ANSYS, Inc., Canonsburg, PA, USA) was used to solve the flow field and particle trajectories through the domain. The model settings use the best practices developed by our group in previous projects (Longest et al., 2015; Longest, Tian, Walenga, et al., 2012). In brief, this includes double precision accuracy, use of the SIMPLEC algorithm for pressure-velocity coupling, second-order upwind spatial discretization for flow variables, and the Runge-Kutta scheme for particle tracking.

The model simulates the infant lung under mechanical ventilation, which uses a sinusoidal volumetric flow rate over a 0.5 s interval (further details are described below). Therefore, the problem is time-dependent by nature, and the model requires transient flow conditions with first-order implicit temporal discretization. The solver uses a relatively small time-step size, and runs a suitable number of iterations between these time steps.

For all cases, a time step size of 0.005 s is small enough that the change in inlet velocity between time steps is minimized and 100 iterations per time step accurately resolves the flow field.

The peak inlet velocity is 2.68 m/s for the CFD-PB B4+ case, which occurs halfway through the sinusoidal ventilation inhalation profile and is the highest inlet velocity considered. This gives an estimated maximum Reynolds number at the inlet of approximately 400. This is far below the critical Reynolds number value for internal flow, so the laminar viscous model is sufficient for the flow environment. Therefore, particles are not subject to turbulent conditions, such as turbulent dispersion or the effects of turbulent anisotropy near wall boundaries.

As the CFD-PB model represents the lung distal to at least B4, the gravity force is included to capture the sedimentation deposition mechanism, which becomes more important as the velocity slows. In the PB geometry, the effect of gravity acting in 3 separate orientations is considered. Because particle diameters are 0.5 µm and higher, effects of Brownian motion are neglected.

Considering particle injection profiles, the CFD-PB models implement a parabolic particle distribution (Longest & Vinchurkar, 2007b). This particle profile captures the fact that particle flux into the geometry starting from a well-mixed upstream concentration is proportional to the local fluid velocity flux. For the CFD-PB CS case, where particles enter throughout the PB geometry, a random uniform concentration is assumed at each of the multiple inlets.

The injected size distribution separates the particles into nine bins, with particle diameters between 0.5 and 10 µm. The particle injection introduces 500 particles of each

bin size per time step, which totals 450,000 particles tracked through the domain. Previous work by our group has shown that this method gives suitable particle convergence (Longest, Tian, Walenga, et al., 2012).

At birth, the 50th percentile weight for girls and boys is 3.2 and 3.4 kg respectively, based on the WHO Child Growth Chart (WHO, 2006). The selected ventilation parameters for an infant in this weight range are a tidal volume (V_t) of 28.4 ml and inspiration time (t_{in}) of 0.5 s (Walsh & DiBlasi, 2010). For a sinusoidal flow profile, the transient inlet velocity (v_i) based on ventilator parameters and inlet area (A_i) is:

$$v_i = \frac{1}{2} \frac{\pi C V_t}{t_{in} A_i} \sin\left(\frac{\pi}{t_{in}} t\right)$$

(2.3.1)

Equation (2.3.1) is found by using an arbitrary sinusoidal volumetric flow rate curve ($Q = A\sin(\omega t)$) and integrating to get the volume of air added to the lung at any given time ($V = \int Q\, dt$). The known added volumes at zero time ($V(0) = 0$) and inspiration time ($V(t_{in}) = V_t$) are applied to determine the A and ω parameters that defined the volumetric flow rate. The volumetric flow rate is then divided by the inlet area to find the transient inlet flow velocity. The scaling parameter (C) is included to control the fraction of the tidal volume that enters through the inlet of the CFD-PB models, as they represent a fraction of the entire lung. For the CFD-PB models, the scaling parameter is the inverse of the number of outlets at the upstream bifurcation level, so that the flow though the CFD-PB model represents the fraction of the lung in question. For example, if the CFD-PB model represents B4-B15, the scaling parameter is one eighth, as there are eight outlets at the B3 level.

For the CFD-PB models, evaluating a sub-domain of a larger packed bed imposes challenges when defining the boundaries between adjacent domains in a numerical

model. Each CFD-PB case uses wall boundaries at the left, rear, top, and bottom sides of the simulated domain (see Figure 2.3), and the results assume that these boundaries have little influence, as they are sufficiently far away from the region of interest. To verify this assumption, the velocity magnitude close to these wall boundaries is evaluated for all cases and the geometry is deemed suitable if the magnitude is small relative to the region of primary particle deposition. Furthermore, particle deposition on the domain extremes are checked, and the geometry is considered sufficiently large if very few (<0.1%) particles deposit on these wall boundaries.

As the sides of the CFD-PB sub-domain that connect to adjacent domains are walls, the side opposite the inlet defines an outlet boundary to permit flow through the sphere array. An outflow defines the boundary condition at this outlet, with a weighting of one, such that all flow entering through the inlet leaves through this boundary. For the CFD-SIP model, outlets also use outflow boundary conditions, except that each outlet has half of the mass flow rate that enters the inlet at each bifurcation level.

Comparison Criteria

Deposition efficiency (DE) is the mass of particles that deposit in a pre-defined region, over the mass of particles that enter that region, expressed as a percentage:

$$DE_i = \frac{\text{Mass Deposited in Region i}}{\text{Mass Entering Region i}} \times 100 \qquad (2.3.2)$$

The advantage of the DE is that results can compare individual regions of interest directly by excluding upstream particle deposition.

Deposition fraction (DF) is the mass of particles that deposit in the entire computational domain, over the mass of particles that enter the domain through the inlet, expressed as a percentage:

$$DF = \frac{\text{Mass Deposited}}{\text{Mass Injected}} \times 100 \qquad (2.3.3)$$

The DF can be calculated from the DE by:

$$DF = 1 - \prod_{i=1}^{n} (1 - DE_i) \qquad (2.3.4)$$

where n is the number of bifurcations or sphere layers in a given range. DF provides an estimate of total deposition in a region by considering all upstream losses.

Residence time (t_{res}) is the amount of time that a particle spends within a pre-defined region of the domain. For the entire domain, the residence time is the difference between the time the particle escapes through the outlet boundary and the time the particle entered the domain. Similarly, for a given range of sphere layers, the residence time is the difference between the times that the particle crosses the first and last layer of spheres in the range.

2.4   Results

Comparison of CFD Predictions and Algebraic Correlations for Deposition

To verify that the CFD predictions of infant aerosol deposition are reasonable, comparisons were made across a particle size range of 0.5 to 10 μm to established algebraic correlations. The CFD model included the infant mouth-throat (MT), upper tracheobronchial region through B3, and remaining TB region as a SIP geometry through B15, resulting in an Infant MT-B15 model. The algebraic correlations for comparison capture particle deposition due to sedimentation and impaction. Three correlation models were considered, which implement different approximations for deposition. Specifically, the Finlay model (W. H. Finlay, 2001) combines an analytical approximation for sedimentation (Heyder & Gebhart, 1977) and an empirical impaction probability (Chan &

Lippmann, 1980). The ICRP (ICRP, 1994) and Rudolf (Rudolf, Kobrich, & Stahlhofen, 1990) models both use the same empirical expressions, but use different parameters to predict DE in the MT, upper tracheobronchial, and lower tracheobronchial regions.

Figure 2.4 shows that the CFD results from the Infant MT-B15 model compare reasonably well with the range of established algebraic correlations. The Infant MT-B15 model deposition data also exhibits the expected S-shape profile, where smaller particles with lower Stokes numbers are able to follow the flow streamlines, and larger particles deviate from the streamlines and deposit due to impaction. As predictions from the Infant MT-B15 CFD model compare well with these established algebraic correlations for impaction and sedimentation in the airways, it is acceptable to use it as a benchmark for comparison when evaluating the suitability of packed bed *in vitro* lung models. Hence, the deposition characteristics for a range of bifurcations in the CFD-SIP model can be compared with the CFD-PB model to determine whether the latter accurately represents drug deposition in an infant lung.

Influence of CFD-PB Walls on Velocity Field

To ensure the CFD-PB domain is sufficiently large, the velocity magnitude near the top, bottom, left and rear of the model is evaluated for all cases before analyzing particle deposition. Figure 2.5 shows an example of such a velocity field, and that applying wall boundaries conditions at all locations, except the inlet and outlet, does not influence results. The velocity field in Figure 2.5 is for the CFD-PB B4+ case at the peak of the sinusoidal inhalation, which gives the highest inlet velocity for all cases considered. The nodal value at Point A is 1.2e-5 m/s and is considerably smaller than the maximum value in the domain (3.8 m/s). Figure 2.5 also shows that the air entering the domain is a

54

relatively high velocity jet directed at the first sphere opposite the inlet duct, which is immediately diffused. The implications of this phenomenon on particle deposition are discussed further below.

Effect of Inlet Style on Particle Deposition in CFD-PB Models

The outlet from the prototyped upper airways can be located in the CFD-PB model in a number of different configurations, which are presented in Figure 2.6b-d. The naming convention for CFD-PB inlet configurations refers to the direction of the duct with respect to the sphere array. As randomly filling the pleural cavity makes it difficult to determine the sphere arrangement around the prototyped bifurcation, the sensitivity of the model to each inlet configuration is evaluated.

Figure 2.6a compares the three inlet configurations and the possible gravity orientations for each case based on transport during the infant inhalation period. The X and Y inlet configurations both show very similar deposition profiles, whereas the Z inlet configuration resulted in less deposition than the other cases. The Z inlet requires the removal of one sphere from the array to include the inlet duct, which means there is a greater distance between the inlet and the nearest wall where particles may deposit. This is the likely cause of differences in results and demonstrates the importance of the inlet configuration. Note that the distance from the inlet to the first sphere opposite the duct matches the carinal length for B4 for the X, Y, and Z inlet configurations.

Changing the gravity orientation for each inlet configuration has little influence on the DF for all particle sizes. As expected, there is a very small amount of deposition due to sedimentation in the upper tracheobronchial airways. Subsequent subsections

investigate the total and regional deposition characteristics of the CFD-PB model in more detail.

Figure 2.6 demonstrates that the model is not sensitive to the inlet direction with respect to gravity, but it is sensitive to how close the spheres are to the inlet duct. To minimize the influence of the inlet position on deposition results, the sphere arrangement around the bifurcation outlet can be included in a prototyped model. Using the Z inlet configuration, the first sphere in the packed bed can be located at a given distance from the inlet duct. To ease the transition from realistic airway bifurcations to the packed bed, the first sphere can be located at a distance from the inlet that matches the distance to the carina for the next bifurcation. Therefore, subsequent cases that require an inlet duct use this type of inlet configuration, with carinal lengths of 3.92 mm for the CFD-PB B4+ case and 2.25 mm for the CFD-PB B7+ case.

Effect of Sphere Size on Particle Deposition in CFD-PB Model

Figure 2.7 compares the deposition profiles over inhalation for three CFD-PB B4+ cases that each use a different sphere diameter; as the sphere size increases, the DF decreases. This demonstrates that *total deposition* in a packed bed experimental model can be potentially tuned to match the behavior of an infant lung by varying the sphere size. However, the results show that deposition is very sensitive to small changes in sphere size for larger particles (>3 µm). For example, the DF for 5 µm particles drops by approximately 50% and 80% (relative difference) as the sphere size increases from 1.0 mm to 1.5 mm and 2.5 mm respectively. Therefore, selecting an appropriate single sphere size, or even several sphere sizes, to represent the infant lung for a wide range of particle diameters would be difficult.

Comparison of Particle Deposition in CFD-SIP and CFD-PB Models

Figure 2.8 compares deposition in the CFD-SIP results with the CFD-PB B4+ and B7+. In Figure 2.8a, the CFD-PB B4+ model uses 6 mm spheres and represents the infant lung distal and inclusive of B4, and the CFD-SIP results show DF from B4 to B15. The total DF compares quite well between the CFD-SIP and CFD-PB B4+ models, with the absolute error decreasing from 5.22% for the 0.5 µm particles to -7.55% for the 7 µm particles. Note that particles larger than 7 µm are neglected here as it is expected that most would deposit in the MT-B3 region.

In Figure 2.8b, the CFD-PB B7+ model again uses 6 mm spheres, but this time uses the inlet from B7 to introduce flow into the domain. The CFD-SIP results show DF data from B7 to B15. In this case, the CFD-PB B7+ model matches the DF of the CFD-SIP model better for the sub-micrometer particles than CFD-PB B4+, with absolute errors that are less the 1%. However, the results do not compare well for the larger (>4 µm) particles.

The deposition profiles in Figure 2.8 show how the models behave with regard to total deposition, but do not describe the spatial deposition through the lung. Figure 2.9 shows the particle deposition in three regions for the CFD-PB B4+ case. The three regions are the sphere directly opposite the inlet duct, the spheres that surround the inlet duct, and then the remaining spheres in the domain. The inset image shows the 3D particle deposition on the first sphere. From Figure 2.9, it is clear that the majority of deposition occurs on the first sphere that the particles encounter as they enter the packed bed. This goes against the intended behavior of the model, as the packed bed should

replicate the lung bifurcations by allowing particles to penetrate into downstream regions of the domain matching both total and regional deposition.

If a packed bed model can be designed to overcome the impaction issue at the inlet that is apparent in Figure 2.9, it is important to evaluate how the particles travel through the rest of the packed bed domain. Figure 2.10 compares the deposition profile from a CFD-PB CS case through a number of layers with the results from B5 to B15 of the CFD-SIP. Up to 16 layers of spheres are included in the CFD-PB CS model, as this covers the maximum distance that the particles travel through the domain during the transient inhalation profile. Note that consistent residence time between the CFD-PB CS and CFD-SIP models is not considered at this stage, but is explored below. These results show that the total DF is much higher across all 16 sphere layers than the CFD-SIP model. The only way to match particle deposition between the two models is to consider just one layer of spheres in the CFD-PB CS model. Again, this shows that regional deposition in a packed bed model does not compare well with what is expected in the infant lung.

Comparison of Particle Residence Time in CFD-SIP and CFD-PB Models

Figure 2.11a and b show frequency plots of particle residence time through the B4-B7 and B8-B15 regions of the CFD-SIP model respectively. Table 2.1 shows the mean and range of particle residence times for the full CFD-SIP model. The results for CFD-PB B4+ through two sphere layers are presented in Figure 2.11c and Table 2.2. Two sphere layers were selected so that the mean residence time for all particle sizes compares well with the CFD-SIP data (0.089 s for CFD-PB vs. 0.097 s for CFD-SIP). However, the standard deviation (SD) and spread of data in the plots shows that there is considerably

more variability in residence time in the CFD-PB model (SD = 0.080 for CFD-PB vs. 0.023 for CFD-SIP). This is likely due to the number of different pathways that particles can take when they reach a sphere junction compared to a bifurcation. Similar behavior is seen when looking at the results for the CFD-PB CS case in Figure 2.11d and Table 2.3. Here the CFD-PB CS model covers nine sphere layers to match the mean residence time (0.099 s for CFD-PB vs. 0.097 s for CFD-SIP), but again there is more variability in the particle residence times (SD = 0.053 for CFD-PB vs. 0.023 for CFD-SIP).

Comparative Dimensions of CFD-PB and CFD-SIP Models

These results have so far focused on quantitative values for DF and the residence time of particles travelling through the CFD-PB domains. A qualitative comparison between the size of the CFD-PB and CFD-SIP models can also be made. The bounding box around the B4-B7 and B8-B15 sections of CFD-SIP have a diagonal length of approximately 18 mm and 13 mm respectively. This means roughly five sphere layers of the 6 mm spheres are required in the CFD-PB model to match the length of the CFD-SIP model. The results from Figure 2.11 show that two layers of 6 mm spheres after the inlet duct are required to match residence times between the CFD-PB B4+ and CFD-SIP models, and nine layers of 6 mm spheres are required for the CFD-PB CS case. Therefore, the overall dimensions of either version of the PB model that would be capable of representing residence time are considerably different from the SIP model. This finding is further complicated by the other fundamental issue highlighted by the results of this study, which is the majority of particles impact on the first sphere of the CFD-PB model. As such, regional deposition results for an optimized packed bed model, in terms of both deposition and dimensions, would not be representative of human lungs.

2.5 Discussion

This study concludes that packed bed models do not provide a realistic representation of aerosol deposition in an infant lung. Although total deposition compares well between the CFD-PB and CFD-SIP models, regional deposition via impaction behaves very differently in a packed bed than it does in lung bifurcations. The positive outcomes from this investigation are that the Infant MT-B15 model matches the deposition profile predicted by well-known algebraic correlations, and that the application of packed bed models for *a* complete-airway *in vitro* model have been more completely evaluated with a clear conclusion.

The lung deposition data from the Infant MT-B15 model were benchmarked against three well-known algebraic correlations (W. H. Finlay, 2001; ICRP, 1994; Rudolf et al., 1990), but ideally this study would compare with *in vivo* results. Unfortunately, in the literature to date, little *in vivo* aerosol deposition data are available due to ethical concerns associated with studies on infants. One study (Salmon, Wilson, & Silverman, 1990) evaluated aerosol delivery in 9 to 36 month old boys via a face mask and nebulizer system. However, the deposition was assessed by collecting urine samples and estimating lung absorption of the delivered dose, which only provides total lung deposition results. Several other studies (Amirav et al., 2002; Chua et al., 1994; Fok et al., 1996; Mallol, Rattray, Walker, Cook, & Robertson, 1996) used gamma scintigraphy to obtain regional deposition data, but were all performed on diseased lungs (cystic fibrosis, bronchiolitis, or bronchopulmonary dysplasia), which makes it difficult to compare the results with healthy infant lungs.

The geometry of the packed bed results in a flow field that is considerably different from airway bifurcations. This in turn gives particle deposition characteristics that are not comparable to the lung. The images in Figure 2.12 show the two possible ways that spheres may contact each other in a close-packed array, and the resulting voids available for airflow. Note that each of the voids shown in Figure 2.12b is connected to one of the orifices on the voids in Figure 2.12d, and so on in the sphere array.

The geometry in Figure 2.12b can be described as a trifurcation with triangular inlets and outlets. The walls of the trifurcation are very close to any potential outlets, which may explain the amount of impaction deposition seen in the results. The general shape of the geometry also contrasts greatly with lung pathways, which are typically bifurcations with circular or elliptical cross sections and have longer straight sections approaching each bifurcation. The geometry in Figure 2.12d is further removed from observations of human lung anatomy. Here, multiple flow pathways converge in a relatively large cavity, which suggests a chaotic flow field and particle motion. In summary, the shape and characteristics of the voids between packed bed spheres do not resemble lung bifurcations, which explains why the aerosol deposition results do not compare well in this study.

It is important to recall that the focus of this study was on impaction deposition in a packed bed that is dimensionally similar to airway bifurcations. The major finding is that spatial and temporal deposition of aerosols in packed beds is very different from lung bifurcations. Hence, the packed bed model as constructed in this study cannot be used to form a complete-airway deposition model for particles in all size ranges that can correctly capture regional particle deposition. It does appear that a correctly configured

PB model can capture total lung deposition from impaction provided that multiple sizes of spheres are used.

These results have limited impact on previous studies that employed packed beds as lung models. For example, the study of Gebhart and Heyder (1985) focused on diffusion and sedimentation deposition of particles less than or equal to 1.5 μm in diameter. The study of Rosenthal et al. (1992) has already established that particles in PB models are dispersed differently over time than in human lungs, as we observed in Figure 2.11. However, this finding should not preclude the use of PB geometries as a uniform testing standard for comparison studies that require a model with fine scale structures or large surface-area to volume ratios as in the lungs. For example, the PB geometry remains an excellent model for evaluating the sensitivity of the Aerosol-Derived Airway Morphometry (ADAM) technique as with Brand et al. (1994).

One difference between an *in vitro* packed bed model and the CFD implementation in this study is the sphere arrangement. The geometry in the CFD model uses closely packed spheres, whereas an experimental model would typically lead to random packing. However, it is expected that the conclusions would be the same with a random fill sphere arrangement, as the key issue with packed beds is that the geometry is very different from lung bifurcations. A random fill sphere arrangement would only exacerbate the difference between a packed bed and the human lung, and lead to more variability in the flow field and particle deposition.

Based on the results of this study, we view the use of a PB in a complete-airway *in vitro* model as limited. One potential solution may be to 3D print airway bifurcations through the impaction zone of the TB airways and implement a PB for sedimentation and

diffusion deposition in the alveolar region. However, 3D printing all conducting airway pathways down to approximately B15 is currently not practical and may result in a very fragile structure. A PB alveolar region can accurately reproduce the deposition surface-area to air-volume ratio of the lungs. However, the overall volume of the model will be significantly larger than *in vivo* conditions due to the large volume occupied by the spherical solids. Hence, spatial resolution of regional deposition cannot be reproduced for direct comparisons with gamma scintigraphy radiolabeled aerosol deposition results. Provided that it is not important to match spatial resolution of deposition, the hybrid-style model of Saini et al. (2002) may be capable of capturing regional aerosol deposition. This model was composed of a laryngeal structure attached to a triangular geometry containing multiple levels of different sizes of spheres. Based on the illustration of the model, there are only 2 or 3 layers of spheres on each level, consistent with CFD predictions that large regions of bifurcating airways can be reproduced with several layers of spheres. Furthermore, the triangular structure of the container will allow for different uniform cross-sectional velocities in different zones of the model, enabling multiple deposition mechanisms to be captured. Provided that the lung is viewed as a series of concentric shells that are opened, laid flat, and stacked, the Saini et al. model may be worth further exploration as a complete-airway alternative. In contrast, truly resolving spatial and temporal deposition with an *in vitro* complete-airway model, which was the focus of this study may require the consideration of 3D printed *in vitro* upper airways together with tissue engineering or excised (*ex vivo*) animal lung models.

2.6 Figures
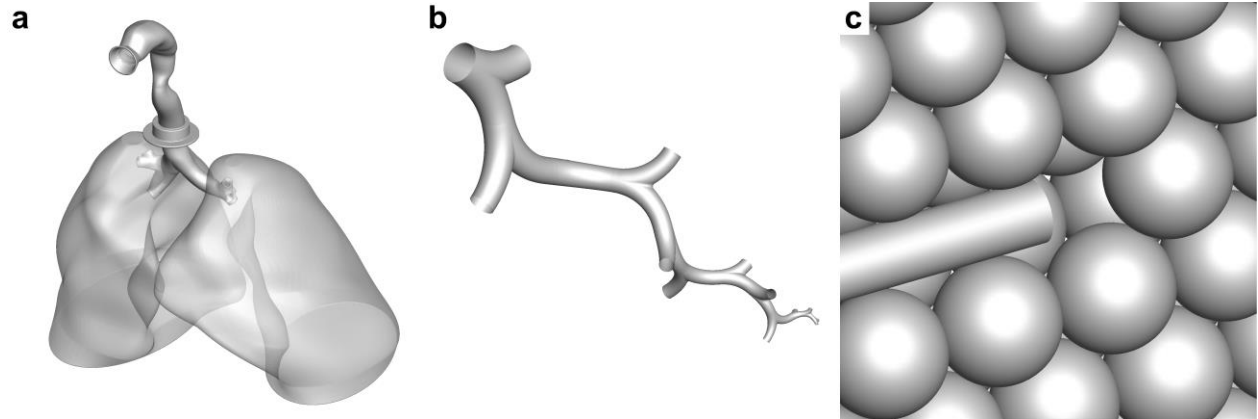
Figure 2.1:   Overview of models described throughout the study: (a) *In Vitro* Complete Airway Model, (b) CFD-SIP (B4-B15), and (c) CFD-PB (with B4 inlet duct).

a

∅6mm

R0.29mm

1

b

0.29mm

1

R3mm
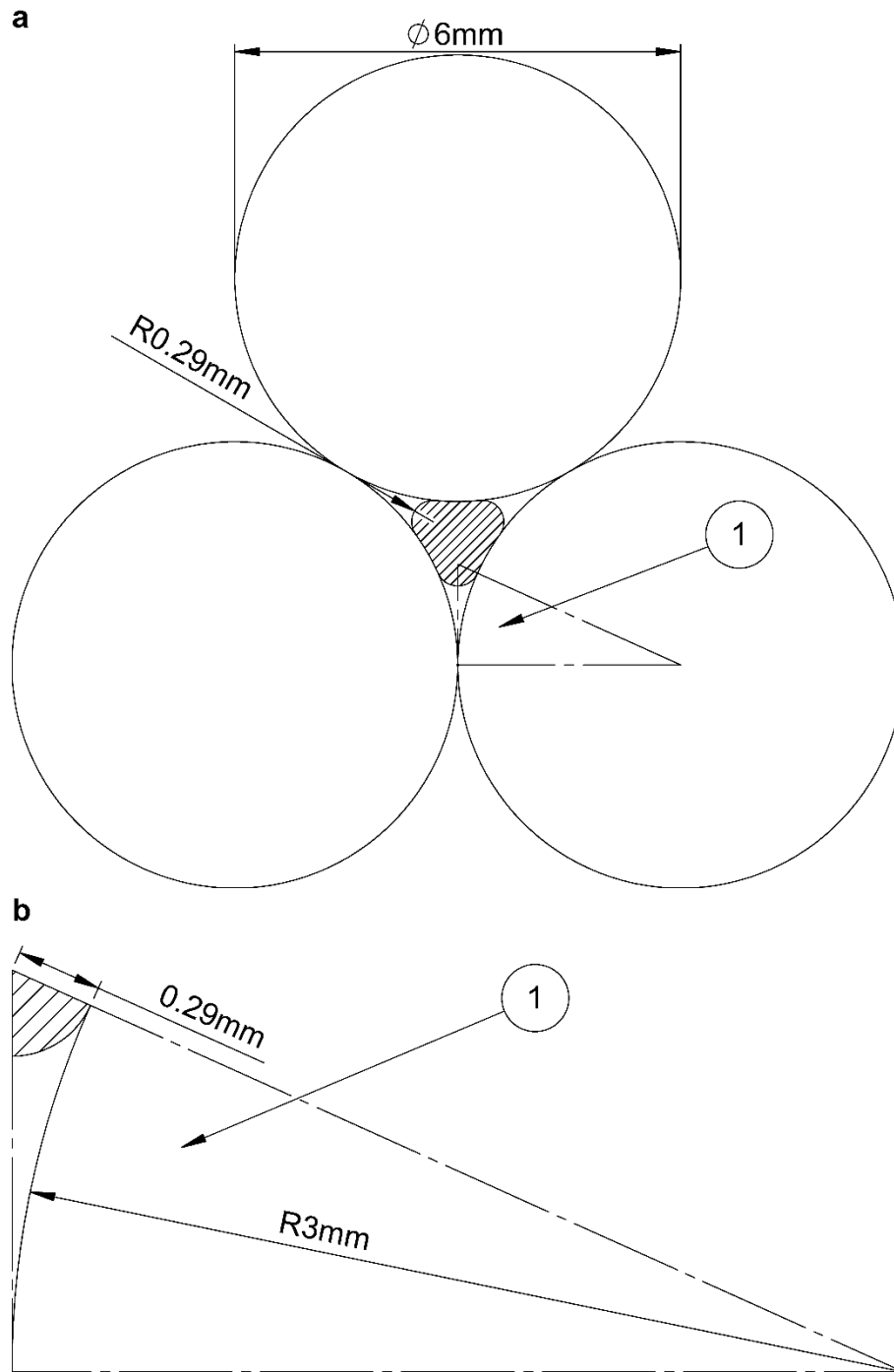
Figure 2.2: Geometry of (a) 6 mm packed bed with fillets between connected spheres and (b) close-up view of Triangle 1.
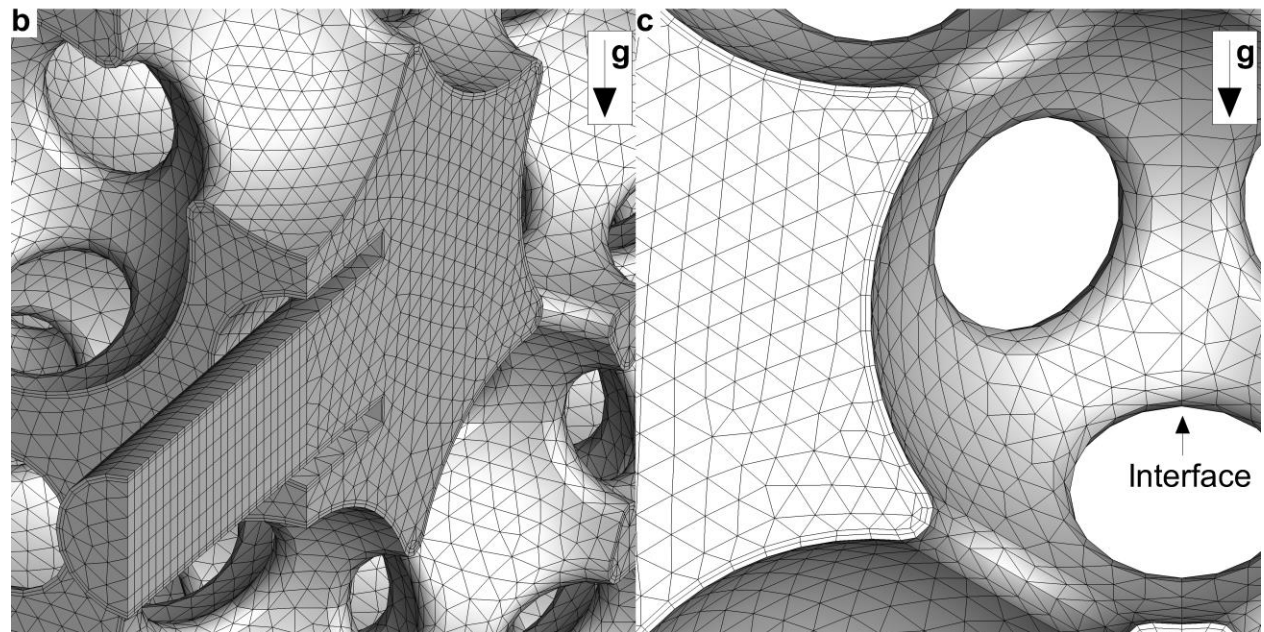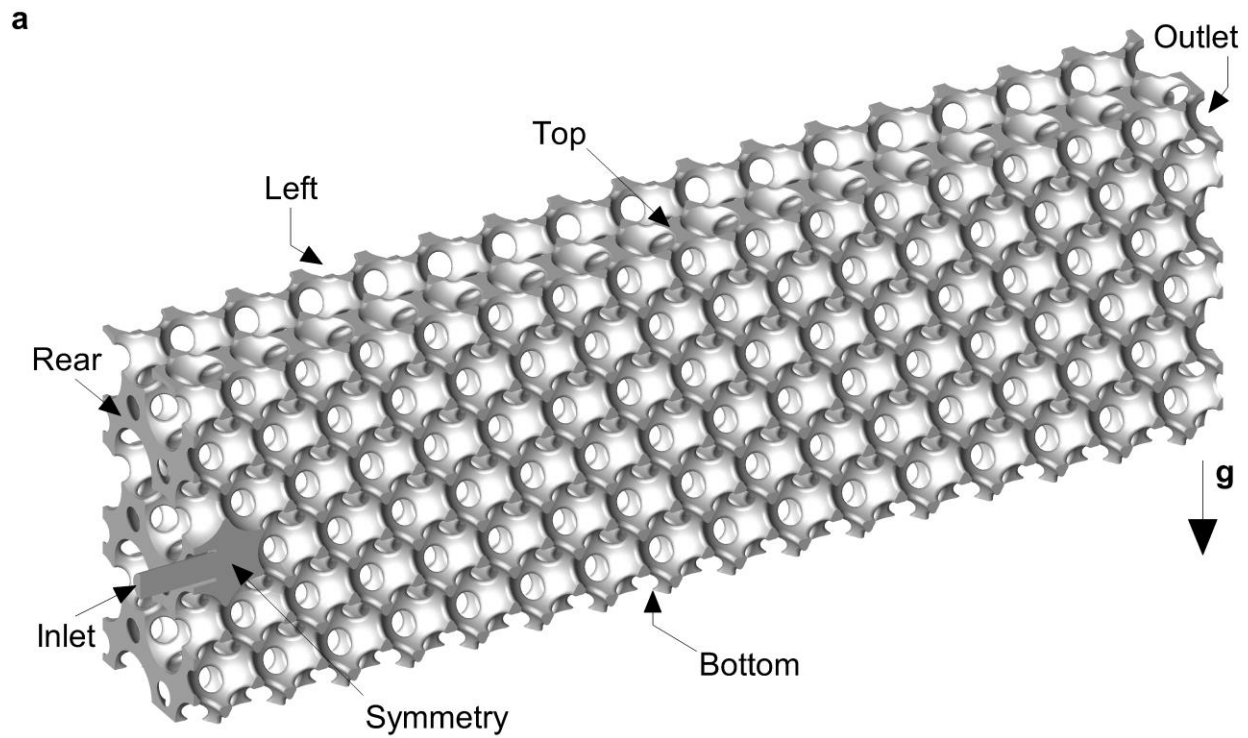
Figure 2.3:   CFD-PB mesh and geometry showing (a) isometric view of full sphere array, (b) close-up view of inlet duct mesh (with length to carina included), and (c) close-up view of first sphere that shows the conformal interface between unit cells, aligned mesh lines to capture fillets accurately, and near-wall prism layer mesh.
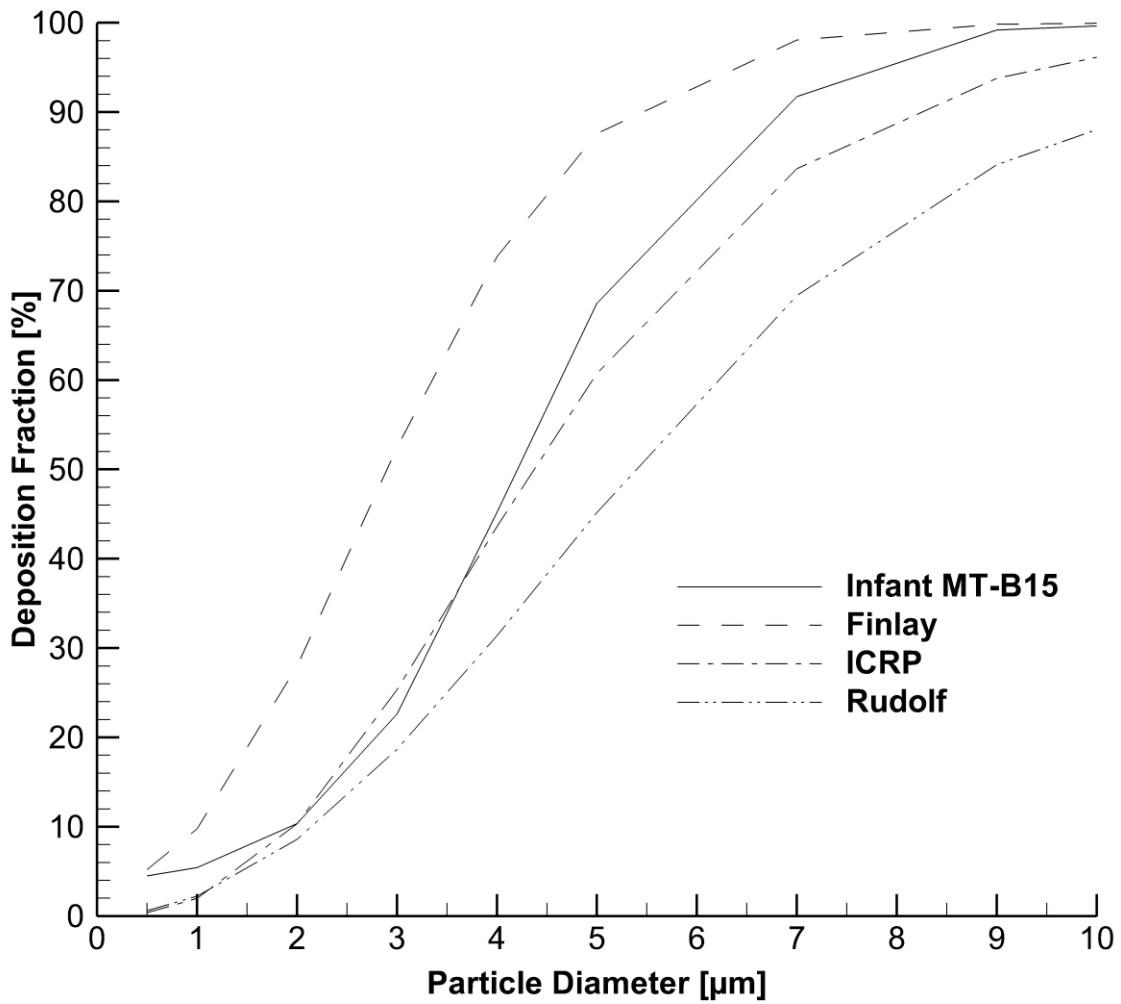
Figure 2.4:   Comparison of deposition profile for the Infant MT-B15 model predicted by
CFD with three well-known algebraic deposition correlations.
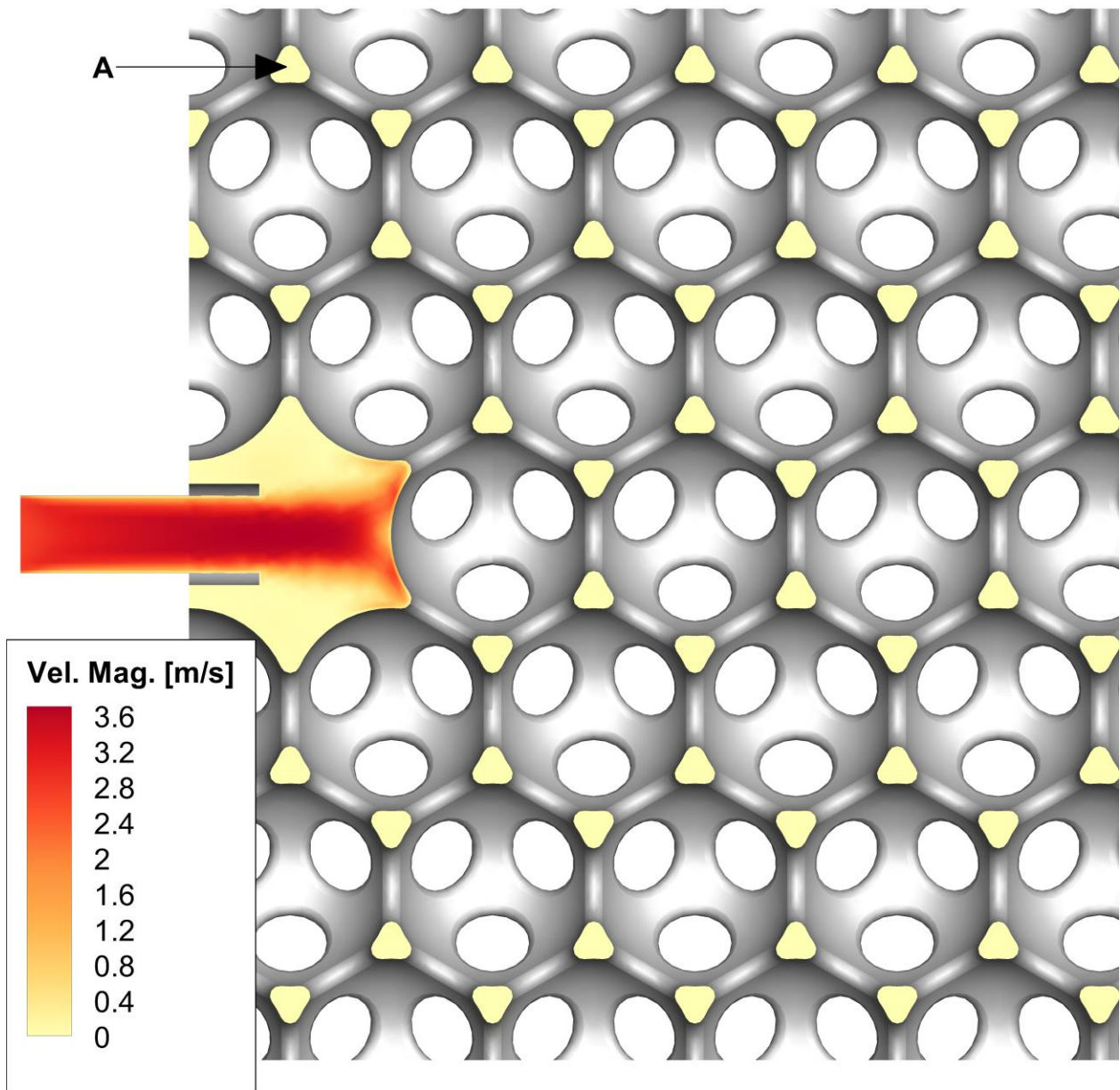
Figure 2.5:   Reduction of velocity magnitude close to the wall boundaries on the top, bottom, rear, and side of the domain, with a nodal value of 1.2e-5 m/s at Point A.
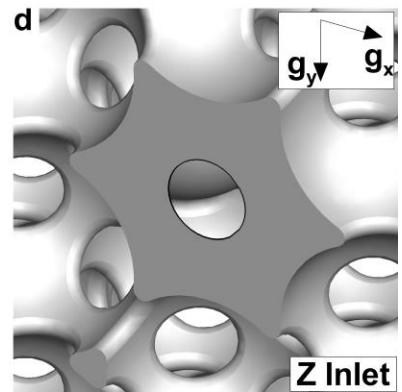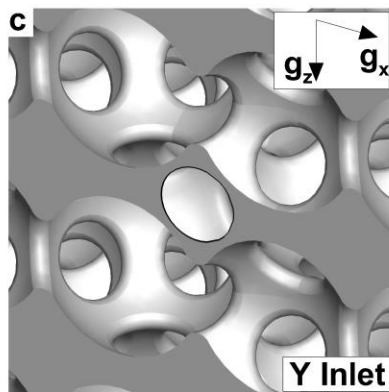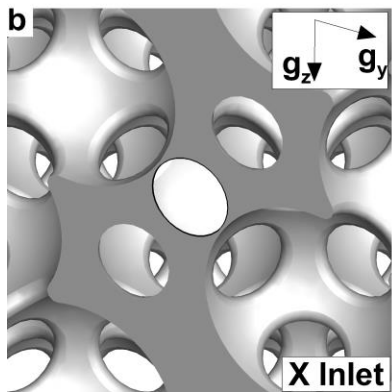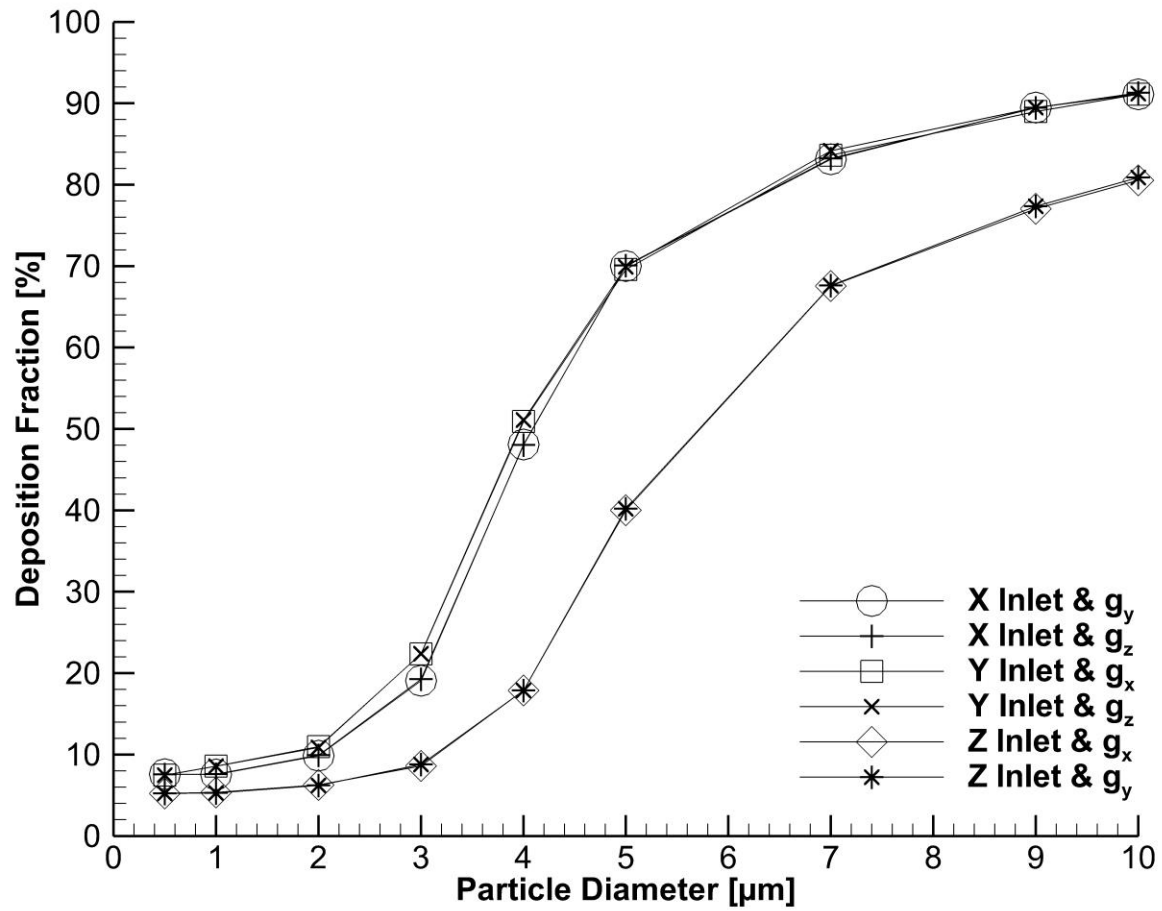
Figure 2.6:   Evaluation of inlet configurations with (a) showing the deposition profile for each case, and (b), (c), and (d) showing the X, Y, and Z inlet configurations, respectively.
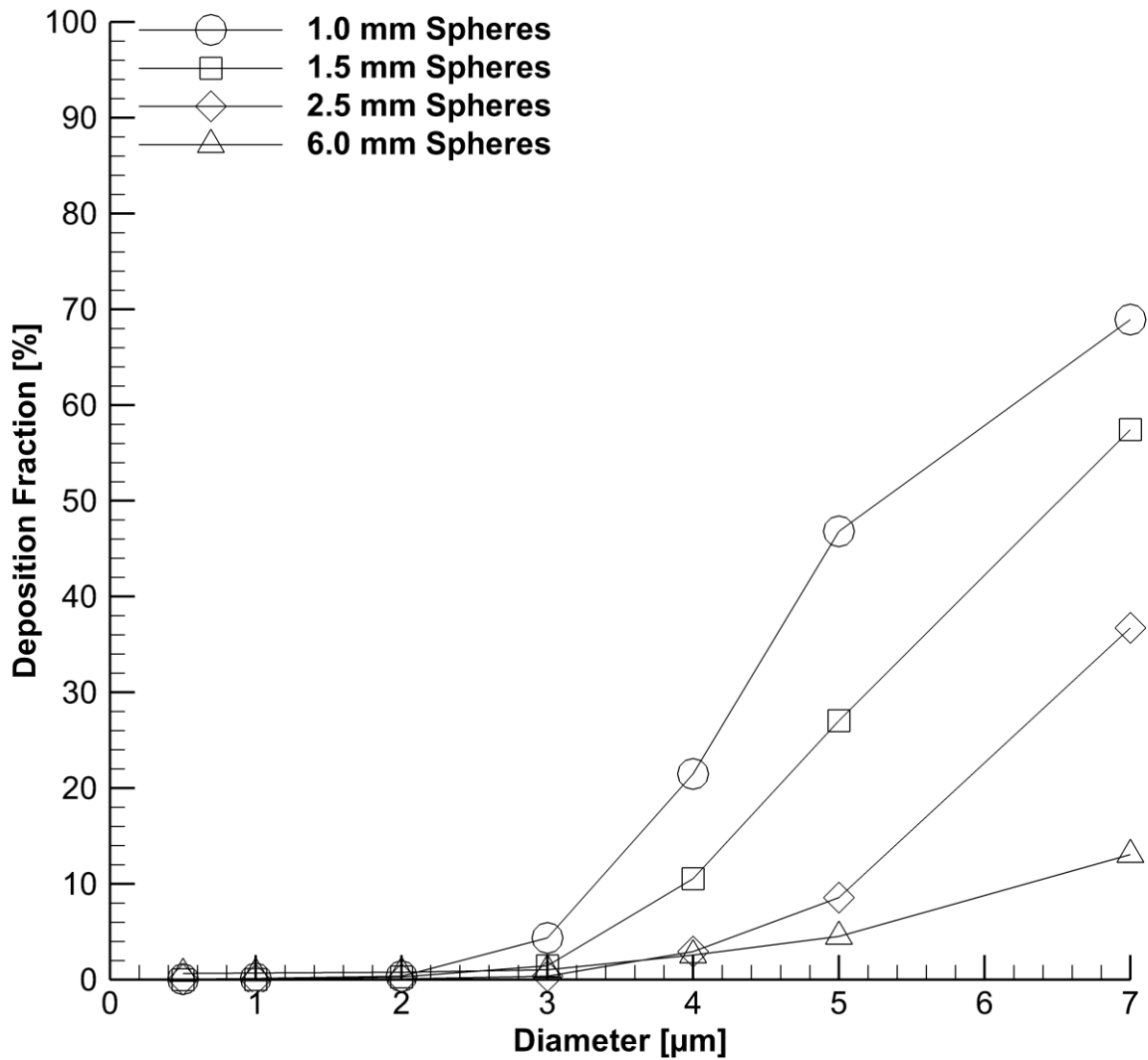
Figure 2.7:   Comparison of deposition profiles when varying the sphere diameter in the

CFD-PB B7+ model. Only the 0.5 to 7 μm particles are shown as the majority of larger

particles deposit in the upstream airways.
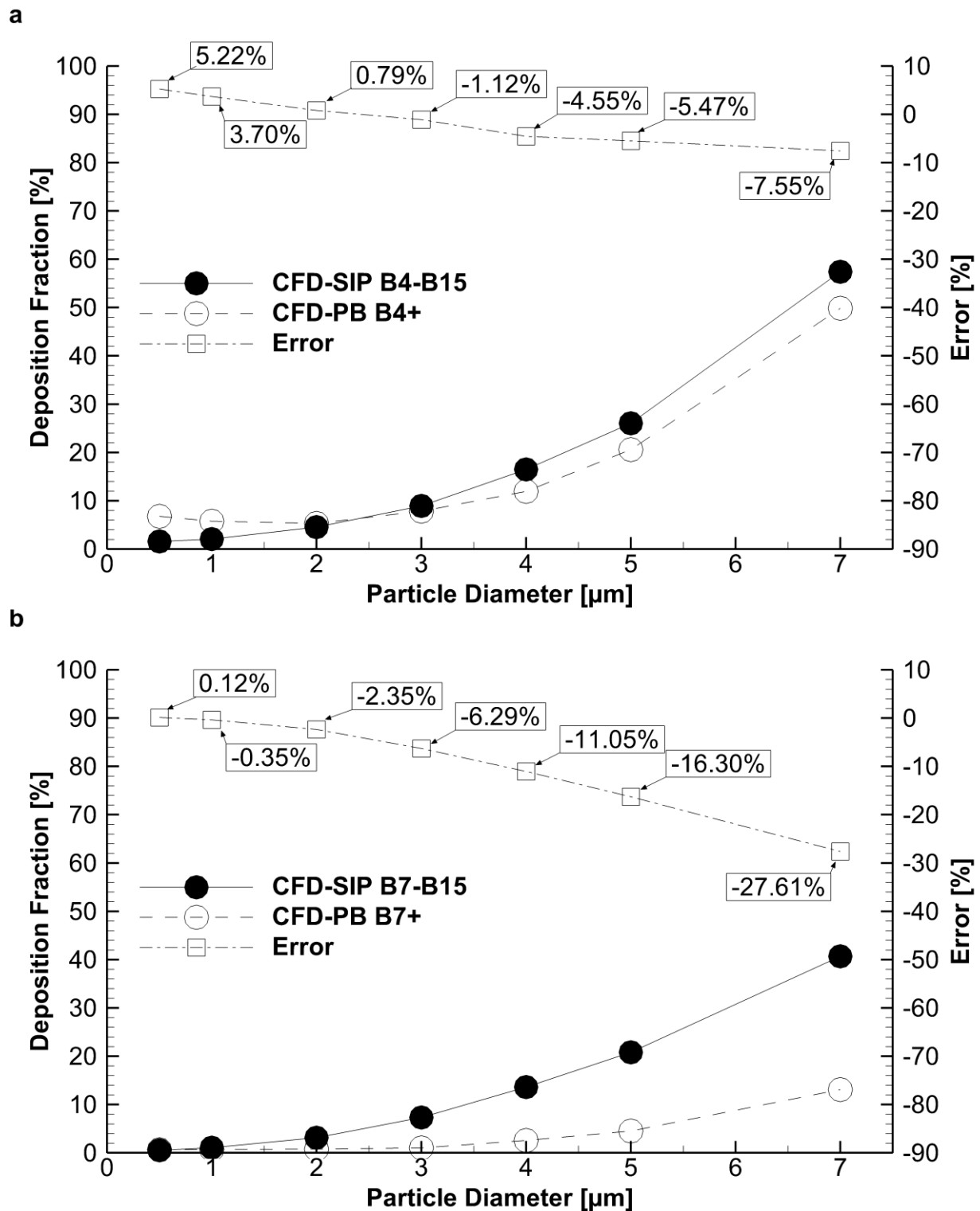
Figure 2.8:   Comparison of CFD-SIP results with (a) CFD-PB B4+ and (b) CFD-PB B7+.

Error (%) is presented as the absolute difference between the deposition fraction in the

CFD-SIP and CFD-PB models.
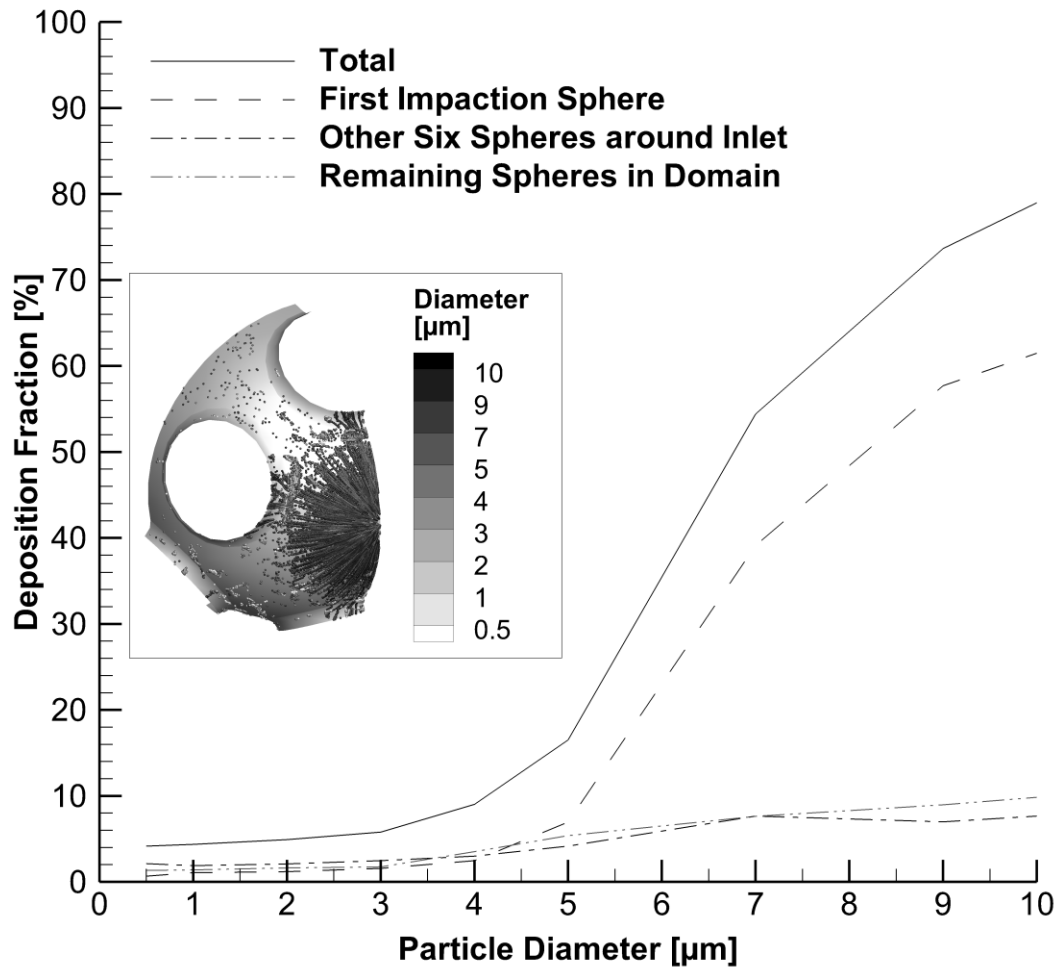
Figure 2.9:   Comparison of deposition fraction in multiple sphere zones of CFD-PB B4+.
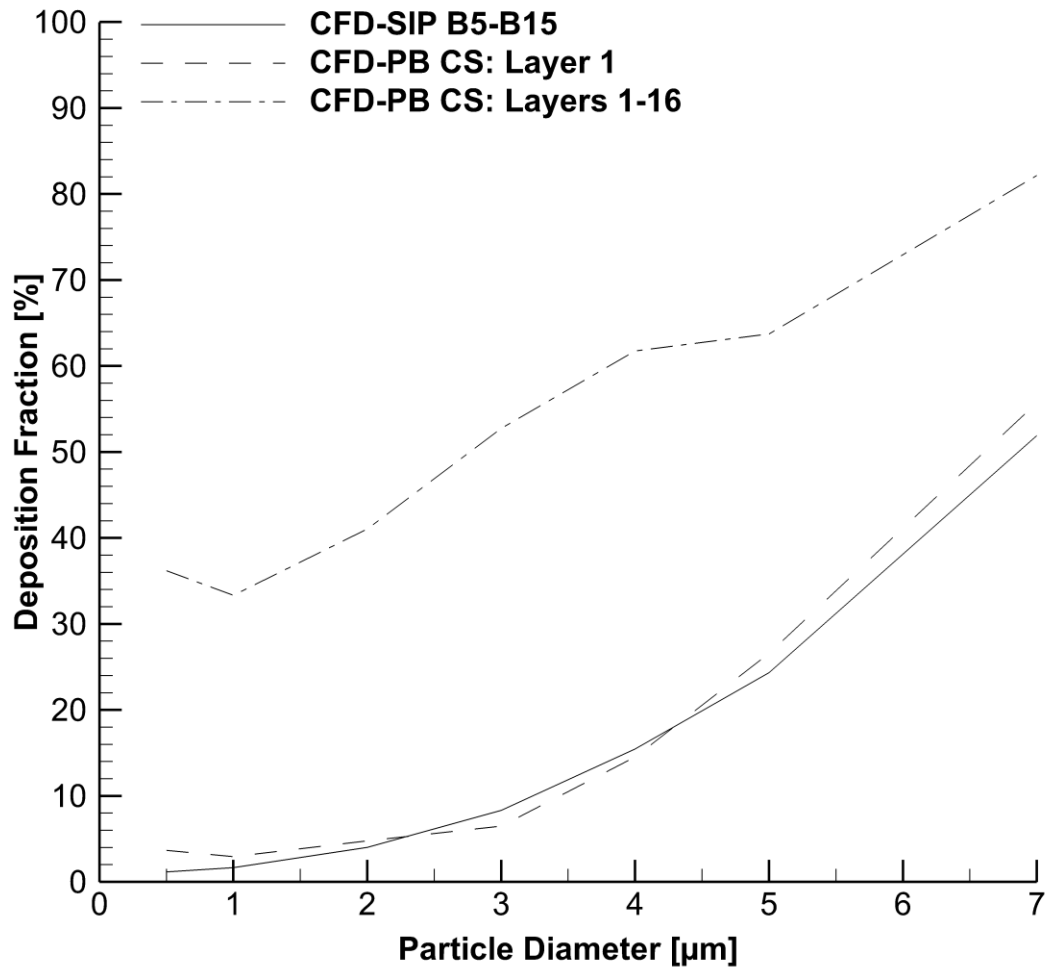
Figure 2.10: Number of sphere layers required in CFD-PB CS to match CFD-SIP deposition fractions.
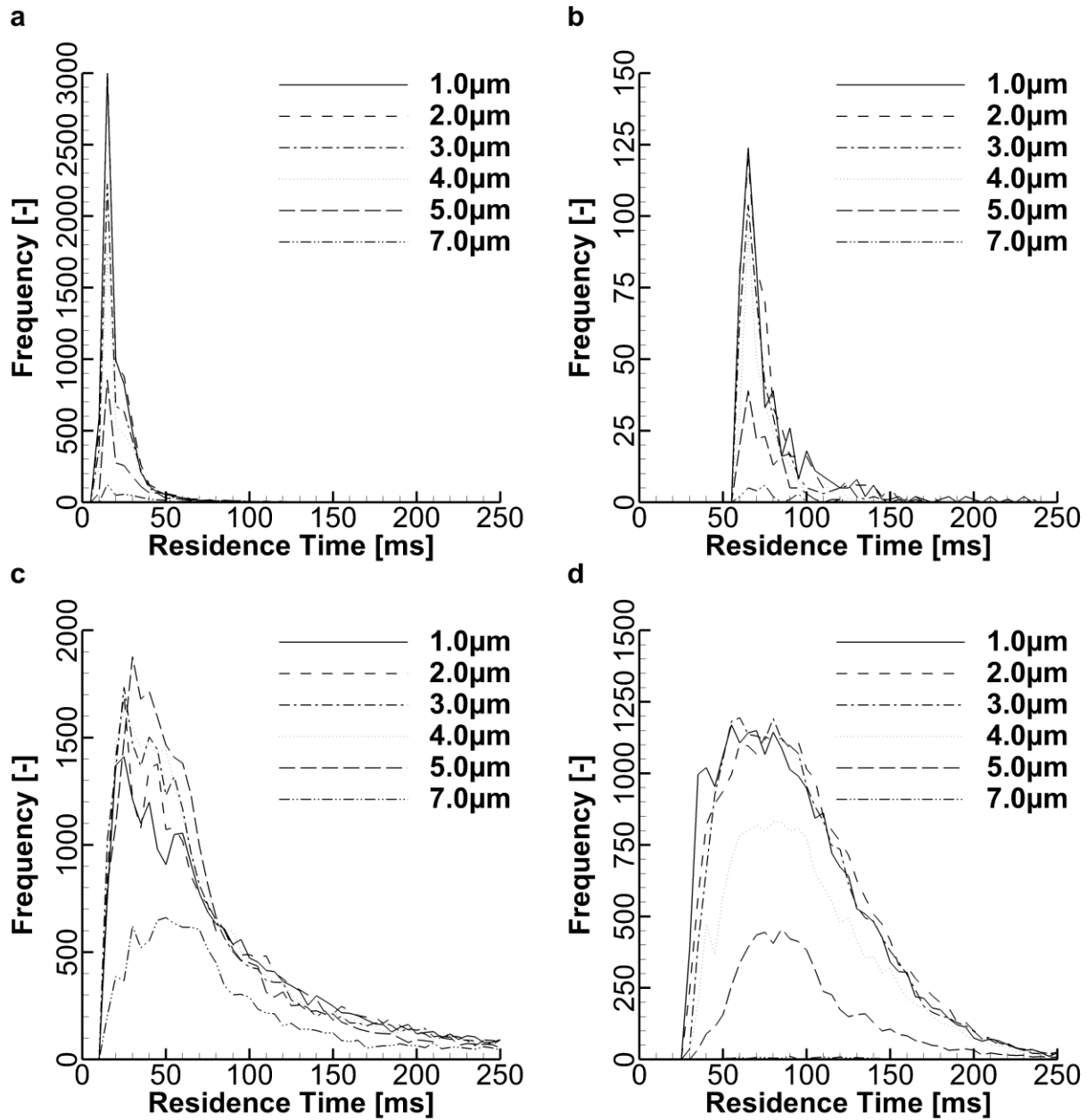
Figure 2.11: Particle number frequency distribution vs. residence time for (a) CFD-SIP B4-B7 and (b) CFD-SIP B8-B15, (c) CFD-PB B4+ through two sphere layers, and (d) CFD-PB CS through nine sphere layers. Number of spheres layers in each CFD-PB case was selected to match the mean residence time in the equivalent CFD-SIP model.
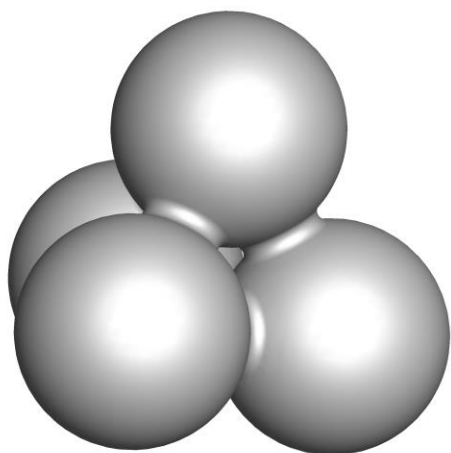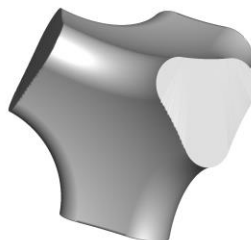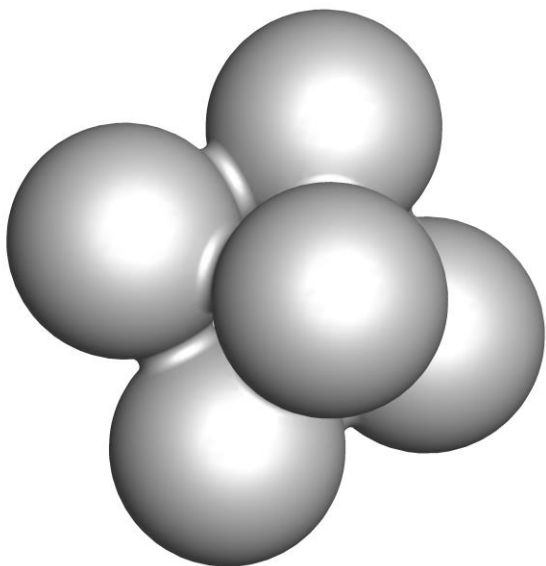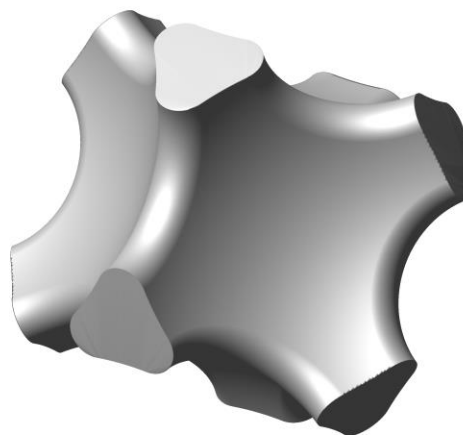
Figure 2.12: Basic geometry showing (a) trifurcation spheres, (b) trifurcation void (fluid), (c) large cavity spheres, and (d) large cavity void.

2.7 Tables

Table 2.1:   Residence time for the CFD-SIP model.

Particle Diameter [μm]	Count [-]	Mean (SD) Residence Time [s]	Minimum Residence Time [s]	Maximum Residence Time [s]
0.5	7073	0.102 (0.033)	0.076	0.427
1	7024	0.100 (0.029)	0.076	0.394
2	7228	0.098 (0.023)	0.077	0.413
3	5355	0.093 (0.018)	0.078	0.250
4	4225	0.095 (0.019)	0.078	0.251
5	2151	0.093 (0.014)	0.080	0.186
7	408	0.099 (0.014)	0.084	0.141
0.5-7	33464	0.097 (0.023)	0.076	0.427

Table 2.2:   Residence time for the CFD-PB B4+ model through two sphere layers.

Particle Diameter [μm]	Count [-]	Mean (SD) Residence Time [s]	Minimum Residence Time [s]	Maximum Residence Time [s]
0.5	24630	0.090 (0.081)	0.011	0.489
1	23925	0.093 (0.081)	0.011	0.482
2	24886	0.089 (0.078)	0.010	0.471
3	25796	0.086 (0.079)	0.011	0.494
4	26031	0.086 (0.078)	0.012	0.477
5	26478	0.082 (0.076)	0.011	0.485
7	12570	0.099 (0.085)	0.012	0.490
0.5-7	164316	0.089 (0.080)	0.010	0.494

Table 2.3:   Residence time for the CFD-PB CS model through 12 sphere layers.

Particle Diameter [μm]	Count [-]	Mean (SD) Residence Time [s]	Minimum Residence Time [s]	Maximum Residence Time [s]
0.5	26354	0.091 (0.048)	0.025	0.448
1	23697	0.091 (0.046)	0.026	0.466
2	23744	0.096 (0.046)	0.026	0.452
3	22847	0.094 (0.044)	0.027	0.448
4	16105	0.099 (0.046)	0.027	0.435
5	6847	0.099 (0.045)	0.031	0.455
7	126	0.124 (0.086)	0.046	0.421
0.5-7	119720	0.099 (0.053)	0.025	0.466

Chapter 3: Recommendations for Simulation of Microparticle Transport and Deposition Using Two-Equation Turbulence Models

3.1 Objective

The objective of this study is to determine both mesh and CFD solution parameters that enable the accurate simulation of microparticle deposition under flow conditions consistent with the upper respiratory airways including turbulent flow. To represent conditions similar to the upper respiratory airways, a simple 90° curved tube is selected as a characteristic geometry. This geometry provides a different test scenario than the constricted tube model that is typically used to represent turbulence in the upper airways. Both the nasal and MT airways contain curved tube features that are associated with high particle deposition. Furthermore, deposition in bifurcations is often approximated with correlations for deposition in curved tubes (Martonen et al., 2000). The comparison metric considered will be total microparticle deposition, based on the well documented experimental results of Pui et al. (1987) with Re = 6,000 and Re = 10,000. For comparison, Breuer et al. (2006) previously published LES in curved tubes with excellent agreement when compared with Pui et al. (1987). In addition to an evaluation of mesh and solution parameters, a key question to be addressed is whether the LES agreement with experiments (Breuer et al., 2006) can be matched with the correct use of a much simpler and computationally efficient two-equation turbulence approach.

3.2 Introduction

Laminar, transitional and fully turbulent flows are all expected to occur in the upper respiratory airways. Transitional and turbulent flow as well as the process of flow regime change from laminar to turbulent flow is notoriously difficult to predict and can be

influenced by upstream conditions, wall surface roughness and even environmental noise (Schlichting, 1987; Tennekes & Lumley, 1972; Wilcox, 1998). Transitional and turbulent flows are known to have a significant impact on particle deposition through the interaction of turbulent eddies and discrete elements, which typically increases deposition compared with the laminar flow case (Crowe, Troutt, & Chung, 1996). Therefore, accurate predictions of lung doses arising from either inhaled pollutant particulate matter or pharmaceutical aerosols requires reasonable approximations of both the turbulent flow field and the interaction of turbulent eddies with particles.

The upper airways consist of the oral and/or nasal geometry, trachea and approximately the first six airway bifurcations. Jets of airflow with flow detachment and recirculation are formed in the nasal valve and larynx (Xi et al., 2008; J. X. Xi et al., 2012). As described in previous experimental and numerical results (Ahmed & Giddens, 1983a, 1983b; Ghalichi et al., 1998), transition to turbulence in flow constrictions of 50 and 75% area reductions occurs at Reynolds numbers of approximately 1,100 and 400, respectively, which are significantly lower than the typical value of 2,300 for a straight cylindrical conduit. Considering a mean inhalation flow rate of 60 L/min (LPM), upper-airway Reynolds number values for an adult range from approximately 10,620 (larynx) to 553 (bifurcation B6). Peak inhalation flow rate with a dry powder inhaler (DPI) can reach 160 LPM (R. R. Delvadia, Wei, Longest, Venitz, & Byron, 2016), significantly multiplying these Reynolds number estimates at the point in time when the largest concentration of an inhaled pharmaceutical aerosol is entering the lungs. Furthermore, inhalers introduce air jets or sprays in the mouth-throat (MT) geometry, which are frequently turbulent and significantly impact MT depositional loss of the aerosol (DeHaan & Finlay, 2004; Longest,

80

Hindle, Das Choudhuri, & Xi, 2008). In a previous study of the laryngeal jet, Xi et al. (2008) showed that the turbulent viscosity ratio maintained a value of at least 2 through bifurcation B6 at an inhalation flow rate of 30 LPM. The study of Lin et al. (2007) also showed turbulence intensity values of 20% extending from the laryngeal jet into the lungs. A number of studies have demonstrated the importance of turbulence on deposition throughout the upper airways (Ball, Uddin, & Pollard, 2008; Jayaraju, Brouns, Lacor, Belkassem, & Verbanck, 2008; Lambert, O'Shaughnessy, Tawhai, Hoffman, & Lin, 2011; Longest, Tian, Delvadia, et al., 2012; Matida, Finlay, Breuer, & Lange, 2006; Xi et al., 2008; J. Xi & Longest, 2007; Z. Zhang & Kleinstreuer, 2011). Surprisingly, some of these studies have shown that turbulence can increase or decrease depositional loss (Longest & Vinchurkar, 2007b; Xi et al., 2008). While eddy interaction serves to increase depositional particle losses, the blunt turbulent velocity profiles can actually reduce impaction at carinal ridges. Furthermore, increased eddy viscosity can reduce secondary flows and associated particle impaction on bifurcation sidewalls.

Turbulence has been captured in respiratory airway geometries with models that range in complexity from the one-equation Spalart-Allmaras model (Wilcox, 1998) to full resolution of all turbulence scales with direct numerical simulation (DNS) (C. L. Lin et al., 2007). Specific examples include two-equation turbulence models such as the k-ε (Stapleton, Guentsch, Hoskinson, & Finlay, 2000) and k-ω (Xi et al., 2008; Z. Zhang & Kleinstreuer, 2011), detached eddy simulation (Jayaraju et al., 2008), large eddy simulation (LES) (Jayaraju et al., 2008; Jin, Fan, Zeng, & Cen, 2007; Matida et al., 2006) and DNS (C. L. Lin et al., 2007). In general, studies that compare results from multiple models typically find that the simpler model is inadequate compared with the more

complex model. This move to more complex turbulence models makes the simulation of large airway regions including the influence of transient inhalation over a 5 s period impractical due to the time and computational power that is required to run the simulations. Critical questions that are often overlooked in turbulence model comparison studies include: (i) what impact will discrepancies in velocity and turbulence parameters have on particle deposition, (ii) are the simpler models being properly applied, and (iii) is the most developed version of each simpler model being applied. For example, Ball et al. (2008) compared experimental results with predictions of two-equation turbulence models and found discrepancies in the velocity and turbulent kinetic energy (TKE) results. However, particle deposition was not considered and the more recent Low Reynolds Number (LRN) k-ω model was not included. Matida et al. (2006) compared aerosol deposition between LES and shear stress transport (SST) k-ω turbulence models and found significantly better predictions with the LES model compared to *in vitro* experiments. While these results were based on particle deposition, they did not include LRN k-ω predictions and neglected near-wall (NW) corrections, which were previously shown to be important (Matida, Finlay, & Grgic, 2004). Similar findings of superior performance with a LES model compared with a standard k-ω model without NW corrections were reported by Jayaraju et al. (2007). Furthermore, while LES has been found to be more accurate than two-equations models based on the predictions of turbulence properties, the increase in computational cost is very large. In a simple representative geometry of a curved pipe at Re = 10,000, Breuer et al. (2006) reported that grid convergent results required approximately 2.3 million control volumes. In a constricted pipe test geometry, Zhang and Kleinstreuer (2011) reported that LES

simulations required approximately 100-fold more computer power than using a two-equation turbulence model.

Two-equation turbulence models implement the Reynolds Averaged Navier Stokes (RANS) equations and simulate turbulent effects typically with a kinetic energy (k) and dissipation (ε or ω) term. Transport equations are formed for the two turbulence terms, which are then combined into a turbulent viscosity scalar that is present in the RANS equation and functions as an added viscosity on the flow field (Wilcox, 1998). The effect of turbulence on particle dispersion is then approximated through the use of an eddy interaction model, which implements the turbulence terms to stochastically recreate eddy structures and predict associated chaotic motion of particles as a random walk (Crowe et al., 1996). A primary shortcoming of all two-equation turbulence models is the assumption of isotropic (direction independent) turbulent fluctuations near wall boundaries (Wilcox, 1998). Matida et al. (2004) provided a NW correction for anisotropic turbulence effects, which has frequently been applied (Longest & Hindle, 2009a; Longest et al., 2007; Longest et al., 2008). Longest and Xi (2007) reported that improved NW interpolation of the velocity field was also needed in turbulent simulations using two-equation models. Of the available two-equation models, the LRN k-ω model has been most successful in predicting transitional and turbulent flows including reasonable predictions of particle deposition (Kleinstreuer & Zhang, 2003; Longest & Hindle, 2009a; Longest et al., 2007; Longest et al., 2008; Longest, Tian, Delvadia, et al., 2012; Longest, Tian, Walenga, et al., 2012; Longest & Xi, 2007; Tian et al., 2011; Z. Zhang & Kleinstreuer, 2003, 2011). Low Reynolds number refers to the fact that the model simulates the flow field all the way through the viscous sub-layer, i.e., the low Reynolds number region, and

can be successfully applied to both low and high Reynolds number flows (Wilcox, 1998). The primary advantage of two-equation models is high efficiency approximation of very complex transitional and turbulent flow phenomena. However, questions remain if these models can successfully be applied to predict particle deposition in the upper respiratory airways (Ball et al., 2008; Matida et al., 2006).

Studies that have used the LRN k-ω model with NW anisotropic and sometimes velocity interpolations have reported reasonable agreement with experimental results of turbulence metrics and particle deposition. Zhang and Kleinstreuer (2003) compared the performance of two-equation turbulence models in a constricted flow geometry and showed that the LRN k-ω model reproduced laminar, transitional and turbulent flow characteristics comparable with the experimental measurements of Ahmed and Giddens (1983a, 1983b, 1984). Other studies also using the constricted tube geometry have reached similar conclusions (Ryval, Straatman, & Steinman, 2004; Varghese & Frankel, 2003). The more recent study of Zhang and Kleinstreuer (2011) considered a series of two-equation turbulence models compared with LES in constricted tube and MT geometries. The LRN k-ω model was again shown to perform well and predictions of nanoparticle deposition in the MT were similar to LES. Our group has successfully applied the LRN k-ω model to predict particle deposition in the upper respiratory airways with good agreement to *in vitro* (Longest & Hindle, 2009a; Longest, Tian, Walenga, et al., 2012; Longest & Vinchurkar, 2007b; Longest & Xi, 2007) and *in vivo* (Longest et al., 2015; Walenga & Longest, 2016) studies. These simulations have considered pharmaceutical aerosols including jet and spray effects from DPIs (Longest, Tian, Delvadia, et al., 2012; Longest, Tian, Walenga, et al., 2012; Tian et al., 2011), metered dose inhalers (MDI)

(Longest, Tian, Walenga, et al., 2012; Walenga & Longest, 2016; Walenga et al., 2013), and soft mist inhalers (R. R. Delvadia, Longest, Hindle, & Byron, 2013; Longest & Hindle, 2009a; Longest, Hindle, & Das Choudhuri, 2009). For example, Longest et al. (2012) showed that the MT deposition predicted by the LRN k-ω model with NW corrections was within 10% of *in vitro* experimental data for complex pharmaceutical aerosols including the effect of polydisperse aerosol size, transient inhalation over an approximately 5 s period and turbulence for MDI and DPI devices.

Based on successful applications of the LRN k-ω model with NW corrections in predicting aerosol deposition in upper airway geometries, it appears that this model provides a good compromise between accuracy and efficiency. However, in other studies we have shown that computational mesh structure and type can have a dramatic effect on solution accuracy (Longest & Vinchurkar, 2007a; Vinchurkar & Longest, 2008). Guidelines for the use of the LRN k-ω model and for two-equation models in general are not well defined for applications to the respiratory airways. The current specification of 20 layers of computational cells through the turbulent wall region including the buffer layer (ANSYS, 2012) may be computational prohibitive for large complete-airway simulations (Longest, Tian, Delvadia, et al., 2012), and not necessary. Current recommendations may also be difficult to implement in complex geometries such as the nasal valve and larynx where flow passages are very narrow (Subramaniam, Richardson, Morgan, Kimbell, & Guilmette, 1998). For example, Walenga et al. (2014) reported excellent agreement with experimental results of particle deposition in the nose with a nasal cannula interface using only 5 NW cell layers. Furthermore, no recommendations are currently available for overall layer-to-layer (L2L) thickness of the NW mesh, or recommendations on the

method used to calculate gradients within control volumes, which interact with mesh type and resolution to influence the solution accuracy. Finally, mesh style in conjunction with turbulence modeling has previously not been considered in respiratory airway geometries.

3.3   Methods

Experimental Model and Results

This numerical study aims to evaluate mesh and CFD solution parameters based on comparisons with the experimental data from Pui et al. (1987) in a 90° curved tube geometry. The Pui et al. data was collected by measuring the deposition of monodisperse aerosols with Stokes numbers from 0.1 to 1.4 through glass and stainless steel 90° bends with internal diameters (ID) of 0.93, 3.95, 5.03, and 8.51 mm and Reynolds numbers (Re) of 100, 1,000, 6,000, and 10,000.

In this study, CFD-predicted aerosol deposition results are compared with the following Pui et al. (1987) experimental data sets: Re = 6,000 with ID = 5.03 mm; and Re = 10,000 with ID = 8.51 mm, which were both evaluated with stainless steel tubes. This covers a range of turbulent conditions and changes in the geometry by increasing the tube diameter. The correlation from the experimental study gives aerosol deposition efficiency (η) as a function of particle Stokes number (St), as:

$$\eta = 1 - 10^{-0.963St} \tag{3.3.1}$$

The deposition efficiency and correlation results for the selected experimental models are given in Table 3.1.

86

Numerical Geometry and Meshes

The inset in Figure 3.1a shows the full computational domain that matches the experimental setup of the Pui et al. (1987) geometry. The straight entry and exit sections of the tube were included to ensure that the flow is fully developed at the 90° bend inlet and smoothly exits the geometry, as was the case with the experiemental model. The curvature ratio (bend radius over tube radius) also matches the original setup, with ratios of 5.7 and 5.6 for the Re = 6,000 and 10,000 cases, respectfully.

Mesh Dependency

Preliminary results compared five meshes to evaluate the dependency of results on mesh resolution. The 90° bend section for each case had approximately 1,400,000, 672,000, 368,000, 208,000, and 83,000 hexahedral cells, inclusive of the NW layers. Initially, only the three finer meshes were compared, but results were almost identical, so the two coarser meshes were also evaluated. Consistency between deposition profiles (deposition fraction vs. particle diameter), velocity profiles at the inlet and outlets, and pressure drop across the tube were considered. Sensitivity of the turbulent flow to mesh resolution was also assessed by comparing u^+ vs. y^+ plots between the five meshes and to Spalding's equation (1961). These u^+ vs. y^+ plots were generated from data in the region of fully developed flow within the turbulent buffer and sub-layer near the wall.

The mesh dependency evaluation concluded that the coarse case (368,000 cells) gave the best compromise of small numerical error and reduced cell count. In several of the meshes that are evaluated in subsequent sections of this study, the resolution of the mesh in the NW region is adjusted to determine the influence on results. In all cases, the

core mesh (covering the bulk flow) for the grid independent case was retained, and different NW mesh resolution parameters are then applied.

Near-wall Mesh Resolution

Traditionally, there are two approaches to modelling the NW region when using two-equation RANS turbulence models. The wall function method uses an empirical formulation to model the flow in the inner and outer layer with a relatively large NW cell height. Wall y^+ values should ideally be greater than 30, with 15 as an acceptable minimum. For low to medium Reynolds number flow, such as the respiratory airways, the ANSYS FLUENT Theory Manual (2012) advises against using the wall function approach as the assumptions that the method uses are not applicable to this flow regime. The other approach is to use the enhanced wall treatment (EWT) method where the mesh aims to fully resolve the NW turbulent layers. This method is considered to be y^+ independent, but wall values of one are recommended. The main concern when using the EWT method is that there are an adequate number of cell layers to resolve the flow in the NW region. When using the k-ω turbulence model in ANSYS FLUENT, the EWT method is implemented by default.

Initially four meshes are compared that each have varying degrees of NW mesh resolution and are suitable for the EWT method. These meshes are referred to as the Recommended, Intermediate, Targeted, and Poor Ratio cases, and are presented in Figure 3.2a. The Recommended mesh follows the NW mesh resolution guidelines in the ANSYS FLUENT Theory Guide (2012), with 20 cell layers that cover the region from the wall up to a y^+ value of approximately 60 and a first layer thickness that gives a wall y^+ of approximately one. These recommended guidelines aim to model the flow in the sub-

layer and buffer region accurately when using the EWT option by using a high-fidelity mesh in the NW region. However, there are several close proximity surfaces in the nasal cavity, especially the meatuses, where such a high level of mesh resolution is not feasible. Ideally, the NW mesh in an upper airway model would be similar to the Targeted mesh, with five equally spaced NW cell layers and a first layer height that gives a wall y^+ of approximately one. Here the resolution is fine enough to capture the large flow field gradients near the wall, but the overall cell layer height is thin enough to be included between close proximity surfaces. Fewer cell layers also drastically reduces the total cell count, so accurate results from the Targeted mesh would provide a more computationally efficient model. The Intermediate model uses 10 equally spaced NW cell layers with a wall y^+ of approximately one. This provides a level of mesh resolution that falls within the Recommended and Target models. Finally, the Poor Ratio mesh is similar to the Targeted case, with the exception that the L2L ratio from Layer 1 to 2 is 1.8, and the layers are then equally spaced from Layer 2 to 5. This mesh is included in the evaluation to determine how poorly defined L2L thicknesses can influence the results. In complex geometries, the meshing software can stretch and shrink cell layers in order to conform to the surface. Therefore, it is possible to have large increases in the L2L ratio such as the Poor Ratio case, which may not accurately capture high gradients in the flow field.

After evaluating the four NW mesh conditions described above, both first cell layer height and L2L ratio are considered. The effect of increasing the thickness of the first NW layer is evaluated using the meshes shown in Figure 3.2b. The definition of these Wall y^+ meshes uses only one NW layer to neglect the influence of L2L ratio on results. Consistency in deposition profiles between cases will indicate that first layer thickness

89

does not influence results within the range considered. The effect of L2L ratio between Layer 1 and 2 is explored further with the meshes in Figure 3.2c. The Ratio meshes determine at what point the ratio between Layer 1 and 2 becomes excessive and begins to influence results. The NW layer thickness in Figure 3.2c is consistent between each of the Ratio meshes and gives a wall y+ of approximately one.

The NW meshing parameters require known values of wall y+ in order to be defined. These values can be estimated before running the CFD simulation using the following equations. The skin friction (C_f) is approximated from the Reynolds number (Re) by using Blasius' equation for turbulent flow in a circular pipe (Blasius, 1913), which is given by

$$C_f \approx 0.0791 \mathrm{Re}^{-1/4} \tag{3.3.2}$$

The wall shear stress (τ_w) is defined with the skin friction, fluid density (ρ), and average flow velocity (u) as

$$\tau_w = \frac{1}{2} C_f \rho u^2 \tag{3.3.3}$$

The wall friction velocity (u^*) is given by

$$u^* = \sqrt{\frac{\tau_w}{\rho}} \tag{3.3.4}$$

Finally, the distance from the wall to the center of the first NW cell (Δy_w) is determined from the desired wall y+ (y_w^+), fluid dynamic viscosity (μ), fluid density, and wall friction velocity as

$$\Delta y_w = \frac{y_w^+ \mu}{\rho u^*} \tag{3.3.5}$$

Note that Equations (3.3.2) to (3.3.5) do not give exact mesh definitions, but serve as good estimations to get sensible NW layer thicknesses. Table 3.2 summarizes each of the meshes described here and includes the meshing parameters that are used to generate the required NW cell layers.

Mesh Construction and Cell Types

The meshes shown in Figure 3.2 were generated by the ICEM CFD 14.5 meshing package (ANSYS, Inc., Canonsburg, PA, USA). The effects of the NW cell layer parameters were initially explored using hexahedral cells, as shown in Figure 3.2d for the Targeted case. This mesh type was constructed using the block mesh approach available in ICEM CFD 14.5, which allows the user to create a regular, mapped, hexahedral mesh.

Regular hexahedral meshes are ideal for CFD analysis in airway type systems, as they generally give the best accuracy when applied to the finite volume method (Vinchurkar & Longest, 2008). However, this type of mesh construction is not possible when developing models of nasal anatomy and potentially the MT, as the geometry is often too complex. Irregular tetrahedral meshes are employed in such cases, as they are able to conform to intricate surfaces, but numerical accuracy and robustness is sacrificed to some degree (Vinchurkar & Longest, 2008). Therefore, this study will compare the results of hexahedral and tetrahedral meshes directly to determine if there are substantial drawbacks associated with using tetrahedral meshes when modelling aerosol deposition. The mesh on the right side of Figure 3.2d is an example of the tetrahedral meshes used in the evaluation, specifically the Targeted NW cell layer case. These meshes were also generated with ICEM CFD 14.5 using the Tetra meshing capabilities. First, a CAD model of the 90° bend was supplied to the meshing software, and a patch-dependent, triangular

shell mesh was generated for each of the surfaces. A Delaunay algorithm was then utilized to fill the 3D volume with tetrahedral cells based on the triangular shells. Next, cell layers were inflated from the tube walls into the fluid volume to generate a prismatic NW mesh. After this inflation stage, the mesh is smoothed to ensure that the quality metric for all cells is greater than 0.1. Finally, the entry and exit sections of the model were extruded normal to the inlet and outlet of the 90° bend. This extrusion process generates prismatic cells that are aligned with the flow direction, which helps model the fully developed behavior in this region. The tetrahedral meshing method outlined here ensures good mesh quality, but is surprisingly more involved that hexahedral mesh construction. That said, tetrahedral meshing of complex geometries is much simpler than trying to apply the blocking method to irregular surfaces.

Physics Model and Solver Settings

The ANSYS FLUENT 14.5 CFD software package (ANSYS, Inc., Canonsburg, PA, USA) solves the transport equations that describe the flow field and particle trajectories through the numerical models. Initially, existing best practices developed by our group for modelling aerosol deposition in the extrathroacic region were applied to the Recommended, Intermediate, Targeted, and Poor Ratio meshes. The k-ω model solves the TKE and specific dissipation rate (SDR) fields, as is generally recommended for internal flows. The LRN correction uses a coefficient to dampen the turbulent viscosity that is determined when the TKE and SDR transport equations are combined. This coefficient is calculated from the material properties, turbulent field quantities, and model constants; the details of which are given by Wilcox (1998). The LRN correction should be applied when flow is close to the transition regime. Currently, the solver uses the

92

SIMPLEC scheme for Pressure-Velocity coupling, with Least Squares Cell Based (LSQ) gradient discretization, and second-order upwind schemes for flow variables. Particle trajectories through the domain are modeled using Lagrangian tracking with the Runge-Kutta scheme (Longest et al., 2015; Longest & Hindle, 2009a; Longest et al., 2007; Longest, Tian, Delvadia, et al., 2012; Longest, Tian, Walenga, et al., 2012; Longest & Vinchurkar, 2007b; Tian et al., 2011; Walenga & Longest, 2016). The particle drag, turbulent dispersion, and eddy interaction model are modified with NW correction user-defined functions (UDFs), which correct for turbulent anisotropy near wall boundaries (Longest et al., 2008; Matida et al., 2004) and perform NW velocity interpolation (Longest & Xi, 2007). The NW correction may mask the behavior of the underlying physics models and solver settings, so they are neglected when comparing the variability between the four meshes. Once mesh and CFD solution parameters are defined that reduce the inconsistency in flow and particle deposition results, the UDFs will be applied to compare with the Pui et al. (1987) experimental data.

Turbulence

To date, LRN k-ω turbulence has been the two-equation model of choice for CFD particle deposition studies from our group. It has been extensively validated against *in vitro* (Longest & Hindle, 2009a; Longest et al., 2007; Longest, Tian, Delvadia, et al., 2012; Longest, Tian, Walenga, et al., 2012; Longest & Vinchurkar, 2007b; Tian et al., 2011) and *in vivo* (Longest et al., 2015; Walenga & Longest, 2016) experimental data, and provided accurate results in these studies. Advanced models, specifically the k-ω SST and Reynolds Stress Model (RSM), are available that aim to model turbulence with greater accuracy and detail. The SST k-ω model combines the free-stream advantages of the k-

ε model with the NW benefits of k-ω. It is the recommended RANS turbulence model in the ANSYS FLUENT User Guide (2012), and includes a LRN option for modeling flow that is close to transition. Chen et al. (2009) used the SST k-ω model for a CFD assessment of flow through the nasal cavity in patients with septal deviations, although their study did not include particle deposition. The RSM has both ε and ω formulations, and solves seven additional transport equations for each of the Reynolds stresses. Rygg and Longest (2016) applied RSM to model pharmaceutical aerosol deposition in the adult nasal cavity, as its formulation includes turbulence anisotropy near walls without additional UDFs.

Despite the advanced formulation of SST and RSM k-ω, preliminary work for this study showed that these models increased processing times by approximately 30% and did not show substantially different results in terms of NW mesh sensitivity compared with the LRN k-ω model. In addition, RSM gave a very unusual velocity profile at the inlet and outlet of the 90° bend when compared to the other turbulence formulations. Therefore, the remainder of this investigation will use the LRN k-ω model, based on its previous successful use. Preliminary results also show that particle deposition appears to be dependent on the NW mesh only when the turbulent dispersion model is activated. This suggests that results are sensitive to resolution of the NW TKE field, as this quantity drives the turbulent dispersion model and its influence on particle deposition. Therefore, consistency in the NW TKE field between meshes is the primary initial focus of this study, which in turn is shown to give consistency between deposition profiles.

Gradient and Spatial Discretization Schemes

The default gradient discretization scheme available in ANSYS FLUENT is the LSQ scheme developed by Anderson and Bonhaus (1994). This method computes the cell gradient by using a weighting that is based on the distance from the cell centroid to its adjacent cells. The two other options available for gradient discretization are the Green-Gauss Node-based (GGN) and Green-Gauss Cell-based (GGC) methods. Equation (3.3.6) describes the Green-Gauss Theorem , which defines the gradient of any field variable at the cell centroid ($\nabla\phi$) by using the cell volume (V), number of cell faces (N_f), field variable value at the face centroid (ϕ_f), and the face area vector ($\overrightarrow{A_f}$).

$$\nabla\phi = \frac{1}{V}\sum_{f=0}^{N_f}(\phi_f\overrightarrow{A_f}) \qquad (3.3.6)$$

In the CFD solution, everything in Equation (3.3.6) is known except for ϕ_f, which is where the GGN and GGC methods are applied. The GGN method approximates ϕ_f by taking it as the average of the face node values, as given by Equation (3.3.7):

$$\phi_f = \frac{\phi_0 + \phi_1 + \cdots + \phi_n}{N_n} \qquad (3.3.7)$$

As the GGN method requires calculation of nodal values, it is generally more computationally expensive than other methods. Note that, N_n is eight for a hexahedral cell, four for a tetrahedral cell, and six for a prismatic cell. The GGC method approximates the field variable value at the cell face by taking it as the average of the current cell (ϕ_0) and the other cell that is attached to the face (ϕ_1), as given by Equation (3.3.8):

$$\phi_f = \frac{\phi_0 + \phi_1}{2} \qquad (3.3.8)$$

Preliminary results showed that switching from the LSQ to GGC method had little influence on the flow field and deposition results. Therefore, the Results section will only focus on how the model behaves when the LSQ vs. GGN methods are applied. The disadvantage of the GGN method being more computationally expensive will be acceptable if it is capable of providing consistent results between the different NW meshes.

It is noted that preliminary work also evaluated spatial discretization methods that are alternatives to second-order upwind in ANSYS FLUENT, including the third-order MUSCL scheme. These schemes were all excluded from further evaluation as they either did not apply to tetrahedral meshes, or did not have a positive effect on results at the Reynolds numbers considered in this study.

Wall Roughness

Preliminary work showed that activating the wall roughness model, with parameters that are consistent with the tube materials used in the Pui et al. (1987) experiments, had a negligible effect on the CFD deposition profiles (changed by <1%). This is most likely because the tubes were made from stainless steel and glass, which are relatively smooth materials, hence the associated wall roughness height was very small (<2 μm). However, the layered additive manufacturing process of common 3D printers often leads to rough surfaces and should be considered when evaluating regional and highly localized deposition (Holbrook & Longest, 2013).

Near-wall Correction

The NW correction UDFs developed by Longest and Xi (2007) have been used extensively by our group when validating numerical results against *in vitro* (Longest &

Hindle, 2009a; Longest et al., 2007; Longest, Tian, Delvadia, et al., 2012; Longest, Tian, Walenga, et al., 2012; Longest & Vinchurkar, 2007b; Tian et al., 2011) and *in vivo* data (Longest et al., 2015; Walenga & Longest, 2016). These UDFs perform two corrections: (i) anisotropic velocity fluctuations are introduced, and (ii) the wall-normal velocity is damped in the NW region, which is consistent with particle-wall hydrodynamic interactions. Furthermore, whenever velocity and turbulence field quantities are required for a calculation, they are interpolated at the particle location instead of using cell centroid values. Including anisotropic turbulence and damping velocity fluctuations in the NW region for pharmaceutical aerosols was originally implemented by our group in a study by Longest et al. (2008). This method built upon work reported by Matida et al. (2004), which in turn was based on DNS data from Wang and James (1999). The NW correction UDF also redefines the drag force (F_D) for all particles as a function of the particle Reynolds number (Re_p):

$$F_D = 18\big(1 + 0.15\mathrm{Re}_p^{0.687}\big) \tag{3.3.9}$$

Two control parameters are used to determine at what point each correction is applied to the particle. If the normal distance from the particle to the wall is less than the NW limit parameter, the UDFs use linear interpolation (based on the particle distance to the wall) to approximate the velocity and TKE values at the particle's current location, and the wall-normal velocity component of the continuous phase is damped. The NW limit parameter is typically mesh, flow, and particle size dependent, and as such, is modified during the model development stage to match experimental data.

If the non-dimensional particle y^+ is below the y^+ limit, the eddy lifetime is calculated based on the interpolated TKE value, and an anisotropic fluctuating velocity is defined

with the new TKE value and random numbers from a Gaussian distribution. The eddy lifetime and fluctuating velocity are then updated each time the particle enters a new eddy. Unlike the NW limit, the y^+ limit parameter is not case dependent and set to a value of 60, as this has given good results in a numerous previous studies (Longest et al., 2015; Longest & Hindle, 2009a; Longest et al., 2007; Longest, Tian, Delvadia, et al., 2012; Longest, Tian, Walenga, et al., 2012; Longest & Vinchurkar, 2007b; Matida et al., 2004; Tian et al., 2011; Walenga & Longest, 2016).

In previous work, the linear method for NW interpolation that the NW correction UDFs use is best described by Walenga and Longest (2016). For this project, interpolation of the velocity and TKE fields was modified in an effort to make the NW correction less mesh dependent, as the objective is to improve consistency in results for different NW meshes. The modified approach first uses an inverse-distance weighted method to calculate all nodal velocity and TKE values in the domain, based on the cell centroid values to which each node is connected. Next, the cell in which the particle is currently located is identified, and the same inverse-distance weighted method is used to interpolate the velocity and TKE values at the particle location from the nodes that define the cell. In order to minimize computational effort, Shephard's method for interpolating irregularly-spaced data is employed (1968), and extended for use in 3D space. Computation time is also reduced by storing all nodal values in memory, and retrieving the data as needed when interpolating to the particle location. In all, processing times for this modified method are negligible when compared to the time taken to reach a converged solution for the flow and turbulence transport equations.

Boundary Conditions

Due to the simplified model geometry, the boundary conditions for this study are relatively straightforward. At the inlet, a uniform velocity magnitude of 17.42 m/s was specified for the Re = 6,000 case and 17.16 m/s was specified for Re = 10,000 (as the tube diameter is larger). Despite applying a uniform inlet velocity, the flow reaches a fully developed state before it enters the 90° bend section. Default values for Turbulence Intensity (5%) and Turbulent Viscosity Ratio (10) are applied, as the length of the straight section should minimize the effects of inlet conditions on the turbulence field in the 90° bend. The outlet from the domain simply uses the outflow condition, whereby all mass that enters though the inlet also leaves through the outlet. All walls on the straight and 90° bend sections use a no-slip condition, and particles are trapped upon wall contact with the particle center of mass.

Particle Injection

Particles are introduced into the domain with a blunt, random spatial distribution, as recommended by Longest and Vinchurkar (2007b). The blunt profile defines a uniform proportion of particles throughout the bulk flow, and then rapidly decreases the proportion as the particles near the wall. This realistic distribution is used as more particles enter along higher flux rings of flow. For the circular tube, a center point, normal vector, and radius define the random inject coordinates. The center point is selected so that particles are injected into the tube where the straight entry section of the tube ends and the 90° bend starts.

For the Re = 6,000 case, the injected particle size distribution uses seven bins with particle diameters that match the Pui et al. experimental data as described in Table 3.1.

The size distribution for the Re = 10,000 CFD case also uses seven bins, with the 4.56-7.66 μm particles matching the sizes in the Re = 10,000 experimental data, and the 1.50-3.80 μm selected to match the Stokes numbers in the Re = 6,000 case. No experimental data is available for these three smaller bin sizes, and these particles are included to compare against the correlation at the lower end of the size range. The CFD model injects 5,000 particles for each bin size, as previous validation of steady-state models by our group have shown that tracking this number of particles per bin gives good particle convergence (Longest, Tian, Walenga, et al., 2012).

Comparison Criteria

Deposition Fraction

The deposition fraction (DF) is defined as the ratio of the deposited particle mass to the injected particle mass and is expressed as a percentage:

$$\text{DF} = \frac{\text{Particle Mass Deposited}}{\text{Particle Mass Injected}} \times 100 \tag{3.3.10}$$

Continuous Phase Velocity

As mentioned previously, preliminary results showed that the differences in the NW mesh layers are most sensitive to the effects of the turbulent dispersion model. This model uses the combination of the mean ($\bar{u}$) and fluctuating (u') parts of the flow velocity, which is hereafter referred to as the continuous phase velocity (u) where:

$$u = \bar{u} + u' \tag{3.3.11}$$

The fluctuating velocity used by the turbulent dispersion model is defined by a random number from a Gaussian distribution (ζ) and the TKE (k), given by:

$$u' = \zeta \sqrt{\frac{2}{3}k}$$

(3.3.12)

3.4 Results

Sensitivity Study

Application of Current Best Practices

Figure 3.3 shows the TKE profile at 20°, 40°, 60°, and 80° around the 90° bend for the Recommended, Intermediate, Targeted, and Poor Ratio meshes. The plot shows a steep gradient near the wall, with a profile shape that is consistent with the DNS results from Wang and James (1999). In Figure 3.3a, the results for each mesh are all similar, as the flow is relatively uniform as it leaves the straight entry section of the tube. However, as the flow becomes more disturbed moving through the bend from Figure 3.3a to d, the profiles show more variability between the four meshes. Variability between each of the TKE profiles in Figure 3.3 can be evaluated by applying a 6th-order polynomial line of best fit ($R^2 > 0.999$) and taking 30 equally-spaced sample points throughout the NW region. Moving from a location of 20° to 80° in the bend, the average and maximum standard deviation increases from 0.20 to 0.46 m^2/s^2 and 0.41 to 0.90 m^2/s^2 respectively. Qualitatively, both the peak TKE value near the wall and incline of the NW gradient vary considerably in each case. In order to achieve accurate and consistent results from the turbulent dispersion model, the TKE field in this NW region must be well resolved.

The continuous phase velocity, which the particles experience near the wall in each of the four meshes, is shown graphically in Figure 3.4. The continuous phase velocity is calculated from Equations (3.3.11) and (3.3.12), with the random number assumed to have a value of one for the purpose of comparison between different CFD

models. This assumption is necessary, as the random number that the commercial code uses is not known.

The values are sampled at the outlet of the 90° bend on the outer edge of the curved tube radius, as this location has the most variability and clearly deomonstrates the difference between each NW mesh. The mean velocity profiles for each case are very similar (not shown), but Figure 3.4 demonstrates how different the flow field can be when the fluctuating velocity is included. From Figure 3.4a to c, a sample particle moves through the NW cell layers of each mesh at a wall-normal distance of 60, 50, and 40 µm, respectively. The y^+ values are included to indicate the non-dimensional wall distance for reference, with the average value for all four cases used, as the flow field varies for each mesh. From this figure it is clear that the particles are exposed to very different continuous phase velocities between each mesh. As the continuous phase velocity varies for each mesh, the particle trajectories through each computational domain are also different.

The variability in the TKE field close to the wall in turn affects the particle deposition profile between each of the four meshes, as seen in Figure 3.5. At the smaller end of the microparticle size range, particles are more susceptible to turbulent dispersion (Hjelmfelt & Mockros, 1966; S. L. Lee & Durst, 1982; Sommerfeld, 1990) and as such, show more variation in DF for each mesh. As diameters move towards the nanoparticle size range, the particle momentum becomes too low to be influenced by dispersion or pass though the viscous sublayer. Between the Targeted and Poor Ratio mesh, the DF decreases by about 25% for 2.89 µm particles (40.32% vs. 30.10%), 50% for 2.38 µm particles (30.30% vs. 15.28%), and 73% for 1.10 µm particles (2.28% vs. 8.58%). Note that meshes in Figure 3.3 that gave lower peak TKE values and a shallower gradient also gave less

particle deposition. That is, lower TKE provides less turbulent dispersion, which results in lower DFs for particles less than 4 μm, as expected.

Including the Green-Gauss Node-based Discretization Scheme

Using the GGN method for gradient discretization greatly reduces the sensitivity of the TKE field to the NW mesh resolution, as shown in Figure 3.6. As before, the differences between the four meshes become more varied as the flow progresses through the 90° bend. However, there is less overall variability between each case. Using the same method as before, GGN decreases the average and maximum standard deviation by 40% and 45% respectively for the 20° profile (0.20 vs. 0.12 m^2/s^2 and 0.41 vs. 0.23 m^2/s^2), 33% and 40% for the 40° profile (0.29 vs. 0.20 m^2/s^2 and 0.60 vs. 0.36 m^2/s^2), 22% and 32% for the 60° profile (0.38 vs. 0.29 m^2/s^2 and 0.75 vs. 0.51 m^2/s^2), and 13% and 25% for the 80° profile (0.46 vs. 0.40 m^2/s^2 and 0.89 vs. 0.67 m^2/s^2). Furthermore, the peak TKE values compare closely with one another, and the incline of the gradient near the wall is similar for all four meshes. Removal of the Poor Ratio mesh from this comparison would further improve agreement in the TKE field.

As a result of less variability in the TKE values, there is much better consistency in the deposition profiles for each mesh, as shown by Figure 3.7, especially for particles less than 4 μm in diameter. Now, between the Targeted and Poor Ratio mesh, the DF decreases by about 5% for 2.89 μm particles (42.46% vs. 40.06%), 18% for 2.38 μm particles (31.06% vs. 25.58%), and increased by 6% for 1.10 μm particles (4.30% vs. 4.54%). Table 3.3 summarizes the mean and standard deviation for the DF across all four meshes and compares the LSQ and GGN methods. This confirms that less variability in the TKE field gives less variability in particle deposition results. More importantly, these

results show that application of the GGN method greatly reduces the sensitivity of the flow field and particle trajectories to the NW mesh resolution.

Near-wall Mesh Resolution

Figure 3.8a shows that increasing the L2L ratio for Layer 1 to 2 from a value of 1.0 (i.e. the same mesh as the Targeted case) to 1.1, 1.2, and 1.5 (as shown in Figure 3.2c) does not appreciably influence the particle deposition profile when using the GGN method. This is consistent with the reduced variability between results, especially the Poor Ratio case, which was presented in Figure 3.7. This means the variable L2L ratio capabilities that are available in meshing software can be employed without negatively affecting the aerosol deposition results. These meshing features allow the thickness of NW cell layers to be reduced when the surface-to-surface proximity decreases, which maintains the required mesh resolution near the wall.

Figure 3.8b demonstrates how increasing the thickness of the first NW layer from an approximate wall y^+ of 0.5, 1.0, 2.0, and 5.0 affects the deposition profile. Note that these meshes use only one NW layer so the L2L ratio does not mask the sensitivity of results to the target wall y^+. For comparison, the Targeted mesh, with a wall y^+ of one and five equally-spaced layers, is also included in this figure. From this plot it is clear that increasing the thickness of the first NW cell layer, and associated wall y^+ value, rapidly increases the DF for small (<4 μm) particles. Convergence of the deposition profiles occurs when using a first layer height that gives an approximate wall y^+ of 1.0.

In summary, the results show that the Targeted NW mesh, which is desirable for infant nasal models, is capable of producing deposition results that are comparable with

the Recommended NW mesh in a simplified model, when suitable best practices are applied.

Tetrahedral Mesh Type

Using a tetrahedral mesh, as depicted in Figure 3.2d, and the GGN method gives a very consistent deposition profile across the four NW meshes considered, as shown in Figure 3.9. This draws parallels to the behavior seen when activating the GGN method in Figure 3.7. Table 3.4 summarizes the mean and standard deviation across all four meshes, and shows that the variability between each case is much less than the hexahedral meshes (see Table 3.3). Therefore, highly mesh independent results can be produced with tetrahedral meshes and the GGN method, which are desirable for the complex surfaces.

Figure 3.9 also includes the deposition profile for the hexahedral mesh that uses the Targeted NW mesh parameters from Figure 3.7. Interestingly, the DF of the 1.10 µm particles for the tetrahedral meshes is much greater than the hexahedral results (14.26% vs. 4.30%). The fact that smaller particles are more influenced by subtle changes in the velocity and TKE field is the likely cause of this discrepancy between results. Recall that the NW correction UDFs also influence DFs for the smaller particles, and have not been applied at this stage in the study.

Near-Wall Correction

Figure 3.10a and b present the effects of applying the NW correction UDFs to the hexahedral and tetrahedral mesh with targeted NW cell layers respectively. For reference, the No UDF lines in each plot are the deposition profiles for the Targeted hexahedral and tetrahedral meshes from Figure 3.7 and Figure 3.9 respectively. As expected, increasing

the NW limit parameter decreases the DF for particles less than 4 µm, as the UDF begins damping the wall-normal flow velocity further away from the wall. The plots also show that setting the NW limit to zero, effectively disabling the damping of wall-normal velocity, still influences the results as the particle drag force and turbulence anisotropy correction are applied outside of this limit.

Adjusting the NW limit parameter allows the computational results to be tuned to match experimental data. The results from the tetrahedral mesh in Figure 3.10b show that increasing the NW limit leads to a gradual decrease in DF for small particles, which makes it easier to fine-tune the results. Figure 3.10a shows that the hexahedral mesh gives a very abrupt change in DF when adjusting the NW limit parameter beyond 2 µm. This is most apparent when looking at the results when changing from a NW limit of 2 to 5 µm for the 2.38 µm particles, as the DF drops from 14.28% to 2.24%. Generally, setting the NW limit parameter to a value of approximately 1 to 2 µm gave consistent results between mesh types, and compares well with experimental data (as detailed in the following section).

Comparisons with Experimental Data

Figure 3.11a and b compares the CFD deposition profile for the 90° bend hexahedral and tetrahedral models, with the Re = 6,000 experimental data and correlation from Pui et al. (1987). From this comparison, it is clear that applying the best-case mesh and solver parameters, with the NW correction UDFs, gives a very good match between experimental and numerical results. To provide the best match to the Pui et al. data, the hexahedral case uses a NW limit value of 1.0 µm, and the tetrahedral case uses 2.0 µm. Note that the CFD results also exhibit the characteristic S-curve that is common for

deposition profiles in the pharmaceutical aerosol size range. This profile shape is not represented by the correlation, but is apparent in the experimental data points. It is noted that the CFD predictions match the experimental data points better than the algebraic correlation at a majority of the points considered.

Figure 3.11c and d show the comparison between a hexahedral and tetrahedral CFD model that also adheres to the recommended guidelines developed by this study, and the Re = 10,000 experimental model. The experimental and numerical data also match well, which suggests that the CFD meshing and solver guidelines that are recommended by this work are applicable to a range of flow characteristics. Interestingly, both of these cases gave the best match to the Pui et al. data with NW limit values of zero; hence, the wall-normal fluctuating velocity does not need to be damp for these models. This may be a specific characteristic of high Reynolds number cases. Recall that the Re = 10,000 case uses both a larger diameter tube and higher inlet flow rate, so the recommended CFD guidelines are independent of model geometry and inlet conditions.

3.5   Discussion

This study determines a set of meshing and solver guidelines that provide consistent results across several different NW meshes, and have been validated against experiments of aerosol deposition. The selected meshes have evaluated the effects of the number of cell layers, wall y^+, L2L ratio, and cell type (hexahedral or tetrahedral) on the flow field and particle trajectories, in order to determine the most efficient use of NW cell layers for aerosol deposition models. The investigation explored different discretization schemes and control parameters for anisotropic turbulence correction, with final results showing a reliable match with the Pui et al. data. The guidelines are applicable

across a range of flow Reynolds numbers and particle sizes. Table 3.5 summarizes the recommended guidelines at the conclusion of this study.

As expected, the DF of particles less than 4 μm is most sensitive to the NW TKE field, because particles in this size range are largely influenced by eddy motion and have sufficient momentum to maintain an eddy dispersion velocity. Lower TKE in the NW region leads to less deposition of these smaller particles, and as such, one should strive for CFD models that give a reliable TKE field before having confidence in deposition results. Application of the GGN discretization scheme greatly reduced the variability of the TKE and particle deposition results across all the evaluated NW meshes with the small expense of an 11% increase in computational time (over 5,000 iterations). Therefore, the reasonable upper airway meshes, with five equally-spaced layers, can be applied to future work in contrast with the previously recommended NW mesh with 10-20 layers. Further exploration of the NW mesh parameters with the GGN scheme showed that it is important to aim for a wall y^+ of approximately 1.0, and that varying the L2L ratio did not drastically influence the variability of results between cases. This means that should the meshing software increase or decrease layer thickness to confirm to the model geometry, the results should not be significantly affected.

Use of the NW correction UDFs allows the numerical results to be tuned to match experimental data. As with previous studies (Longest et al., 2015; Longest & Hindle, 2009a; Longest et al., 2007; Longest, Tian, Delvadia, et al., 2012; Longest, Tian, Walenga, et al., 2012; Longest & Vinchurkar, 2007b; Matida et al., 2004; Tian et al., 2011; Walenga & Longest, 2016), a y^+ limit of 60 was suitable for the anisotropic turbulence correction. For the Re = 6,000 case, a NW limit of 1-2 μm was required to match

experimental data for the hexahedral and tetrahedral cases, below which the wall-normal velocity is damped. For the Re = 10,000, a NW limit of zero was used, which means that the velocity damping correction was not required in the more turbulent case.

Generally, CFD results tend to over-predict deposition, especially for smaller particle diameters. The UDFs correct this over-prediction by introducing anisotropic fluctuating velocity components with random numbers from a Gaussian distribution, and damps the wall-normal velocity component as the particle approaches the wall. The current study improved the UDFs by introducing an inverse-distance weighted interpolation method to approximate velocity and TKE values at the particle location, based on cell centroid values. This modification aims to make the correction less mesh dependent. Results show how the NW limit parameter adjusts the deposition profile for hexahedral and tetrahedral meshes. Based on the results of this study with the recommended meshing guidelines, we recommend NW limit values of 1-2 μm for transitional flows with Reynolds number below 10,000, and removing the NW limit correction when the Reynolds number exceeds 10,000. In summary, use of the aforementioned guidelines and anisotropic turbulence correction leads to a very good match between the numerical and experimental data for this 90° bend model.

The findings from this study are consistent with previous work that has evaluated the LRN k-ω model in simplified models of biological internal flow. Studies by Varghese and Frankel (2003) and Ryval et al. (2004) both concluded that the LRN k-ω model gave a good match to experimental data when modeling flow through a stenosed tube, which is similar to constrictions in blood vessels or the respiratory airways. These models have similar flow conditions to the 90° bend model presented in this article, as they all

experience laminar, transitional, and turbulent flow. Matida et al. (2004) demonstrated realistic NW corrections are required in order to match deposition results from the k-ω model to experiments. The same conclusions are drawn from the current study, as application of the NW correction UDFs, which were in part (anisotropy but not NW interpolation) based upon the findings of Matida et al. (2004), allows the deposition profile to be tuned to match the Pui et al. data (1987). Specific to modelling pharmaceutical aerosol deposition in the lungs with LRN k-ω, Xi and Longest (2007) reported good comparisons between numerical models, of both realistic and simplified geometries, and experimental data. The meshing and solution parameter recommendations presented in this paper add to the research field by providing clear guidelines for using the LRN k-ω model. This will streamline the CFD model development process for future work that plans to take advantage of the efficiency and accuracy that the LRN k-ω turbulence model provides for microparticle deposition.

Recently in the literature, there has been a shift towards using more complex turbulence models in CFD studies. The LES model resolves the turbulence field in greater detail than two-equation RANS models. Its formulation is also capable of overcoming some of the inherent NW issues with the k-ω model, which are outlined by this study, without the need for corrections. However, LES models demand much longer meshing and solver processing times, as very small cell sizes are necessary to resolve the required length scales, which in turn gives high cell counts. Zhang and Kleinstreuer (2011) compared the LRN k-ω, SST transition, and LES models for nanoparticle deposition in a constricted tube and idealized human airway model. They observed negligible differences between the three turbulence models for predicting laminar, transition and turbulent flow.

110

They also report that the more complex LES model required 100-fold more computational resources than the two-equation RANS model. Conversely, Jayaraju et al. (2008) concluded that LES/DES provided a better agreement with experimental data for a MT model than k-ω. However, their study used the standard implementation of the k-ω model, which does not include the LRN correction. It is noted that the two-equation RANS CFD models that are discussed here and have successfully matched experimental data (Ryval et al., 2004; Varghese & Frankel, 2003; J. Xi & Longest, 2007; Z. Zhang & Kleinstreuer, 2011), including the present study, have used the k-ω model with LRN correction.

Similar to how this study compared the LRN k-ω CFD results to the Pui et al. model (1987), Breuer et al. (2006) provided a comparison between LES results and the same experimental data set. They showed a good match between the DF from their computational model and the curve fitted correlation. Figure 3.12 reproduces the deposition profile for the Re = 10,000 model from Breuer et al. (2006), and includes the results from this study for the Re = 6,000 and 10,000 cases, and both hexahedral and tetrahedral meshes. This comparison across different Reynolds numbers is reasonable as the Pui et al. correlation is only a function of Stokes number, and hence is independent of Reynolds number. Figure 3.12 shows that the LRN k-ω models gives similar deposition results to the LES model across a range of particle diameters (Stokes number). Therefore, we believe that the LRN k-ω model, with the guidelines and NW corrections defined by this study, is capable of modeling aerosol deposition under conditions consistent with the upper respiratory airways. Advanced turbulence models are invaluable for modeling complex phenomena and aiding the development and validation of two-equation RANS models. For example, the NW correction UDFs utilized by this work rely

on findings from the DNS data from Wang and James (1999). However, the LRN k-ω model provides a more computationally efficient method that can resolve the flow field in sufficient detail to capture microparticle deposition with the same degree of accuracy as LES models.

Future work will apply these guidelines to upper airway geometries and aim to provide the same reliable and validated results that are presented here. This investigation showed that both hexahedral and tetrahedral meshes can be used with little drawbacks for either cell type. Using tetrahedral meshing capabilities makes the modelling of complex airways like the nasal cavity much easier, where using a regular hexahedral mesh on complex geometries is not possible. Cut-cell meshing technologies should be explored, where a Cartesian grid is fitted to the geometry by excluding and cutting cells outside of the domain. This method results in a mesh that is mostly regular and hexahedral in the core, with some tetrahedral, pyramid, and other polyhedra near the surface. The core mesh would provide the robust and computationally efficient benefits that are common with regular hexahedra, but it is unclear at this stage how the cut cells near the surface affect turbulence properties and aerosol deposition in airway CFD models.

In conclusion, this study has provided a set of recommendations for mesh and solver settings that give consistent and validated results for a characteristic geometry. It is expected that application of these guidelines to more complex geometries will improve the model development process and provide more reliable aerosol deposition results in the upper respiratory airways.

3.6 Figures
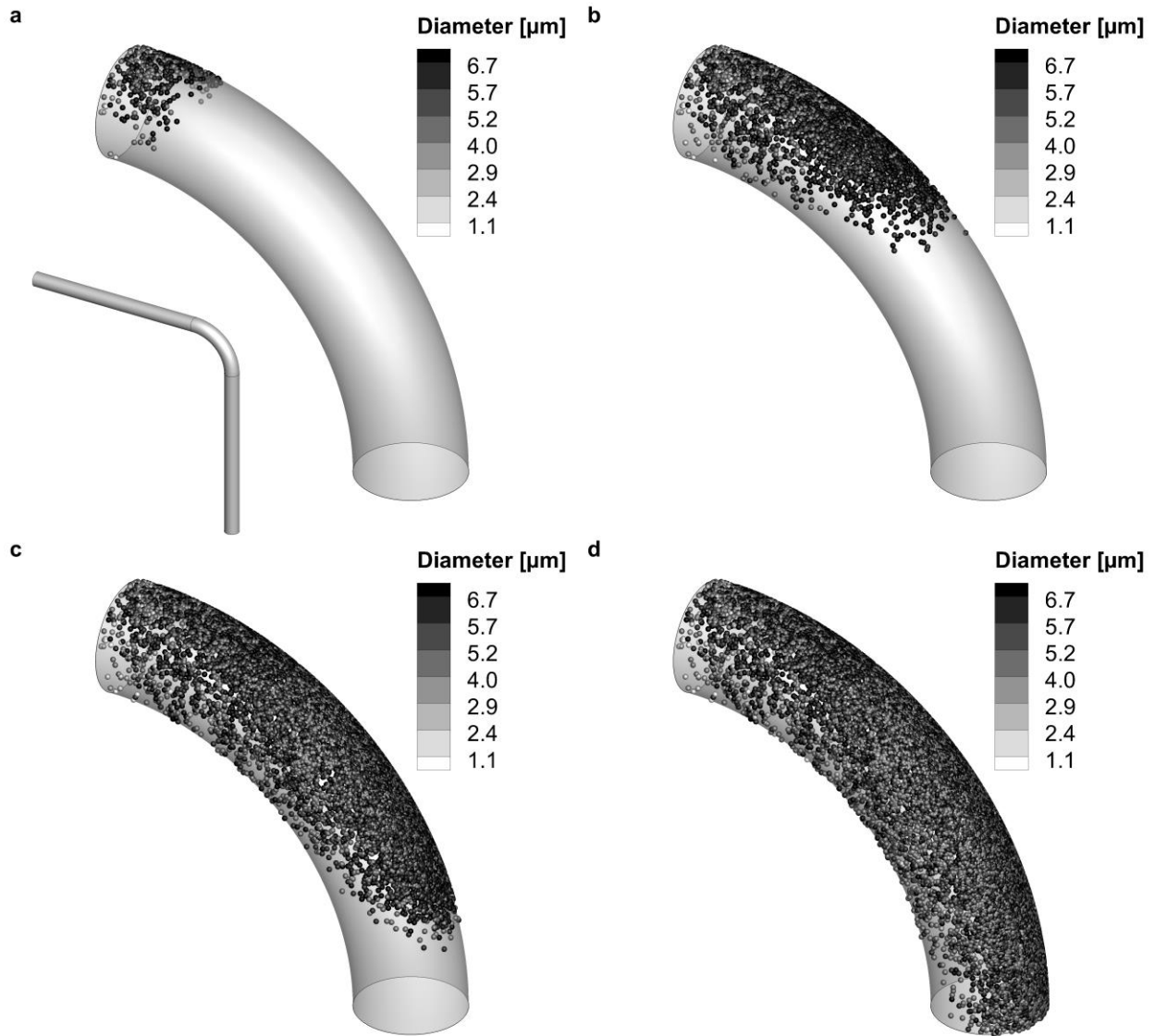
Figure 3.1:   Overview of geometry and particle deposition locations on the 90-degree bend at deposition times of (a) 0.003 s, (b) 0.006 s, (c) 0.009 s, and (d) 0.012 s. Results shown are for the Re = 6,000 case that follows the CFD guidelines recommended at the conclusion of this study.
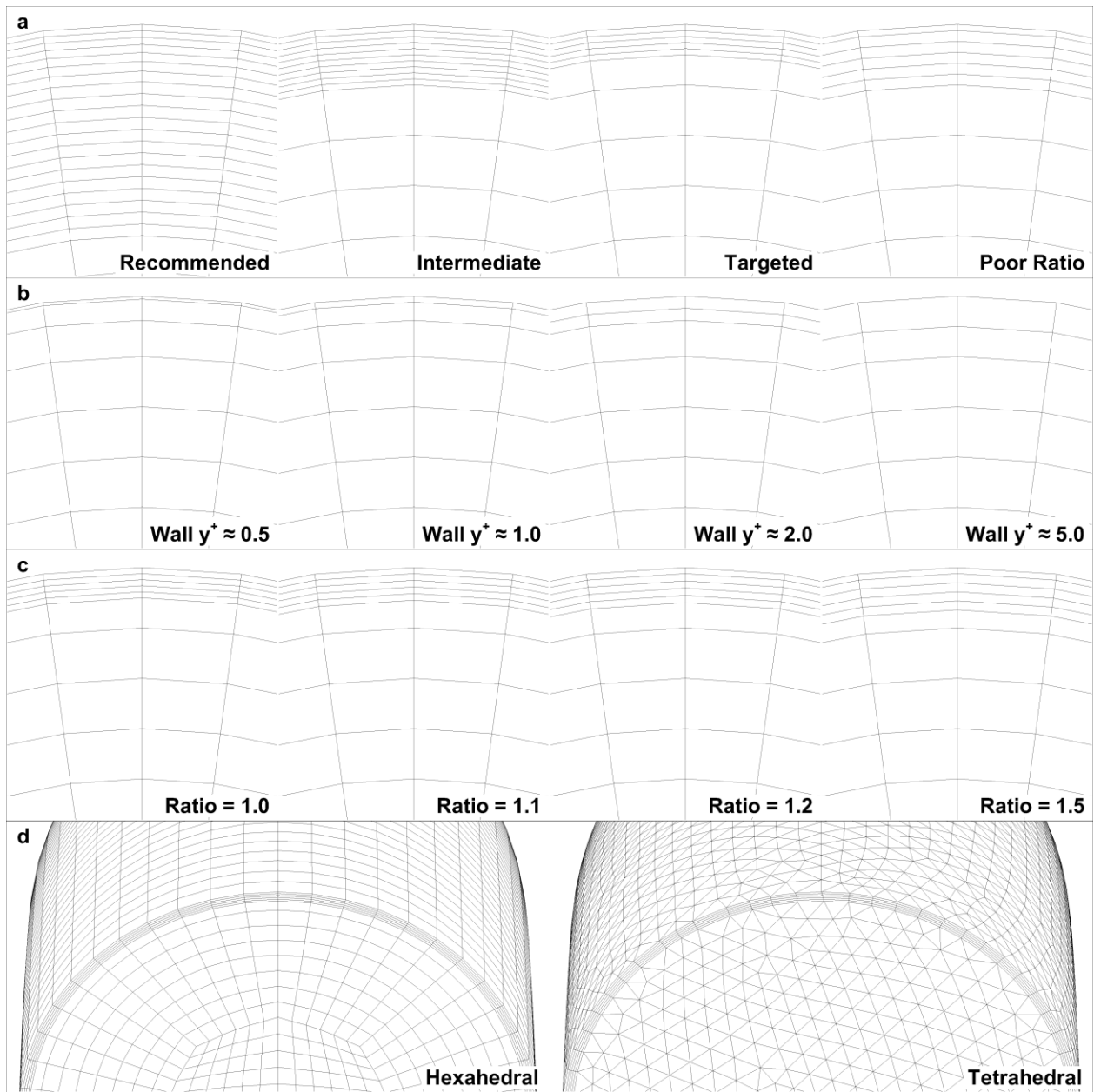
Figure 3.2:   Summary of meshes used to evaluate the sensitivity of the TKE field and particle deposition related to near-wall resolution and cell type.
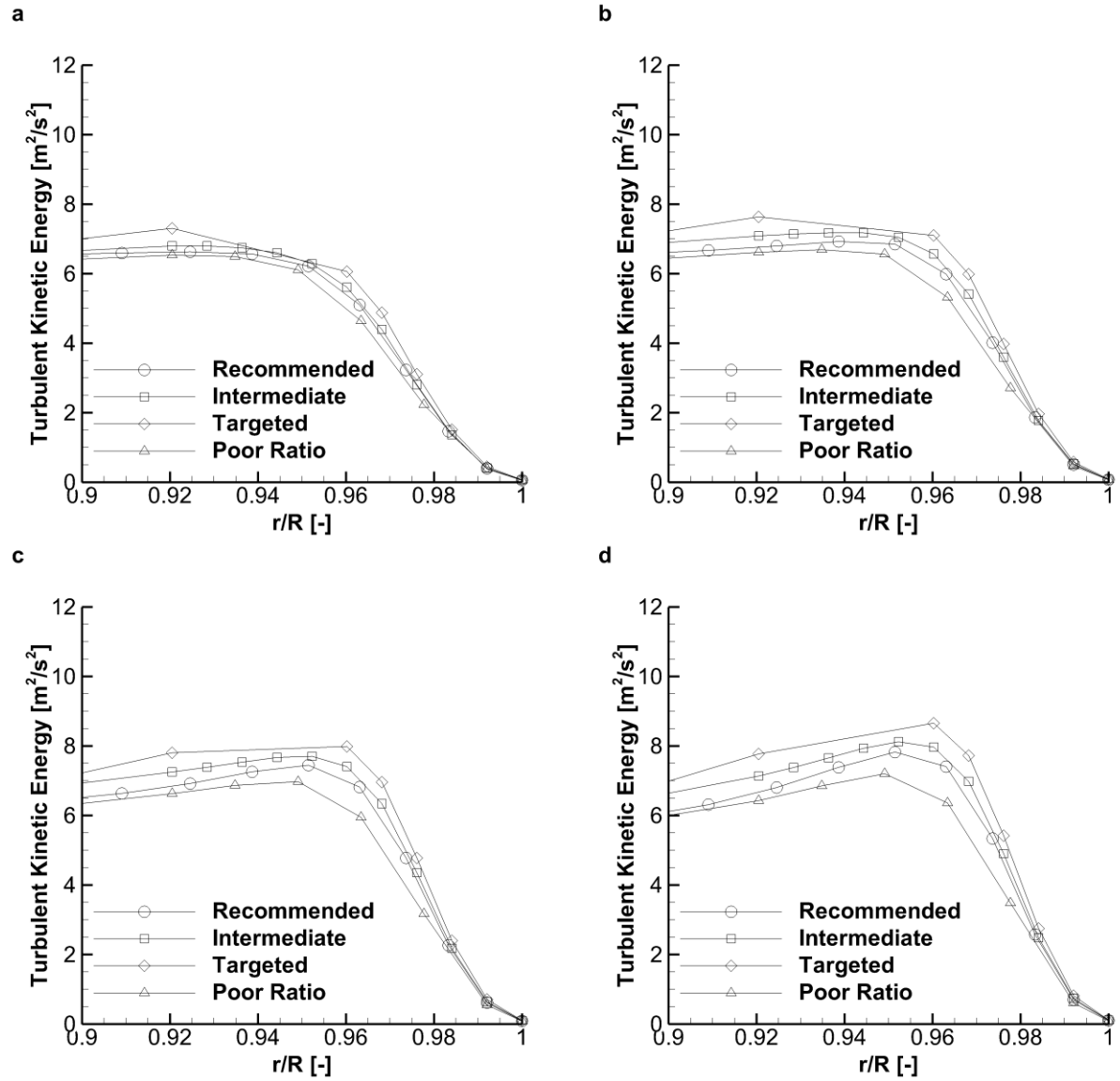
Figure 3.3:   Initial near-wall TKE profiles for each of the four meshes at angles around

the 90-degree bend of (a) 20 degrees, (b) 40 degrees, (c) 60 degrees, and (d) 80 degrees.
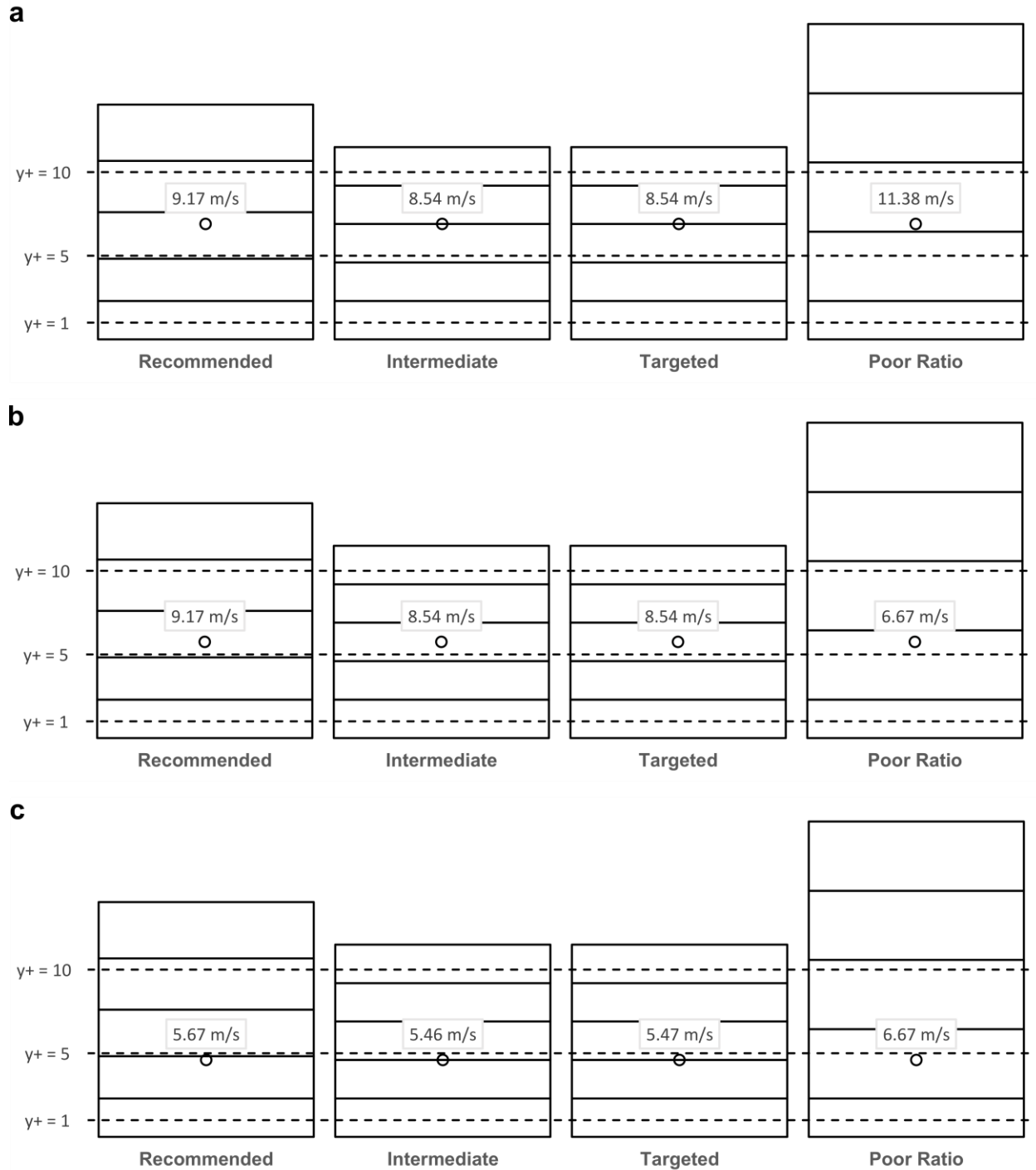
Figure 3.4:   Continuous phase velocity (combined mean and fluctuating parts) to which the particle is exposed at wall-normal distances of (a) 60 μm, (b) 50 μm, and (c) 40 μm, for several mesh configurations.
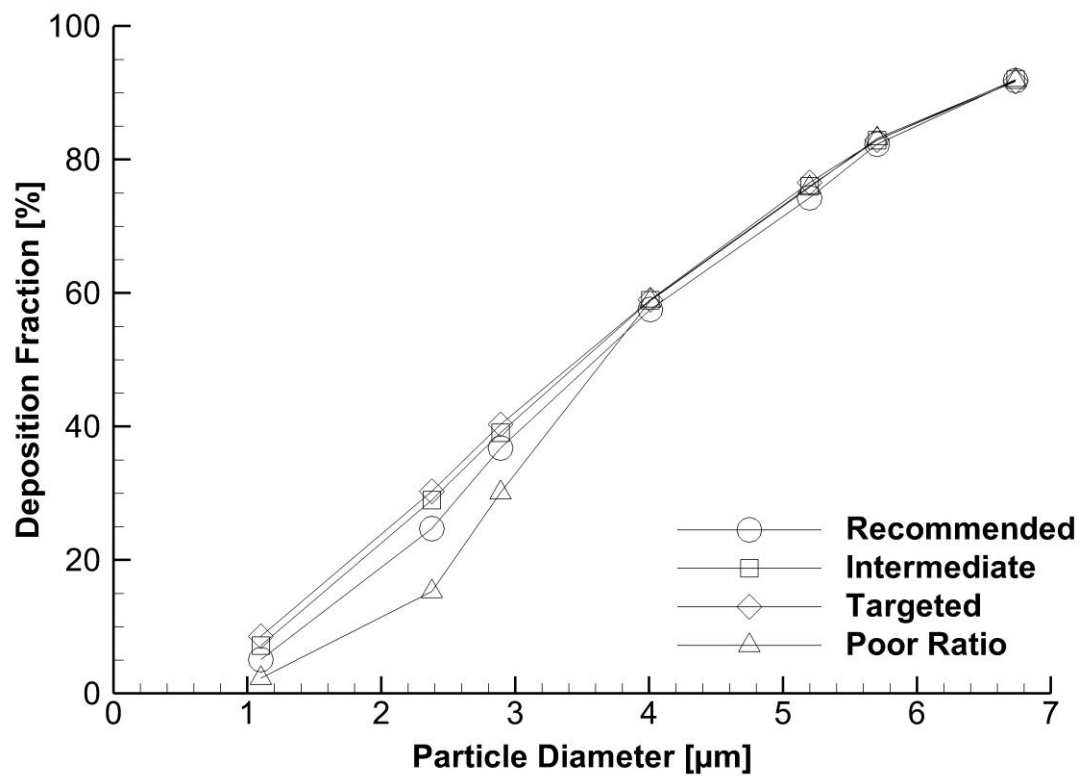
Figure 3.5: Comparison of particle deposition profiles between the four meshes.
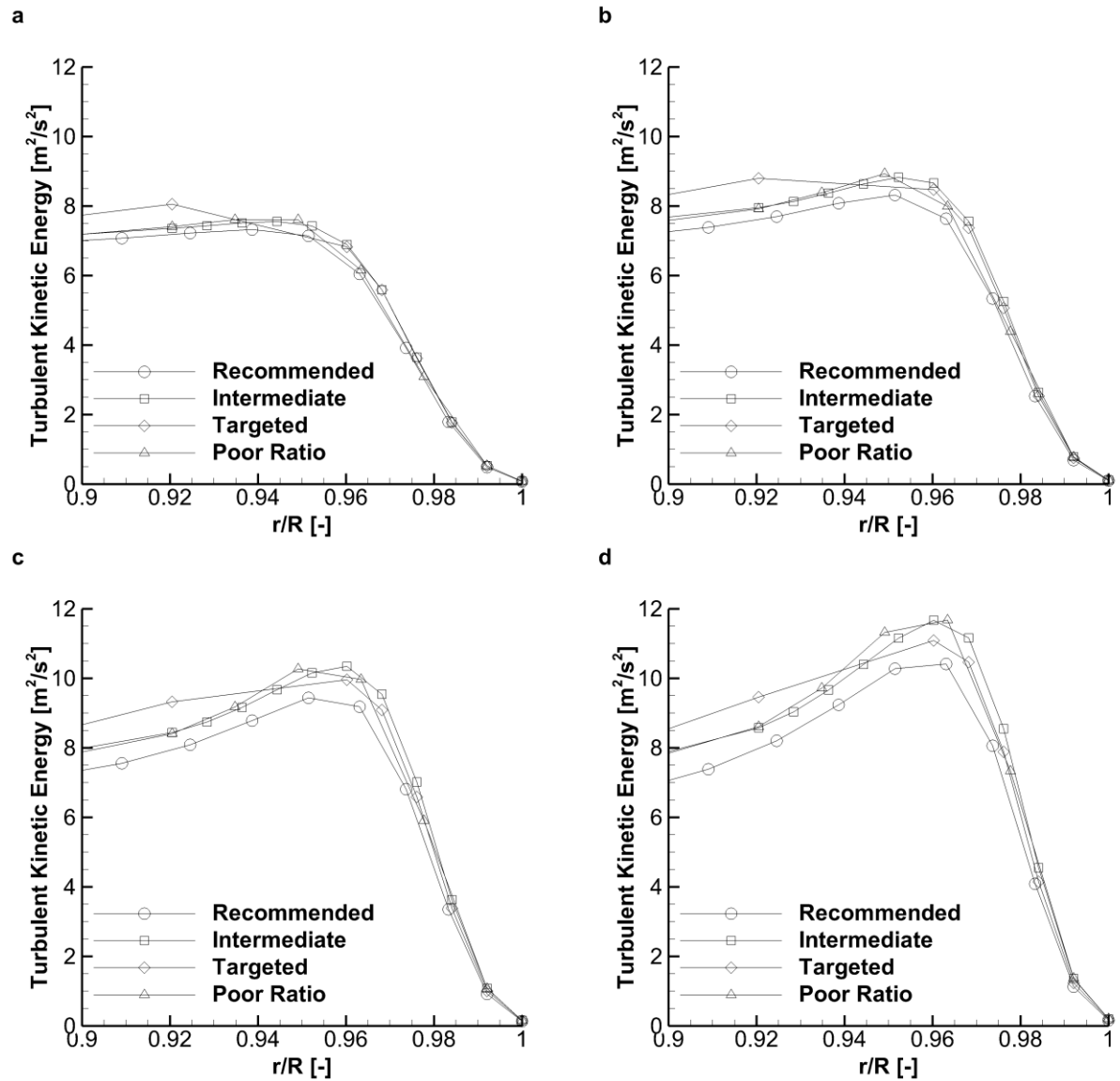
Figure 3.6:   Reduced sensitivity of TKE to the mesh when using Green-Gauss Node-
based discretization scheme at angles around the 90-degree bend of (a) 20 degrees, (b)
40 degrees, (c) 60 degrees, and (d) 80 degrees.
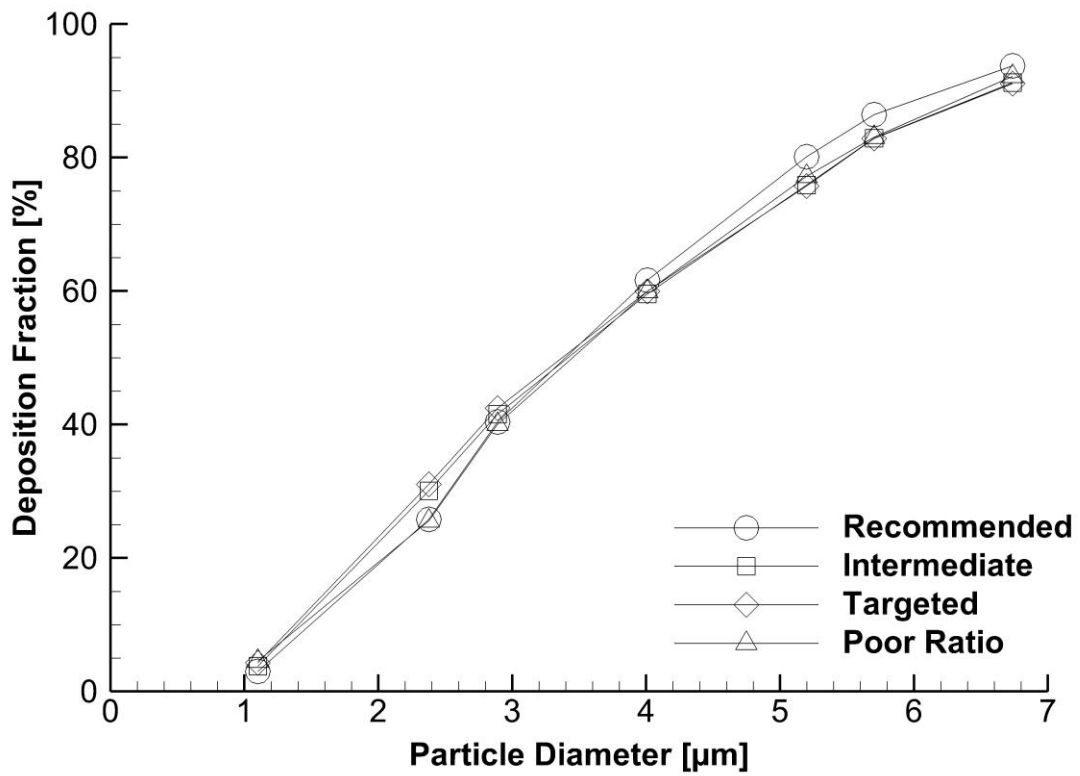
Figure 3.7: Reduced sensitivity of deposition when using Green-Gauss Node-based method.

a

b
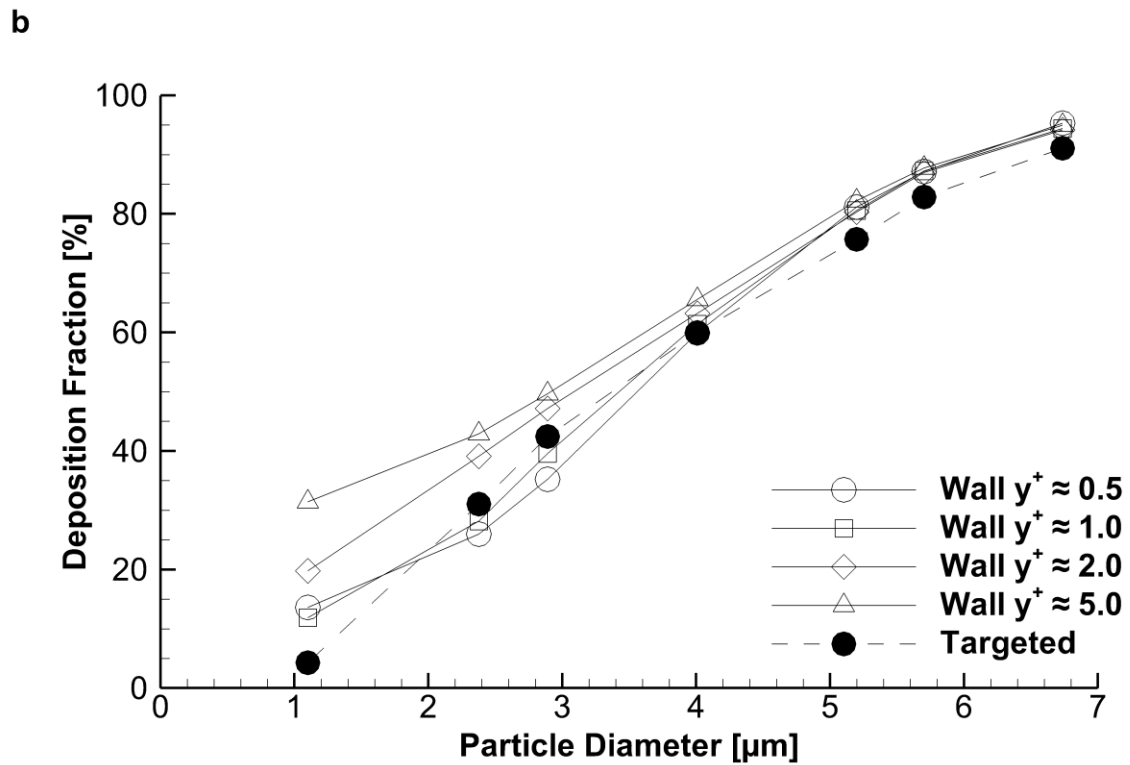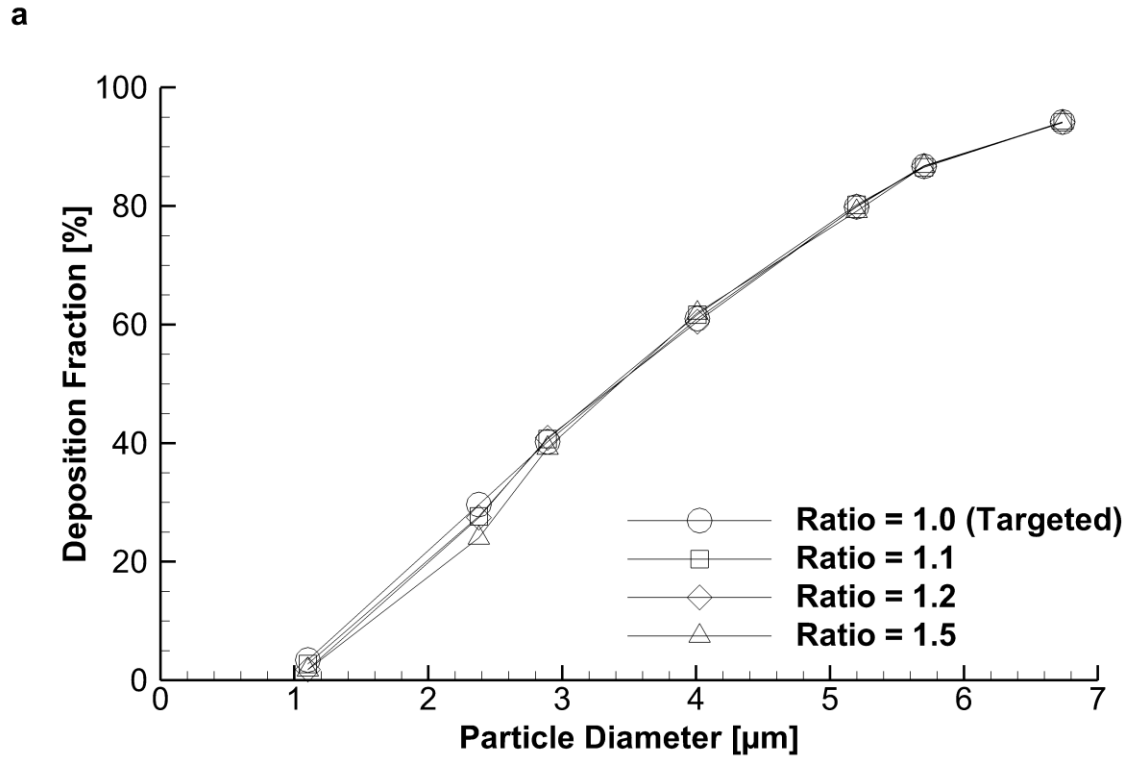
Figure 3.8:   Comparison of results when varying the (a) layer-to-layer ratio and (b) target

wall y^+ value.
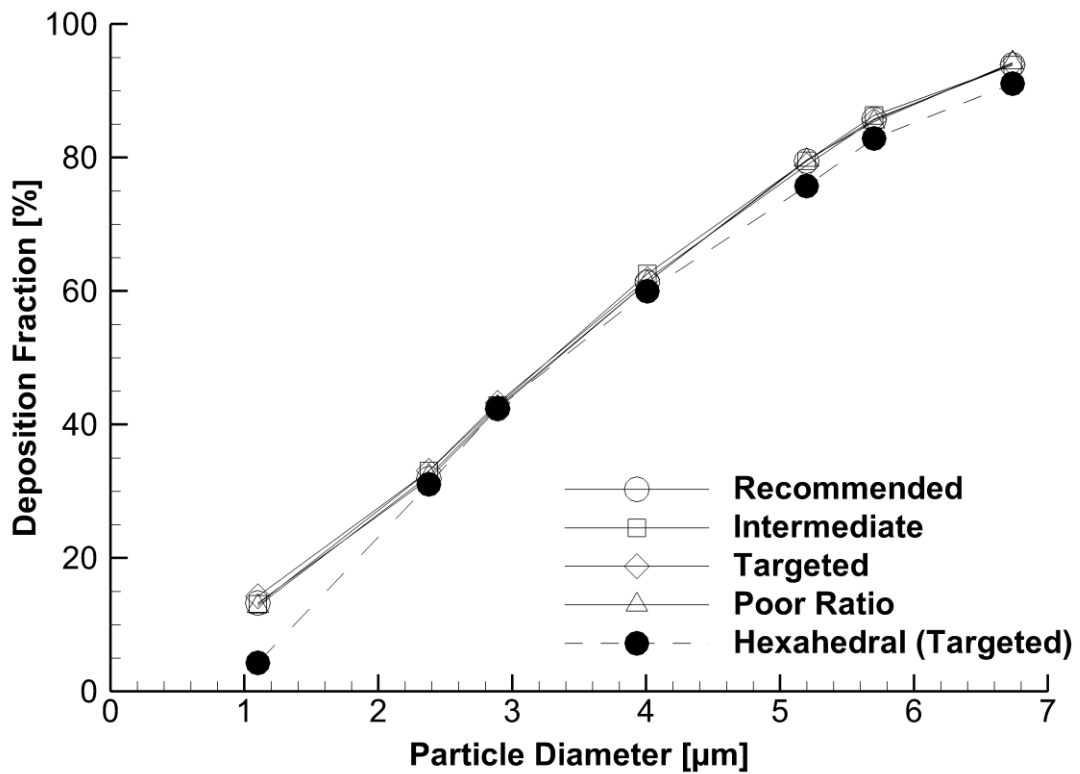
Figure 3.9: Deposition comparison when using a mesh with a triangular surface, prismatic near-wall layers, and tetrahedral core. Each of the near-wall mesh resolutions presented use the same parameters as the hexahedral cases.
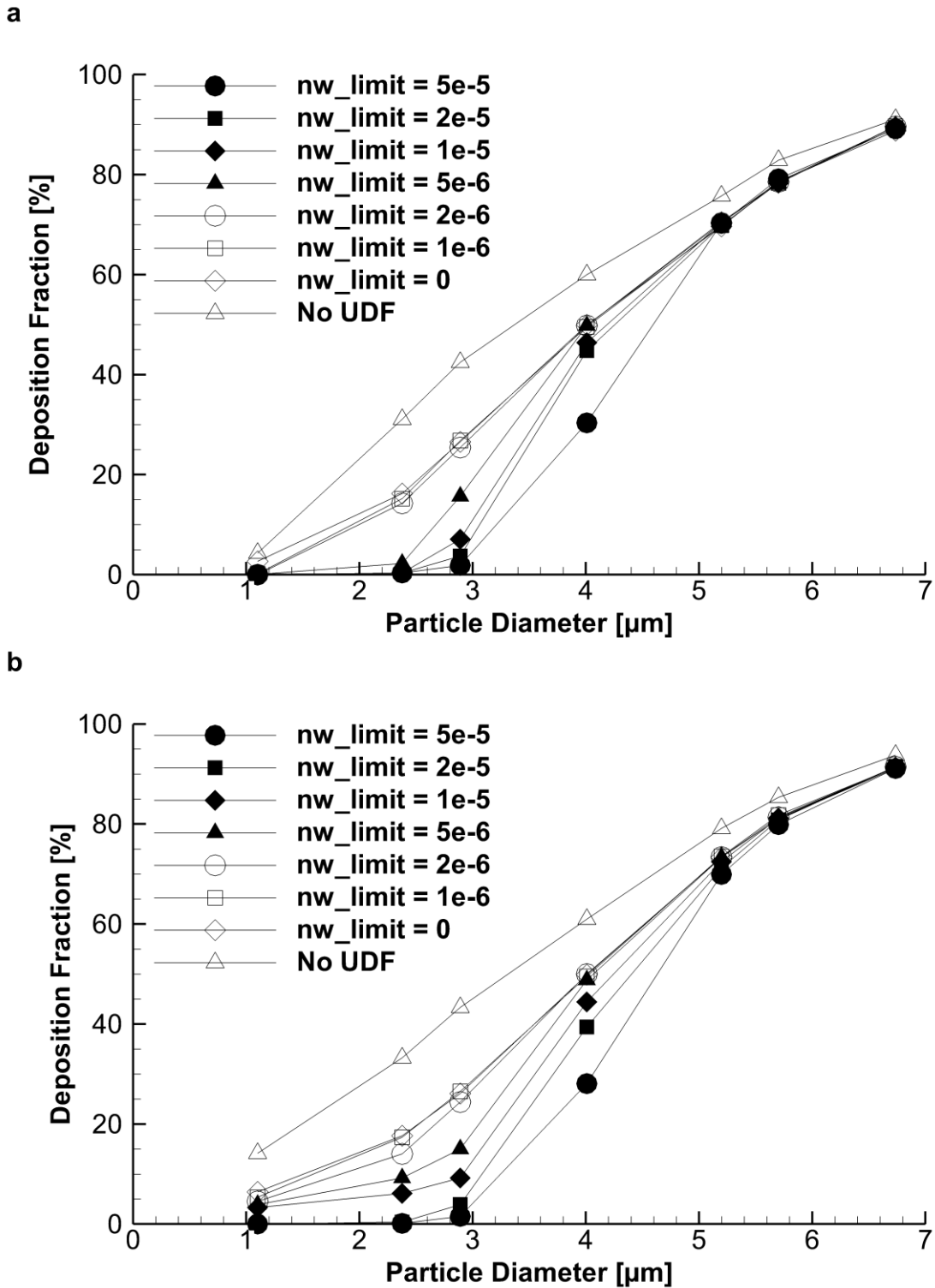
Figure 3.10: Adjustment of near-wall UDF parameters to tune deposition results and match experimental data for the (a) hexahedral and (b) tetrahedral mesh with targeted NW parameters.
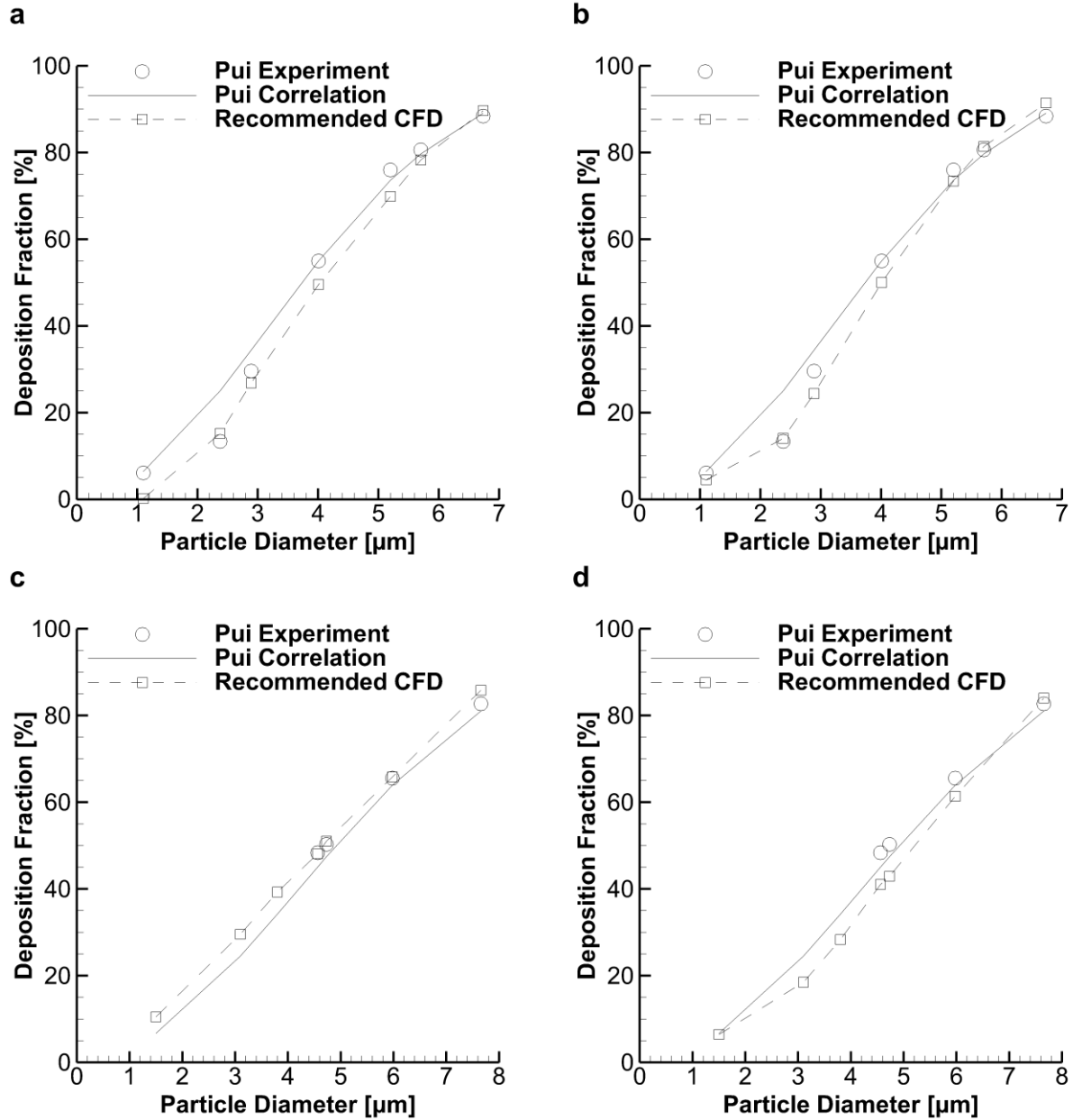
Figure 3.11: Comparison to Pui et al. (1987) data when all CFD recommendations are applied for (a) Re = 6,000 with the hexahedral mesh, (b) Re = 6,000 with the tetrahedral mesh, (c) Re = 10,000 with the hexahedral mesh, and (d) Re = 10,000 with the tetrahedral mesh.
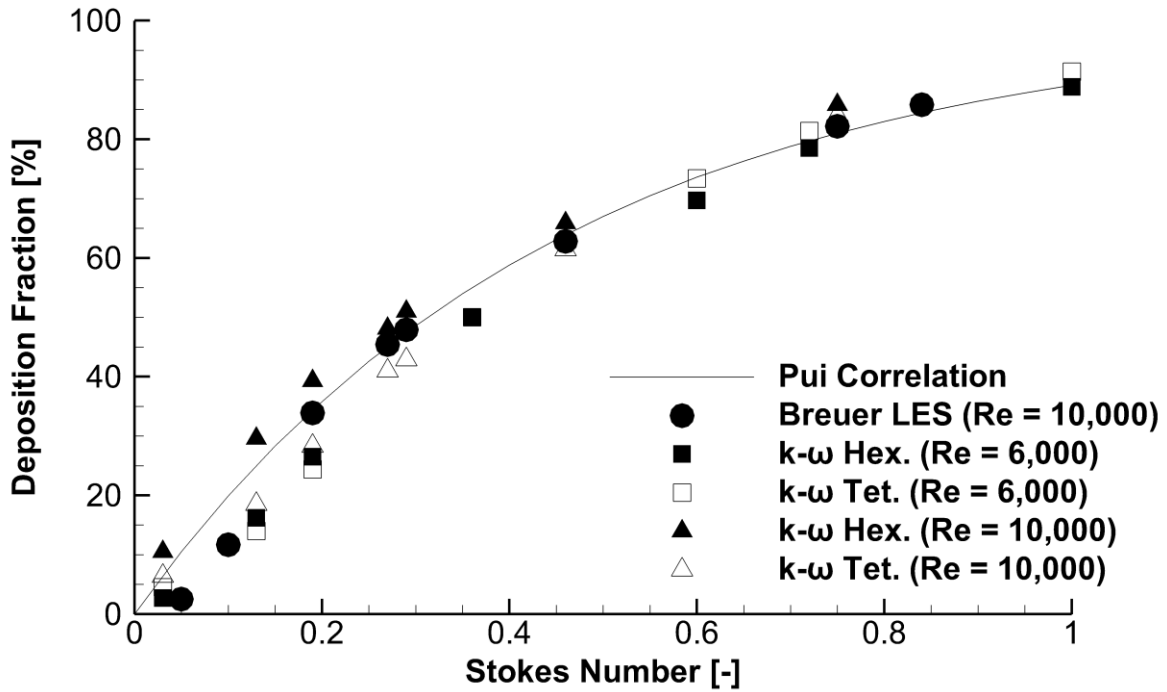
Figure 3.12: Comparison of LRN k-ω results using the best practices from this study with LES data from Breuer et al. (2006). Particle diameters converted to Stokes number to be consistent with the LES study and across different tube diameters.

3.7 Tables

Table 3.1: Experimental results and correlation predictions for selected Pui et al. (1987) models.

Reynolds Number [-]	Tube ID [mm]	Stokes Number [-]	Particle Diameter [µm]	Experimental DE [%]	Correlation Prediction [%]
6,000	5.03	0.03	1.10	6.1	6.4
		0.13	2.38	13.4	25.0
		0.19	2.89	29.6	34.4
		0.36	4.01	55.0	55.0
		0.60	5.20	76.0	73.6
		0.72	5.70	80.6	79.7
		1.00	6.74	88.4	89.1
10,000	8.51	0.03	1.50	N/A	6.4
		0.13	3.10	N/A	18.5
		0.19	3.80	N/A	28.3
		0.27	4.56	48.4	45.0
		0.29	4.73	50.3	47.4
		0.46	5.98	65.6	63.9
		0.75	7.66	82.7	81.0

Table 3.2: Summary of near-wall meshes and parameters.

Name	# NW Layers	First Layer Thickness (y^+)	Layer-to-Layer Ratio	Total NW Thickness
Recommended	20	0.02 (≈1.0)	Layers 1-8: 1.1 Layers 8-20: 1.0	0.70
Intermediate	10	0.02 (≈1.0)	1.0	0.20
Targeted	5	0.02 (≈1.0)	1.0	0.10
Poor Ratio	5	0.02 (≈1.0)	Layer 1-2: 1.8 Layers 2-5: 1.0	0.20
Wall $y^+ \approx 0.5$	1	0.01 (≈0.5)	N/A	0.01
Wall $y^+ \approx 1.0$	1	0.02 (≈1.0)	N/A	0.02
Wall $y^+ \approx 2.0$	1	0.04 (≈2.0)	N/A	0.04
Wall $y^+ \approx 5.0$	1	0.10 (≈5.0)	N/A	0.10
Ratio = 1.0	5	0.02 (≈1.0)	1.0	0.10
Ratio = 1.1	5	0.02 (≈1.0)	Layer 1-2: 1.1 Layers 2-5: 1.0	0.12
Ratio = 1.2	5	0.02 (≈1.0)	Layer 1-2: 1.2 Layers 2-5: 1.0	0.15
Ratio = 1.5	5	0.02 (≈1.0)	Layer 1-2: 1.5 Layers 2-5: 1.0	0.26

Table 3.3:   Mean and standard deviations of the deposition fraction for the Recommended, Intermediate, Targeted, and Poor Ratio meshes when using the Least Squares Cell-based (LSQ) and Green-Gauss Node-based (GGN) gradient discretization methods.

Particle Diameter [μm]	LSQ Mean (SD) DF [%]	GGN Mean (SD) DF [%]
1.10	5.77 (2.37)	3.91 (0.59)
2.38	24.82 (5.88)	28.12 (2.47)
2.89	36.57 (3.94)	41.11 (0.95)
4.01	58.58 (0.60)	60.29 (0.80)
5.20	75.67 (0.85)	77.24 (1.77)
5.70	82.83 (0.32)	83.81 (1.52)
6.74	91.87 (0.10)	92.05 (1.06)

Table 3.4:   Mean and standard deviations of the deposition fraction for the Recommended, Intermediate, Targeted, and Poor Ratio meshes when using a tetrahedral volume mesh, prismatic near-wall cell layers, and the Green-Gauss Node-based (GGN) gradient discretization method.

Particle Diameter [μm]	Tetrahedral Mesh Mean (SD) DF [%]
1.10	13.35 (0.55)
2.38	32.58 (0.50)
2.89	42.78 (0.32)
4.01	61.76 (0.51)
5.20	79.38 (0.31)
5.70	85.78 (0.34)
6.74	94.02 (0.15)

Table 3.5:   Summary of recommended mesh and solver parameters.

	Model/Parameter	Setting/Method
Mesh	Target Wall y^+	0.5-1
	Number of NW Layers	5
	L2L Ratio	1.0 (may be increased with no negative effects)
Flow	Turbulence	LRN k-ω
	P-V Coupling	SIMPLEC
	Mom. & Turb. Schemes	Second-order Upwind
	Gradient Discretization	Green-Gauss Node-based
	Numerical Accuracy	Double Precision
Particles	Tracking Scheme	Lagrangian with Runge-Kutta
	Turbulent Dispersion	Interpolate TKE at particle location from nodes
	Eddy Interaction Model	Modified via UDF
	NW Correction	NW Limit = 1.0-2.0 µm

Chapter 4: Validating CFD Predictions of N2L Aerosol Delivery in a 6-Month-Old Infant Airway Model

4.1 Objective

The primary objective of this study is to validate mesh and CFD parameters against experimental data for accurate modelling of microparticle deposition in an infant nasal airway for the assessment of N2L aerosol administration. Previously developed meshing and solution parameters will be applied to the CFD model, with other considerations specific to infant nasal models observed. Specifically, the commonly used tetrahedral and new polyhedral mesh types are compared, as well as laminar and turbulent flow conditions, and monodisperse versus polydisperse aerosol approximations. To validate the CFD predictions, *in vitro* experiments are reported in an identical nasal airway geometry with a nasal cannula interface. As a secondary objective, high efficiency N2L aerosol delivery is demonstrated in an infant airway model using both CFD and *in vitro* approaches, which is enabled by the use of micrometer-size particles as with the EEG strategy.

4.2 Introduction

The enhanced excipient growth (EEG) method of pharmaceutical aerosol delivery (Hindle & Longest, 2012), with nose-to-lung (N2L) administration via a streamlined nasal cannula, can vastly reduce deposition loses in the patient interface and extrathoracic airways (Longest et al., 2015) leading to high efficiency lung delivery. The EEG approach employs a spray-dried formulation of the drug, which when aerosolized, generally has a micrometer or sub-micrometer mass-median aerodynamic diameter (MMAD) (Son, Longest, & Hindle, 2013; Son, Longest, Tian, et al., 2013). The low inertia of these small

particles allows them to follow flow streamlines and penetrate deep into the conducting airways with little depositional loss. The aerosol formulation includes a hygroscopic excipient, which absorbs moisture from the humid airways, thereby causing the particles or droplets to grow and reach conventional sizes for respiratory aerosols (3-6 μm) as they reach the distal regions of the lungs. This aerosol size increase is associated with an increase in inertial deposition and sedimentation, which minimizes exhalation of the aerosol and may allow for targeted aerosol delivery. The EEG method therefore reduces device and extra-thoracic depositional losses, while allowing targeted delivery and greater retention in the conducting airways (Longest et al., 2015; Tian et al., 2014; Tian et al., 2013).

Using N2L aerosol administration via a streamline nasal cannula provides several benefits over alternative methods of aerosol delivery, which make it well suited for efficient aerosol administration to infants. Infants are generally nose breathers (ICRP, 1994), so delivery through the nasal passage can occur simultaneously while the patient is on non-invasive ventilation. For aerosol delivery to infants, facemasks are often used instead of cannulas, but present several drawbacks. Two notable review papers on aerosol delivery to infants report that patient distress (Everard, 2003) and crying infants (Amirav, 2011) lead to reduced lung drug dose during aerosol administration via a facemask. Studies also report that an airtight seal is required between the facemask and patient face for optimal delivery (Amirav & Newhouse, 2001; El Taoum, Xi, Kim, & Berlinski, 2015), which is difficult to achieve. Furthermore, there is evidence in the literature that nasal cannula systems may provide improved lung delivery efficiency compared to facemasks in infants and children (Amirav, Borojeni, Halamish, Newhouse, & Golshahi, 2015; Reminiac et al.,

2017). It is expected that using small diameter particles (MMAD < 2 μm) for N2L aerosol delivery leads to high efficiency lung doses, as the likelihood of impaction deposition is reduced as particles travel through the nasal cavity and nasopharynx (Storey-Bishoff et al., 2008; Tavernini et al., 2018).

Multiple studies from our group have demonstrated that a concurrent experimental and computational fluid dynamics (CFD) approach can successfully develop and evaluate aerosol delivery systems, with successful validations compared with both *in vitro* (Longest & Hindle, 2009a; Longest et al., 2007; Longest, Tian, Delvadia, et al., 2012; Longest, Tian, Walenga, et al., 2012; Longest & Vinchurkar, 2007b; Tian et al., 2011) and in *vivo* data (Longest et al., 2015; Walenga & Longest, 2016). Deposition results from CFD models can provide valuable insight into the behavior of the aerosol transport through the delivery system and the nasal cavity, in terms of both the flow field and deposition sites. For example, a high concentration of deposition in a localized region of the CFD model may indicate the potential for design improvements, which may not be apparent in experimental data. However, one can only have confidence in results from a numerical model after it has been validated against experimental data based on the parameters of interest. Based on this approach, both numerical and experimental aspects of an analysis can be used simultaneously to facilitate improvements in a targeted drug delivery strategy or device.

To achieve validation of CFD results with experimental data, it is imperative that sound methodology is used in the numerical model in the areas of geometry development, mesh generation, sub-model selection, and solution parameters. Bass and Longest (2018b) recently developed a set of meshing and solution guidelines for application of the

132

low-Reynolds Number (LRN) k-ω turbulence model when simulating microparticle deposition under conditions similar to the upper-airways. This previous study presented an excellent match to both experimental and Large Eddy Simulation (LES) deposition data across a range of particle sizes and flow conditions in a representative 90°-bend geometry. However, it is important to confirm the same meshing and solution guidelines are applicable to a more complex model of the infant nasal cavity. For example, it is currently an open research question if turbulence should be included in simulations of nasal particle deposition. This is further complicated by the presence of the nasal cannula interface, which forms two jets of airflow entering the nasal vestibule and progressing through the narrow nasal valve.

4.3   Methods

Nasal Model Development from Computed Tomography Scans

Pre-existing medically necessary computed tomography (CT) scans of nasal airways from 3-6-month-old infants were reviewed for scan quality and completeness under an institutional review board (IRB) approved protocol. To develop an infant model with a targeted age of approximately 6 months, the selected scan was of a 68.2 cm and 7.7 kg male that was approximately 20 weeks (5 months) old. The patient height and weight both fell within the 25th and 75th percentiles for a 6-month-old (6mo) infant (WHO, 2006). Therefore, it was expected that the model was representative of the target age (Tavernini et al., 2018), despite being approximately one month younger. Of the available scans, the selected scan was chosen because the infant's mouth was closed, it was complete from the nostrils through the larynx, and the slice resolution was sufficiently

small at 1 mm. The scan was reviewed by a pediatric otolaryngologist and found to be free of nasal abnormalities.

The CT scan was segmented by the Mimics software suite (Materialise, Leuven, Belgium) to generate a 3D model of the infant nasal cavity from the 2D image slices. The process of segmentation involves selecting pixels in the CT scan, which combined with the slice thickness become voxels for each slice. The tools and capabilities provided by Mimics allow users to speed up the process by selecting threshold regions of pixels that fall within a greyscale range that are considered internal airways (i.e. not bone or soft tissue). Mimics also automatically smooths the block-shaped voxels to provide a realistic representation of physical anatomy. Once image segmentation is complete, the 3D model is transferred to 3matic (Materialise, Leuven, Belgium) where additional post-processing steps are performed such as wrapping, STL mesh quality improvements, and surface triangle reduction. Surface wrapping covers the initial surface with a second STL surface that removes any non-manifold faces (where three or more faces share a single edge), free edges (holes), or sliver faces, thereby removing any erroneous triangles from the surface. The STL surface is then converted to CAD data using the skin surface capabilities available in SpaceClaim (ANSYS, Inc., Canonsburg, PA, USA). This process involves manually creating polygonal patches (approximately 50) that are wrapped to conform to the faceted surface. Therefore, instead of the nasal cavity being defined by thousands of STL triangles, it is represented by approximately 50 CAD format surfaces. This step makes it possible to import the model into third-party CAD software.

In SolidWorks (Dassault Systèmes, Paris, France), the nasal cavity was further modified to generate a suitable experimental model that can be produced with 3D printing.

This included supports for locating the streamlined nasal cannula and connections to an outlet filter to measure recovered lung dose. Design considerations were also made to simplify the 3D printing of the model. The model was separated into three regions that approximate the anterior nose, middle passage, and nasopharynx, as this makes it easier to clean support material from inside the nasal cavity and provides insight into the regional deposition within the model. The nasopharynx part of the model was also split in half to remove support material from around the glottis, and then sealed with locating pins and epoxy.

Figure 4.1a shows the CAD surfaces of the 6mo airway experimental model with cannula support, outlet filter connection, and connections between the three regions. Figure 4.1b shows the air interface of the cannula, nasal cavity, and filter connection that form the CFD model surfaces. Figure 4.1b also clearly illustrates the complexity of the infant nasal airway, especially in the region of the turbinates and larynx.

Experimental Set-up

Micrometer-sized aerosols were generated using a novel mixer-heater in combination with a commercial nebulizer operating with reduced aerosol output. The mixer-heater delivery system is shown in Figure 4.2. The mixer-heater (61.6 mL internal volume) was designed to efficiently mix nebulized aerosol with incoming ventilation gas and then heat the aerosol to reduce it to micrometer or sub-micrometer size for inhalation. Consistent with infant high flow nasal cannula ventilation, air at a flow rate of 6 L/min was introduced into the mixer-heater with the heating element set to 60 °C, which resulted in an exit aerosol temperature from the streamlined cannula of 35 °C. Aerosol was generated from a 0.5% w/v albuterol sulfate solution prepared by dissolving albuterol

sulfate USP (Letco Medical, LLC, Decatur, AL) in water. The particle size of the emitted aerosol was similar to previous EEG studies, however an EEG excipient was not included, as hygroscopic growth in the airway model was not investigated in this study. An Aerogen Pro nebulizer (Aerogen, Galway, Republic of Ireland) was used in the mixer-heater, however the mean (SD) output of the nebulizer was reduced to 70 (7) µL/min compared to typical values of 300-400 µL/min when operated using the Aerogen Controller. Reducing the output of the nebulizer was required to ensure drying of the aerosol to micrometer-size at the infant gas flow rate. This was achieved by reducing the sinusoidal operating voltage amplitude of the controller to 14.1 V_{rms} compared to the normal operating value of 50 V_{rms} for the commercial nebulizer. The nebulizer was filled with 3.5 mL of the nebulizer formulation and weighed prior to and following nebulization for each run (duration of 20 minutes). The mass of nebulized formulation and the concentration of the formulation was used to calculate the nominal dose of nebulized drug. Standard infant ventilator tubing with a diameter of 10 mm was used to connect the mixer-heater device to the streamlined infant cannula.

Aerodynamic particle sizing experiments were performed using the Andersen Cascade Impactor (ACI, Copley Scientific, Nottingham, UK) placed in an environmental chamber (Espec, Hudsonville, MI) set to 35 °C and 99% relative humidity (RH) to minimize effects of evaporative size changes during measurements. The aerosol output at the exit of the nasal cannula was positioned at the entrance to the ACI. The ACI inlet entrained the aerosol exiting the nasal cannula plus additional makeup air from the environmental cabinet for a total ACI flow rate of 28.3 L/min. Drug was collected from the impactor stages and filter to determine the emitted dose, the MMAD and particle mass fraction less than

1 µm and less than 5 µm. MMAD and particle fractions were determined by linear interpolation. MMAD values were directly calculated as the size associated with a cumulative count of 50% based on mass percentages calculated relative to the impactor dose. Particle mass fractions were calculated as the cumulative mass fraction frequency associated with sizes of 1 µm and 5 µm, respectively. A minimum of three measurements were performed.

Studies were also performed to determine the regional deposition of the mixer-heater generated micrometer drug aerosol in the infant model as shown in Figure 4.2. Aerosols were continuously generated in these steady-state flow experiments as described above, with the outlet of the streamlined infant nasal cannula inserted into the nostrils of the airway model. Aerosol delivered through the infant nasal model was captured on a low resistance respiratory filter positioned at the exit of the trachea and was considered as the delivered *in vitro* N2L dose. A constant flow of 7 L/min was drawn through the airway model. As described previously, the physical model was identical to the CFD model and included the nostrils, turbinates, nasopharynx, larynx and a portion of the trachea. The model was segmented into three portions: 1) the anterior nose, 2) the middle passage, and 3) the nasopharynx, larynx and trachea. Drug deposited on the model components and respiratory filter was recovered and analyzed using a validated isocratic HPLC method. AS quantification was performed with a validated HPLC method using a Waters 2695 separations module with a 2475 fluorescence detector (Waters Co., Milford, MA). Chromatography was performed using a Restek Allure PFP 150 mm × 2.1 mm column (Bellefonte, PA). The mobile phase, consisting of methanol and ammonium formate buffer (20 mM, pH 3.4) in a ratio of 70:30, respectively, was eluted at a flow rate

of 0.4 mL/min and the detector was set to an excitation wavelength of 276 nm and emission at 609 nm. The column temperature was maintained at 25 °C, and the volume of each sample injected was 100 μL. The limit of quantification was 0.5 μg/ml (Behara, Longest, et al., 2014b; Son, Longest, & Hindle, 2013). The recovered emitted dose from the mixer heater was calculated as the mass of drug deposited on the ventilator tubing, cannula, nasal airway model and respiratory filter. Regional drug deposition was expressed as a percentage of the recovered emitted dose from the mixer heater.

Numerical Model

As with all CFD to experimental comparisons, the numerical model aims to replicate the experimental set-up as closely as possible. The following sections detail aspects of the CFD model set-up and the steps taken to ensure accurate and reliable deposition results.

Meshing and Solution Guidelines

Bass and Longest (2018b) recently provided a set of CFD meshing and solution guidelines for modelling aerosol deposition in the respiratory airways, under transitional and turbulent flow conditions, using the LRN k-ω turbulence model. These guidelines detailed near-wall (NW) mesh parameters and solver settings that provided a good match to experimental and LES data of micrometer (from approximately 1.0 to 7.5 μm) particle deposition in a characteristic 90° bend geometry. Table 4.1 summarizes the recommendations from that study, which will be applied to the current numerical model, with the intention of validating the mesh and solver settings against experimental data of micrometer particle deposition in an infant nasal cavity during N2L aerosol administration.

In addition to validating the CFD meshing and solution guidelines, this study explores the assumption of laminar flow versus a turbulence approximation modeled with the LRN k-ω turbulence model for infant nasal airways. Results evaluate the turbulent nature of the flow and its influence on both monodisperse and polydisperse aerosols. Flow through the infant nasal cavity is generally in the laminar or transitional regime when considering the Reynolds number at the connection tubing inlet (approximately 900). However, the complexity of the nasal passages and transition from the patient interface to nostrils may induce turbulence in the flow. Specifically, the nasal cannula interface creates air jets that enter the most constricted portion of the nose, i.e. the nasal valve.

CFD models with the LRN k-ω turbulence approximation generally tend to over-predict microparticle deposition, due to the assumption of isotropic NW turbulence. Longest and Xi (2007) developed a method of NW correction by utilizing FLUENT user-defined functions (UDFs), which built upon previous work by Matida et al. (2004) and Wang and James (1999). The NW correction UDFs include anisotropic velocity fluctuations in the continuous phase and damp the wall-normal velocity in the NW region to represent particle-wall hydrodynamic interactions (Longest, Kleinstreuer, & Buchanan, 2004). Further details on these corrections have been reported in previous studies from our group (Longest & Xi, 2007; Walenga & Longest, 2016), and recent improvements to interpolation methods were reported by Bass and Longest (2018b). The key control parameter used by the NW correction UDFs is the NW limit, as it determines the particle-to-wall distance below which wall-normal velocity is damped. This parameter is adjusted to match numerical and experimental deposition data, with Bass and Longest (2018b) reporting values of 1-2 μm provided good comparisons in their 90° bend study. The

present work will compare results using the NW corrections versus the standard turbulent particle dispersion model, and a case that includes the LRN k-ω turbulence approximation of the flow field, but without the particle dispersion model activated. This investigation will also determine whether the NW limit control established in the simple 90° bend study can be applied to the highly complex infant nasal cavity model.

Meshing Approaches

This study compares two types of unstructured meshes for modeling aerosol deposition in the patient interface and nasal cavity. Ideally, numerical models use structured hexahedral meshes, as they generally give the best solution accuracy, stability, and computational efficiency. However, the complex geometry of the infant nasal cavity makes it prohibitively difficult to apply a structured mesh. Unstructured tetrahedral meshes are often used when a hexahedral mesh is not possible, as they are able to conform to complex surfaces and efficiently fill the domain volume with good-quality cells. Bass and Longest (2018b) concluded that a tetrahedral mesh with five prismatic NW cell layers provides similar microparticle deposition to a hexahedral mesh in a simplified geometry under flow conditions similar to the infant airways. However, differences in the deposition predictions were observed for 1 µm particles between meshes with tetrahedral and prismatic NW cells, which required more correction. In the current study, the tetrahedral and prismatic NW cell mesh is explored and applied to the infant nasal geometry, with mesh parameters that were established in the much simpler 90°-bend considered by Bass and Longest (2018b), as shown in Table 4.1. Figure 4.3a shows the meshing structure of the tetrahedral cells with prismatic NW cell layers at the tube inlet,

and Figure 4.3c shows a cut through the middle meatus that exposes the interior nasal mesh.

The tetrahedral and prism mesh shown in Figure 4.3a and c was generated using the FLUENT meshing capabilities (ANSYS, Inc., Canonsburg, PA, USA). The process begins by producing a triangular surface mesh that conforms to the complex geometry. Curvature, proximity, and locally defined size controls are used to adjust the mesh sizing in order to obtain an accurate representation of the geometry surface and increase fidelity in regions of interest and importance. To generate the volume mesh, the software uses a Delaunay algorithm to fill the domain with tetrahedral cells, and the five-sided prismatic NW cells are added by inflating the surface mesh towards the cell interior. Definition of the NW cell layers follows the recommendations provided by Bass and Longest (2018b) of five equally spaced layers with an approximate wall y^+ of one (see Table 4.1.) Once the meshing process is complete, the cell nodes are smoothed using the capabilities in FLUENT meshing to ensure that all cells have an orthogonal quality greater than 0.25, which provides a high-quality discretization of the domain.

In addition to tetrahedral meshes, FLUENT meshing is capable of producing polyhedral meshes, which are composed of cells with any number of faces, edges, and vertices. Polyhedral cells generally have more faces than hexahedral or tetrahedral cells, which results in more cell neighbors, and hence better resolution of gradients in and out of the control volume (Sosnowski, Krzywanski, & Gnatowska, 2017). The various orientations of each cell face (see Figure 4.3d) also increases the likelihood of having flow aligned with a cell face, which can reduce numerical diffusion, as it does for flow-aligned hexahedral meshes. There is much anecdotal evidence in the CFD community

that polyhedra provide faster convergence with lower cell counts than tetrahedra. However, a review of the literature shows there has been no direct evaluation of these two unstructured meshing approaches in the field of respiratory drug delivery research. The closest comparison comes from Lotfi et al. (2016) who concluded that polyhedra provided superior results to tetrahedra when modelling flow through a stented artery. However, their study did not provide details on convergence or computational efficiency. A study from van Ertbruggen et al. (2008) developed a CFD model representation of alveolar structures in the lungs, which used a polyhedral mesh, and made good comparisons with experimental data for laminar, very low speed flow. However, a direct comparison of results from tetrahedra and polyhedra was not made. Furthermore, both of these previous studies did not include particle transport and deposition. Peric (2004) provided a complete comparison of polyhedral and tetrahedral meshes for a simple 3D lid-driven cavity flow model under laminar conditions, and showed that polyhedra required 50% less memory and less than 20% of the computation time.

The advantages described here make polyhedral meshes a promising approach for developing computationally efficient airway models. Figure 4.3b shows the polyhedral mesh at the tube inlet and Figure 4.3d shows the interior mesh in the middle meatus. These images show that the polyhedral cell faces are generally 5- or 6-sided polygons, and as such, the NW cell layers have a varying number of sides. The process of generating a polyhedral mesh is similar to tetrahedral meshing, including the generation of a tetrahedral volume mesh. Once the volume mesh is complete, the software uses dualization and agglomeration algorithms to convert the tetrahedral cells to polyhedral. The details of this conversion are covered in more detail in the ANSYS User Guide (2017)

142

and other resources. As with the tetrahedral mesh, the final step is to smooth the mesh and ensure all cells are high quality with orthogonal quality greater than 0.25.

In the preliminary stages of this project, other meshing approaches were considered. In particular, we initially evaluated the cut-cell meshing capabilities of FLUENT meshing. A cut-cell mesh is generated by starting with a Cartesian grid that encloses the geometry. Cells outside the domain are then excluded or cut to conform to the complex surfaces, which results in hexahedral cells in the bulk of the domain and irregular polyhedral cells near boundaries. This approach is appealing as it provides the numerical accuracy and stability of hexahedral cells with the ability to conform to complex geometry. However, cutting the cells near close-proximity surfaces, such as the thin-walled cannula prongs, generated poor quality cells and an inaccurate representation of the geometry. This issue could be overcome by locally refining the mesh near these close-proximity surfaces, but the cell count for the coarsest cut-cell mesh exceeded that of the finest tetrahedral mesh. Furthermore, the core hexahedral cells are Cartesian, but not flow aligned, so there may be no numerical benefit to using this mesh technology in the airways. Therefore, we decided not to pursue the cut-cell meshing approach further for respiratory aerosol simulations.

Mesh Dependency Study

A mesh dependency study was performed on both the tetrahedral and polyhedral meshes to determine the optimum grid resolution. In Figure 4.4, the volume-average velocity magnitude, turbulent kinetic energy (TKE), and nasal cavity deposition efficiency (DE) are compared for a coarse (2.76 million cells), medium (5.71 million cells), and fine (11.50 million cells) tetrahedral mesh, and also a coarse (0.88 million cells), medium (1.80

million cells), fine (3.56 million cells), and extra fine (7.42 million cells) polyhedral mesh. The DE is calculated from particles that are exposed to the turbulent dispersion model, but no NW corrections are applied. The comparison shows that the 5.71 million cell tetrahedral mesh and 3.56 million cell polyhedral mesh each give the best compromise between grid convergence and solution processing times. Between the medium and fine tetrahedral mesh, the volume-average velocity magnitude, TKE, and nasal cavity DE differ by only 0.008 m/s, 0.004 m^2/s^2, and 0.2% respectively. Similarly, the fine and extra fine polyhedral mesh differ by 0.003 m/s, 0.004 m^2/s^2, and 0.2%. Therefore, the remainder of this study uses the 5.71 million cell tetrahedral mesh and 3.56 million cell polyhedral mesh to compare each cell type and validate the CFD solution parameters. These cell counts are similar to grid convergence established in other nasal studies including the 3-6 million cells used by Walenga et al. (2014) and the 4 million cells used by Frank-Ito et al. (2016).

Boundary Conditions

Boundary conditions in the CFD model were set to replicate the flow in and out of the experimental model. Mass flow inlet and outlet boundary types were applied at the tube inlet and filter connection outlet, with mass flow rates that gave 6 and 7 LPM respectively. The inlet conditions in the delivery tube, with a 10 mm inner diameter (ID), gave an inlet Reynolds number of approximately 900, which suggests the flow in the tube will be laminar. However, it is known that changes in cross-section, obstructions, and changes in flow path can induce transitional and turbulent flow regardless of inlet flow conditions (Wilcox, 1998). As mentioned previously, the effect of laminar and LRN k-ω models on flow and particle deposition are evaluated in the Results section. Pressure

inlet boundaries were applied to both the left and right nostrils in the gap between the cannula surface and airway walls, which were exposed to ambient pressure (gauge pressure of 0 Pa). The additional 1 LPM flow from the difference between the delivery tube inlet and filter connection outlet flow rates enters the domain through the nostrils, and using pressure inlets enables this inflow to vary in local velocity.

For the LRN k-ω model cases, turbulence boundary conditions are required at each of the inlet boundaries, which were defined with hydraulic diameter and turbulence intensity. For the tube inlet, the hydraulic diameter is simply the 10 mm tube ID, as the cross section is circular. Turbulence intensity at the tube inlet is estimated to be approximately 6% based on the approximation:

$$I = 0.16 \text{Re}_D^{-\frac{1}{8}} \tag{4.3.1}$$

where: I is turbulence intensity and Re_D the Reynolds number using the inlet hydraulic diameter (ANSYS, 2017). For the nostril inlets, the hydraulic diameter is calculated by considering each boundary as an annulus and estimating the inner and outer diameters by measuring the perimeters in the CAD software, which resulted in approximately 8.1 mm for both boundaries. As inlet velocity and Reynolds number at the nostrils is not known *a priori*, the turbulence intensity at the nostril inlets is assumed to be 1%. Preliminary work tested the effect of this assumption on particle deposition by changing turbulence intensity to 5% at the nostril inlets, and negligible influence was seen in deposition fractions (DFs) throughout the domain. Therefore, the turbulence intensity estimates made here will not largely affect the particle deposition results.

An additional geometry extension was applied to the inlet, which was 30 mm long (3 times the inlet diameter), to better match the experimental conditions. Similarly, a

numerical extrusion was also added to the filter connection outlet, but due to recirculation in the filter connection, its length was increased until there was no reverse flow at the mass flow outlet. Particle deposition was checked on the inlet extrusion wall in the unlikely event there was reverse flow in this region, but this did not occur in any of the considered cases. Particles did deposit on the outlet extrusion wall, but these particles were not included in evaluations of deposition in the nasopharynx region. That is, it is assumed that any particles that deposit on the outlet extrusion are collected by the outlet filter.

Solution Strategy

As is typical for CFD simulations, the first convergence check was that the residuals for all transport equations fall below at least 1e-4. Flow rates through the pressure inlet nostrils were also checked to ensure that mass was conserved through the domain. Due to the difference in flow rates between the filter connection outlet and tube inlet, flow through both nostrils should be 1 LPM. Therefore, we were confident that mass through the domain was conserved if the flow rate through the pressure inlet boundaries is within plus or minus 0.01% of this expected value. Volume-average velocity magnitude and TKE were also monitored for the entire domain, and the solution was deemed converged when these quantities converge to a stable value with negligible fluctuation.

During the CFD model development, we were unable to reach a converged solution using the steady-state formulations due to mass imbalance in a number of cells in the filter connection region. Further investigation of the flow field in this region showed an area of recirculation where the flow leaves the nasopharynx and enters the filter connection. Physically, this recirculating region is unstable, with the re-attachment point oscillating in time, making the problem fundamentally transient (time-dependent). To

correct this issue, we switched from the partially converged steady-state solution to a time-dependent formulation. This solution strategy, with an appropriately small time-step, allows the model to capture the physically correct oscillatory flow and reach a high degree of convergence, which was less than 1e-5 on all residuals. To confirm this method is valid, flow quantities are compared at the end of each time step to ensure there is little change in the flow field outside of the oscillating region. Particle DFs are also compared at the 10th and 20th time step to make sure particle trajectories do not change with respect to time. For all cases considered, switching from the partially converged steady-state solution to transient provided excellent convergence and showed negligible change in the flow field and deposition characteristics. Furthermore, evaluation of the flow field revealed the flow recirculation was in a region outside of the infant nasal cavity and nasopharynx (in the filter connection), and therefore does not contribute to extrathoracic loses. However, the effect of flow recirculation on the *in vitro* deposition results is discussed in later sections of this study.

Particle Injections

In the experimental model, the tube that connects the mixer-heater device to the streamlined nasal cannula has a 10 mm ID, but the outlet from the mixer-heater used for aerosol generation is 6 mm ID. That is, the 10 mm tubing fits around the outside of the 6 mm mixer-heater outlet, which has a 2 mm wall thickness. Therefore, particles are injected into the CFD model at the inlet to the tube, with a 6 mm circular diameter and a blunt profile distribution in space.

Both monodisperse and polydisperse particle size distributions were evaluated in this study. The polydisperse size distribution used in the CFD model neglects the three

147

larger particle size bins (5.8 µm, 9.0 µm, and 10.0 µm) of the ACI analysis, as these bins

combined account for less than 1% of the total particle mass delivered to the experimental

model (0.28%, 0.19%, and 0.15% respectively). To ensure good particle deposition

convergence Tian et al. (2015) recommended 10,000 particles be injected for each size

bin, which in this case results in 60,000 total particles. To compare the total DF in each

region of the CFD model to the experimental data, the DF for each size bin is multiplied

by the mass of particles for that bin and divided by the total injected mass, which is then

summed over all bins. This is described as

$$\text{DF}_i = \frac{n_i}{N_i} \tag{4.3.2}$$

$$\varphi_i = \frac{DF_i \times m_i}{M} \tag{4.3.3}$$

$$DF_{Region} = \sum_{i=1}^{6} \varphi_i \tag{4.3.4}$$

where n_i is the number of particles deposited for size bin i, N_i is the number of particles

that enter the CFD domain for bin i, DF_i is the deposition fraction for size bin i, m_i is the

mass of particles from the experimental size distribution for size bin i, M is the total

injected aerosol mass, and φ_i is the deposited mass fraction for size bin i. The region-

based DFs presented in the Results section use the above equations, with n_i given as

the number particles that deposit in a given region.

A monodisperse aerosol is also evaluated by the CFD model to determine whether

it gives comparable results to a polydisperse size distribution. The monodisperse particle

size is 25% larger than the MMAD of the polydisperse aerosol, which results in 1.78 µm

(where the measured MMAD is 1.4 µm). This approach has previously given comparable

results for both *in vitro* (Longest, Tian, Delvadia, et al., 2012) and *in vivo* (Longest et al., 2015) deposition in the upper airways. Theoretically, the multiplication factor is needed because the particle deposition increases at a non-linear rate for an increasing particle diameter. For particle deposition convergence, 90,000 particles are injected into the domain for the monodisperse aerosol (Longest et al., 2015). The monodisperse aerosol also uses the same diameter and spatial distribution at the tube inlet as the polydisperse injection.

4.4   Results

Experimental

The droplet size of the albuterol sulfate aerosol exiting the infant cannula was determined to have a mean (SD) MMAD of 1.4 (0.1) μm and GSD of 1.4 (0.0) with 99.5% and 25.5% of the particles less than 5 μm and 1 μm, respectively.

For the aerosol deposition experiments, the overall mean (SD) drug recovery was 84.3 (3.4) % of the nominal dose. Deposition in the mixer heater was low (2.1% of the nominal dose) demonstrating the efficiency of the delivery system. Table 4.2 shows the mean (SD) experimentally determined deposition fractions expressed as a percentage of the recovered emitted dose from the mixer heater. Deposition on the patient interface (tubing and cannula) was low with only 2.23% of the dose being found in this region. Similarly, deposition in the infant nasal airway model was also low, with less than 5% of the recovered emitted dose being deposited in the combined nasal passages. For this micrometer-sized aerosol generated using the mixer heater, the mean drug deposition fraction on the respiratory filter was 92.96 %, indicating highly efficient N2L delivery under these steady-state inhalation flow conditions.

Comparison of Polyhedral and Tetrahedral Meshes

As discussed in the Methods section, it is expected that polyhedral meshes may provide faster convergence than tetrahedra. Figure 4.5a and b respectively plot the volume-average velocity magnitude and TKE in the CFD domain against solution iterations for the steady-state solution of the flow field. These plots show that the polyhedral mesh reaches a converged solution in approximately 2,000 iterations compared to approximately 3,500 iterations for the tetrahedral mesh. Recall that the steady-state model is switched to a transient formulation, with constant boundary conditions, to capture flow oscillations in the filter connection and thereby enable convergence. Also note that the mesh-independent polyhedral case uses 3.56 million cells and the tetrahedral cases required 5.71 million cells. Therefore, the polyhedral mesh is capable of reaching a converged solution faster, and with less computational expense. These combined benefits of polyhedral cells result in CFD models that provide a flow field solution almost 3 times faster than tetrahedra, making them extremely computationally efficient, which is very beneficial for time-consuming transient simulations.

In addition to improvements in processing time, polyhedral cells provide the benefits described in the Methods section, specifically better cell-face gradient resolution and reduced numerical diffusion. The accuracy of polyhedral cells is evaluated by comparing CFD particle deposition results with experimental data, as shown below.

Comparison of Laminar and Turbulence Models

A Reynolds number of approximately 900 at the 10 mm ID inlet suggests laminar conditions. However, changes in cross-section and flow obstructions can induce turbulence in the flow field, especially in regions of air jets and shear layers. Figure 4.6

shows iso-surfaces of turbulent viscosity ratio (TVR) in the CFD model, which is the ratio of turbulent viscosity to laminar viscosity. That is, a TVR of two means the turbulence in the flow makes the fluid twice as viscous as the laminar case. From Figure 4.6 it is clear that that the TVR is at least two in a large portion of the nasal cavity, and reaches a ratio of at least five where the flow transitions from the patient interface to nasal cavity and around the glottis, as it is a flow obstruction. Therefore, a turbulence model is required, in this case the LRN k-ω model, in order to capture the flow conditions in the CFD domain. The inclusion of turbulence in the model also has an influence on particle trajectories and deposition, as the particles interact with both the mean flow and turbulent eddies. It is also interesting to note that the filter connection region exhibits a large amount of turbulent flow, which may reduce the number of particles that reach the outlet filter and over-estimate deposition in the nasopharynx region.

Figure 4.7 shows the DF as a function of particle aerodynamic diameter ($\rho_p = 1000$ kg/m^3) for the laminar flow field and turbulent flow field with turbulent particle deposition, over a span of aerosol sizes. The MMAD of the test aerosol (1.4 µm) is labelled within this span. Interestingly, at this small aerodynamic diameter there is practically no difference between the laminar and turbulent model DFs. This is because particles less than approximately 1.5 µm lack sufficient inertia to remain on the random paths induced by turbulent fluctuations at the low level of turbulence in this flow field. They also lack sufficient inertia to traverse the viscous sublayer that is formed in turbulent flow. Note that the LRN k-ω model captures the viscous sublayer, which in this application has off-wall height dimension of approximately 0.25 mm, or approximately 175 times greater than the MMAD. In contrast, as the particle aerodynamic diameter increases beyond 1.5 µm,

particles are able to follow dispersion paths and reach the NW region by crossing the viscous sublayer. Therefore, for CFD models of aerosol deposition in the nasal airways to be applicable to the widest range of particle sizes, turbulence models should be included. In this instance, the small size of the test aerosol means that total DFs between laminar and turbulent models are similar. However, for an accurate and realistic representation of the flow field deposition across a relevant particle size distribution (i.e. 1-7 μm), CFD models should include turbulent flow conditions and dispersion.

Comparisons between CFD and Experimental Data

Comparisons of the CFD monodisperse and polydisperse deposition predictions to experimental data are provided in Table 4.2 to Table 4.5. Table 4.2 presents the DFs for the laminar CFD case, Table 4.3 is the LRN k-ω case with turbulent particle dispersion deactivated, Table 4.4 is the LRN k-ω case with turbulent particle dispersion activated, and Table 4.5 is the LRN k-ω case with turbulent dispersion and NW correction UDFs. The difference parameter (Diff.) is defined as the absolute value of absolute difference between the CFD and experimental data (i.e. $\left|DF_{CFD} - DF_{Exp}\right|$). All four cases show good agreement with the experimental data, with the highest average difference across all model regions being 1.75% for the polydisperse case with turbulent dispersion activated and without NW corrections (see Table 4.4).

The polydisperse laminar case gives the closest match to the experimental data with an average difference of 0.29% across all regions and a maximum difference of 0.68% in the anterior nose. However, from Figure 4.6 and Figure 4.7 we conclude that turbulence should be included in the CFD model to provide a physically realistic representation of flow through the domain, and be applicable to a relevant range of

microparticle sizes. Of the turbulent cases considered, both the monodisperse and polydisperse case that used NW correction UDFs gave very close matches to the experimental data, with average differences of 0.52% and 0.63%, respectively. It is noted that the NW correction UDFs used a NW limit control parameter of 2 μm on all wall surfaces and for both the monodisperse and polydisperse cases. This NW limit value corresponds well with the 1-2 μm values used by Bass and Longest (2018b) in their previous validation work.

In general, the monodisperse aerosol, which has a particle size 25% larger than the polydisperse MMAD, under-predicts deposition in the proximal regions (nearest the inlet) of the nasal cavity compared to the experimental data and polydisperse deposition. For example, in the patient interface for the NW correction UDF case, the monodisperse aerosol predicts 1.21% less deposition (absolute difference) than the polydisperse case. In downstream regions, the monodisperse and polydisperse cases compare closely to one another. This is due to the larger particles in the polydisperse aerosol being filtered by the patient interfaces and to some extent the anterior nose, so the size distribution in the later stages is closer to the monodisperse aerosol. However, using a monodisperse aerosol with a particle aerodynamic diameter that matches the MMAD of the polydisperse aerosol would under-predict both regional and overall deposition in the CFD model. Therefore, using a representative monodisperse aerosol that is 25% larger than the MMAD gives a better approximation of overall deposition.

The close comparison between each aerosol type is apparent in Table 4.2 through Table 4.5 and Figure 4.8, which shows particle deposition sites in the model for the monodisperse (Figure 4.8a) and polydisperse (Figure 4.8b) aerosols for the laminar flow

153

case. The key difference between Figure 4.8a and b is the polydisperse case highlights deposition hot spots that are not apparent in the monodisperse case, in particular the cannula bifurcation and in the nasal cavity close to the left prong. Both cases show a region of deposition at the rear of the nasopharynx, which is expected as this is the region where the bulk flow undergoes its most abrupt change in direction. Therefore, the polydisperse aerosol gives better physical insight, but the monodisperse aerosol gives good overall deposition results, and reduced computational expense. As such, there are benefits and drawbacks to both approaches that make them desirable for either high fidelity or high efficiency models.

Figure 4.9 compares the deposition in the turbulent flow field with the standard dispersion model (Figure 4.9a) and with NW correction UDFs (Figure 4.9b). Figure 4.9b shows that applying the NW correction UDFs, with a NW limit value of 2 μm, gives a better overall match to the experimental DFs, and validates the CFD mesh and solution parameters for infant N2L aerosol administration. The standard dispersion model in Figure 4.9a tends to over-predict deposition in regions where there is the most change in flow direction, specifically the patient interface and nasopharynx. Both of these figures also show a large amount of deposition on the filter connection, which may suggest higher deposition in the *in vitro* nasopharynx than would occur *in vivo*. Based on this observation, future *in vitro* studies should consider a smaller diameter filter size to avoid unnecessary deposition in the filter connection and housing that would not occur *in vivo*. This region also showed a large amount of flow recirculation, which is not desirable for either a CFD or *in vitro* model.

4.5   Discussion

This study demonstrates the N2L EEG approach is a viable method for aerosol delivery to infant lungs. The small aerodynamic diameters and low inertia allows a large amount of the aerosol to penetrate the nasal cavity, which results in a high lung dose with greater than 90% of the aerosol delivered through the connection tube. The previously developed CFD mesh and solution guidelines from Bass and Longest (2018b) were found to be appropriate for simulating microparticle deposition in the infant nasal airway based on good matches to experimental DFs. The best practice set-up, which includes the LRN k-ω turbulence model with NW corrections and follows the other recommendations in Table 4.1, resulted in an average absolute difference of 0.63% across all regions considered compared to the experimental results. The physical insight provided by the CFD model highlights deposition hot spots, specifically the cannula bifurcation and close to the prong outlets, which can be optimized in future studies to further reduce drug delivery loses in the patient interface and nasal cavity. The particle deposition patterns also show inadequacies in the *in vitro* model, where deposition on the filter connection suggests higher loses in the nasopharynx than would likely occur in a patient.

A close match between numerical and experimental results is only possible when the numerical model has been appropriately developed and applied. In addition to the fundamental recommendations in Table 4.1, this nasal cavity simulation required additional key aspects to be considered. The transient nature of the flow recirculation in the filter connection required a time-dependent formulation and solution of the transport equations, despite the experimental model being run under steady-state flow conditions. While not surprising in hindsight, it is notable that the CFD solution would not converge

until the correct physics of the transient oscillatory flow were added to the solution. Correct prediction of particle deposition in the patient interface required an accurate spatial distribution for particle injection into the domain, which matched the outlet diameter of the mixer-heater device. In addition to previous work from our group and others (Vaish, Kleinstreuer, Kolanjiyil, Saini, & Pillalamarri, 2016; Y. Zhang, Finlay, & Matida, 2004) Table 4.3 to Table 4.5 show how the NW corrections address the over-prediction of microparticle deposition that is present with the standard two-equation turbulent dispersion model, and gives the closest match to experimental data for all turbulent cases considered.

Beyond the meshing and CFD solution parameters, several other approaches to CFD model set-up were compared and evaluated; specifically, the mesh cell type, whether turbulence is required, and monodisperse and polydisperse particle size distributions. This study evaluated the capabilities of polyhedral cells compared to traditional tetrahedral cells for CFD simulations with complex geometry. The topology of polyhedral cells provides several numerical advantages, and results show that polyhedra provide a converged solution in less iterations with a lower cell count than tetrahedra, while also comparing well to experimental deposition data.

With regard to flow conditions, flow and microparticle deposition in the nasal cavity were evaluated for both the laminar and LRN k-ω model. The laminar flow case provided a good match with experimental DFs, but using the LRN k-ω model gives a more physically realistic flow field and is suitable for a broader range of N2L applications across the relevant microparticle size range. Furthermore, evaluation of TVR showed regions of relatively high turbulence around abrupt changes in cross section and flow obstructions,

156

which must be accounted for in the CFD model. Viewed another way, running the nasal simulation as a laminar flow would be equivalent to conducting a physical experiment with a gas that had a viscosity two to five times below that of air (which does not exist), and assuming the fluid was air.

The results compared both monodisperse and polydisperse aerosol deposition, where the monodisperse aerosol was represented with a particle size that is 25% larger than the MMAD of the polydisperse aerosol. The CFD model showed that the monodisperse aerosol can be comparable to polydisperse and experimental data for total and regional deposition. However, the polydisperse aerosol highlights deposition hot spots that are not apparent in the monodisperse case. Therefore, monodisperse aerosols are useful in the model development phase, as they required less computation time, but more accurate results require a polydisperse size distribution, which enables additional useful insights.

As a secondary objective, this study demonstrates high efficiency N2L delivery using an aerosol with a small initial size (MMAD of 1.4 µm). The aerosol was produced with a mixer-heater similar to the study of Longest et al. (2013), but with a lower device volume and using a reduced nebulizer output. The primary advantage of this mixer heater system is that it employs a commercial mesh nebulizer, but uses heating elements to dry the droplets into smaller particles while maintaining a temperature and relative humidity that are safe for direct inhalation. Using this approach, lung delivery efficiencies greater than 90% of the aerosol that enters the connection tube were demonstrated in a 6mo airway model under steady state flow conditions.

In comparison to similar studies with infants, Lin et al. (2015) used a commercially available vibrating mesh nebulizer and humidifier, and evaluated delivery flow rates of 3, 6, and 12 LPM across two different face masks for a 2-year-old nasal model. They reported MMADs of 2.8 µm to 3.3 µm exiting the facemask, and an inhaled mass of 2.8% to 6.4% (expressed as a percentage of dose loaded in the nebulizer). El Taoum et al. (2015) compared numerous scenarios for a 7-month-old model, including seven different patient interfaces, jet and vibrating mesh nebulizers, and three breathing patterns. In their study, lung doses (as a percent of nominal dose) range from <0.001% to 2.97%, but aerosol MMADs were not reported. Regarding nasal cannula systems, Sunbul et al. (2015) evaluated HFNC, Bubble CPAP, and SiPAP systems on a 26-week-old model (approximately 6 months) with different nebulizer positions, and found optimized lung doses (as a percent of nominal dose) of 0.79% to 1.30%. Reminiac et al. (2017) studied nasal high flow nebulization both *in vitro* and *in vivo* using the SAINT infant airway model (Janssens et al., 2001) and a non-human primate (macaque) for jet and vibrating mesh nebulizers, which were also placed in different locations within the system and with varying flow rates. They reported low aerosol MMADs at the cannula outlet, similar to the present study, from 1.05 µm to 1.43 µm. However, they also reported low lung doses ranging from 0.03% to 0.85% *in vivo* and 0.46% to 4.15% *in vitro*, due to high system loses in the humidifier, tubing, and cannula.

The aerosol size considered in the current study is similar to that recommended by Longest et al. (2014), who demonstrated 45% to 60% lung deposition in an infant model of invasive mechanical ventilation. A recent correlation from Tavernini et al. (2018), which built upon work from Storey-Bishoff et al. (2008), estimates that for the

158

monodisperse case presented in the current study, approximately 1.23% of particles that enter the nostril will deposit in the cavity and nasopharynx. Furthermore, Clark et al. (2018) demonstrated the need for using smaller aerosol sizes to maximize lung aerosol delivery to pre-term infants. However, it is noted that only EEG aerosol delivery offers a method to retain small particles or droplets, once they are inhaled and enter the lung airspace.

A primary limitation of the current study is the use of steady state inlet and outlet boundary conditions in both the experimental and numerical models. Infants have very short inhalation times. Therefore, efficient aerosol delivery will require synchronizing aerosol generation from the nebulizer with a portion of the inhalation period. The effective synchronization of the aerosol delivered to an infant was recently demonstrated by Dhapare et al. (2018). An additional limitation is the absence of a hygroscopic excipient in the test aerosol. As mentioned previously, the aerosol delivered to the experimental model had similar particle aerodynamic diameter to EEG aerosols, but used 0.5% w/v albuterol sulfate instead of an EEG formulation. Previous studies have shown that particle size increase has an influence on upper airway deposition (Schroeter et al., 2001; Walenga et al., 2014).

This study has expanded recommendations for the accurate simulation of particle deposition during N2L aerosol delivery. Using these recommendations, close agreement between the CFD predictions and *in vitro* experimental results of regional drug deposition was attained. This study has also further demonstrated how a concurrent CFD and *in vitro* approach (Hindle & Longest, 2013; Longest & Hindle, 2009c) can lead to valuable insights regarding drug delivery strategies. Finally, the validated CFD model now provides a useful

tool to further understand and improve the N2L approach for administering

pharmaceutical aerosols to infants.

4.6 Figures
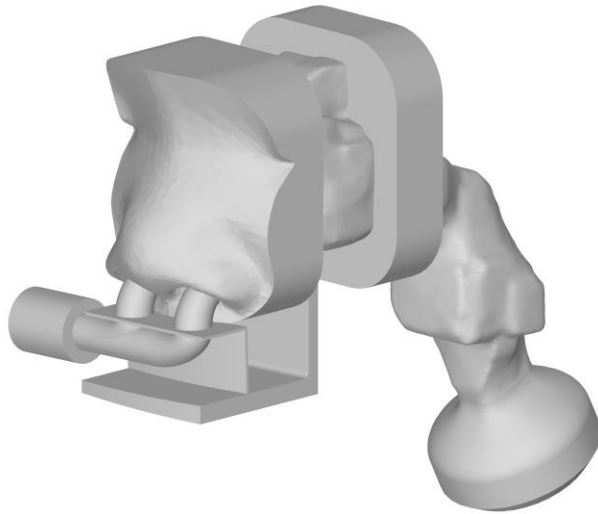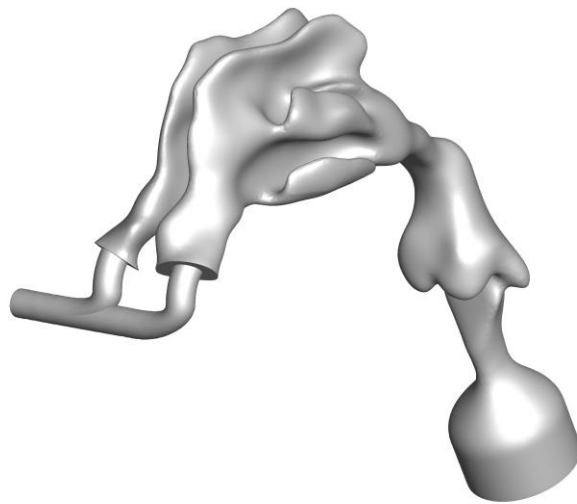
Figure 4.1:　Overview of geometry showing (a) experimental CAD model and (b) air interface of the CFD model. Images show the streamlined nasal cannula, three sections of the experimental model, complex surfaces of the nasal cavity, and outlet filter connection.
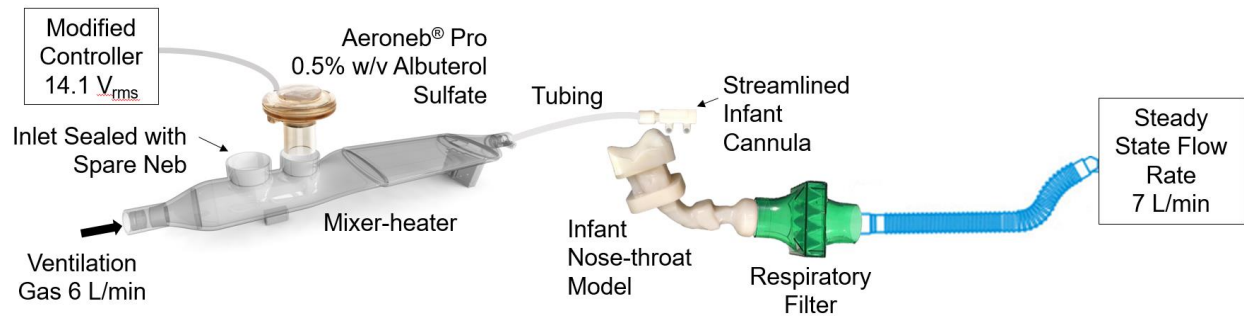
Figure 4.2: Experimental set-up schematic showing the mixer-heater aerosol generation device, patient interface, and nose-to-lung model.
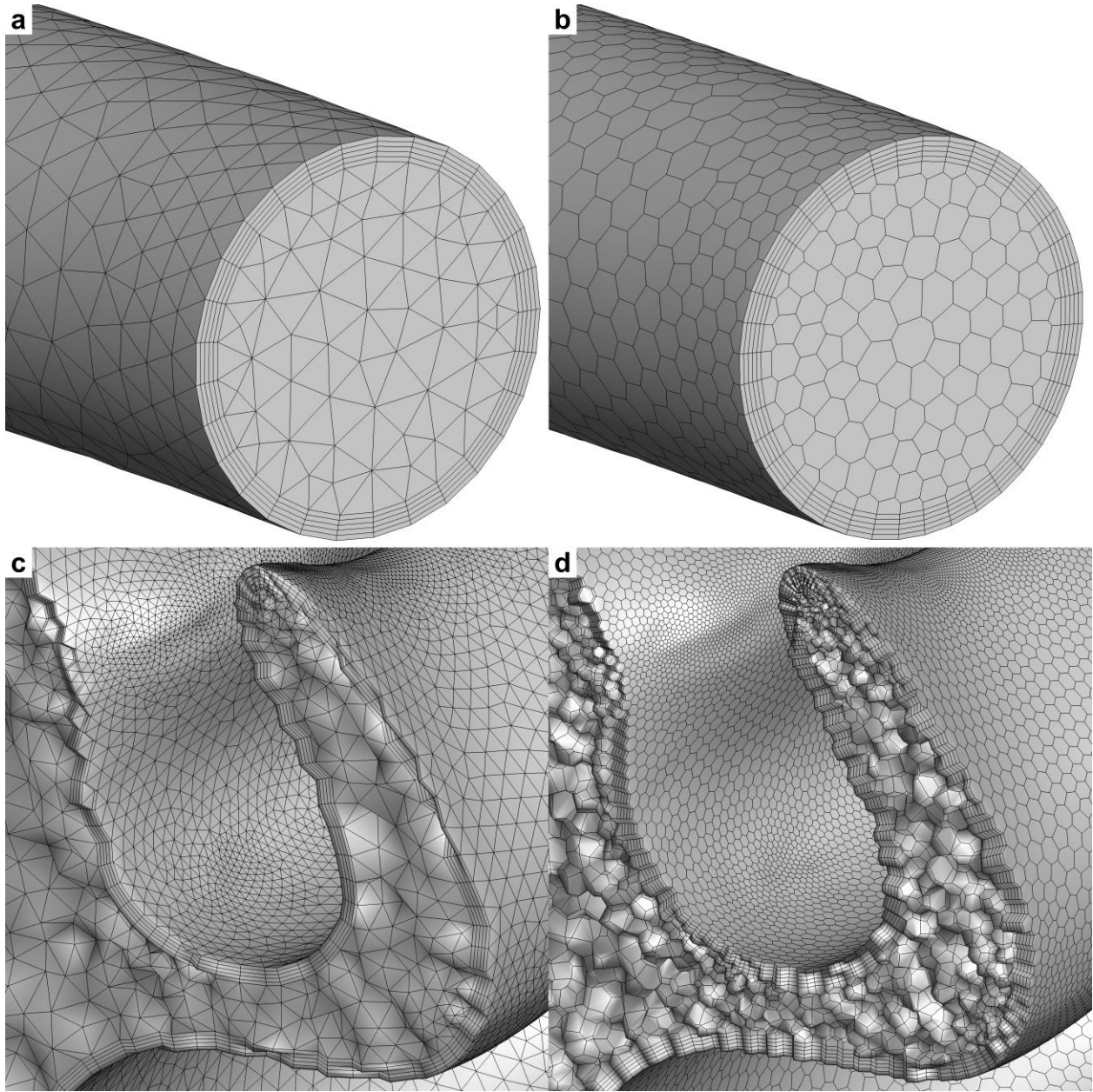
Figure 4.3: Examples of polyhedral and tetrahedral volume meshes of the domain showing the (a) 5.7 million cell tetrahedral mesh, (b) 3.6 million cell polyhedral mesh at the inlet boundary, (c) 5.7 million cell tetrahedral mesh, and (d) 3.6 million cell polyhedral mesh in the middle meatus.
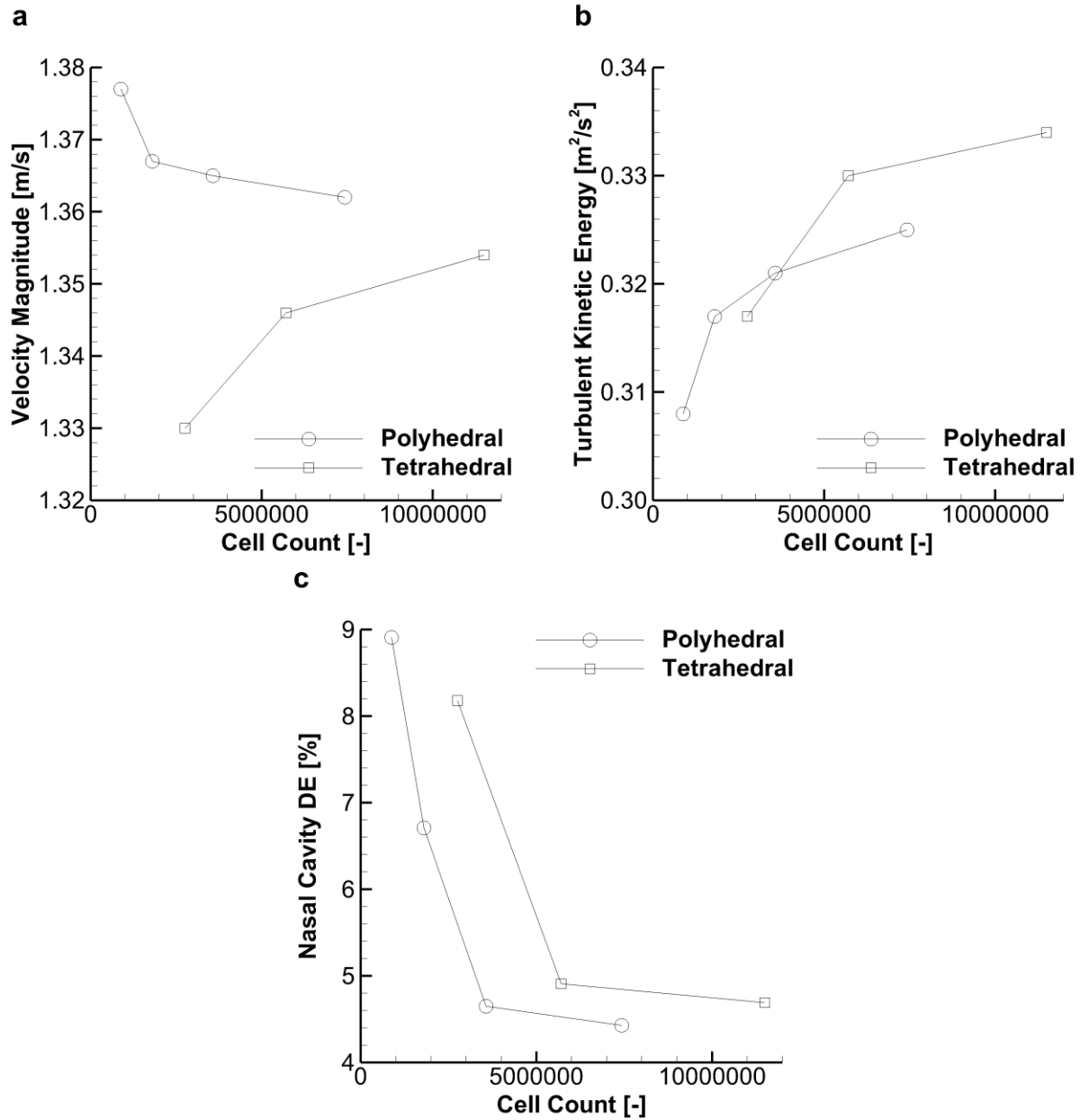
Figure 4.4:   Summary of mesh convergence for both polyhedral and tetrahedral mesh types for key flow and turbulence field quantities and particle deposition characteristics; specifically (a) velocity magnitude, (b) turbulent kinetic energy, and (c) deposition efficiency on nasal cavity wall surfaces.
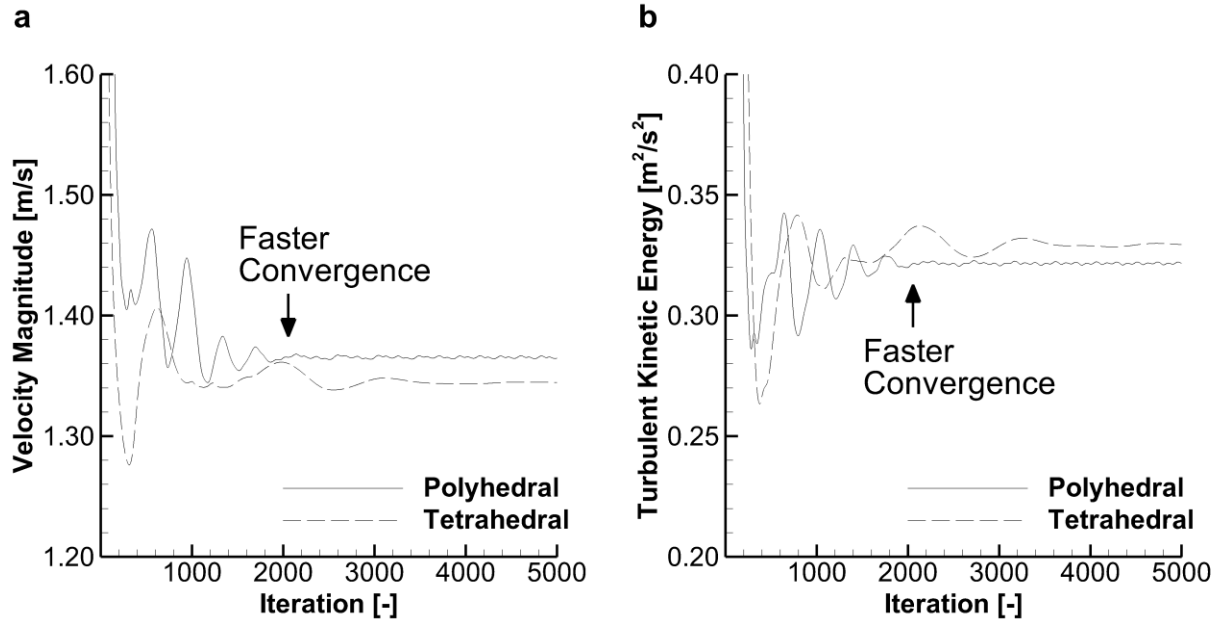
Figure 4.5:   Progression of volume-averaged (a) velocity magnitude and (b) turbulent

kinetic energy during solver iterations, which shows faster convergence for the 3.6 million

cell polyhedral mesh compared to the 5.7 million cell tetrahedral mesh.
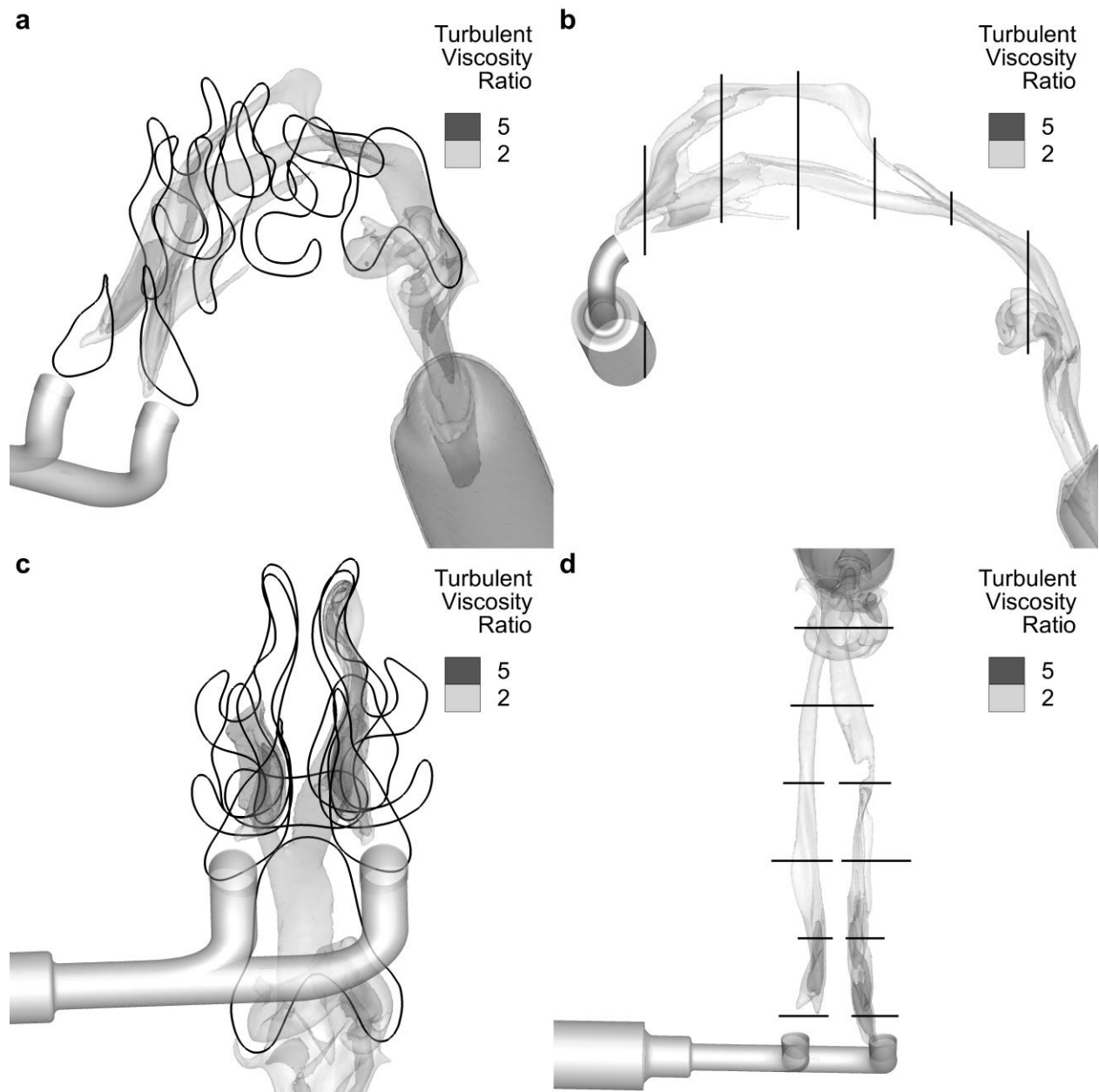
Figure 4.6: Iso-surface plots showing turbulent viscosity ratio values of 2 and 5 in (a) isometric, (b) side, (c) front, and (d) top views, which demonstrates large regions of the domain experience noticeable turbulence, especially at the interface from the cannula prongs to nasal cavity and around the glottis. Slices aim to show the model geometry without obscuring the iso-surfaces.
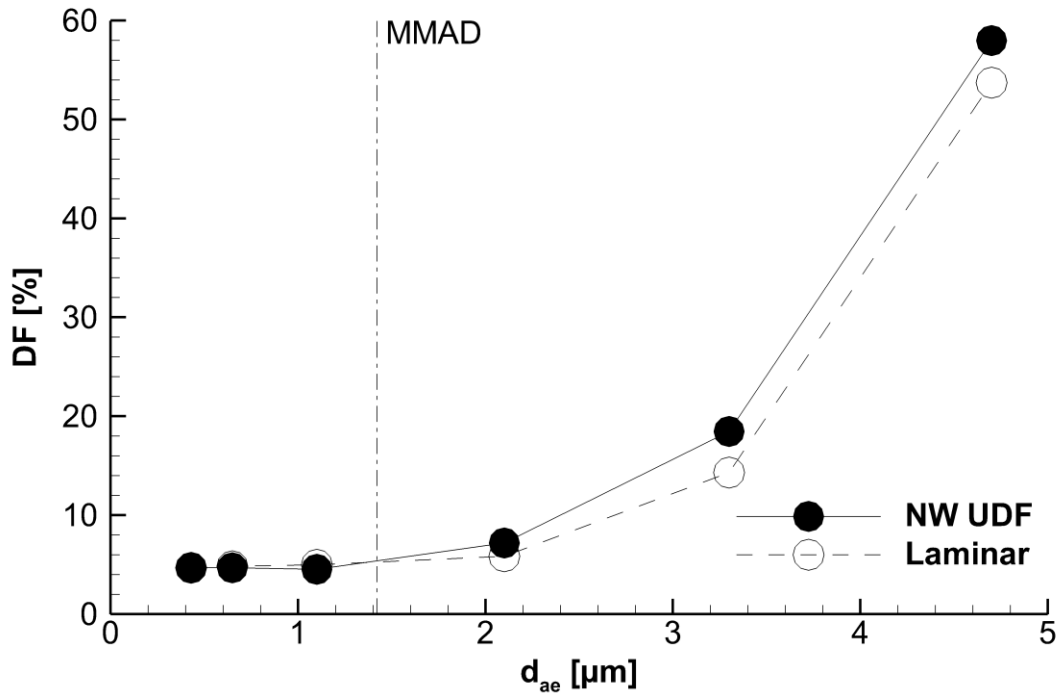
Figure 4.7: Comparison of deposition profiles for laminar and turbulent with near-wall correction cases. Deposition fractions are similar between the two cases for small (<2µm) particles, but as the particle aerodynamic diameter increases (ρ_p = 1000 kg/m³) the laminar flow field predicts less deposition.

a

Middle:
$DF_{exp} = 1.51\%$
$DF_{mono} = 1.53\%$

Nasopharynx:
$DF_{exp} = 2.18\%$
$DF_{mono} = 1.83\%$

Anterior:
$DF_{exp} = 1.11\%$
$DF_{mono} = 1.21\%$

Interface:
$DF_{exp} = 2.24\%$
$DF_{mono} = 1.06\%$

Filter:
$DF_{exp} = 92.96\%$
$DF_{mono} = 94.37\%$

b

Middle:
$DF_{exp} = 1.51\%$
$DF_{poly} = 1.50\%$

Nasopharynx:
$DF_{exp} = 2.18\%$
$DF_{poly} = 1.79\%$

d_{ae} [μm]
4.70
3.30
2.10
1.10
0.65
0.43

Anterior:
$DF_{exp} = 1.11\%$
$DF_{poly} = 1.79\%$

Interface:
$DF_{exp} = 2.24\%$
$DF_{poly} = 2.28\%$

Filter:
$DF_{exp} = 92.96\%$
$DF_{poly} = 92.64\%$
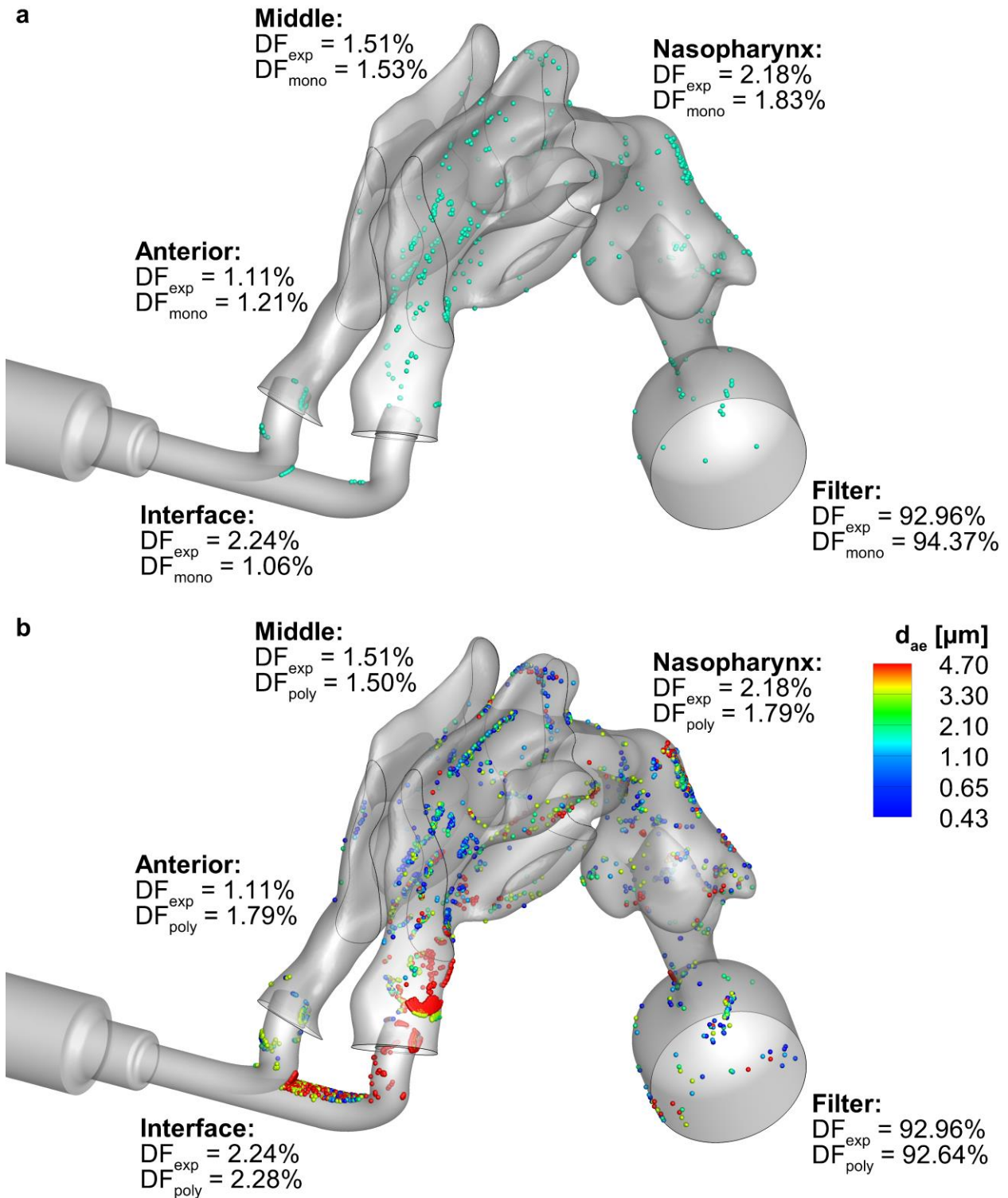
Figure 4.8:   3D particle deposition sites, with comparisons to experimental (exp) data, for laminar flow with (a) monodisperse aerosol and (b) polydisperse aerosol.
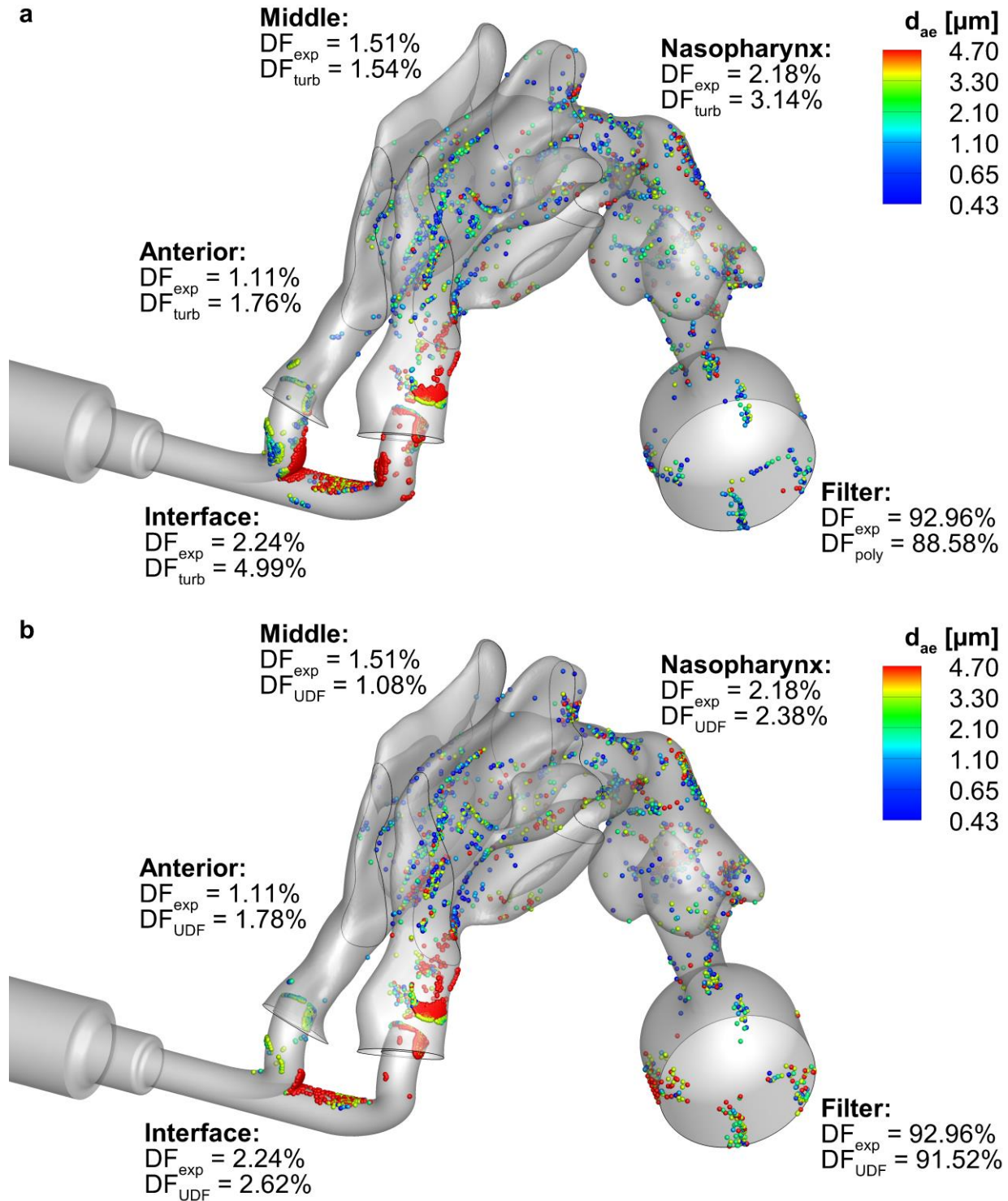
Figure 4.9: 3D particle deposition sites, with comparisons to experimental data, for the polydisperse aerosol with (a) the standard turbulent dispersion model and (b) turbulent dispersion with NW corrections.

4.7   Tables

Table 4.1:   Summary of recommended mesh and solver parameters.

	Model/Parameter	Setting/Method
Mesh	Target Wall y^+	0.5-1
	Number of NW Layers	5
	L2L Ratio	1.0 (may be increased with no negative effects)
Flow	Turbulence	LRN k-ω
	P-V Coupling	SIMPLEC
	Mom. & Turb. Schemes	Second-order Upwind
	Gradient Discretization	Green-Gauss Node-based
	Numerical Accuracy	Double Precision
Particles	Tracking Scheme	Lagrangian with Runge-Kutta
	Turbulent Dispersion	Interpolate TKE at particle location from nodes
	Eddy Interaction Model	Modified via UDF
	NW Correction	NW Limit = 1.0-2.0 μm

Table 4.2:   Summary of deposition fractions for the monodisperse (Mono.) and polydisperse (Poly.) laminar cases.

Region	Exp. Mean DF (SD)	Mono. DF	Diff.	Poly. DF	Diff.
Patient Interface	2.23% (0.16%)	1.06%	1.17%	2.28%	0.05%
Anterior Nose	1.11% (0.15%)	1.21%	0.10%	1.79%	0.68%
Middle Passage	1.51% (0.26%)	1.53%	0.02%	1.50%	0.02%
Nasopharynx	2.18% (0.87%)	1.83%	0.35%	1.79%	0.39%
Filter	92.96% (2.93%)	94.37%	1.41%	92.64%	0.32%
Average			0.61%		0.29%

Diff. is defined as the absolute value of absolute difference between the CFD and Experimental (Exp.) data.

Table 4.3: Summary of deposition fractions for the monodisperse (Mono.) and polydisperse (Poly.) turbulent cases with dispersion deactivated.

Region	Exp. Mean DF (SD)	Mono. DF	Mono. Diff.	Poly. DF	Poly. Diff.
Patient Interface	2.23% (0.16%)	1.62%	0.61%	3.44%	1.21%
Anterior Nose	1.11% (0.15%)	1.71%	0.60%	2.43%	1.32%
Middle Passage	1.51% (0.26%)	1.43%	0.08%	1.60%	0.08%
Nasopharynx	2.18% (0.87%)	3.07%	0.89%	2.73%	0.55%
Filter	92.96% (2.93%)	92.17%	0.80%	89.81%	3.16%
Average			0.60%		1.26%

Diff. is defined as the absolute value of absolute difference between the CFD and Experimental (Exp.) data.

Table 4.4: Summary of deposition fractions for the monodisperse (Mono.) and polydisperse (Poly.) turbulent cases with dispersion activated.

Region	Exp. Mean DF (SD)	Mono. DF	Diff.	Poly. DF	Diff.
Patient Interface	2.23% (0.16%)	2.73%	0.50%	4.99%	2.76%
Anterior Nose	1.11% (0.15%)	1.27%	0.16%	1.76%	0.65%
Middle Passage	1.51% (0.26%)	1.42%	0.10%	1.54%	0.02%
Nasopharynx	2.18% (0.87%)	3.00%	0.82%	3.14%	0.96%
Filter	92.96% (2.93%)	91.58%	1.39%	88.58%	4.39%
Average			0.59%		1.75%

Diff. is defined as the absolute value of absolute difference between the CFD and Experimental (Exp.) data.

Table 4.5: Summary of deposition fractions for the monodisperse (Mono.) and polydisperse (Poly.) turbulent cases with near-wall correction UDFs.

Region	Exp. Mean DF (SD)	Mono. DF	Diff.	Poly. DF	Diff.
Patient Interface	2.23% (0.16%)	1.42%	0.82%	2.62%	0.39%
Anterior Nose	1.11% (0.15%)	0.99%	0.13%	1.78%	0.67%
Middle Passage	1.51% (0.26%)	1.15%	0.37%	1.08%	0.44%
Nasopharynx	2.18% (0.87%)	2.42%	0.25%	2.38%	0.20%
Filter	92.96% (2.93%)	94.03%	1.06%	91.52%	1.45%
Average			0.52%		0.63%

Diff. is defined as the absolute value of absolute difference between the CFD and Experimental (Exp.) data.

Chapter 5: CFD-based Optimization of an Inline DPI for EEG Tobramycin Formulations

5.1 Objective

The objective of this study was to implement CFD simulations to develop quantitative correlations that predict the aerosolization behavior of an inline air-jet DPI for children and then use these correlations to optimize aerosolization performance. In order to develop the flow-field based correlations for aerosolization performance, CFD simulations of four initial devices were conducted and compared with the previous experimentally determined aerosolization metrics reported by Farkas et al. (2019). Based on these findings, a second iteration of designs was developed and tested both experimentally and with the evolving CFD model. The complete set of ten devices was then used to identify the best CFD-based dispersion parameters for predicting MMAD and ED in the pediatric air-jet DPIs. These dispersion parameters were then used to develop a CFD optimized design for improved performance with increased ED and reduced MMAD compared with previous studies. As a final step, the best-case designs were produced and tested experimentally to validate the CFD predictions and optimization method.

5.2 Introduction

In the field of respiratory drug delivery, computational fluid dynamics (CFD) is proving to be an increasingly useful tool for the development and optimization of dry powder inhalers (DPIs). For example, in a series of papers, Coates et al. used CFD to investigate the effects of mouthpiece length and grid design (2004), capsule size (2005), flow rate (2005), air inlet size (2006), and mouthpiece geometry (2007) on DPI

performance in terms of capsule, device, and extrathoracic losses. More recently Shur et al. (2012) modified the air inlets of a Cyclohaler, guided by CFD analysis, to match the aerosolization performance of the HandiHaler.

Our group has developed a series of high efficiency air-jet DPIs that are operated with 10 ml of air (via a syringe) (Farkas, Hindle, & Longest, 2018b; Longest & Farkas, 2018; Longest, Farkas, Bass, & Hindle, 2019). These air-jet DPIs use small-gauge hollow capillaries that pierce a powder-containing capsule as part of loading the device, and serve as the air inlet and aerosol outlet. The inlet capillary supplies a high-velocity, compressible, turbulent jet that initially fluidizes the powder bed. It is expected that significant turbulence and high shear forces further break up the initially formed aggregates, which reduces the particle size while in the capsule chamber (Longest & Farkas, 2018; Longest et al., 2019). Once the size of an aerosolized aggregate is sufficiently reduced, it is able to escape the powder chamber through the outlet capillary and enter the patient interface.

A detailed approach to modeling DPI aerosolization and transport in CFD could utilize Lagrangian particle tracking (Longest & Farkas, 2018; Longest et al., 2019) or discrete element modeling (DEM) (X. Chen, Zhong, Zhou, Jin, & Sun, 2012; Tong, Zhong, Yu, Chan, & Yang, 2016; Yang, Wu, & Adams, 2014) as a representation of the powder. However, CFD with DEM becomes computationally expensive when a complete device and powder dose need to be simulated in order to make design improvement predictions. For example, current DEM simulations that attempt to capture powder structural properties with particle-particle and particle-wall interactions are currently limited to one or two particle agglomerates (Ariane, Sommerfeld, & Alexiadis, 2018; Wong, Fletcher,

Traini, Chan, & Young, 2012). In contrast, an effective approach for predicting the aerosolization behavior of a DPI is to develop predictive correlations that relate dispersion parameters, which use CFD-predicted flow and turbulence quantities, to aerosolization performance metrics (Coates, Chan, et al., 2005; Longest & Farkas, 2018; Longest et al., 2019; Shur et al., 2012).

Specific to the air-jet DPI development in the current study, Longest and Farkas (2018) developed quantitative flow-field-based and tracer-particle-based correlations that related device aerosolization to flow and turbulence dispersion parameters for a very low volume of actuation air (i.e. 10 mL). The tracer-particle method used a relatively small number of Lagrangian particles, compared to modelling the entire powder bed, to sample turbulence and flow quantities throughout the domain. To quantify device performance, the aerosolization metrics of mass-median aerodynamic diameter (MMAD) and emitted dose (ED) (also often referred to as emitted fraction) were used. Their study showed that MMAD had a strong direct correlation ($R^2 > 0.8$) with two flow-field-based dispersion parameters, which were a non-dimensional form of turbulent kinetic energy (k), denoted by k^*_{field}, and the product of non-dimensional k and non-dimensional specific dissipation rate (ω), denoted by $k^*_{field} \times \omega^*_{field}$. The ED also showed a strong correlation with k^*_{field} and $k^*_{field} \times \omega^*_{field}$, as well as $k^*_{field}/\omega^*_{field}$ and wall shear stress (WSS). The predictive capabilities of these correlations were evaluated by Longest et al. (2019) by comparing the predicted MMAD and ED from CFD models to experimental results *a priori*, with results showing a low root-mean-square (RMS) error (again, for a 10 mL actuation air volume). The findings from these two studies demonstrated that dispersion parameters can be correlated to be predictive of MMAD and ED performance for air-jet DPIs. They

also suggested that the powder goes through a two-stage aerosolization process, where the first stage involves the initial dispersion from the stationary powder bed to the flow field, followed by secondary breakup in the high-velocity, highly-turbulent air jet.

The present study builds upon the previous development of a high-efficiency inline air-jet DPI, and applies this platform to the delivery of tobramycin to children with cystic fibrosis (CF). A primary symptom of CF is dehydration of the airway surface liquid in the lungs, due to poor ion transport through epithelial cells (Matsui et al., 1998; Tarran et al., 2001), which produces thickened mucus and poor mucociliary clearance (Stoltz et al., 2015). Poor lung clearance and abnormal ion concentrations lead to frequent bacterial infections, the most predominant of which is *Pseudomonas aeruginosa* (*Pa*) (Elborn, 2016), which can be treated by inhaled antibiotics. tobramycin was the first commercial inhaled antibiotic (A. L. Smith, 2002), and is available as either a solution or powder for nebulizers or DPIs, respectively. The efficacy of treating *Pa* infections with tobramycin was demonstrated in a clinical trial by Ramsey et al. (1999) who reported an average 12% increase in FEV_1 (forced expiratory volume over 1 second), 26% decrease in pulmonary exacerbations, less hospitalization, and a 1.1 $\log_{10}$ CFU/g reduction in *Pa* infection.

Our group is developing a pediatric DPI for the administration of spray-dried excipient enhanced growth (EEG) powder formulation to children with CF as young as 2 years old. As described by Farkas et al. (2019), the delivery system is intended to provide the aerosol and a full inhalation through either a sealed nasal cannula or mouthpiece interface. By delivering a full inhalation from a positive pressure gas source, the device has multiple advantages compared with typical passive DPIs including consistent

178

actuation, the flexibility of oral or nasal lung delivery, potential expansion of the upper airways, and resistance to exhalation through the device. The study of Farkas et al. (2019) previously established that improved aerosolization was achieved when all of the available gas flow was passed through the powder chamber. To achieve the much higher flow rates (~15 LPM) compared with the previous studies of Longest and Farkas (2018) and Longest et al. (2019) (~3 LPM), capillary diameters were increased, which alters the turbulence and shear stress profiles within the device. As a result, aerosolization characteristics and dispersion parameters are expected to be considerably different for the current pediatric devices compared with the previous devices that were operated with 10 mL of actuation air.

The proposed pediatric device for tobramycin uses an inline, positive-pressure actuation and air-jet aerosolization. Specifically, a standard ventilation bag is connected to the inlet, which provides the actuation air volume (~750 mL) and a pressure drop (~6 kPa) across the device. The inlet capillary then supplies a high-velocity, highly-turbulent air jet to the capsule chamber to aerosolize the powder. Initial devices are developed for patients in the age ranges of 2-3, 5-6, and 9-10 years old, and aim to provide the inhalation volume for one breath as part of the actuation process. The present study focuses on the 5-6-year-old group, with a target inhalation volume of 750 mL and total device air flow rate of 15 LPM.

Experimental aerosolization performance from four prototyped versions of the proposed pediatric air-jet DPI are presented by Farkas et al. (2019) which forms the basis of correlation development for the current study. The minimum device aerosolization performance goals of the experimental study were an ED > 85% (of loaded dose), MMAD

< 1.75 μm, fine particle fraction of ED < 5 μm ($FPF_{<5μm/ED}$) > 90%, and $FPF_{<1μm/ED}$ > 20%, all of which were achieved by the Case 4 device ($FPF_{<1μm/ED}$ was 19.5%). Considering aerosol administration through *in vitro* airway models of a five-year-old child, the Case 4 device delivered 60.7% to the tracheal filter, with 8.3% nose-throat losses, when coupled to the best-case nasal cannula design; and 63.8% to the tracheal filter, with 6.6% mouth-throat losses, when coupled with the best-case mouthpiece design. This is a marked improvement over the typical DPI performance for aerosol administration to children that is reported in the literature. Specifically, for oral aerosol delivery to a 4-5 year-old *in vitro* model, Below et al. (2013) reported 5% and 22% of nominal dose deposited on the tracheal filter with the Novolizer and Easyhaler; and Lindert et al. (2014) reported 9% to 11% lung delivery efficiency with the Cyclohaler, HandiHaler, and Spinhaler. For trans-nasal aerosol delivery to children in the age ranges considered, little data is available in the literature. The closest available study is Laube et al. (2012) who reported <4% of loaded dose delivered to the tracheal filter in the 9-month-old *in vitro* SAINT model (Janssens et al., 2001).

5.3   Methods

The current study builds upon the initial experimental work with pediatric air-jet DPIs presented by Farkas et al. (2019), and the devices and results from that study are referred to as Experimental Iteration 1. In the current study, CFD models are developed for the devices in Experimental Iteration 1 and initial CFD dispersion parameters are calculated based on our previous work with low (~10 mL) actuation volumes (Longest & Farkas, 2018; Longest et al., 2019). A second round of pediatric air-jet devices is then prototyped and tested experimentally, which is referred to as Experimental Iteration 2.

New dispersion parameters, which are appropriate for the higher flow volumes of the pediatric air-jet DPIs (~750 mL), are then developed for both device sets (Experimental Iteration 1 and 2) and compared with the experimental data to determine their ability to predict ED and MMAD. Device optimization then begins by evaluating numerous design configurations with CFD and using the refined dispersion parameters to estimate performance. The entire experimental, CFD, and optimization approach is described in detail in the following sections.

Optimization Process

To meet the objective, the device optimization process is outlined by the block diagram in Figure 5.1. This process utilizes concurrent experimental and CFD models to provide physical insight into aerosolization performance, and iterations through the process aim to refine the dispersion parameters and optimize the device performance. The overarching aims of the process are to (i) provide an *a priori* validation of CFD-based dispersion parameter predictions of aerosolization performance and (ii) determine the best performing device parameters within the design space.

The *Initial Device Development* stage (Figure 5.1) is largely covered by the work presented in our previous publications on pediatric air-jet DPI development (Farkas et al., 2019; Longest & Farkas, 2018; Longest et al., 2019). Here the initial air-jet DPI concept was developed with a combination of analytical, experimental, and numerical methods. Fabrication of prototype air-jet DPIs uses computer aided design (CAD) models and 3D printing for the plastic components, with small gauge stainless steel hollow tubes used for the inlet and outlet capillaries. Once prototype devices are built, the *Aerosolization Experiments* stage tests the aerosolization performance (MMAD and ED) of the DPI. The

experimental setup uses a next-generation impactor (NGI) and high-performance liquid chromatography (HPLC) to determine the particle size distribution and capsule retention, both of which are used to establish performance metrics. In parallel to the *Aerosolization Experiments* stage, the *CFD Evaluation* stage uses numerical models to provide insight into the flow and turbulence conditions within the devices. It is expected that numerous CFD simulations will be conducted during the optimization process (over 100 design configurations), so the geometry, meshing, model set-up, and post-processing steps are automated as much as possible. In the *Correlation Development* stage, the flow and turbulence quantities from the CFD simulations are used to identify and develop dispersion parameters that are predictive of the aerosolization performance metrics.

After predictive correlations are developed, the process loops back through the *Aerosolization Experiments* and *CFD Evaluation* stages to test the correlations for accuracy and develop insights into newly defined dispersion parameters (see Iteration 2 in Figure 5.1). Following correlation development and testing, it is important to evaluate how changes to the device design influence the dispersion parameters and associated aerosolization performance predictions. The flow and turbulence quantities from CFD models of numerous design configurations are evaluated to determine trends between design factors and device flow characteristics. These quantities are then used in the dispersion parameters and correlations to provide predictions of aerosolization performance. Finally, the predictions of aerosolization performance from the previous stage are used to identify optimized device designs. The optimized device should both provide good aerosolization performance and be an improvement over the devices from Experimental Iteration 1. *A priori* validation of the CFD predictions was conducted by

182

producing and experimentally testing the optimized devices to determine whether the aerosolization performance predictions are accurate, without adjusting the models or correlations after the simulations are conducted.

Experimental Materials and Powder Formulation

Albuterol sulfate (AS) USP was purchased from Spectrum Chemicals (Gardena, CA) and Pearlitol® PF-Mannitol was donated from Roquette Pharma (Lestrem, France). Poloxamer 188 (Leutrol F68) was donated from BASF Corporation (Florham Park, NJ). L-leucine and all other reagents were purchased from Sigma Chemical Co. (St. Louis, MO). Quali-V, Hydroxypropyl methylcellulose (HPMC) capsules (size 0) were donated from Qualicaps (Whitsett, NC).

Multiple batches of a spray-dried AS EEG powder formulation were produced based on the optimized method described by Son et al. (Son, Longest, & Hindle, 2013; Son, Longest, Tian, et al., 2013) using a Büchi Nano spray dryer B-90 (Büchi Laboratory-Techniques, Flawil, Switzerland). The EEG powder formulation contained a 30:48:20:2% w/w ratio of AS, mannitol, L-leucine, and Poloxamer 188.

Device Design and Experimental Methods

The devices that were tested in Experimental Iterations 1 and 2, along with their inlet and outlet diameter configurations and operating conditions are summarized in Table 5.1. The naming convention for cases in Experimental Iteration 2 gives the inlet capillary diameter followed by the outlet capillary diameter, as that is the primary design factor that was evaluated. For example, a case called 1.83/2.90 uses a 1.83 mm inlet diameter and a 2.90 mm outlet diameter, and all other design factors and operating conditions are the same as Cases 3 and 4 in Experimental Iteration 1. This includes an operating inlet

pressure of 6 kPa, which is easily generated with one hand operation of a pediatric size ventilation bag (Farkas et al., 2019). The Half Q case is the exception to this naming convention as it is the same device as Case 4, but implements a pressure drop of 1.5 kPa to reduce the flow rate through the device by a factor of two. The 1.32/2.39 case used the same outlet capillary diameter and pressure drop as Case 4, but included a 1.32 mm inlet capillary to increase flow resistance and give a similar flow rate to the Half Q case. Likewise, the 1.60/2.39 case used a 1.60 mm inlet capillary to give a flow rate that was approximately 75% of Case 4. The 2.08/2.69 case has a similar outlet to inlet diameter ratio (d_o/d_i) as Case 4 (i.e. ~1.30). The 1.32/2.90 case has the same average capillary diameter ($0.5 \times (d_i + d_o)$) as Case 4 (i.e. 2.11 mm) and tests an example where the outlet diameter is much larger than the inlet. Finally, the 3.00/2.08 case tests the influence of having a larger inlet compared to the outlet diameter, and maximizes the flow rate (and hence available flow energy) through the device.

Details on the device design and experimental methods for Experimental Iteration 1 are discussed in depth by Farkas et al. (2019). The additional experimental work carried out for Experimental Iteration 2 in the present study followed the same device design, operation, and methods as Experimental Iteration 1. In brief, a size 0 HPMC capsule was loaded with 10 mg of AS EEG powder formulation, and the device used hollow capillaries to pierce the capsule when the device was closed with a single twisting action. Actuation of the device passes a high velocity air jet through the inlet capillary, which aerosolizes the power, and the particles leave the capsule via the outlet capillary leading to the patient interface. In the present study, the only design factors that were manipulated were the inlet and outlet capillary diameters. Design factors that were kept constant included the

184

insertion length of the capillary in the capsule, capsule size, piecing angle, piercing location (along the long axis of the capsule), and a horizontal orientation of the device. Preliminary experimental work considered angling the inlet capillary relative to the outlet capillary, similar to Case 7 in the Longest et al. study (2019), in an effort to increase secondary flow, but there was little improvement in aerosolization performance. Similarly, preliminary work extended the outlet capillary length in an effort to expose the aerosol to high shear flow for a longer duration, but again there was no improvement in MMAD or ED compared with Experimental Iteration 1. Figure 5.2a shows a rendering of the Case 4 device in transparent plastic, with the capsule and capillaries clearly visible. Figure 5.2b shows the internal flow path, which represents the computational domain for CFD models, and the height to which the 10 mg powder bed fills the capsule.

All devices were actuated with a 6 kPa pressure drop via a compressed air line and solenoid valve. Previous results indicated very similar device performance with either a hand-operated ventilation bag or compressed air and solenoid valve setup (Farkas et al., 2019). Inlet flow rate thorough each device was recorded before loading a capsule, and the time of actuation (controlled by the solenoid valve) was adjusted to ensure that 750 ml passed through the device, which is consistent with a deep inhalation volume for a 5-6 year old child (75% of total lung capacity) (ICRP, 1994). The aerosol characterization was performed using an NGI and AS drug mass was quantified using HPLC, with the device actuated into the NGI using a custom adaptor. After actuation, HPLC was used to determine recovered drug masses in the capsule and device, and the amount of powder that deposited on each stage of the NGI. As minimal size change is expected in the aerosol under ambient temperature and relative humidity (RH) conditions,

185

experiments were conducted with ambient air (T = 22°C ± 3°C and RH= 50% ± 5%) with the NGI at room temperature. AS quantification was performed with a validated HPLC method using a Waters 2695 separations module with a 2475 fluorescence detector (Waters Co., Milford, MA). Chromatography was performed using a Restek Allure PFP 150 mm × 2.1 mm column (Bellefonte, PA). The mobile phase, consisting of methanol and ammonium formate buffer (20 mM, pH 3.4) in a ratio of 70:30, respectively, was eluted at a flow rate of 0.4 mL/min and the detector was set to an excitation wavelength of 276 nm and emission at 609 nm. The column temperature was maintained at 25 °C, and the volume of each sample injected was 100 µL. The limit of quantification was 0.5 µg/ml (Behara, Longest, et al., 2014b; Son, Longest, & Hindle, 2013). The recovered dose from HPLC analysis for all experimental data presented in this study was greater than 90%.

The ED was defined as the difference between the loaded AS dose and the mass of AS retained in the capsule and device after one actuation, divided by the loaded dose, and expressed as a percentage. The MMAD was identified with linear interpolation of a cumulative percentage drug mass vs. cut-off diameter plot from the NGI. The cut-off diameters of each NGI stage were calculated using the formula specified in USP 35 (Chapter 601, Apparatus 5) for the operating flow rate of 45 LPM. The exception in the present study is that the higher flow rate of some devices required the NGI to be operated at a flow rate of 60 LPM. To account for this when determining the MMAD for these devices, the cut-off diameters were recalculated using the formula from USP 35 for a flow rate of 60 LPM.

CFD Models

The computational domains and meshes were generated according to our previously established best practices (Bass & Longest, 2018b; Longest & Holbrook, 2012; Longest & Vinchurkar, 2007a). Meshes were composed of very high quality hexahedral cells, with orthogonality greater than 0.25, and followed a similar construction style as our previous air-jet DPI studies (Longest & Farkas, 2018; Longest et al., 2019). To reduce the time required for CFD model development, geometry and mesh generation were automated as much as possible using an input file with design parameters and automation scripts, as it was expected that numerous design configurations would be explored during the optimization process. This automation reduced the time to create each mesh from approximately an hour of repetitive manual work to less than two minutes, and minimized the possibility of human error. To confirm mesh independent results, CFD quantities specific to flow, turbulence, and compressibility were evaluated for a coarse (230,208 cells), medium (496,128 cells), fine (976,000 cells), and extra fine (2,044,588 cells) mesh that represented the Case 4 device configuration, with mesh independence established between the fine and extra fine mesh. Between these two meshes, the volume-averaged velocity magnitude had an absolute difference of -0.05 m/s (-0.30% relative difference), the volume-averaged turbulence kinetic energy had an absolute difference of -0.02 m^2/s^2 (-0.19% relative difference), and the inlet and outlet volumetric flow rates had an absolute difference of -0.102 LPM and -0.103 LPM respectively (-0.54% and -0.53% respectively). This mesh resolution is also consistent with the cell counts used in our previous air-jet DPI CFD work (Longest & Farkas, 2018; Longest et al., 2019).

For Experimental Iteration 1, cases have inlet boundary Mach and Reynolds numbers ranging from 0.18-0.27 and 6,300-13,200 respectively. These cases are below the recommended Mach number threshold of 0.3 for compressible flow, but the ideal gas law for density modelling was implemented to be consistent with previous DPI studies (Longest & Farkas, 2018; Longest et al., 2019) and to ensure CFD models are capable of handling higher inlet velocity if the flow rate is increased during optimization. Based on inlet Reynolds numbers, some cases exhibit highly turbulent behavior, and at the very least flow is beyond the transitional regime. As such, the low-Reynolds number (LRN) k-ω turbulence model was implemented, which has been extensively validated for drug delivery applications by our group (Bass & Longest, 2018b; Longest, Son, et al., 2013; Longest & Vinchurkar, 2007b), and was shown give a good compromise between computational accuracy and efficiency. Despite very high inlet Reynolds numbers, the LRN correction was applied to account for the possibility of low turbulence regions within the domain, particularly at locations far from the inlet capillary jet. The form of the LRN corrections makes the model applicable to both high and low turbulence regions, as the eddy viscosity damping coefficient approaches unity in regions of high turbulence and hence has little effect. Based on the presence of a high velocity inlet jet and compressible flow, shear flow corrections and compressibility effects were also implemented (Wilcox, 1998).

Consistent with our previous air-jet DPI CFD studies (Longest & Farkas, 2018; Longest et al., 2019), a steady-state approach for transport equation discretization would not provide a converged solution due to the presence of relatively high frequency (~1000 Hz) flow oscillations. As such, the CFD model used a partially converged steady-state

solution as the initial condition, then switched to a transient approach, with a time step of 1e-4 s that provided good convergence and accurately resolved the flow oscillations. Differences between volume-average flow and turbulence quantities were observed to be negligible after approximately 100 time-steps, suggesting that start-up effects had dissipated. As dispersion metrics are based on volume-average quantities, it is expected that this solution strategy will be capable of providing predictive correlations, as was the case when a similar approach was implemented by Longest and Farkas (2018).

Both flow-based and particle-based dispersion parameters were originally presented by Longest and Farkas (2018), which demonstrated the predictive capabilities of CFD models for DPI aerosolization performance. The former used volume-averaged flow and turbulence quantities as the basis of the dispersion parameters, and the latter used tracer particles to sample flow and turbulence quantities as their trajectories moved from the powder bed and through the domain. As both flow-based and particle-based dispersion parameters performed well in previous studies, the current study will analyze an extended set of flow-based parameters, which reduces overall processing time.

All flow and turbulence transport equations were solved using ANSYS Fluent v19.0, including the necessary sub-models and corrections described previously. CFD models adhered to the recommended guidelines presented by Bass and Longest (2018b), in particular the implementation of the Green-Gauss Node-based method for gradient discretization. Spatial discretization of transport equations, including k and ω, were second-order accurate. Convective terms used a second-order upwind scheme and diffusion terms used central difference. Further details on the mass, momentum, and turbulence transport equations are available in other publications (Longest et al., 2007;

Longest, Vinchurkar, & Martonen, 2006). As with the meshing stage of CFD model development, the setup in ANSYS Fluent that was required for each case was automated as much as possible by utilizing the scripting capabilities of the Fluent text user interface.

In all experimental runs, the DPI was activated by applying a 6 kPa pressure drop across the device. The CFD models implement this pressure gradient with a pressure inlet boundary condition set to 6 kPa and a pressure outlet boundary condition set to 0 kPa, with all pressures given as gauge pressure. The pressure difference between the inlet and outlet boundary drives flow through the computational model, and the device geometry determines flow resistance and hence the volumetric flow rate. As an initial validation check of both the model selection and boundary conditions, the inlet flow rate between CFD models and available experimental flow rate data was compared to ensure the numerical results were similar to the actual devices. On average, the absolute difference between CFD and experimental flow rate differed by approximately 1 LPM, or a relative difference of 6%. Generally, the CFD over-predicted flow rate compared to the experimental results, which can be attributed to the surface roughness of plastic components increasing flow resistance and minor simplifications of the geometry in the CFD model.

Dispersion Parameters

The CFD-predicted dispersion parameters used in the current study and previous work by our group (Longest & Farkas, 2018; Longest et al., 2019) use flow and turbulence quantities to characterize the conditions that drive powder aerosolization within in the pediatric air-jet DPI. Flow quantities are generally ubiquitous and well understood across all scientific fields, such as inlet flow velocity, but turbulence quantities are less common

in fields outside of CFD, such as turbulent kinetic energy (k) and specific dissipation rate

(ω). In turbulence modeling, the flow velocity is typically decomposed into time-averaged

and fluctuating components. The time-averaged component is the mean flow through the

domain and is represented by $\bar{u}$, $\bar{v}$, and $\bar{z}$ in the x-, y-, and z-directions, respectively. The

fluctuating velocity component represents the random and chaotic instabilities that the

turbulent eddies contribute to the flow, and is represented by u', v', and w' in the x-, y-,

and z-directions, respectively. The combination of mean (time-averaged) and fluctuating

velocity components provides the instantaneous flow field velocity, i.e. $u = \bar{u} + u'$.

Turbulent kinetic energy (k) is the specific energy (per unit mass) that turbulence

contributes to the total flow field energy, and is defined as (Wilcox, 1998):

$$k = \frac{1}{2}\left(\overline{u'^2} + \overline{v'^2} + \overline{w'^2}\right)$$

(5.3.1)

with units [m^2/s^2]. A common analogy to describe the mean and fluctuating velocity

components is to consider a probe that samples instantaneous velocity at a single point

in a turbulent flow. The resultant sampling trace would show erratic oscillations in velocity

against time. In this case, the mean velocity ($\bar{u}$, $\bar{v}$, and $\bar{z}$) would be the time-averaged

value of the oscillations, and the fluctuating component is the difference between the

instantaneous and mean velocity across any given time integration (White, 1991).

The second modeling quantity used in the two-equation k-ω model is the specific

dissipation rate (ω), which defines the rate at which turbulent eddies dissipate, and is

defined as:

$$\omega = \frac{k^{1/2}}{C_\mu^{1/4} l}$$

(5.3.2)

with units [1/s], where l is the turbulence length scale and C_μ is an empirical model constant (typically set to 0.09 as default). Physically, the specific dissipation rate represents the rate at which turbulent energy (per unit mass) is converted to internal flow energy. The presence of turbulence in the flow field contributes to the diffusive behavior of the fluid with an effect similar to kinematic viscosity (ν). To model this additional turbulence diffusion, the k and ω quantities are used to define a turbulent kinematic viscosity:

$$\nu_T = \frac{k}{\omega}$$

(5.3.3)

with units of [m^2/s].

In the dispersion parameters, flow and turbulence quantities are calculated as volume-averaged values within the region of the capsule and outlet capillary. With turbulence kinetic energy as an example, the volume-averaged quantities within the discretized computational domain are defined as:

$$k = \frac{1}{V_T} \sum_{i=1}^{n} k_i \times V_i$$

(5.3.4)

where V_T is the volume of the capsule and outlet capillary, k_i is the turbulent kinetic energy in Cell i, V_i is the volume of Cell i, and the summation is across all cells in the capsule and outlet capillary region.

Evaluation of preliminary dispersion parameters began by identifying the correlation strength between experimental aerosolization metrics and the CFD-based parameters presented by Longest and Farkas (2018), which were developed for low-volume devices (10 mL of actuation air) operated at higher pressures. In that study, the MMAD correlated well with k^*_{field} (ratio of volume-averaged k to inlet velocity squared)

giving an R² value of 0.87, and with $k^*_{field} \times \omega^*_{field}$ (where ω^*_{field} is ω non-dimensionalized with a characteristic time scale) giving an R² value of 0.94. However, correlations of these dispersion parameters to MMAD for Experimental Iteration 1 devices in this study were not as strong, with R² values less than 0.6. Other dispersion parameters from the previous paper were also considered for MMAD correlation, but did not achieve an R² value greater than 0.8. For ED, the previous Longest and Farkas study (2018) showed that k^*_{field} and $k^*_{field} \times \omega^*_{field}$ had a strong correlation with R² values of 0.96 and 0.98 respectively, again for different low-volume high pressure devices. Though similar to MMAD in the present study, these dispersion parameters did not show the same correlation strength to ED with Experimental Iteration 1, with R² values again below 0.6. Therefore, new dispersion parameters were required that were developed specifically for this pediatric air-jet DPI and its operating conditions.

In parameter development for the pediatric air-jet DPI, approximately 40 dispersion parameters were correlated with both MMAD and ED. These dispersion parameters used various combinations of variables for flow quantities, turbulence characteristics, design parameters, and operating conditions. The strongest correlations (R² > 0.8) from this new batch of dispersion parameters for Experimental Iteration 1 were identified and the variables used in their development were tested for accuracy and robustness in Experimental Iteration 2. The strength of correlation for the new dispersion parameters developed in the present study are given in the Results section. They are summarized here to discuss the variables from which they are constructed and how they aim to describe the device flow conditions.

For MMAD, the dispersion parameters that gave to the strongest correlation with Experimental Iterations 1 and 2 ($R^2 > 0.8$) are summarized in Table 5.2. To improve correlation agreement with the MMAD experimental data, a common theme in all of the dispersion parameters was the inclusion of the actuation pressure, or ΔP, which represents the input flow energy per unit volume (J/m³). The dispersion parameter that gave the strongest correlations with MMAD was:

$$\frac{kd^*}{\Delta P v_i} \tag{5.3.5}$$

where d^* is the ratio of outlet to inlet capillary diameters and v_i is the inlet capillary velocity. The physical basis for this dispersion parameter is the input turbulent kinetic energy (k in J/kg) per input flow energy (ΔP in J/m³). Division by air density can be used to eliminate the differing basis of the energy terms, but it is not necessary considering that all cases are actuated with room air. Based on trial and error experimentation, the correlation with MMAD was significantly improved by multiplying the dispersion parameter by d^*/v_i, similar to the result of Longest et al. (2018).

The $\Delta P/k^* d^*$ parameter in Table 5.2 is similar to Equation (5.3.5), but the ratio of k to inlet velocity is non-dimensionalized as it was by Longest and Farkas (2018). The numerators and denominators are also reversed as this gave a better R^2 value. The $k\mu/v_i\Delta P d_o$ parameter again includes similar variables as the previous two parameters, but uses inspiration from the Bejan number (Bhattacharjee & Grosshandler, 1988) ($\mathrm{Be} = \Delta P L^2/\mu v$, which represents a non-dimensional pressure drop) to non-dimensionalize the parameter. The $k^* \omega^* d^*$ parameter applies the ratio of outlet to inlet diameter to the $k^* \times \omega^*$ parameter from Longest and Farkas (2018), which had a positive influence on the R^2 value for all cases considered. Finally, the $v_i' d^*/v_i\Delta P$ parameter is again similar to the

first dispersion parameter discussed here, but the ratio of k to inlet velocity is non-dimensionalized by using the fluctuating velocity component ($v' = \sqrt{2/3k}$) instead of k.

For ED, the dispersion parameters that gave to the strongest correlation with Experimental Iteration 1 and 2 ($R^2 > 0.8$) are summarized in Table 5.3. In contrast to Longest and Farkas (2018), none of the dispersion parameters that utilize a combination of flow and turbulence quantities (such as v_i and k) had a strong correlation with ED in the current study, which evaluates a pediatric air-jet DPI as opposed to a low actuation volume DPI. All dispersion parameters for ED presented in this study use inlet volumetric flow rate (Q_i) with a scale factor as a prediction of aerosolization performance. The scale factors that were most effective were d^*, k, and d_o, which all improved the correlation from an R^2 value of 0.74 to over the threshold of 0.8 for a strong correlation in this study.

Evaluation and Comparison Criteria

This study uses the following metrics to quantify device performance improvements, compare the match between experimental and CFD results, and determine the accuracy of dispersion parameter predictions.

The Relative Δ metric compares the predicted aerosolization performance of design configurations with Experimental Iteration 1, in order to quantify performance improvements over the initial designs. It is defined as the difference between the CFD-predicted MMAD (MMAD_{CFD}) and the estimated MMAD (MMAD_{Est}), based on the estimated MMAD from Experimental Iteration 1, relative to the estimated MMAD:

$$\text{Relative }\Delta = \frac{\text{MMAD}_{\text{CFD}} - \text{MMAD}_{\text{Est}}}{\text{MMAD}_{\text{Est}}} \times 100\% \qquad (5.3.6)$$

Specifically, estimated MMAD (MMAD_{Est}) is determined from the experimental data by the linear line of best fit between MMAD and ED for Experimental Iteration 1, which is

hereafter referred to as Experimental Iteration 1 Best Fit. That is, if a device configuration has a predicted MMAD and ED that lies on Experimental Iteration 1 Best Fit, its Relative Δ is zero and there is no improvement over the initial devices. If the Relative Δ is negative, its MMAD is smaller than would be predicted by ED alone, based on the results from Experimental Iteration 1, and *vice versa* for a positive Relative Δ. Therefore, a negative Relative Δ shows an improvement in aerosolization performance over Experimental Iteration 1 for a given ED.

Relative difference (Rel. Diff.) is a standard statistical measure, but has different definitions given the application. In this instance, the difference is between the CFD-predicted and experimental (Exp) MMAD or ED, relative to the experimental value:

$$\text{Rel. Diff.} = \frac{\text{MMAD}_{\text{CFD}} - \text{MMAD}_{\text{Exp}}}{\text{MMAD}_{\text{Exp}}} \times 100 \text{ or } \frac{\text{ED}_{\text{CFD}} - \text{ED}_{\text{Exp}}}{\text{ED}_{\text{Exp}}} \times 100 \tag{5.3.7}$$

This provides a basis for comparison between the CFD-predicted and experimentally determined aerosolization performance.

RMS error is also commonly used in statistical methods. It is the square-root of the sum-square of the difference between CFD-predicted and experimental results divided by the number of data points:

$$\text{RMS Error}$$

$$= \sqrt{\frac{\sum_{i=1}^{n} \left(\text{MMAD}_{\text{CFD,i}} - \text{MMAD}_{\text{Exp,i}} \right)^2}{n}} \text{ or } \sqrt{\frac{\sum_{i=1}^{n} \left(\text{ED}_{\text{CFD,i}} - \text{ED}_{\text{Exp,i}} \right)^2}{n}} \tag{5.3.8}$$

This quantifies the error between the CFD-predicted and experimentally observed aerosolization performance across all cases considered by the study.

5.4   Results

First and Second Experimental Iterations

Figure 5.3 plots the MMAD against ED for Cases 1-4 from Experimental Iteration 1, and the dashed line is Experimental Iteration 1 Best Fit (R^2 = 0.98). The numerical annotations in the plot correspond to the markers for each device in Table 5.4. This plot shows that for these cases, increasing ED also increases MMAD. This is undesirable for DPI aerosolization performance, as we want both a small MMAD and large ED to deliver as much drug to the target area of the lungs as possible. Therefore, for improvement in aerosolization performance we intend to develop devices that perform below this dashed line. That is, for a given ED, the MMAD should be smaller than estimated from the linear fit performance of Experimental Iteration 1.

Experimental Iteration 2 intended to test the accuracy and robustness of initial dispersion parameter development, identify additional dispersion parameters, and evaluate what aspects of device design and operation would plot MMAD and ED above or below the Experimental Iteration 1 Best Fit. Figure 5.4 adds the MMAD and ED data from Experimental Iteration 2 (Table 5.4) to Figure 5.3. The numeral annotations in the plot correspond to the markers for each device in Table 5.4. From this figure it is clear that the majority of cases exhibited similar or worse performance than Experimental Iteration 1, as they plot close to or above the dashed line. The exception is Case 3.00/2.08 (VI), which has an MMAD that is approximately 0.5 µm smaller than what is expected from its ED and performance estimations from Experimental Iteration 1.

The experimental results from Experimental Iteration 1 and 2, with CFD predictions of the flow and turbulence fields for each device, were used to develop the dispersion

parameters for MMAD and ED that were summarized by Table 5.2 and Table 5.3, respectively. The strength of MMAD and ED correlations that use these parameters is presented in subsequent sections. In line with the study objective, CFD-predictions of aerosolization performance use the dispersion parameters, and their associated correlations, to drive optimization of the device design.

Flow and Turbulence Characteristics

Before presenting details on the dispersion parameters, aerosolization performance, and device optimization, it is important to understand the flow field behavior and characteristics within the device. As mentioned in the Methods, the flow is highly turbulent and moderately compressible, with inlet Reynolds numbers over 10,000 and Mach numbers up to 0.27 for the cases in Experimental Iterations 1 and 2. Figure 5.5 shows contours of k and velocity streamlines within the capsule of Case 4. The highest level of turbulence, represented with k, occurs in the shear layer where the inlet jet meets the relatively quiescent flow in the capsule, which propagates through the outlet capillary. There is also a large velocity gradient between the center of the inlet jet and the dose chamber. Points A (center of the jet) and B (top of powder bed) in Figure 5.5 have velocity magnitudes of 110.36 and 4.39 m/s respectively (or Mach numbers of 0.32 and 0.01) with only 1.88 mm between them. The velocity streamlines in Figure 5.5 demonstrate very dynamic and chaotic behavior in the secondary flow patterns within the capsule.

As mentioned previously, preliminary experimental work tested whether angled inlets or a longer outlet capillary would improve aerosolization performance with increased secondary flow or more exposure to highly turbulent flow, respectively. It is reasonable to expect that increased secondary flow patterns would entrain more particles

from the powder bed and provide an improvement in ED. However, the preliminary work showed little aerosolization improvement for devices with an inlet capillary angled at 30°, 60°, and 90° relative to the long axis of the capsule. CFD-predictions of secondary flow, with the stream-wise flow considered to be aligned with long axis, also did not correlate well with ED. It is also reasonable to expect that exposing particle agglomerates to highly turbulent flow for a longer duration would aid secondary breakup and reduce MMAD. However, extending the length of the outlet capillary from 18 mm to 30 mm and 60 mm also showed negligible improvement in aerosolization performance.

This raises questions over the mechanisms within the device that are responsible for the most effective forms of powder aerosolization. The large velocity gradient between the inlet jet and remainder of the capsule region creates the correct amount of secondary flow in order to maintain a high ED and not fluidize the powder bed too quickly. Also, the maximum k to which particle agglomerates are exposed may drive secondary breakup and determine particle size, as opposed to time of exposure. That is, if agglomerates pass through the region of highest energy eddies and break up as small as that energy permits, additional exposure time to smaller energy eddies may not reduce the particle size further. This observation would explain why a longer outlet capillary length did not further reduce MMAD.

Particle Size and Emitted Dose Dispersion Parameters

Figure 5.6 plots MMAD as a function of the dispersion parameter from Table 5.2 with the strongest correlation. For the $kd^*/v_i \Delta P$ dispersion parameter, the R^2 value is 0.96 and standard error (SE) is 0.06 μm when correlated with MMAD. The dashed line on the plot is the linear line of best fit between cases considered, and represents the

correlation used to predict MMAD from the dispersion parameter. Considering the 95% interval on a normal distribution, we can assume the correlation is accurate between plus or minus double the SE, which is 0.12 µm and represented by the solid lines on Figure 5.6. For context, the coefficient of variation (CoV) is defined as the ratio of SE to the mean MMAD, which in this case is 3.3%.

The high R^2 value, small SE, and small CoV demonstrates a very strong correlation between MMAD and the $kd^*/v_i\Delta P$ dispersion parameter. Beyond the statistical measures, the plot of data points for each case relative to the linear correlation line also suggests the $kd^*/v_i\Delta P$ dispersion parameter will accurately predict MMAD from CFD results. The correlation closely matches the full range of data points, from devices with a relatively small (1.6 µm) to larger (2.4 µm) MMAD, and also captures the effect of operating Case 4 with a lower pressure drop with the Half Q case. Furthermore, the correlation provides an accurate prediction for Case 1.32/2.90, with its MMAD in the middle ground between the 1.6-1.8 µm cases and the 2.4 µm Half Q case, which further demonstrates the correlation is accurate across a range of dispersion parameters and MMAD values. Finally, CFD results for Case 1.32/2.39 and 2.08/2.69 both show these devices had very similar dispersion parameter values, and the correlation is able to accurately predict they have the same MMAD. That is, if these cases had the same dispersion parameter value, but very different experimentally determined MMADs, the correlation would clearly be inaccurate.

Similar to the MMAD dispersion parameters, Figure 5.7 plots ED as a function of the dispersion parameter from Table 5.3 with the strongest correlation. As before, the dashed line is the linear correlation (or line of best fit) and the solid lines represent plus

or minus double the SE (or the 95% interval on a normal distribution). For the Qd^* dispersion parameter, the R^2 value is 0.86, the SE is 3.0%, and CoV is 3.8% when correlated with ED. As mentioned previously, out of all the dispersion parameters considered, the device ED consistently showed the best correlations with parameters that used the flow rate (Q) through the device. Correlating ED with Q alone showed an R^2 value of 0.74, and scaling by the variables summarized in Table 5.3 improved the correlations.

Influence of Design Factors on Dispersion

To be predictive of device aerosolization performance, it is necessary to understand how the CFD-predicted flow and turbulence variables in the MMAD and ED dispersion parameters behave in response to design factor changes. These variables are volume-averaged turbulent kinetic energy (k) and inlet capillary velocity (v_i) in the MMAD dispersion parameter, and inlet volumetric flow rate (Q_i) in the ED dispersion parameter, with v_i directly calculated from Q_i. Figure 5.8 is a 3D surface plot of the CFD-predicted k vs. inlet and outlet capillary diameters on the independent axes; and Figure 5.9 shows CFD-predicted Q vs. inlet and outlet capillary diameters. These data points are the result of running an array of 144 CFD models for every possible combination of 12 different inlet and outlet capillary diameters ranging from 0.41 to 3.00 mm. An effort was made to combine the inlet and outlet diameters into a single function that could describe the device behavior, with respect to the dispersion parameter variables, in a standard x-y plot. However, the clearest representation of how the flow and turbulence quantities vary in response to design factor changes is with a 3D surface plot, as both k and Q_i are dependent on d_i and d_o by different relations. To estimate variable values in between the

CFD-predicted data points, one could define a high-order bivariate polynomial to establish a surface of best fit. However, in this case, the large number of CFD simulations was sufficient to identify design factor configurations that were possible candidates for an optimized device.

Considering both Figure 5.8 and Figure 5.9 together, there is a region where d_i and d_o are greater than 2.5 mm that shows k decreases (reducing MMAD) while Q continues to increase (improving ED). This region of high Q and decreasing k is labeled with ✳ in Figure 8 and Figure 9. Combining this with the MMAD and ED dispersion parameters ($kd^*/\Delta Pv_i$ and $Q_i d^*$ respectively), Figure 5.8 and Figure 5.9 suggest that device configurations in this region would give a small MMAD and high ED, which is the desirable aerosolization performance. For a constant ΔP and d^*, reducing k and increasing v_i would give a smaller MMAD dispersion parameter and predicts a smaller particle size. Likewise, for a constant d^*, increasing Q_i would give a larger ED dispersion parameter and predict less device losses. However, the predicted aerosolization performance from design factors is not quite as simple as what has been described here, as changing the inlet and outlet capillary diameters also changes the d^* variable, which has an effect on both the MMAD and ED dispersion parameters. Furthermore, the Q through the devices in the region where d_i and d_o is greater than 2.5 mm is over 20 LPM, which for an inhalation volume of 750 mL gives an actuation time of less than 2 seconds. Therefore, the Q for these devices might be too high for the target age of a 5-6-year-old subject. That said, it is valuable insight for developing devices that may target older patients that inhale at higher flow rates. One final consideration regarding actuating DPIs with higher flow rates is the resultant impaction parameter (typically given as $d_a^2 Q$, where

d_a is aerodynamic particle diameter) may be higher, which would suggest the possibility of increased extrathoracic losses (Golshahi, Noga, Thompson, & Finlay, 2011; Javaheri et al., 2013; Storey-Bishoff et al., 2008; Tavernini et al., 2018).

Aerosolization Performance and Device Optimization

As described above, possible device design configurations from 12 inlet and outlet capillary diameters were considered, ranging from 0.41 to 3.00 mm, which required the evaluation of 144 CFD models. The majority of these models, especially those with relatively small capillary diameters, showed little improvement over Case 4, which has exhibited the best aerosolization performance from Experimental Iteration 1 and 2. Table 5.5 summarizes the CFD-predicted aerosolization performance, from flow and turbulence quantities and dispersion parameter correlations, of 25 cases that had inlet and outlet diameters greater than 1.83 mm (as this is the inlet capillary diameter for Case 4). The naming convention for the markers, which are used in subsequent plots to identify each case, uses the first letter to identify the inlet capillary diameter and the second letter for the outlet, where A is 1.83 mm, B is 2.08 mm, C is 2.39 mm, D is 2.69 mm, and E is 3.00 mm. The cases with markers highlighted in light grey are those where CFD-based predictions suggest that both the MMAD and ED will be better than the aerosolization performance of Case 4, and makers highlighted in dark grey are predicted to be worse than Case 4. Here, better means the CFD-predicted MMAD and ED plot below Experimental Iteration 1 Best Fit. What is most interesting from this data set is the CFD-based predictions show that ED can increase as MMAD decreases (as Figure 5.8 and Figure 5.9 suggested), which was not apparent from Experimental Iteration 1. For example, for Case AD and CD, the inlet diameter changes from 1.83 mm to 2.39 mm and

outlet diameter is constant at 2.69 mm, with the CFD-predicted MMAD improving from 1.92 to 1.75 µm and ED improving from 87.7% to 92.7%. Conversely, in Experimental Iteration 1, Case 3 and 4 had the same outlet diameter, but inlet diameters of 2.39 mm and 1.83 mm respectively, and they showed little difference in aerosolization, with Case 4 having a marginally better ED.

Figure 5.10 adds the MMAD and ED data for the cases that CFD-based predictions suggest are better than Case 4 (i.e. the light grey cases in Table 5.5) to Figure 5.4. The additional annotations in the plot correspond to the markers for each case in Table 5.5. As mentioned previously, cases that plot below the dashed line exhibit an improvement in aerosolization performance compared to Experimental Iteration 1. The Evaluation and Comparison Criteria section defined the Relative Δ metric that compares the estimated MMAD (for a given ED) with the performance of devices from Experimental Iteration 1. This provides a quantitative value to measure the difference between the CFD-based predictions and the dashed line in Figure 5.10. Table 5.6 summarizes the Relative Δ metric for each of the cases added to Figure 5.10, with a negative value indicating the performance is an improvement over Experimental Iteration 1 and the value quantifying the percentage improvement in aerosolization performance. From all the design configurations considered here, Case 2.69/2.69 and 3.00/2.69 (DD and ED) are selected for device optimization evaluation as they are predicted to have a smaller MMAD than Case 4, a negative Relative Δ, and an ED greater than 90%. These two cases are highlighted with the dotted ellipse in Figure 5.10.

Figure 5.10 also provides a comparison between the CFD-based predictions and experimentally measured MMAD and ED for Cases 3 and 4. These data points lie within

the SE of the MMAD and ED correlation and the standard deviation (SD) of the experimental data. The accuracy of CFD-based predictions, with statistical observations, is discussed in greater detail in the following section.

Experimental Validation

Table 5.7 summarizes the comparison between CFD-based predictions and experimentally measured MMAD and ED for all experimentally tested devices. The comparison to Experimental Iteration 1 and 2 serves as the typical validation of CFD methods and the dispersion parameter correlations with experimental data. The comparison with the two optimized devices provides an *a priori* validation of the optimization process. That is, the CFD-based predictions of the MMAD and ED for those two design configurations were established before validating their accuracy with experimental testing, and no adjustments to either the CFD models or dispersion parameter correlations were made after obtaining the experimental data. The relative difference (Rel. Diff.) in Table 5.7 uses the standard definition for observed and predicted data. The average Rel. Diff. between CFD-based predictions and experimental measurements for MMAD is 2.9%, and the range of absolute error is from -0.07 to 0.13 µm (Case 1 and Case 2.69/2.69 respectively). Similarly, for ED the average Rel. Diff. is 3.5% and the range of absolute error is from -7.9% to 5.6% (Case 3.00/2.08 and 1.32/2.90 respectively). The RMS Error for MMAD and ED is 0.06 µm and 3.4% respectively, which compares well with the SE from each of the MMAD and ED dispersion parameter correlations. Based on these statistical measures, the CFD flow and turbulence fields with $kd^*/\Delta P v_i$ and Qd^* dispersion parameters provide a very good prediction of device aerosolization performance, verified with *a priori* validation.

Finally, the design configurations that were selected as candidates for optimized devices provided improved aerosolization performance compared to Case 4. The MMAD decreased from 1.69 µm to 1.55 µm and 1.59 µm, which is an absolute difference of 0.14 µm and 0.10 µm, for Cases 2.69/2.69 and 2.69/3.00, respectively. Similarly, the ED increased from 86.0% to 90.4% and 92.3%, which is an absolute difference of 4.4% and 6.3%. This device optimization would not be possible without the insight into the relationship between aerosolization performance and design factors that was possible with a concurrent CFD and experimental approach.

5.5 Discussion

This study meets the objective by establishing dispersion parameter correlations ($kd^*/\Delta Pv_i$ and Qd^*) that accurately predict the aerosolization performance (MMAD and ED) of a pediatric air-jet DPI. Using these dispersion parameters, a full sweep of 144 CFD models, covering every configuration of 12 different inlet and outlet diameter capillaries, was evaluated for optimized predicted performance. Two candidate optimized design configurations were validated *a priori*, and found to have improved aerosolization performance compared to Case 4. Throughout the study, valuable insights into the flow and turbulence conditions within the capsule were obtained, and relationships between CFD flow and turbulence fields and design factors were established.

The flow within the capsule during actuation of the DPI is surprisingly complex given the relatively simple geometry. Inlet Mach and Reynolds numbers suggest moderately compressible and highly turbulent flow, especially for cases with larger capillary diameters and high flow rates, and high frequency flow oscillations require a transient solution strategy. Analysis of the CFD velocity field shows a large velocity

206

gradient between the center of the inlet jet and quiescent capsule (from 110.4 m/s to 4.4 m/s across a distance of 1.88 mm). The velocity gradient has an equally large negative pressure gradient that generates the correct amount of secondary flow to aerosolize the powder bed at an adequate rate. This premise is supported by the fact that ED correlated well with device flow rate, meaning higher flow and velocities through the device lead to greater entrainment of particles from the powder bed. Furthermore, Experimental Iteration 1 showed that MMAD increased with ED, which suggests that a larger negative pressure gradient is capable of lifting the larger particles from the powder bed, hence the simultaneous increase in both aerosolization performance metrics for Experimental Iteration 1.

Beyond meeting the primary objective, this study also demonstrated how the flow and turbulence fields, which are used in the definition of the dispersion parameters, behave in response to changes in design factors. 3D surface plots show that k and Q vary relative to inlet and outlet capillary diameters as independent variables. Results showed that capillary diameters larger than approximately 2.5 mm lead to a relative decrease in k and increase in Q, which according to the dispersion parameters gives the desired decrease in MMAD and increase in ED. However, given the administration of the air-jet DPI to children, there is a relatively low upper limit on the available flow rate through the device to maintain low extrathoracic depositional losses, with the target being approximately 15 LPM for a 5-6-year-old subject.

The dispersion parameter correlations established in previous work by our group (Longest & Farkas, 2018; Longest et al., 2019) did not correlate well with Experimental Iteration 1 in the present study, and were further weakened when applied to Experimental

Iteration 2. This is because of differences in the device and operation, including a larger air volume, higher flow rates, and larger capillary sizes in the current study. As such, new dispersion parameters were established that gave strong correlations, for both MMAD and ED, when applied to the current data set of ten experimental runs (see Table 5.4). What is consistent between the dispersion parameters used in the present study and previous work is that the MMAD is at least partially dependent on the ratio between volume-averaged k and inlet flow velocity. As k is specific turbulence kinetic energy and velocity is akin to specific flow kinetic energy, this ratio can be thought of as the ratio of turbulence to flow energy. That is, when aiming for a small particle size, one should strive to minimize this ratio and not necessarily minimize k alone. The addition of pressure drop across the device to the MMAD dispersion parameter accounts for the energy used to actuate the air-jet DPI.

This study also demonstrated the strength of the CFD methods and dispersion parameters used in predictions of aerosolization performance with *a priori* validation. Typically, CFD models are validated against experimental data after the devices have been tested, and the CFD model parameters are adjusted until numerical and experimental results match. In *a priori* validation, the devices are tested after the CFD models are run, and results between the numerical and experimental data are compared and reported with no changes to the CFD model setup. The results showed that the CFD models and aerosolization performance predictions for the two optimized devices were very close to the experimentally tested MMAD and ED, with small relative, absolute, and RMS errors. This demonstrates that the CFD methods for air-jet DPIs established by our

previous work (Longest & Farkas, 2018; Longest et al., 2019) and the newly defined dispersion parameters are accurate predictors of device performance.

The two candidate optimized designs decreased the experimentally measured MMAD by 0.10 μm and 0.14 μm (relative difference of 5.9% to 8.3%) and increased ED by 4.4% and 6.3% (relative difference of 5.1% to 7.4%) compared to Case 4. Therefore, these two devices demonstrated improved aerosolization performance compared to previous air-jet DPI designs. However, there is more to consider when administering pharmaceutical aerosols to children with air-jet DPIs than only the device aerosolization performance. As mentioned previously, the flow rate through the optimized devices is approximately 25 LPM, which, for a 750 mL inhalation volume, gives an actuation time of less than 2 seconds. For the target age of a 5-6-year-old child, the inhalation flow rate should be about 15 LPM and an actuation time of 3 seconds, meaning the optimized devices may increase extrathoracic losses for the age of patients selected as the focus of this study. That said, these devices may be suitable for older children with slightly larger extrathoracic airways. The impaction parameter ($d_a^2 Q$) is often used when evaluating extrathoracic aerosol deposition (Golshahi et al., 2011; Javaheri et al., 2013; Storey-Bishoff et al., 2008; Tavernini et al., 2018). There is a large amount of inter-patient variability when using this parameter, but the general trend is that particle deposition in the nasal (or oral) passage typically increases as the impaction parameter increases. This parameter shows that if the particle size (d_a) decreases, the extrathoracic losses may be the same or even increase if the flow rate (Q) increases. Comparing Case 2.69/2.69 and 3.00/2.69 to Case 4, the impaction parameter increases to 59.6 μm²-LPM and 68.3 μm²-LPM from 38.0 μm²-LPM, which indicates extrathoracic losses will be higher for the

optimized devices. However, the deposition vs. impaction parameter plots vary considerably for different age groups (and even from patient to patient within age groups) and typically have a non-linear S-shape profile, so the actual increase in extrathoracic losses may be negligible for the optimized devices.

On the experimental side, limitations in the present study are consistent with those reported by Farkas et al. (2019). One additional limitation is the variability in actuating the device with a ventilation bag, which is the intended actuation method. Experiments used compressed air and a solenoid valve to actuate the devices with a pressure drop of 6 kPa. This provided consistency from device to device and provided a clear definition of boundary conditions for CFD models. However, variability in the operation of a ventilation bag to actuate the device between caregivers could influence aerosolization performance. Results from the Half Q case showed that actuating Case 4 with a pressure drop of 1.5 kPa gave an MMAD of 2.46 µm and ED of 72.0%, which was much worse than actuating Case 4 with 6 kPa. This is perhaps at the extreme end of a low pressure drop, but demonstrates the variability in device performance relative to actuation pressure. As such, this should be taken into consideration when establishing caregiver operation guidelines for actuation of the device.

Another limitation is the large number of design options that are available for the air-jet DPI approach. Despite the large number of inlet and outlet capillary configurations that were considered, many of the design factors available for air-jet DPIs have not been evaluated. Preliminary work showed that angled inlet capillaries relative to the outlet and longer outlet capillaries did not improve aerosolization performance. However, many more aspects of the device design can be explored such as different size and shape

aerosolization chambers (instead of a size 0 capsule), capillary piercing locations and orientation (instead of along the long axis of the capsule), and actuating the device with several smaller volumes of air (instead of 750 mL in one actuation). The negative pressure gradient between the inlet jet and powder bed and its effect on secondary velocities within the capsule has been discussed previously. Changing the aerosolization chamber (or capsule) shape and size could leverage this phenomenon to improve ED, and would also need to be considered when loading the device with larger or smaller drug masses.

Future work on improving the aerosolization performance of air-jet DPIs should focus on expanding the exploration of the many available design factors and their influence on MMAD and ED. Future iterations of air-jet DPIs design can use the physical insight and dispersion parameters identified in the present study to drive the design and optimize performance further. It would also be interesting to test how robust the newly defined MMAD and ED dispersion parameters are when applied to the changes in design that were discussed here. The secondary breakup mechanism that reduces the particle size, after they are entrained in the flow, is also little understood at this stage. The MMAD dispersion parameter shows that the ratio of k to inlet velocity should be minimized to reduce particle size, but the exact characteristics of the flow and turbulence field that are responsible for secondary breakup are unclear. The original concept used in the development of air-jet DPIs by our group aimed to use highly turbulent eddies to break up agglomerates, but this expectation has consistently been shown to be incorrect for the air-jet DPIs. High-resolution, high-speed imaging of the particles within the device may provide some experimental insight into particle break up within the flow. Similarly, utilizing

DEM in numerical models could provide CFD insight into break up mechanisms for air-jet DPIs, but such a model would be difficult to validate and very computationally expensive.

In conclusion, newly developed dispersion parameters with CFD predictions of flow and turbulence quantities were capable of accurately predicting air-jet DPI aerosol performance in terms of MMAD and ED with *a priori* validation. Greater insight in to the flow and turbulence characteristics within the capsule was obtained, and the effect of design factors on these quantities was identified. Optimized devices reduced the MMAD by approximately 0.1 µm and increased ED by approximately 5%. However, these devices may be better suited to children older than 5-6 years old due to increased device flow rates.

5.6   Figures
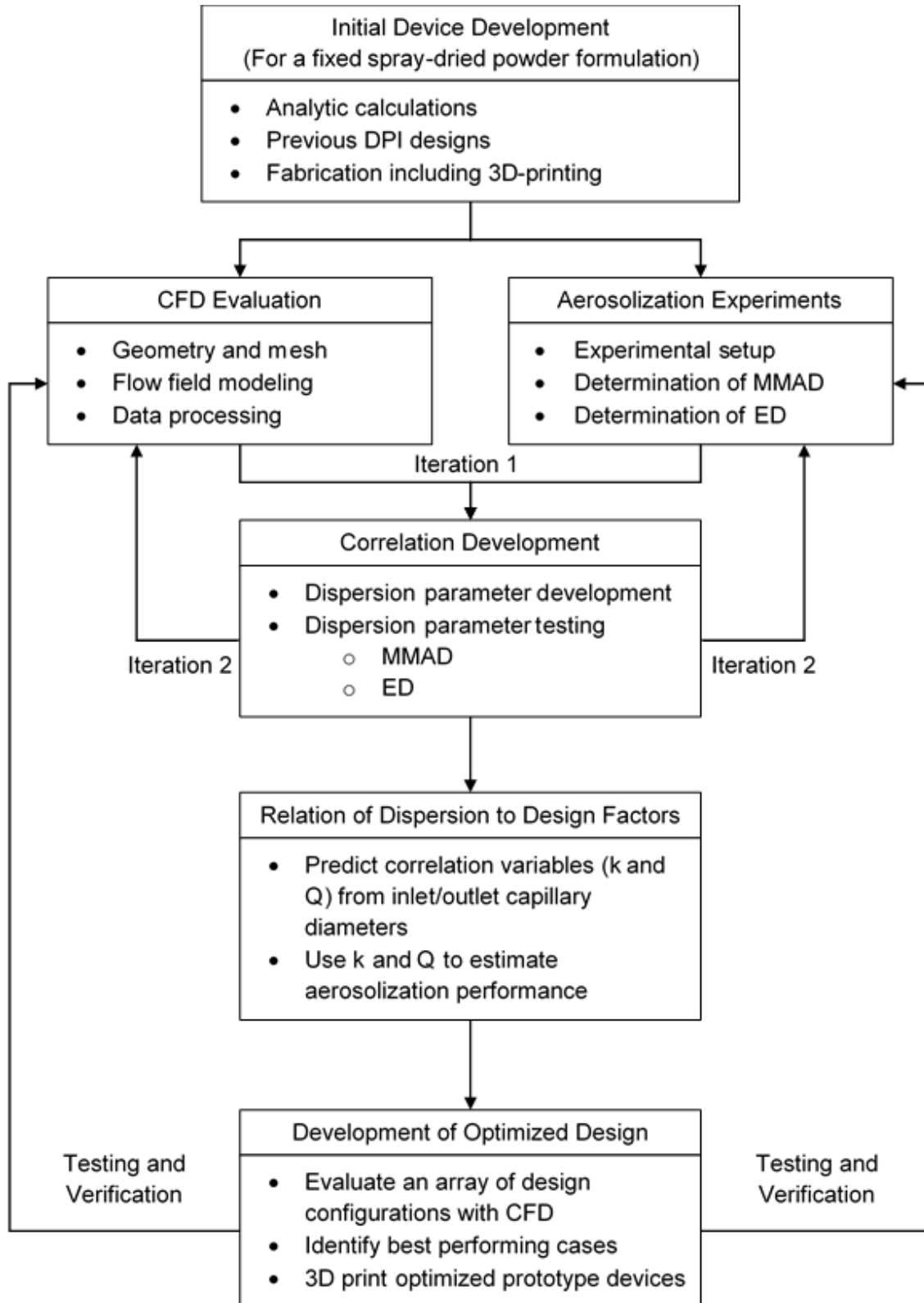
Figure 5.1:   Block diagram of device development and optimization process.
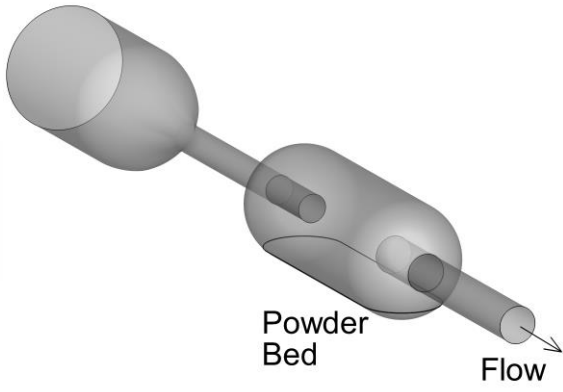
Figure 5.2: Overview of device geometry showing (a) CAD rendering with inlet and outlet connections, stainless steel capillaries, size 0 capsule, and rubber O-ring, and (b) internal flow pathway used for the CFD domain.
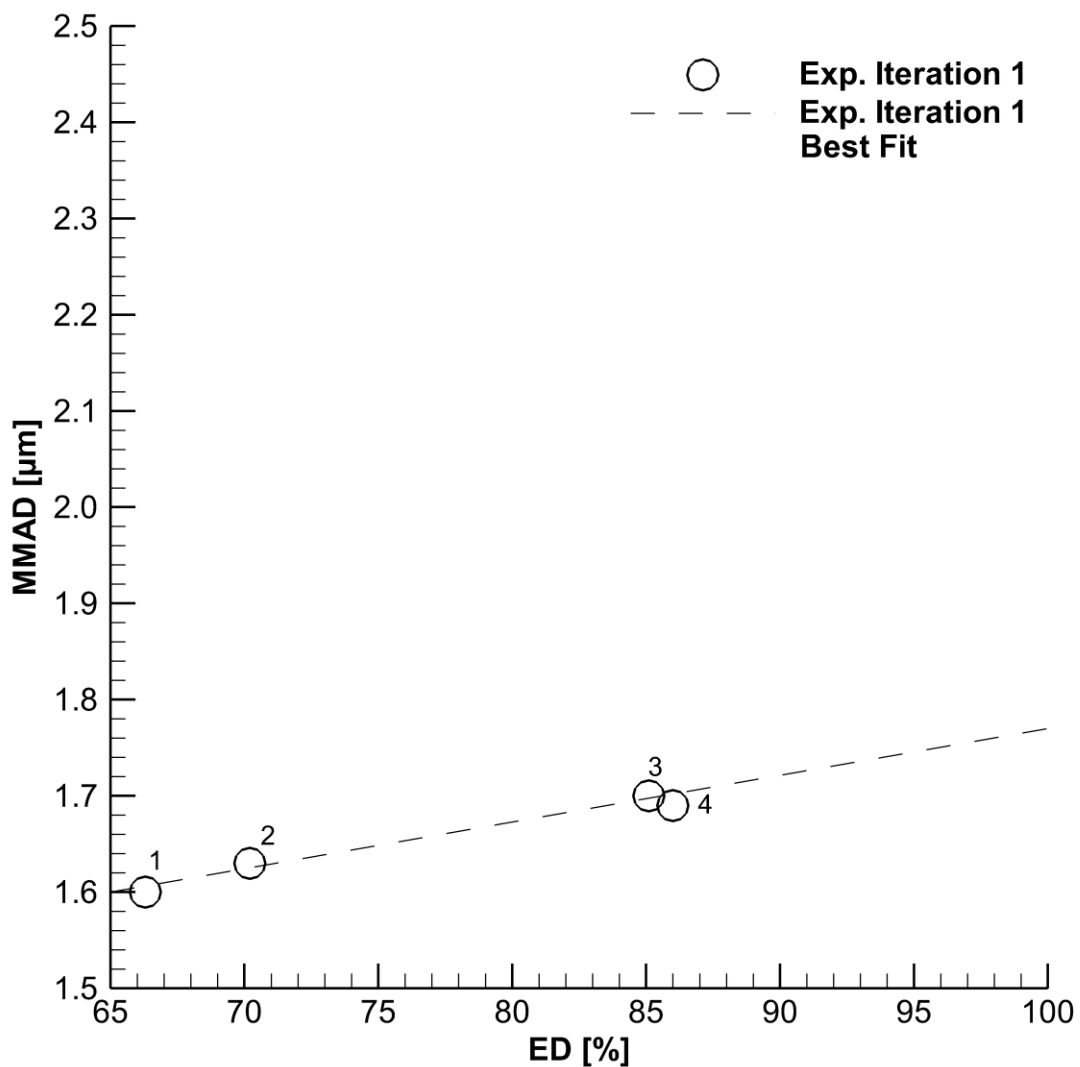
Figure 5.3: Plot of particle mass-median aerodynamic diameter (MMAD) against emitted dose (ED) for Experimental Iteration 1 (Cases 1-4). Annotations correspond with the Markers in Table 5.4. A small MMAD and large ED is desirable for aerosolization performance. The dashed line is Experimental Iteration 1 Best Fit ($R^2 = 0.98$), where particle size generally worsens with an improvement in emitted dose.
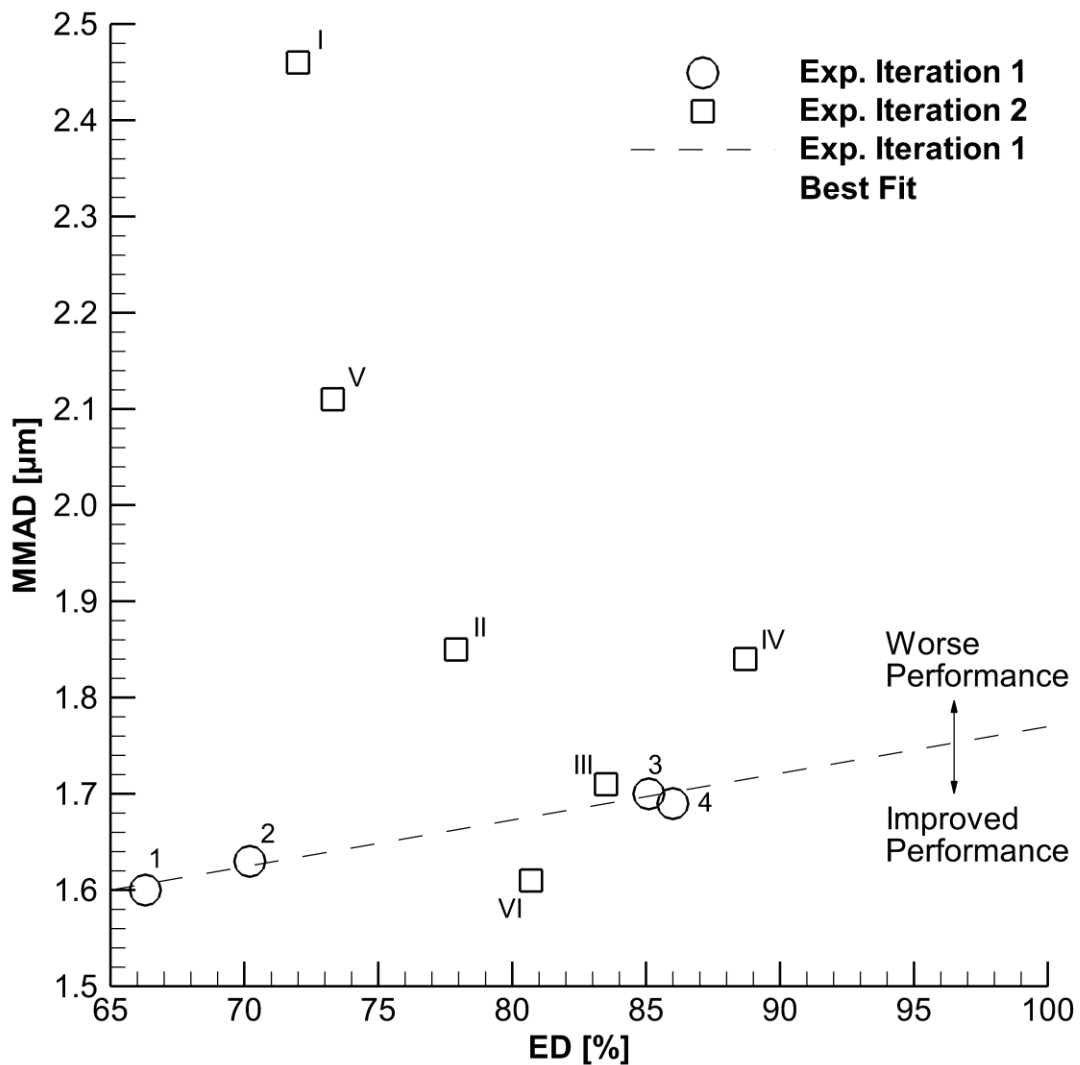
Figure 5.4:   Addition of Experimental Iteration 2 to the MMAD vs. ED plot shown in Figure 5.3. Annotations correspond with the Markers in Table 5.4. Generally, these additional devices perform poorly compared to Cases 1-4, except Case 3.00/2.08 (VI), which has better MMAD for a given ED.
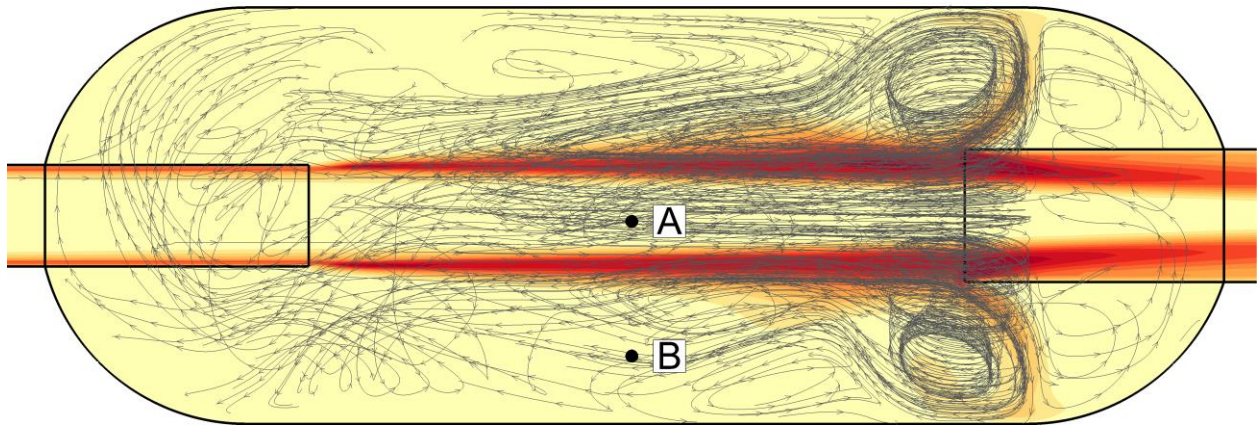
Turbulent Kinetic Energy [m^2/s^2]:   20   40   60   80   100 120 140 160 180 200

Figure 5.5:   Overlay plot on the mid-plane slice of turbulent kinetic energy field and flow streamlines between the inlet and outlet capillaries in the capsule. Velocity magnitudes at Point A and B are 110.36 m/s and 4.39 m/s, respectively.
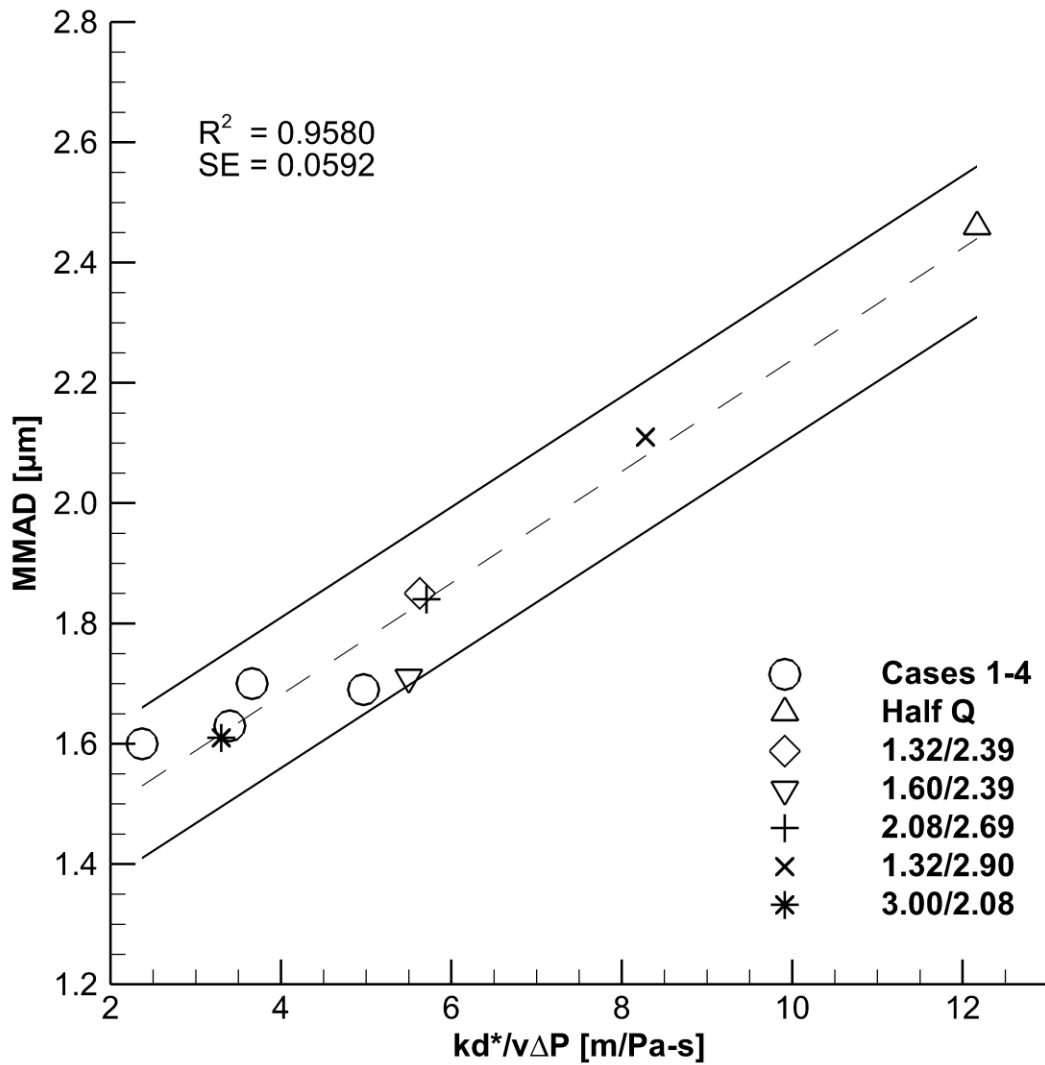
Figure 5.6: Particle mass-median aerodynamic diameter (MMAD) vs. dispersion parameter $kd^*/v_i\Delta P$. The dashed line is the linear best fit and the solid lines show +/- 0.12 µm, which is double the standard error (or the 95% interval on a normal distribution). Note that the Half Q (Δ), 1.32/2.39 ($\Diamond$), 1.60/2.39 (∇), 2.08/2.69 (+), 1.32/2.90 (×), and 3.00/2.08 ($*$) cases are from Experimental Iteration 2 ($\square$ in Figure 5.4).
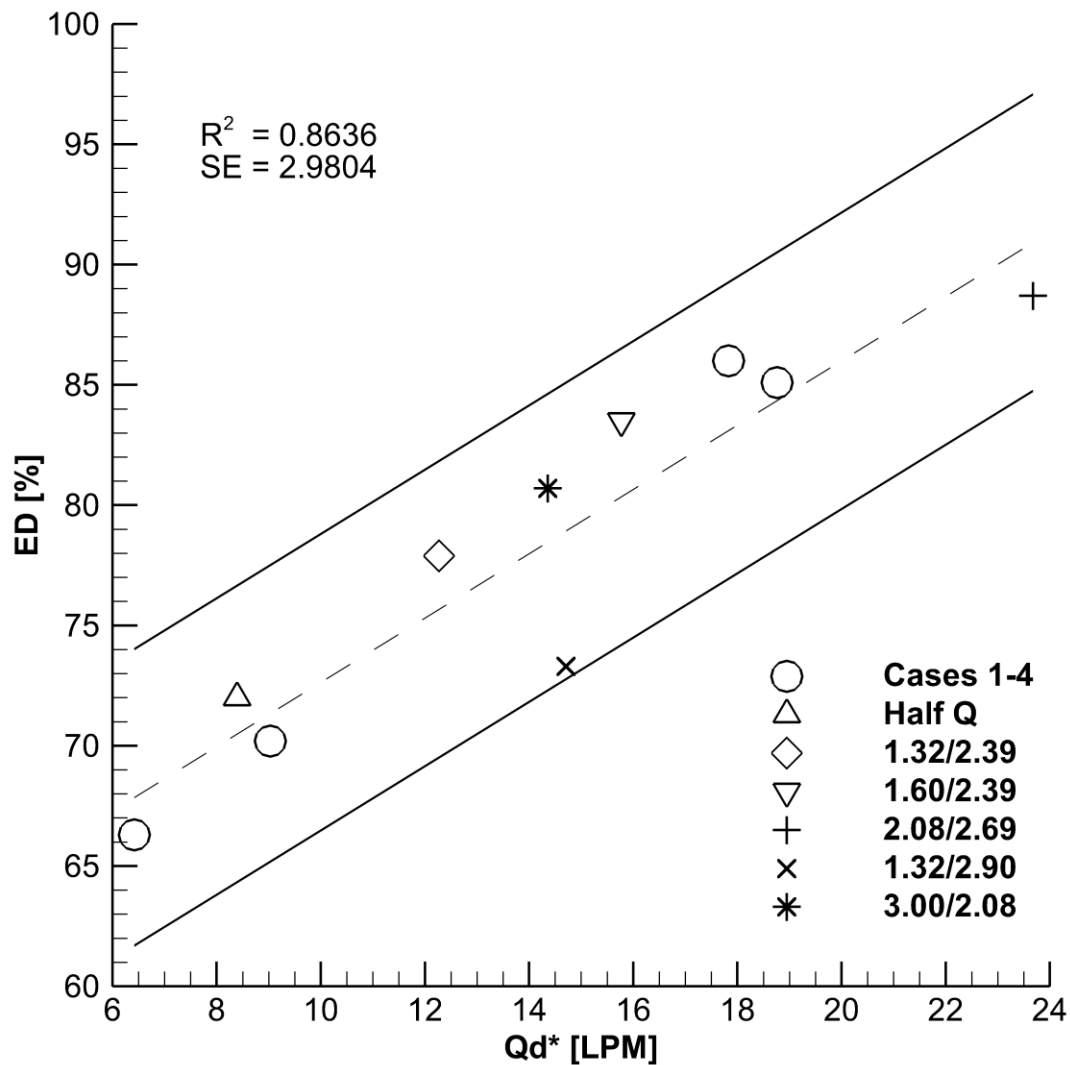
Figure 5.7: Emitted dose (ED) vs. dispersion parameter Qd*. The dashed line is the

linear best fit and the solid lines show +/- 6.17%, which is double the standard error (or

the 95% interval on a normal distribution). Note that the Half Q (Δ), 1.32/2.39 (◊), 1.60/2.39

(∇), 2.08/2.69 (+), 1.32/2.90 (×), and 3.00/2.08 (∗) cases are from Experimental Iteration
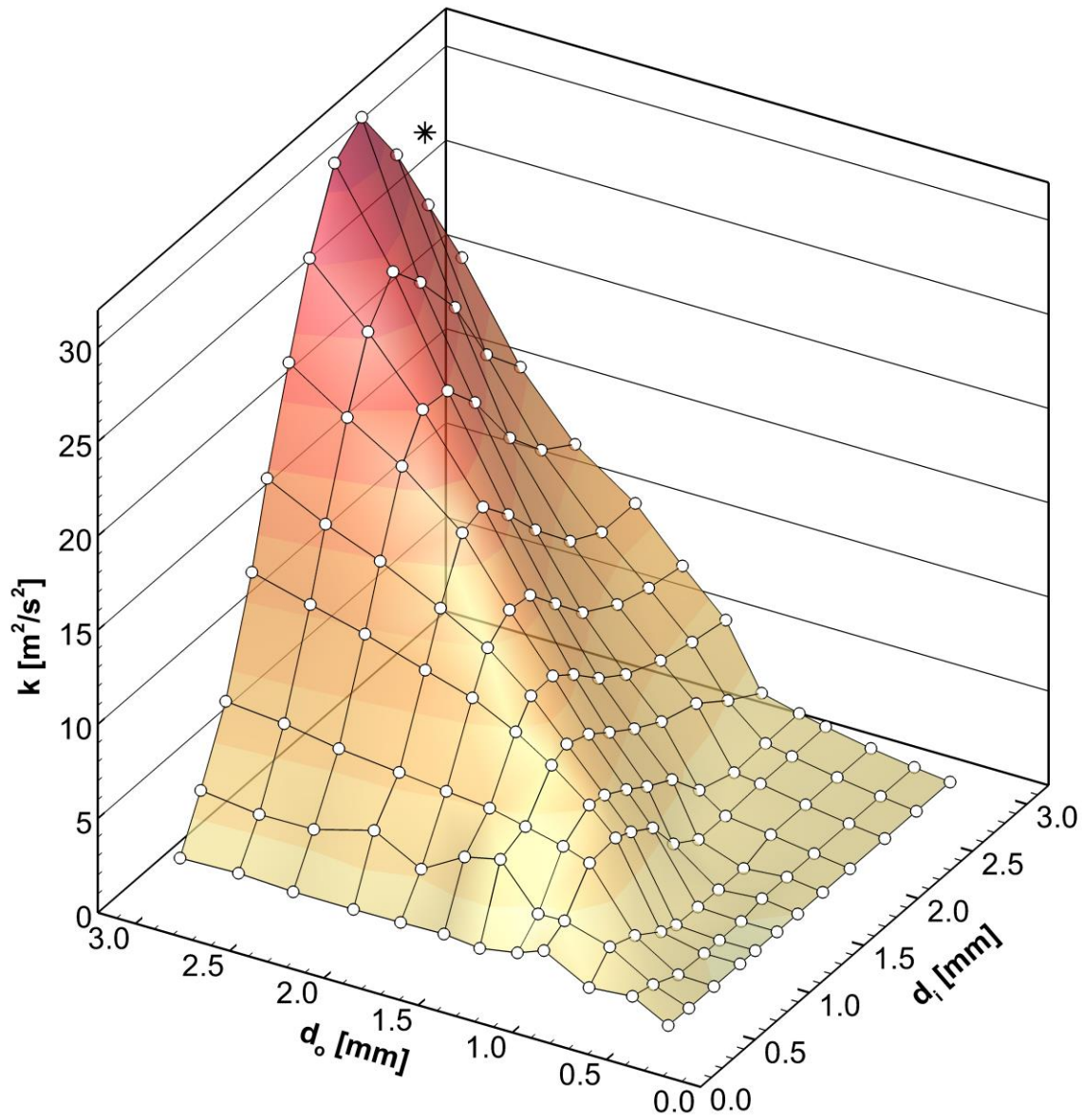
2 (□ in Figure 5.4).

Figure 5.8:   3D plot of CFD-predicted data points for turbulent kinetic energy (k) vs. inlet and outlet capillary diameter (d_i and d_o respectively). The MMAD dispersion parameter (shown in Figure 5.6) suggests smaller particles sizes are produced when k is small and inlet velocity (v_i) is high.
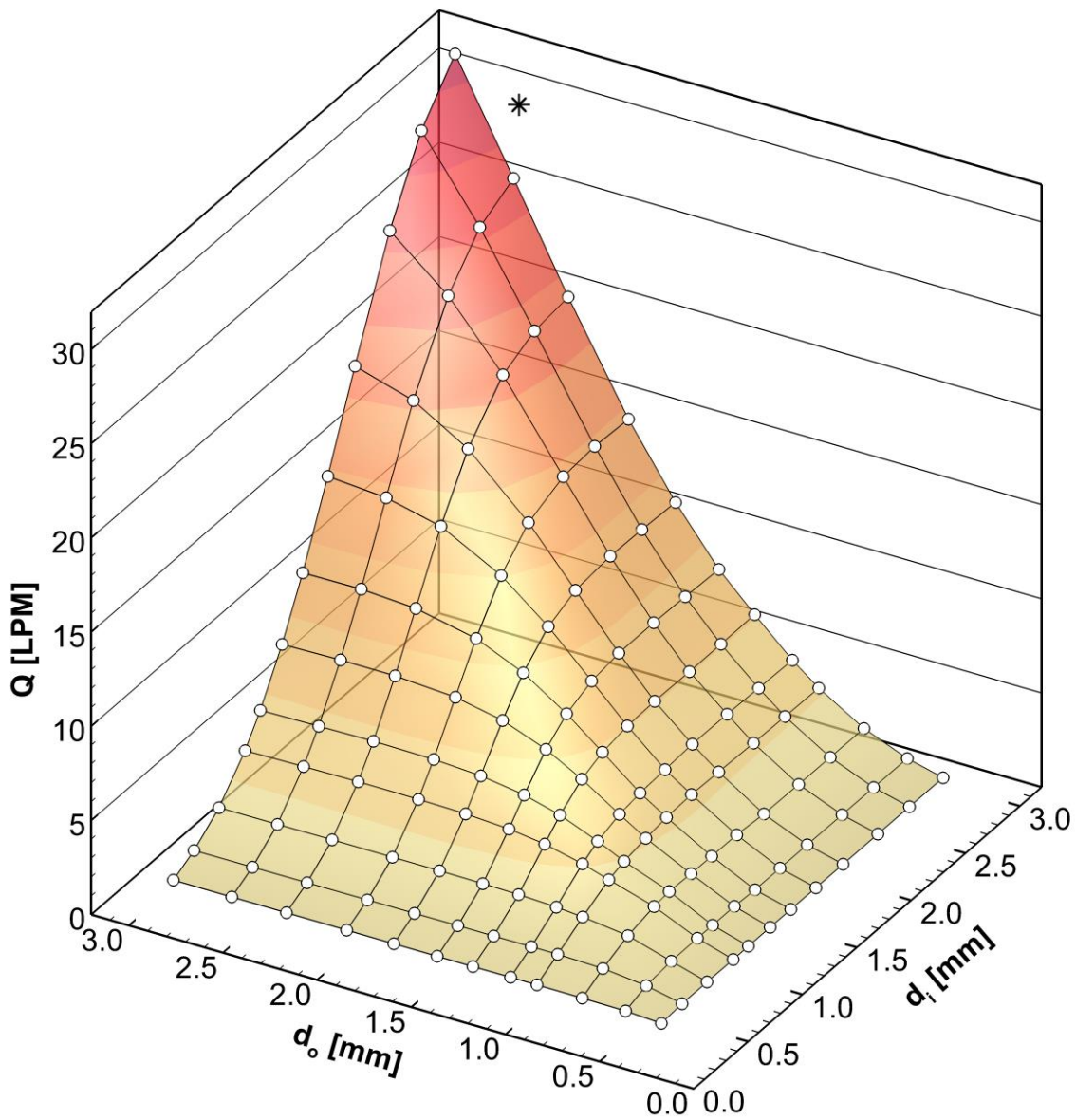
Figure 5.9: 3D plot of CFD-predicted data points for flow rate (Q) vs. inlet and outlet capillary diameter (d_i and d_o respectively). The ED dispersion parameter (shown in Figure 5.7) suggests emitted dose is improved when the flow rate is increased, but there is a limit given the administration of the devices to children.
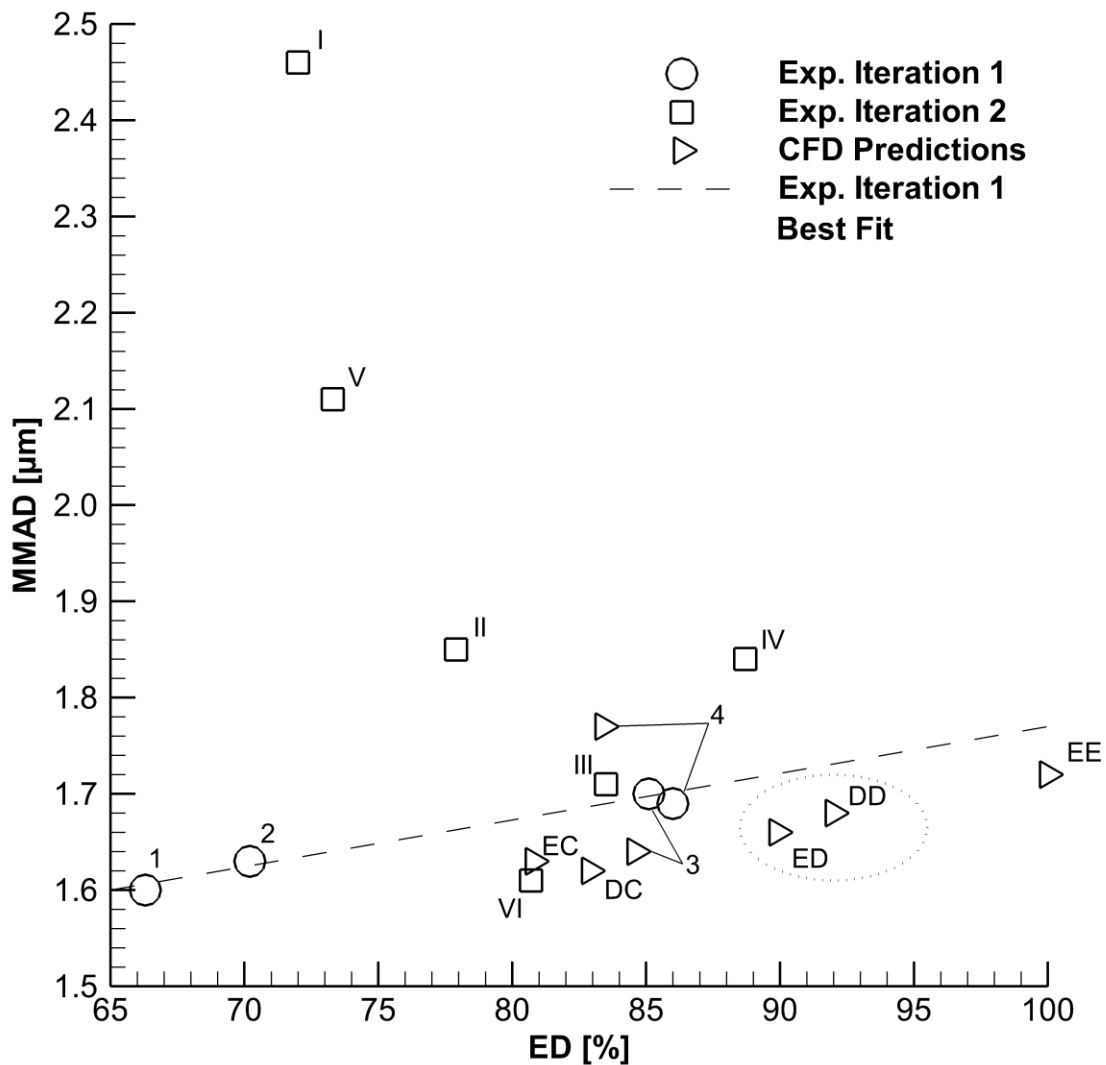
Figure 5.10: Addition of CFD predicted aerosolization performance to the MMAD vs. ED plot shown in Figure 5.4. Annotations correspond with the Markers in Table 5.4 and Table 5.6. The devices annotated with ED and DD are selected as the optimized devices as they have an ED prediction greater than 90%, better predicted MMAD than Case 4, and show improved device performance compared to Experimental Iteration 1.

5.7 Tables

Table 5.1: Summary of experimentally tested device configurations and operating conditions.

Name	di [mm]	do [mm]	Bypass	ΔP [kPa]	Q [LPM]	Notes
Experimental Iteration 1						
Case 1[a]	1.52	1.52	Yes	6.0	11.4	Bypass flow with same diameter inlet and outlet capillaries
Case 2[a]	1.40	1.80	Yes	6.0	11.6	Bypass flow with smaller inlet than outlet capillary
Case 3[a]	2.39	2.39	No	6.0	17.4	No bypass flow with same diameter inlet and outlet capillaries
Case 4[a]	1.83	2.39	No	6.0	13.3	No bypass flow with smaller inlet than outlet capillary, but same outlet as Case 3 (best performing case of Experimental Iteration 1)
Experimental Iteration 2						
Half Q	1.83	2.39	No	1.5	6.7	Pressure drop selected to give 50% of Case 4 flow rate
1.32/2.39	1.32	2.39	No	6.0	5.9	Inlet diameter selected to give 50% of Case 4 flow rate
1.60/2.39	1.60	2.39	No	6.0	9.9	Inlet diameter selected to give 75% of Case 4 flow rate
2.08/2.69	2.08	2.69	No	6.0	16.9	Similar outlet to inlet diameter ratio as Case 4
1.32/2.90	1.32	2.90	No	6.0	6.8	Same average capillary diameter as Case 4
3.00/2.08	3.00	2.08	No	6.0	15.5	Explores the effect of larger inlet compared to the outlet diameter

a: Results presented by Farkas et al. (2019)

Table 5.2: Summary of evaluated MMAD correlation parameters ranked in order of preference based on R^2 value.

Parameter	Units	Variables	Definitions	
$\dfrac{kd^*}{\Delta P v_i}$	$\left[\dfrac{\text{m}}{\text{Pa-s}}\right]$	$d^* = \dfrac{d_o}{d_i}$	k:	Turbulent kinetic energy
			d^*:	Non-dimensional length scale
			v_i:	Inlet capillary velocity
			ΔP:	Pressure drop across device
$\dfrac{\Delta P}{k^* d^*}$	[Pa]	$k^* = \dfrac{k}{v_i^2}$	k^*:	Non-dimensional k[a]
$\dfrac{k\mu}{v_i \Delta P d_o}$	$[-]$		μ:	Fluid velocity
$k^* \omega^* d^*$	$[-]$		ω^*:	Non-dimensional ω[a]
$\dfrac{v'd^*}{v_i \Delta P}$	$\left[\dfrac{1}{\text{Pa}}\right]$	$v' = \sqrt{2/3\,k}$	v':	Fluctuating velocity due to turbulence

a: Non-dimensional turbulence parameters presented by Longest and Farkas (2018)

Table 5.3:   Summary of evaluated ED correlation parameters ranked in order of preference based on R^2 value.

Parameter	Units	Variables	Definitions
$Q_i d^*$	[LPM]	$d^* = \dfrac{d_o}{d_i}$	Q_i: Volumetric flow rate through the inlet capillary
$Q_i k$	$\left[\dfrac{\text{m}^5}{\text{s}^3}\right]$		k: Turbulent kinetic energy
$Q_i d_o$	$\left[\dfrac{m^4}{s}\right]$		d_o: Outlet capillary diameter

Note: The R^2 value for correlation between emitted dose and Q_i alone is 0.7427, hence scaling by d^*, k, or d_o improves the strength of correlation to R^2>0.8

Table 5.4:   Summary of aerosolization performance for Experimental Iterations 1 and 2. Experimental values are given as means with standard deviations shown in parenthesis [n=3].

Name	d_i [mm]	d_o [mm]	MMAD [µm]	ED [%]	Marker
Experimental Iteration 1					
Case 1[a]	1.52	1.52	1.60 (0.16)	66.3 (3.1)	1
Case 2[a]	1.40	1.80	1.63 (0.06)	70.2 (1.7)	2
Case 3[a]	2.39	2.39	1.70 (0.18)	85.1 (8.8)	3
Case 4[a]	1.83	2.39	1.69 (0.01)	86.0 (1.4)	4
Experimental Iteration 2					
Half Q	1.83	2.39	2.46 (0.21)	72.0 (5.6)	I
1.32/2.39	1.32	2.39	1.85 (0.10)	77.9 (1.8)	II
1.60/2.39	1.60	2.39	1.71 (0.03)	83.5 (1.5)	III
2.08/2.69	2.08	2.69	1.84 (0.09)	88.7 (1.2)	IV
1.32/2.90	1.32	2.90	2.11 (0.09)	73.3 (1.2)	V
3.00/2.08	3.00	2.08	1.61 (0.08)	80.7 (5.9)	VI
a: Results presented by Farkas et al. (2019)					

Table 5.5: Summary of cases with inlet and outlet diameters greater than 1.83 mm, which are in the range of design configurations that are similar to Case 4. Cases shown are a sub-set of a full array of 144 CFD runs (all possible configurations of 12 different capillary sizes).

d_i [mm]	d_o [mm]	CFD MMAD [μm]	CFD ED [%]	Marker
1.83	1.83	1.58	72.8	AA
	2.08	1.65	77.6	AB
	2.39	1.77	83.4	4[a]
	2.69	1.92	87.7	AD
	3.00	2.10	91.5	AE
2.08	1.83	1.55	71.9	BA
	2.08	1.61	77.5	BB
	2.39	1.71	84.9	BC
	2.69	1.82	91.0	BD
	3.00	2.03	96.5	BE
2.39	1.83	1.55	70.5	CA
	2.08	1.58	76.1	CB
	2.39	1.64	84.6	3[b]
	2.69	1.75	92.7	CD
	3.00	1.88	100.0[d]	CE
2.69	1.83	1.56	69.2	DA
	2.08	1.59	74.4	DB
	2.39	1.62	82.9	DC
	2.69	1.68	92.0	DD[c]
	3.00	1.79	100.0[d]	DE
3.00	1.83	1.58	68.1	EA
	2.08	1.62	72.7	EB
	2.39	1.63	80.8	EC
	2.69	1.66	89.9	ED[c]
	3.00	1.72	100.0[d]	EE

Markers highlighted with light grey have CFD-predicted MMAD and ED that plot below Experimental Iteration 1 Best Fit, and *vice versa* for the dark grey markers.

a: Same inlet and outlet configuration as Case 4
b: Same inlet and outlet configuration as Case 3
c: Candidate configurations selected for optimized design experimental evaluation
d: Cases where the correlations predicted greater than 100% ED were capped at 100%

Table 5.6:   Summary of CFD-predicted ED and MMAD compared to the estimated MMAD based on Experimental Iteration 1 Best Fit. Cases shown are those that the CFD predicts will perform better than Case 4 based on the data in Table 5.5.

d_i [mm]	d_o [mm]	CFD ED [%]	CFD MMAD [μm]	Estimated MMAD [μm]	Relative Δ [%]	Markers
2.69	2.39	82.9	1.62	1.68	-3.89	DD
	2.69	92.0	1.68	1.73	-2.72[a]	DE
3.00	2.39	80.8	1.63	1.67	-2.65	EC
	2.69	89.9	1.66	1.72	-3.36[a]	ED
	3.00	100.0	1.72	1.76	-2.51	EE

Relative Δ is the relative difference between the CFD-predicted MMAD and the Estimated MMAD based on Experimental Iteration 1 Best Fit.

a: Candidate configurations selected for optimized design experimental evaluation

Table 5.7: Summary of relative difference (RD) between the CFD-predicted (CFD) and experimental (Exp.) MMAD and ED. The data shows how accurately the CFD and dispersion parameter correlations predicted experimental aerosolization performance. Experimental values are given as means with standard deviations shown in parenthesis [n=3].

Name	d_i [mm]	d_o [mm]	MMAD CFD [μm]	MMAD Exp. [μm]	MMAD RD [%]	ED CFD [%]	ED Exp. [%]	ED RD [%]	Marker
Experimental Iteration 1									
Case 1	1.52	1.52	1.53	1.60 (0.16)	4.2	67.9	66.3 (3.1)	2.3	1
Case 2	1.40	1.80	1.63	1.63 (0.06)	0.2	71.3	70.2 (1.7)	1.6	2
Case 3	2.39	2.39	1.65	1.70 (0.18)	2.9	84.3	85.1 (8.8)	0.9	3
Case 4	1.83	2.39	1.77	1.69 (0.01)	4.8	83.1	86.0 (1.4)	3.4	4
Experimental Iteration 2									
Half Q	1.83	2.39	2.44	2.46 (0.21)	1.0	70.5	72.0 (5.6)	2.1	I
1.32/2.39	1.32	2.39	1.83	1.85 (0.10)	0.9	75.7	77.9 (1.8)	2.9	II
1.60/2.39	1.60	2.39	1.82	1.71 (0.03)	6.5	80.3	83.5 (1.5)	3.8	III
2.08/2.69	2.08	2.69	1.84	1.84 (0.09)	0.0	90.9	88.7 (1.2)	2.5	IV
1.32/2.90	1.32	2.90	2.08	2.11 (0.09)	1.6	78.9	73.3 (1.2)	7.7	V
3.00/2.08	3.00	2.08	1.62	1.61 (0.08)	0.5	72.8	80.7 (5.9)	9.8	VI
Optimized Devices									
2.69/2.69	2.69	2.69	1.68	1.55 (0.13)	8.4	92.0	90.4 (2.8)	1.8	DD
3.00/2.69	3.00	2.69	1.66	1.59 (0.05)	4.4	89.9	92.3 (0.2)	2.6	ED

Chapter 6: Develop Dry Powder Inhaler Patient Interfaces for Improved Aerosol Delivery to Children

6.1 Objective

The objective of this study was to explore different internal flow pathways for a pediatric air-jet DPI interface that minimize device and ET depositional loss using validated CFD methods. The design space was constrained to an internal flow pathway less than 75 mm in length to provide a compact and portable device, and preference was given to design concepts that are easy to manufacture and construct. The performance target was total CFD-predicted losses in the flow pathway and ET region of less than 15% for a pediatric subject. Combining this target with approximately 10% device loss from Farkas et al. (2019) results in an expected lung dose of greater than approximately 75% of loaded dose. Validated CFD models were used to evaluate several design iterations that aimed to screen candidate design concepts until the performance targets were met. A leading design concept explored in this study was the use of a 3D rod array, previously designed to maximize aerosol deaggregation (Behara, Longest, et al., 2014a, 2014b; Longest et al., 2015; Longest, Son, et al., 2013), to attenuate the high-velocity air jet that leaves the DPI and thereby reduce depositional losses in the interface and ET regions.

6.2 Introduction

Delivery of pharmaceutical aerosols to the lungs typically requires a nebulizer, metered dose inhaler (MDI), or dry powder inhaler (DPI). For the treatment of lung infections in pediatric patients with cystic fibrosis (CF), tobramycin inhaled powder via a DPI can be administered to potentially eradicate bacterial colonies. DPIs provide several advantages, compared with using tobramycin inhaled solution in a nebulizer, as higher

doses of the antibiotic can be delivered faster and the devices are easier to load and clean (Somayaji & Parkins, 2015). However, DPIs are associated with several disadvantages including poor lung delivery efficiencies, especially in children, as well as requiring inhalation maneuvers that may be difficult for children to achieve. For DPI use in children with oral inhalation, Below et al. (2013) reported 5% and 22% of nominal dose was deposited on a tracheal filter in *in vitro* experiments when testing the Novolizer and Easyhaler, respectively. Similarly, Lindert et al. (2014) reported 9% to 11% lung delivery efficiency when testing the Cyclohaler, HandiHaler, and Spinhaler with pediatric *in vitro* conditions. These devices were developed for use by adults, not the pediatric patients that are the focus of this study, and the poor delivery performance may be attributed to insufficient inhalation flow rates to correctly empty the inhaler and deaggregate the powder. Inhalation flow rate and other device design considerations were considered in two studies by Lexmond et al. (2017; 2014), who concluded that it is of paramount importance to design devices specifically for children when developing DPIs and pediatric delivery systems.

Our group has recently published several studies related to the ongoing development of a pediatric DPI for the delivery of tobramycin, as a spray-dried excipient enhanced growth (EEG) formulation, to children with CF (Bass, Farkas, et al., 2019; Bass & Longest, 2018b; Farkas et al., 2019; Longest et al., 2019). The full delivery system includes a ventilation bag, inline air-jet DPI, and patient interface, which is described in detail by Farkas et al. (2019), and is designed to be as compact and portable as possible. The ventilation bag provides a positive pressure gas source to actuate the device with approximately 750 mL of air for a five-year-old child, which allows for oral or nasal

administration and inhibits exhalation by the patient in the reverse direction through the device. The air-jet DPI is composed of small diameter inlet and outlet capillaries that penetrate a capsule-shaped powder chamber. The inlet capillary provides a high-velocity, compressible, and turbulent air jet to the chamber that aerosolizes the powder and delivers the aerosol to the patient interface via the outlet capillary. Bass et al. (2019) presented an optimized inlet and outlet capillary configuration that maximized aerosolization performance in terms of high emitted dose (ED) and low particle size, which was quantified by the mass-median aerodynamic diameter (MMAD) of the aerosol.

The present study builds upon the experimental work by Farkas et al. (2019), which presented an evaluation of losses in the mouthpiece (MP) and mouth-throat (MT) for oral administration, and nasal cannula (NC) and nose-throat (NT) for nasal administration. The Farkas et al. study (2019) actuated the high-efficiency pediatric air-jet DPI with a inhalation volume for 750 mL, for a 5-6 year old subject, and with a 6 kPa pressure drop, which is consistent with hand actuation of a small ventilation bag. The device was loaded with 10 mg of EEG albuterol sulfate (AS) as a surrogate test formulation (in place of tobramycin powder) and was actuated in connection with either *in vitro* 5-year-old MT or NT models to test MP or NC patient interfaces, respectively. The best-case DPI and MP combination for oral administration resulted in 21.8% device loss, 4.6% interface loss, and 6.6% MT loss, which produced an estimated lung dose of 63.8% on the tracheal filter (96.8% recovery). The best-case DPI and NC combination for nose-to-lung (N2L) delivery resulted in 21.9% device loss, 6.1% interface loss, and 8.3% NT loss, which resulted in an estimated lung dose of 60.7% on the tracheal filter (97.1% recovery). The current study aims to develop the MP and NC further to reduce interface and extrathoracic (ET) losses

232

for oral and nasal administration by utilizing computational fluid dynamics (CFD) based analysis of various design concepts.

The primary disadvantage of the air-jet DPI is that the high-velocity turbulent jet (which efficiently aerosolizes the powder) leads to losses when it leaves the device and enters the patient interface and ET regions (MT or NT). The high velocity of the jet from the outlet capillary imparts a large amount of momentum to the particles, which in turn causes a large amount of impaction deposition downstream of the device. This was clearly apparent from the impaction of the aerosol on the back of the MT model that was observed by Farkas et al. (2019). The jet also tends to attach to the walls of the patient interface, due to the Coanda effect, which directs the aerosol towards deposition surfaces instead of traversing the MP or NC. As such, the flow pathway of the patient interface (MP or NC) should be engineered to dissipate the intensity of the jet to minimize system losses. Previous examples of this type of patient interface optimization include improvements in mouthpiece performance of a capillary aerosol generator (Hindle & Longest, 2013), the use of co-flow spacers with low actuation-air-volume DPIs (Farkas, Hindle, & Longest, 2018a; Farkas et al., 2018b), and multiple design improvements to a mouthpiece coupled to the Aerolizer DPI (Coates et al., 2007; Coates et al., 2004).

6.3 Methods

Overview and System Setup

An overview of the flow passages for the pediatric air-jet DPI system is shown in Figure 6.1 for both oral and nasal aerosol administration. The air-jet DPI consists of an inlet orifice flow passage, aerosolization chamber, outlet orifice flow passage, and smooth expansion. The inlet and outlet orifice flow passages are frequently constructed with

233

hollow metal capillaries and are therefore often referred to as inlet and outlet capillaries. As described by Farkas et al. (2019) the air-jet DPI orients the inlet and outlet capillaries along the long axis of the aerosolization chamber and does not include bypass flow (straight through design). The air-jet DPI is connected to the ET model (MT or NT) through the patient interface. For pediatric aerosol delivery conditions and the straight-through air-jet DPI design, Bass et al. (2019) previously optmized the air-jet DPI design parameters to maximize aerosolization performance. In the current study, the patient interface region is evaluated and optmized to reduce both interface and ET depositional losses. As desribed, a major source of this aerosol loss arises from the high-speed turbulent air jet that enters the patient and ET region from the air-jet DPI outlet capillary. For this reason, the outlet capillary and expansion region are in the pediatric interface models. The fundamental question of this study is then how to design the patient interface for oral or N2L aerosol adminstration that can attenuate a high-speed turbulent air jet while also reducing deposition losses. Considering the interface, potential designs are illustrated in Figure 6.2 based on an axial cross-section and plane of symmetry. Potential design ideas include internal geometry control, wall surface characteristics, and internal flow structures, such as the 3D rod array. Wall geoemtries are intended to either avoid boundray layer separation (gradual expansion) or rapidly move the wall away from the expanding jet (rapid expansion). A rough wall surface is included to improve boundary layer attachment (via boundary layer "tripping"). Internal flow structures are intended to quickly dissipate the turbulent jet with minimal particle depositional loss. Further details of each patient interface design concept are presented later in this study.

Farkas et al. (2019) presented the initial experimental evaluation of two MP designs and three different NCs, as part of the development of an air-jet DPI for pediatric administration of tobramycin. The regional losses for the best-case MP and NC, given as ratios of deposited mass to the emitted dose from the device, are given in Table 6.1. The present study aims to evaluate multiple MP and NC design concepts for use with the same air-jet DPI via CFD predictions of patient interface and ET losses. The CFD models were first validated against the experimental data for the best-case MP and NC from the Farkas et al. study (2019) to ensure the applied methods produce accurate results. The validated CFD models were then used to establish correlations for predicting downstream losses using the outlet flow conditions of the patient interface. Using CFD models and the deposition correlations, numerous design concepts of the MP were evaluated with a focus on minimizing losses in the patient interface and MT model. Best performing design concepts were then assessed in a full model consisting of the chosen MP design and the pediatric MT geometry as a final evaluation of performance improvements. Finally, the same lead design concepts were applied to the NC for N2L delivery, and these designs were also tested in full CFD models of the interface and pediatric NT geometry.

Evaluation Process

To achieve the study objective, the process outlined by the flow diagram in Figure 6.3 was employed to evaluate numerous design concepts and assess the performance improvements of candidate patient interfaces. The primary aims of the evaluation process were to establish CFD-based predictive metrics for estimating the interface and ET depositional losses associated with each design concept and to improve device performance in terms of reducing these losses.

235

As with all numerical models, the computational results must be validated against experimental data to ensure accuracy (Figure 6.3). In the present study, the CFD models for oral and nasal administration were validated against the experimental data presented by Farkas et al. (2019) for their best case patient interfaces. Regional deposition efficiency (DE) in the patient interface (MP or NC) and extrathoracic regions (MT or NT) were compared between the CFD models and experimental data. Initially, meshing and solver parameters adhered to the recommendations from our previous work (Bass, Boc, et al., 2019; Bass & Longest, 2018b; Longest et al., 2007) and adjustments were made due to the specific requirements of this investigation, which are described in detail in subsequent sections. Validation focused on maximizing model accuracy with the MP-MT model, as it was used to screen the design concepts. Once model settings were established for the validated MP-MT model, they were not adjusted for subsequent models to ensure consistency between all cases considered.

With the model validation complete, the metrics to predict losses up to the first impaction point from CFD flow field quantities were developed (Figure 6.3). This required correlation of the chosen metrics with CFD-predicted DEs in the region of interest to determine the strength of the metric for estimating interface performance. The intention of this approach is to model the patient interface flow pathway independently from the rest of the geometry to reduce processing times and increase the turnaround on screening design concepts. That is, evaluation of flow field quantities from a CFD model of only the MP or NC pathway can be used to predict depositional losses in the remainder of the geometry, which combined with CFD predictions of deposition in the patient interface can be used to efficiently determine performance improvements. Next, models

236

of design concepts were developed and screened using CFD predictions of interface losses and the aforementioned deposition metrics (Figure 6.3). Three design screen iterations were required to minimize system losses, with each iteration using insight from the last to improve performance and optimize the design (Figure 6.3).

Finally, four MP designs from the screening stage were selected for testing in a full CFD model of the chosen interface coupled with the MT airway (Figure 6.3). Here the performance of each design is evaluated with CFD-predictions of losses in both the MP and MT regions. Therefore, any inaccuracies that the deposition metrics may have in estimating losses in the MT are removed. The selected design concepts are then applied to the NC, and the combined NC-NT models are tested with full CFD models to assess the performance improvement for nasal administration. From the final four selected design concepts, the best performing patient interfaces for oral and nasal administration were identified based on CFD predictions of patient interface and ET losses. These best-case designs will be experimentally tested to verify the performance improvements in a future study.

CFD Models

Computational Domains and Spatial Discretization

The MT and NT models used in the original experimental work (Farkas et al., 2019) were the scaled 5-6 year old VCU MT geometry (R. Delvadia et al., 2012; Wei et al., 2018), and the realistic pediatric NT geometry from the RDD Online website (www.rddonline.com), respectively. These models were selected for the experimental study as their geometric characteristics were consistent with the 5-6-year-old age group (Farkas et al., 2019) considered by the device design process. The computational

geometry was created by importing these ET airways into SolidWorks 2018 (Dassault Systèmes, Paris, France), and using its 3D modelling capabilities to combine the MT or NT models with either the MP or NC patient interface, respectively. To maintain consistency between the experimental and computational models, the NC prongs were inserted 5 mm into the NT model and surfaces near the prong outlets were modified to provide an airtight seal between the NC and nostrils. As such, there is no flow through the nostrils around the prongs, as the device is designed to provide the full inhalation volume to the subject during actuation. Similarly, the MP is centrally located within the inlet to the MT model with an airtight seal, which is consistent with the patient's lips surrounding the MP during actuation. 3D models were transferred to SpaceClaim v19.0 (ANSYS Inc., Canonsburg, PA) where surface preparation and minor geometry simplifications were made to facilitate the CFD meshing process, such as the removal of small area faces, filleting sharp edges, and the addition of numerical extensions.

Mesh generation (i.e. the volume discretization of the computational domain) was performed by using the meshing capabilities available in FLUENT v19.0 (ANSYS Inc., Canonsburg, PA). Due to the complexity of the geometries that include rod arrays, an unstructured meshing approach was taken to accurately resolve the complex model surfaces. Polyhedral cell topology, with prismatic near-wall (NW) cell layers, were utilized throughout the patient interface and ET region in all models, as we have previously shown that these types of cells are more computationally efficient than traditional tetrahedral cells and provide accurate deposition results (Bass, Boc, et al., 2019). The NW mesh resolution, which is critical to obtaining accurate CFD predictions of particle deposition, was consistent with our previously established best practices (Bass & Longest, 2018b),

which includes a wall y⁺ value of approximately one, five prismatic NW layers, and layer-to-layer growth ratio of 1.2. Final evaluation of all meshes ensured the orthogonal quality metric was greater than 0.25, with cell nodes smoothed until this threshold was achieved, which ensures a high-quality volume discretization.

Mesh independence was established for the MT and NT validation cases using the Roache method for grid refinement studies (Roache, 1994) by evaluating volume-averaged velocity magnitude (v_{mag}) and turbulent kinetic energy (k) between successively higher resolution meshes. Throughout the mesh independence study, solutions were checked to ensure they were within the asymptotic range of convergence for which the Roache method is valid. For the MT model, three meshes with approximately 0.5-, 1.0-, and 2.0-million cells were evaluated, which gave normalized grid spacing ratios of 1.60, 1.32, and 1.00, respectively. Between the 2.0- and 1.0-million cell cases, the grid convergence index (GCI) for v_{mag} and k was 0.07% and 1.54% respectively, which suggests the estimated error from the 1.0-million cell case was low and acceptable for use with this study. For the NT model, higher resolution meshes compared to the MT model were required due to the increased model complexity, with meshes using approximately 1.0-, 2.0-, and 4.0-million cells, which gave normalized grid spacing ratios of 1.58, 1.25, and 1.00, respectively. Between the 4.0- and 2.0-million cell cases, the GCI for v_{mag} and k was <0.001% and 8.75%, respectively. Ideally, the GCI for k in the NT model would be less than 5%, but given that v_{mag} shows a very low estimated error and particle trajectories in the micro-meter size range are more heavily influenced by the velocity field than the turbulence field, the 2.0-million cell case was deemed acceptable. A lower cell count is also preferred, as the transient solver was required (discussed in

subsequent sections), which drastically increased computational expense. As a final check of the selected mesh resolutions, Richardson Extrapolation (Richardson & Gaunt, 1927) was used to estimate the exact solution of each field quantity. The absolute differences between the selected meshes and the estimated exact solution was negligible in all cases, with values of -0.01 m/s and -0.09 m^2/s^2 for v_{mag} and k in the MT model, -0.001 m/s and -0.22 m^2/s^2 for v_{mag} and k in the NT model. Subsequent meshes used in the evaluation of new patient interface designs use similar cell sizes to these validation cases, as opposed to similar cell counts, to ensure the spatial resolution is consistent between models.

Numerical Modeling and Solver Settings

The Mach and Reynolds numbers at the inlet to the patient interface, given a flow rate of 13.3 LPM and inlet capillary diameter of 2.39 mm (Farkas et al., 2019), are 0.14 and 5,200 respectively, which suggest incompressible and transitional-to-turbulent flow conditions. As such, a constant density for the fluid phase was implemented, in contrast to the ideal gas law in previous studies (Bass, Farkas, et al., 2019; Bass & Longest, 2018b; Longest et al., 2019), which had a much smaller inlet jet diameter, as the Mach number is far below the critical value of 0.3 for compressible flow. To model the transitional-to-turbulent flow regime, the low-Reynolds number (LRN) k-ω turbulence model was used, which has been validated by our group for both the evaluation of DPI performance (Longest, Son, et al., 2013) and particle transport through ET airways (Bass, Boc, et al., 2019; Bass & Longest, 2018b; Longest et al., 2007) for adults and children. The formulation of the LRN correction to the k-ω model includes an eddy viscosity damping coefficient that scales from zero to one in regions of low or high turbulence,

which improves solution accuracy outside and inside the highly turbulent jet. Considering the inlet jet, shear flow corrections were applied to model the shear layer between the high-velocity jet and relatively quiescent flow in the patient interface.

Using a steady-state solution approach, preliminary work on the validation cases showed the inlet jet would attach to the wall of the patient interface and move around the domain with erratic behavior, which prevented convergence of the transport equations. Therefore, a transient formulation of the transport equations was implemented to model the transient nature of the inlet jet development. The flow was initialized with quiescent conditions and the boundary conditions at the inlet caused the jet to propagate into the patient interface. As with the preliminary work, the jet attaches to the walls and wanders unpredictably in all cases considered, due to the Coanda effect. The transient solution approach used a time step of 1e-3 seconds, which gave good flow field convergence within 100 iterations per time step, and sufficiently resolved the inlet jet behavior. Also, during preliminary work, observation of regional DE vs. time plots showed that the total and regional deposition converged to a single value within 0.45 seconds, which determined the maximum required simulation time, as an alternative to modeling the full actuation time of 3 seconds. These transient solver settings and the mesh independent spatial discretization resulted in processing times of between 24 and 72 hours (on 10 CPUs) depending on the cell count. This demonstrates the advantage of using the computationally efficient and accurate LRN k-ω model, as more detailed turbulence models with transient flow would drastically increase processing times.

FLUENT v19.0 (ANSYS Inc., Canonsburg, PA) was used to obtain solutions for all flow and turbulence equations, including the aforementioned sub-models and corrections.

As with the mesh generation step, all solver settings followed our recommendations for modeling particle transport in DPIs and the respiratory airways (Bass, Boc, et al., 2019; Bass & Longest, 2018b). Specifically, the Green-Gauss Node-based method for gradient discretization, which combined with the NW mesh resolution requirements mentioned previously, provide an improvement in grid independence in the NW region, and improved consistency and accuracy in particle deposition data. The spatial discretization of flow and turbulence equations were second-order accurate, while the standard pressure interpolation scheme was used. Convective terms used a second-order upwind scheme and diffusion terms used central difference. Further details on the mass, momentum, and turbulence transport equations are available in other publications (Longest et al., 2007; Longest et al., 2006).

A mass flow inlet condition was utilized at the inlet flow boundary to the patient interface, with a mass flow rate that gave a volumetric flow rate of 13.3 LPM, which is consistent with the volumetric flow rate through the Case 4 DPI presented by Farkas et al. (2019). A 10 mm length of the device outlet capillary (inlet to the patient interface) was included in the model to allow the flow to reach a fully-developed state before entering the MP or NC. A pressure outlet condition was used at the outlet of the ET airway model, with gauge pressure (relative to ambient pressure) set to 0 kPa. To minimize the influence of the pressure outlet on the flow field in the ET models, a 60 mm numerical extension was added to the outlet in the CFD domain. All wall boundaries in the CFD model use the no slip shear condition and the effects of surface roughness on the flow field and particle trajectories were neglected. Wall boundaries of the 3D-printed components used the trap discrete phase model (DPM) boundary condition such that any particle that contacts these

242

walls is assumed to deposit on the boundary. Wall boundaries of stainless-steel components used the reflect DPM boundary condition, with default coefficients of restitution, which assumes particles bounce off of these surfaces. This is a necessary assumption about particle behavior when the aerosol interacts with the rod array to keep processing times manageable, which has previously been shown to be acceptable (Longest et al., 2015; Longest, Son, et al., 2013).

Particle Trajectories and Deposition Calculations

Particle trajectories were calculated with the DPM available in FLUENT v19.0 (ANSYS Inc., Canonsburg, PA), with the Runge-Kutta scheme used to integrate the particle equations of motion, which is dependent on the underlying flow and turbulence field quantities. Settings for the DPM follow our best practices (Bass, Boc, et al., 2019; Bass & Longest, 2018b; Longest & Xi, 2007; Walenga & Longest, 2016), which have been successfully validated against experimental deposition data. Microparticle trajectory calculations with the DPM and LRN k-ω turbulence approximation generally over-predict deposition when compared to experimental data, due to the assumption of isotropic NW turbulence and the associated fluctuating velocity components. As such, Longest and Xi (2007) proposed corrections to the NW flow and turbulence fields extending work by Matida et al. (2004) and Wang and James (1999), which are implemented in FLUENT via user-defined functions (UDFs). In summary, the NW corrections interpolate the velocity field from the cell centroid to the particle location, implement anisotropic fluctuating velocity components, and damp the wall-normal velocity to approximate particle-wall hydrodynamic interactions. These NW corrections use a NW limit control parameter that determines the wall-normal distance, below which, the wall-normal velocity is damped.

Previous validation work (Bass, Boc, et al., 2019; Bass & Longest, 2018b) showed that a NW limit of 1-2 μm was suitable for modeling microparticle deposition in the upper airways, with a value of 2 μm used in the present study.

Particles were introduced into the model at the inlet to the air-jet DPI outlet capillary (i.e. the inlet to the CFD domain) with a blunt spatial distribution, as the inlet Reynolds number suggests the flow is in the transitional to turbulent regime. Initial particle velocities also followed a blunt profile based on each particle's radial location relative to the circular boundary. A polydisperse aerosol was used in the CFD models, with the particle size distribution determined by next-generation impactor (NGI) characterization at the Case 4 device outlet presented by Farkas et al. (2019). Particle deposition convergence was ensured by following the recommendations from Tian et al. (2015) with 100 particles per bin per time step, which resulted in 360,000 total particles (considering eight NGI bins and 450 time steps).

Regional particle deposition in the device, interfaces, and ET models are compared via DE, which is the ratio of particles that deposit in a given region to number of particles that enter that region. To convert the DE from the CFD models (with a constant number of particles per bin) to a DE that is consistent with the experimentally determined particle size distribution, the CFD-predicted DE for each NGI bin is multiplied by the mass fraction of particles for each bin, and then summed over all bins. This is defined as:

$$\mathrm{DE}_i = \frac{n_i}{N_i} \tag{6.3.1}$$

$$\varphi_i = \frac{m_i}{M} \tag{6.3.2}$$

$$\mathrm{DE}_r = \sum_{i=1}^{8} DE_i \times \varphi_i \tag{6.3.3}$$

where n_i is the number of particles that deposit in the region for bin i, N_i is the number of particles the enter the region for bin i, DE_i is the DE for bin i, m_i is the mass of particles from the NGI characterization for bin i, M is the total aerosol mass, φ_i is the mass fraction for bin i, and DE_r is the DE for a given region. To determine the mass or number of particles that enter the region, the mass or number of particles that deposit in upstream regions is subtracted from the injected aerosol conditions. Finally, the total deposition fraction (DF) for the entire domain, which is the ratio of particles that deposit in the domain to the particles that enter the domain, can be calculated from the regional DE as follows:

$$\mathrm{DF}_{Tot} = 1 - \prod (1 - DF_r) \tag{6.3.4}$$

Deposition Metrics

In an effort to reduce the computational cost associated with evaluating numerous patient interfaces, CFD-based deposition metrics that are capable of predicting deposition losses were sought. The intention being that only the interface flow pathway would have to be modeled with CFD, and the flow field at its outlet could be evaluated to predict downstream losses. For both the MP-MT and NC-NT models, the patient interface accounted for approximately 25% of the total cell count, thus reducing processing times by a factor of four-fold, which vastly improved the turn-around time on design candidate evaluations. Candidate designs that exhibit reductions in interface and ET losses with this approach were then fully evaluated via CFD models of the improved interface coupled to the ET model in the final stage of this study. That is, numerous design concepts can be

screened in a reduced amount of time before testing candidate interfaces via a full CFD model and evaluating performance improvements.

Figure 6.4a and b show the separation of the MP flow pathway from the MT, and Figure 6.4c and d show the separation of the NC flow pathway from the cannula bifurcation and NT. The NC was split just upstream of the bifurcation as the objective of the study was to evaluate interface designs that reduce the losses associated with the high-velocity jet from the device outlet, and preliminary work showed that losses in the NT region were not affected by changes to the jet intensity. That is, reducing the intensity of the inlet jet to the NC did not reduce ET losses, but deposition on the bifurcation was reduced, which suggests the potential for improvements in interface losses. Put another way, the inlet jet causes impaction deposition on the first surface that it encounters when it leaves the device outlet capillary. In the MP-MT model, this impaction surface is the back of the mouth-throat and the model is split between the MP and MT regions. In the NC-NT model, this impaction surface is the NC bifurcation and the model is split between these two regions.

ET deposition metrics were evaluated by applying four different velocity profiles to the MT and NT models at the inlets labeled in Figure 6.4b and d, respectively. These four velocity profiles were named the Jet (u_{Jet}), Turbulent (u_{Turb}), Laminar (u_{Lam}), and Intermediate (u_{Int}) profiles, and are plotted graphically in Figure 6.5a. The functions that define each profile are:

$$u_{\text{Jet}} = u_{\text{max}} \times \exp\left[-\frac{(r/R)^2}{2\sigma^2}\right] \tag{6.3.5}$$

$$u_{\text{Turb}} = u_{\text{max}} \times \left(1 - \frac{r}{R}\right)^{1/7} \tag{6.3.6}$$

$$u_{\text{Lam}} = u_{\text{max}} \times \left(1 - \left(\frac{r}{R} \right)^2 \right) \qquad (6.3.7)$$

$$u_{\text{Int}} = \frac{u_{\text{Jet}} + u_{\text{Turb}}}{2} \qquad (6.3.8)$$

where u_{max} is the peak velocity, r is the radial location on the inlet boundary, and R is the maximum radius of the inlet boundary. Using the r/R definition for the radial location on the inlet boundary simplified the conversion from circular to elliptical coordinates for the inlet to the MT model. The u_{Jet} profile uses a Gaussian function to define the jet-type profile seen in Figure 6.5a, with u_{max} determined from time-averaged peak velocity from the oral and nasal validation cases and σ selected to provide a volumetric flow rate of 13.3 LPM consistent with the Case 4 DPI (Farkas et al., 2019). The u_{Turb} profile uses the 1/7$^{\text{th}}$ power law for a turbulent profile (White, 2006); the u_{Lam} profile uses the analytical solution for laminar flow; and the u_{Int} profile is simply the average of the u_{Jet} and u_{Turb} profiles. The purpose of these velocity profiles is to evaluate how the ET losses are affected as the jet intensity is reduced from a profile such as u_{Jet} through an intermediate range (u_{Int}) to a full reduction of jet intensity with the u_{Turb} and u_{Lam} profiles for turbulent and laminar flow regimes.

As the velocity profile changes, the spatial distribution of the particles that are introduced to the computational domain must reflect the inlet conditions, as higher velocities will carry in more particles. For example, a velocity profile such as u_{Jet} would give a particle distribution that is more concentrated towards the middle of the inlet, whereas a profile such as u_{Turb} would give a more even distribution of particles. To determine the spatial distribution, each profile was treated as a probability density function (PDF) and split into 32 equally spaced rings, with particles randomly assigned to each

ring based on the PDF. This method of defining particle spatial distributions is similar to that described by Longest and Vinchurkar (2007a), but applied to the four profiles used to evaluate ET deposition metrics. The resulting spatial particle distribution for each MT of NC inlet velocity profile is shown in Figure 6.5b.

Observations from the experimental work presented by Farkas et al. (2019) demonstrated a large amount of deposition on the back of the throat in the pediatric MT model. Therefore, initial work on predicting ET loss aimed to describe the intensity of the jet as it enters the MT or NT model. Specifically, these metrics were the peak velocity, velocity spread, and uniformity index, which were all evaluated on the plane between the patient interface and ET region. Peak velocity is simply the time-averaged maximum velocity on the sampling plane, velocity spread is the standard deviation of velocity on the plane, and uniformity index (UI) is given as:

$$\text{UI} = 1 - \left(\frac{\sum_{i=1}^{N}(|u_i - \bar{u}| \times A_i)}{2 \times \bar{u} \times A} \right) \tag{6.3.9}$$

where u_i is the velocity on face i, $\bar{u}$ is the area-average velocity, A_i is the area of face i, and A is the total plane area. A UI with a value close to one describes a uniform flow velocity, such as the u_Turb profile, whereas a value closer to zero describes non-uniform flow velocity, such as the u_Jet profile.

6.4 Results

CFD Model Validation

Deposition patterns presented in this study generally split the domain into three regions: the device outlet (outlet capillary and expansion), patient interface (MP or NC), and the ET region (MT or NT). For the purposes of model validation, regional DEs are compared between the CFD and experimental results in the patient interface and ET

regions, with DEs on the device outlet provided for completeness. Figure 6.6a shows that CFD predictions of aerosol DE were in close agreement with the experimental (Exp) results in the MP and MT regions, with a maximum absolute error in regional DE of -0.6% in the MT region. Total DF in the entire model also matched well between the CFD and experimental data with an absolute error of 0.2%.

The validation of the NC-NT model, presented in Figure 6.6b, did not match as closely to the experimental data as the oral model, but was still considered acceptable. Maximum absolute error in regional DE was 5.1% in the NT region, and the CFD model over-predicted total DFs in the entire domain by 8.3%. Note that adjustment of the NW limit control parameter in the NW correction UDFs would reduce this over-prediction, but we elected to apply the same CFD model settings to all models to ensure consistency between cases. This lower degree of model validation relative to the MP-MT model was deemed acceptable as the screening iterations focused on the MP design and general trends in improving performance. However, the slight over-prediction of deposition in the NC-NT model must be taken into consideration when interpreting and evaluating results from those patient interfaces.

Deposition Metrics

Of the three deposition metrics described in the Methods section, correlating the time-averaged maximum velocity on the plane at the outlet of the flow pathway with MT (Figure 6.7a) and NC (Figure 6.7b) DE gave the best prediction of losses, with R^2 values greater than 0.95 and standard error ranging from approximately 0.5% to 0.6%. It is noted that the different velocity profiles considered all had the same volumetric flow rate. Therefore, deposition in the MT correlates with not only volumetric flow rate, but also the

peak value of the velocity profile that enters the region. With such a strong correlation, further development of deposition metrics was not required. Figure 6.7a plots the DE in the MT region (Figure 6.4b) against the maximum velocity at the MT inlet for the four imposed velocity profiles (Figure 6.5a). Similarly, Figure 6.7b plots the DE in the NC bifurcation region (Figure 6.4d) against the maximum velocity at the inlet for the jet, turbulent, laminar, and intermediate velocity profiles. As mentioned previously, the NC-NT model was split into the domains shown in Figure 6.4c and d as preliminary work showed that imposing velocity profiles at the inlets of the NT region (outlet of the NC prongs) had little influence on reducing ET losses. However, the deposition metrics show that reducing the intensity of the jet entering the NC bifurcations (as quantified by peak velocity) can reduce interface losses at the first impaction point, just as in the MT with oral aerosol delivery.

Figure 6.8a and b show the deposition patterns in the MP-MT model when the jet (Figure 6.8a) and turbulent (Figure 6.8b) velocity profiles were imposed at the inlet. Figure 6.8a shows a large amount of impaction deposition on the back of the MT, due to the high velocity jet entering the region, which was also observed experimentally by Farkas et al. (2019). In Figure 6.8b, this impaction region was minimized as the intensity of the inlet jet is vastly reduced with the turbulent velocity profile, which leads to a reduction in MT losses from 8.8% to 3.8% at the same volumetric flow rate. In the laryngeal region of the pediatric MT model, deposition patterns were similar between the jet and turbulent profile cases as inlet effects are less apparent downstream in the domain. Similarly, Figure 6.8c and d show the deposition patterns in the NC-NT model for the jet and turbulent velocity profiles, respectively. As with the MT model, minimizing the inlet jet intensity reduces the losses

at the first impaction point, which in the NC-NT model is the cannula bifurcation, from 7.2% to 0.9%. However, there is little difference in NT losses when imposing different velocity profiles, with DEs ranging from 19.2% to 19.7%. This supports the insight from the preliminary work and deposition metrics that NT losses are difficult to minimize with changes to the design of the NC flow pathway, but NC interfaces losses can be improved.

Design Concept Screen 1

Diagrams that illustrate the MP design concepts in the first iteration were presented in Figure 6.2a. These diagrams provide an axial, mid-plane slice of the interface aligned with the top-down view and show the MP geometry along with any internal components. The first iteration implemented four design concepts, with two variations of each concept. The gradual expansion (GE) concept steadily increased the MP diameter from the circular outlet capillary to the elliptical MP outlet. The variations of the GE concept used a smooth (a) and an undulating (b) surface, with the intention being that the undulating surface would increase turbulence through tripping the boundary layer, thereby keeping the flow attached and preventing recirculation. The rapid expansion (RE) concept quickly transitions from the outlet capillary diameter to the elliptical MP cross-section with a dome shape that extends 6.5 mm from the capillary. The variations of the RE concept used a one-step (a) and two-step (b) expansion, where the two-step expansion initially transitioned to an elliptical cross-section that had half the radii lengths of the outlet over the first half of the MP length. The intent of the two-stage RE variation was to determine whether the MP cross-section should be increased incrementally to dissipate the intensity of the inlet air jet. The rod array (RA) concept used 0.5 mm diameter rods arranged in a 3-4-3 configuration and placed in the flow pathway to break up the high-velocity inlet jet

and reduce its intensity. The variations of this design concept placed the rod array close to the outlet capillary (a) or close to the MP outlet (b) to provide insight on the optimal positioning of the rod array. Finally, the tear drop (TD) concept placed a streamlined obstacle in the flow pathway to both break up the inlet jet and minimize recirculation by keeping the flow attached to the outer wall of the MP. The tear drop was suspended in the flow pathway with six supports that were placed in a triangular arrangement and followed a NACA 0012 profile to reduce their influence on the flow field as much as possible. The variations of this design concept used a tear drop shape that extended into the transition region between the outlet capillary and MP, and another design that moved the leading edge of the tear drop away from the outlet capillary. The intent of these two variations was to determine the effects on impaction deposition by moving the blunt edge of the tear drop away from the jet source.

Table 6.2, used in conjunction with Figure 6.2a, presents the CFD-predicted losses on the device outlet (DE_{Dev}) and patient interface (DE_{MP}), and the correlation-predicted MT losses (DE_{MT}) for the eight MP designs described above. The GE cases both reduced peak velocity at the MP outlet, which suggests an improvement in MT losses based on the deposition correlation. However, the interface losses for both variations of the GE concept were high (34.4% and 17.0%) compared to the original MP design (6.4%). It is interesting to note that the undulating surface (GE-b) reduced the CFD-predicted MP losses by approximately half compared to the smooth surface (GE-a). The RE design concept also reduced peak velocity and the associated MT losses, with the added benefit of a reduction in CFD-predicted interface losses compared to the original MP design of 6.4% to 1.8%. The RE-a design gave the best performance improvement of all eight cases

considered in the first iteration, with the total domain DF reduced from 16.7% to 11.8%. The RA-a case gave the best reduction in peak velocity and estimated MT losses of all cases evaluated in the first iteration, from 8.8% to a predicted 4.9% comparing the original MP and RA-a respectively. The two TD cases performed well in terms of minimizing flow recirculation, reducing device outlet losses, and predicted MT losses, but a large amount of impaction deposition on the leading-edge caused very high MP losses (57.0% and 54.7%). Based on the results from Design Screen 1, a combination of the benefits observed for the RE and RA type designs may be utilized to improve patient interface performance further. That is, the 3D rod array can be added to the RE geometry to both give an improved reduction in jet intensity, interface deposition loss, and predicted MT loss.

Design Concept Screen 2

The second iteration of design screening combined aspects of the RE and RA designs from the first iteration, and also introduced the cylindrical expansion (CE) geometry as an alternative to RE, as illustrated by Figure 6.2b. The RE-a+RA-a design combines the geometry from the one-step variation of the RE concept with the rod placement and configuration from the first RA variation in an attempt to leverage the benefits of both designs from the first design screen iteration. RE-a+RA-c is similar to RE-a+RA-a with the rod array moved 6.5 mm downstream of the outlet capillary to gain insight in the placement of the rod array and its effect on losses. RE-c+RA-a uses a two-step expansion with a shorter first section than RE-b, and the first rod array variation, to evaluate the effect of keeping the flow constrained as it passes through the rods. CE+RA-a is similar to RE-a+RA-a except it uses the cylindrical type geometry to provide a direct

comparison between the combined RE+RA with the CE+RA design concepts. The final three designs in the second screening iteration (CE+RA-d/e/f) use the cylindrical geometry with rod arrays that span the full width of the MP with the intention of preventing the jet from reaching and attaching to the walls, as well as reducing the intensity of the jet. The three rod arrays are located at 1.5, 10, and 20 mm from the outlet capillary to evaluate the deposition losses as the rod array is moved away from the source of the inlet jet.

Based on the deposition results in Table 6.3, adding the RA to the RE geometry had the desired effect of improving MT losses by reducing the peak velocity of the inlet jet, which brings the total DF below the target of 15% (see bold DF_{Tot} values). However, the deflection of the jet due to the rod array causes higher interface losses, when compared to the RE-a case, as the flow is directed towards the side walls of the MP. Moving the RA further away from the capillary outlet in the RE-a+RA-c case leads to relatively high MP losses as the inlet jet flowed around the rods and attached to the walls instead of passing through the rod array and diffusing. Of all the design concepts considered in the second iteration, RE-c+RA-a had the worst performance in terms of flow pathway losses due to the close proximity of the interface walls to the rod array. That said, this case provides valuable insight as it shows that positioning the MP walls further away from the rod array reduces patient interface losses, which is explored further in the third design screen iteration. The CE+RA-a case had very similar performance to RE-a+RA-a, which shows that the slight change in the MP geometry has little effect on reducing deposition losses. The final three CE design concepts with rod arrays that span the full width of the interface also all had a similar level of performance (13.1-14.4% total

254

DF). They show that moving the rod array away from the outlet capillary reduces the losses on the device outlet, but increases interface losses, so that total losses remain relatively constant. Despite the cases with rods spanning the full width of the interface having the best performance in the second design screen iteration, it is desirable to find design concepts that use fewer rods to simplify the construction of these patient interfaces.

Design Concept Screen 3

Using insight from the RE-c+RA-a case, the third design screening iteration introduces a forth RE geometry (RE-d), as illustrated by Figure 6.2c. Here, the MP walls are initially twice as far away from the outlet capillary (maximum width of 36 mm) and gradually taper towards the original elliptical cross-section. The intention of this design concept is to keep the patient interface walls away from the flow when it is dispersed by the rod array to reduce device outlet and MP losses. The RE-d+RA-a case was evaluated as this rod array has provided good performance in the previous iterations and for direct comparison with the RE-a+RA-a case. RE-d+RA-e used the best performing rod array from the second design screen iteration and tested whether the large number of rods was necessary to reduce interface losses despite the drawbacks in terms of MP construction. RE-d+RA-g is similar to RE-d+RA-e, but the rods span half the width of the patient, with this design included as an intermediate step. The RE-d+RA-a-434 case is the same as RE-d+RA-a with the rods placed in a 4-3-4 configuration (as opposed to 3-4-3) and was evaluated to determine whether this configuration provided performance improvements over the other design concepts. Finally, the RE-d+RA-c-EC design concept uses the rod array positioning seen in the RA-c case with an extended capillary (EC) that protrudes

6.5 mm into the patient interface. The intention of this design is to keep the inlet jet away from the device outlet and interface walls while forcing the flow through the rod array to disperse the jet and reduce its intensity.

The results in Table 6.4 show all design concepts from the third screening iteration provided CFD-predicted total losses of less than 10% in the device outlet, patient interface, and MT regions. Widening the MP geometry had the expected effect of preventing the dispersed jet from depositing particles on the interface walls, which is clearly apparent when comparing the RE-d+RA-a case with RE-a+RA-a, as the wider geometry reduced total losses by 5.9% absolute difference. There was little difference in performance between the RE-d+RA-e and RE-d+RA-g cases, with the latter preferred as it required less rods and is hence easier to build. Switching the rod array configuration from 3-4-3 to 4-3-4 (RE-d+RA-a-434) gave a marginal improvement in reducing MP losses, but gave a higher peak jet velocity and therefore larger predicted MT losses, with total losses 0.9% higher (absolute difference) compared to the original configuration. Finally, extending the outlet capillary into the MP (RE-d+RA-c-EC) provided the expected improvement of reducing device outlet losses, and had total deposition losses that are comparable with the other design concepts in the third iteration.

Figure 6.9 demonstrates how effective the 3D rod array is at diffusing the air jet in the patient interface. Figure 6.9a shows the highly turbulent, high-velocity jet, which is generated by the DPI outlet capillary, entering the RE-a MP design candidate. This jet extends beyond the outlet of the patient interface and imparts a large amount of momentum on the aerosol, which leads to increased deposition on the first impaction point that the jet encounters, as described previously. The jet diffusion by the 3-4-3

configuration rod array is clearly apparent in Figure 6.9b, with the jet almost fully dissipated by approximately 30 mm into the 75 mm length of the RE-d+RA-a MP design. The vast reduction in peak velocity of the flow leaving the patient interface is expected to both reduce delivery system and ET losses, based on the previously presented deposition correlations. The 3D rod array has the added benefit of providing a secondary breakup mechanism to reduce aerosol size (Behara, Longest, et al., 2014b), which may lead to further improvements in system performance.

Candidate Mouthpiece Designs

Four design concepts from the screening iterations were selected for evaluation with full MP and MT CFD models: RE-a, RE-d+RA-a, RE-d+RA-g, and RE-d+RA-a-EC. Figure 6.10 shows the CFD-predicted deposition patterns and regional DEs for the four candidate design concepts. Only bin sizes from 1.09 to 3.26 μm are included in Figure 6.10 as they account for 84% of the initial particle size distribution and provide a clearer representation of deposition patterns in the CFD domain. Comparing losses in Figure 6.10b-d with Figure 6.10a clearly shows that widening the MP geometry and including a rod array to disperse the inlet jet provides a substantial reduction in CFD-predicted patient interface and ET deposition losses, with an absolute difference in total DF of 10.3%. The best performing case of the four candidate designs was RE-d+RA-a-EC with CFD-predicted total losses of 5.1% on the device outlet, MP, and MT region, which is a three-fold reduction compared with the original MP (see Figure 6.6a). Comparing regional deposition between RE-d+RA-a-EC and the original MP, CFD-predicted losses were reduced from 2.4% to 0.6% on the device outlet, 6.4% to 2.2% on the MP, and 8.8% to 2.4% in the MT region.

Candidate Nasal Cannula Designs

The top four MP design concepts were applied to the NC flow pathway, which consists of the region between the outlet capillary and cannula bifurcation. Figure 6.11 shows the deposition patterns and regional DEs for the four NC designs. As with the MP flow pathway, widening the NC geometry and including a rod array (Figure 6.11b-d) reduces total deposition losses compared to RE-a by a two-fold reduction (Figure 6.11a). Also consistent with the MP designs, the best performing NC case was the RE-d+RA-a-EC design in Figure 6.11d. Comparing the RE-d+RA-a-EC MP and NC directly, device outlet losses were similar (0.6% vs. 0.8%) and interface losses were a little higher in the NC with an absolute difference of 1.1%. The downside to all NC designs is that losses in the NT region are much higher than MT losses in all cases considered, with absolute differences of approximately 18%, which leads to higher total DF losses. That said, recall that the validation cases showed that CFD models over-predicted total deposition in the NT model by 8.3%, so we could optimistically expect total losses to be 15-20% with experimental testing of these NC design concepts.

Optimal Flow Rate for Nasal Administration

The results in Figure 6.11 are consistent with previous findings from this study that changes to the flow pathway in the NC, and the subsequent changes to the flow profile entering the nasal cavity, has little effect on reducing NT losses. Figure 6.8c and Figure 6.6d showed that imposing a jet or turbulent velocity profile resulted in negligible difference in NT losses, and similarly Figure 6.11b-d show little change in NT losses despite the same design concepts reducing MT losses by 6.4% (absolute difference) when applied to the MP interface. One method to reduce impaction deposition in the NT

region is to reduce the size of the aerosol that enters the nasal cavity, but exploratory work of this approach yielded little performance improvement as the 1.69 μm MMAD from the DPI as at the lower end of the characteristic S-curve deposition profile.

The alternative approach to reduce impaction deposition is to lower the flow rate through the patient interface and NT to reduce particle momentum. Figure 6.12 compares the CFD-predicted particle deposition for the best performing NC design concept (RE-d+RA-c-EC) at the original operating flow rate (13.3 LPM) and 75% of that inlet flow rate (9.9 LPM; 25% reduction). The lower flow rate reduces NT losses by 6.9% (absolute difference) and total losses by 7.8%. While the total system and ET losses at 9.9 LPM is 16.3%, experimental results are expected to be even lower based on the validation case study.

6.5   Discussion

This study met its objective by presenting three MP design concepts that provide CFD-predicted total deposition losses of less than 15%, with the best case being the RE-d+RA-a-EC design that showed a total DF on the device outlet, patient interface, and MT region of 5.1%. Combining these CFD-predicted interface and ET losses with the approximate 10% device loss from Farkas et al. (2019) suggests the possibility of a pediatric lung dose greater than 85% of the loaded dose. The NC design concepts did not perform as well as the MP designs with respect to increasing lung dose, as changes to the flow pathway had little effect on reducing NT losses. The combination of the RE-d+RA-a-EC design concept with a reduced operating flow rate of 9.9 LPM (25% decrease) gave a CFD-predicted total DF of 16.3%. Previous work showed that device losses are strongly associated with flow rate through the pediatric air-jet DPI (Bass, Farkas, et al.,

2019); hence operation of the delivery system at a lower flow rate, to reduce NT losses, may lead to increased device losses. However, experimental results of the device (Case 1.60/2.39) that had a 25% reduction in flow rate from the Bass et al. study (2019) gave negligible change in MMAD (1.69 µm vs. 1.71µm) and a 2.5% increase (absolute difference) in device losses . Therefore, overall system losses may be improved when administering the aerosol via N2L delivery at a reduced flow rate. Adding this loss to the experimentally determined DPI loss (Farkas et al., 2019) suggests a lung dose that is approximately 74% of the loaded dose. This is slightly outside the performance targets laid out in the objective (lung dose >75%), but the validation cases showed that the CFD models over-predict deposition in the NC and NT, so there is a possibility that experimentally determined losses may be less than those suggested by these CFD-predictions.

The CFD-predicted patient interface and ET losses, and associated lung dose, for these candidate design concepts must be experimentally tested, which will be the focus of a future study related to the development of this system for administration of tobramycin to pediatric patients with CF. The candidate design concepts also met the sizing and construction considerations that were stated in the objective. The total length to the MP and NC designs is less than 75 mm and no wider than 40 mm, which allows for a compact and portable device. The best performing RE-d+RA-a-EC design concept also requires relatively few rods in the rod array, with a total of seven compared to other concepts that required more than 50, which allows for simplified construction of the patient interfaces. Considering volume, the MP and NC interfaces that employ the RE-d geometry had total

internal volumes of 31 and 21 cm^3, respectively, which can easily be cleared with device actuation volumes on the order of 100s of mL.

In addition to the primary objective, this study presents correlations that predict deposition in the MT and cannula bifurcation regions based on the maximum inlet velocity to each of these regions, with the same volumetric flow rate. The results show that imposing different velocity profiles with varying peak velocities can cause the CFD-predicted deposition to range from 3.8% to 8.8% in the MT region and from 0.9% to 7.2% in the cannula bifurcation. Using these predictive correlations reduced the turnaround time for analyzing numerous design candidates as only the flow pathway for each patient interface was required for each CFD model. The reduction in processing time using this method was especially important in this study as the oscillatory nature of the high-velocity inlet jet required a transient solution of the transport equations.

The deposition correlation results also show that the impaction deposition in the chosen region is dependent on the inlet velocity profile and not simply the inlet volumetric flow rate. Each of the four velocity profiles in Figure 6.5a have the same flow rate, which was 13.3 LPM to be consistent with the chosen DPI, but each resulted in considerably different particle deposition results. A common method of predicting ET losses is to utilize the impaction parameter ($d_a^2 Q$) where particle size (d_a) and flow rate (Q) are used to estimate transmission through the MT or NT region (Golshahi et al., 2011; Javaheri et al., 2013; Storey-Bishoff et al., 2008; Tavernini et al., 2018). Studies that use the impaction parameter typically describe a large amount of variability, with Golshahi et al. (2011), Storey-Bishoff et al. (2008), and Tavernini et al. (2018) providing correlations that reduce this variability for children, infants, and neonates, respectively. The results in Figure 6.8a

and b show that for a constant flow rate the deposition results increased substantially with respect to peak inlet velocity, which suggests that peak inlet velocity is also a significant indicator of ET deposition. As such, the variability in predicting ET losses with the impaction parameter may be reduced further if aspects of the inlet profile were taken into consideration. For example, operating conditions that result in a turbulent flow regime may have a lower peak velocity, due to the blunt turbluent velocity profile, which may result in lower deposition than even laminar flow if turbulent particle dipersion is low. Similarly, if the flow does not reach a fully-developed state before entering the experimental model, the inlet velocity could be very different from either a laminar (parabolic) or turbulent (blunt) profile, which could influence the development of extratoracic deposition correlations.

As mentioned previously, particle deposition was higher in the NT models compared to the MT, which resulted in lower expected lung doses with nasal administration. This apparent disadvantage of the NC designs can be leveraged as a benefit for the treatment of bacterial infections in the nasal cavity. There is evidence in the literature that the nasal cavity and sinuses can harbor bacterial colonies that repeatedly lead to lung infections in patients with CF (S. K. Hansen et al., 2012; Linnane et al., 2015; Moller et al., 2017) despite elimination of bacteria in the lower airways. Therefore, treatment methods may attempt to eradicate infections by administering tobramycin in the nasal cavity and sinuses. This would mean that nasal administration with the NC designs in the current study would be a preferred method, as a portion of the delivered dose is deposited in the NT region. If treatment of bacterial infections in the nasal cavity is not deemed necessary by clinicians and a high lung dose is required, then

oral administration methods with the MP designs presented here would be the preferred method. Beyond discussions of targeting deposition in the various regions of the airways for uniform dosing, there are also practical aspects of oral and nasal administration that should be taken into consideration. The proposed system aims to deliver the lung inhalation volume to the subject during actuation, as well as the tobramycin dose, which requires an air-tight seal between the device and patient.

Limitations of this study primarily include the assumptions and approximations made by the CFD models. Hygroscopic growth is known to increase particle size as the aerosol travels through the humid airways. This phenomenon was neglected from the CFD model as the increase in ET deposition from hygroscopic growth is expected to be small, with Walenga et al. (2014) reporting an approximate 0.1% increase in adult nasal airways. The same negligible impact on ET deposition in infant and pediatric airways can also be assumed in the present study. The rod array was added to the patient interface in an effort to diffuse the high-velocity inlet jet, but rod arrays have also previously been utilized to increase secondary particle breakup and reduce aerosol size (Behara, Longest, et al., 2014a, 2014b; Longest et al., 2015; Longest, Son, et al., 2013). This secondary breakup mechanism was not included in the CFD models due to the associated increase in complexity and processing times. The deaggregation from passing the aerosol through the rod array decreases the particle size, which would be expected to decrease interface and ET losses and lead to further improvements in lung dose. These potential improvements to the delivery system performance that were not captured by the CFD models will be experimentally tested in a future study. The disadvantage of including a rod array in the patient interface design is that placing obstacles in the flow would lead to

an increase in impaction deposition. However, the CFD models assumed the stainless-steel rods did not trap any particles that contact the surface (i.e. a reflection boundary condition was applied). Our previous work with rod arrays has shown the losses on the stainless-steel cylindrical surfaces are small and matched *in vitro* validation data (Longest et al., 2015; Longest, Son, et al., 2013), but this assumption must also be tested experimentally.

In conclusion, candidate MP design concepts were developed that provide total CFD-predicted losses of approximately 5%, and expected lung doses of approximately 85% (when coupled with the best-case DPI from Farkas et al. (2019)). Candidate NC design concepts performed slightly worse than their MP counterparts, but operating the DPI with a 25% reduction in flow rate lead to an expected lung dose of approximately 74%. Development of deposition correlations showed that losses were strongly related to peak velocity on the outlet plane of the interface flow pathway, while the flow rate through the device was maintained at 13.3 LPM. Findings from this study and our previous publications on the subject will be used in the continuing development of a tobramycin delivery system for treating CF lung infections in pediatric patients.

6.6 Figures
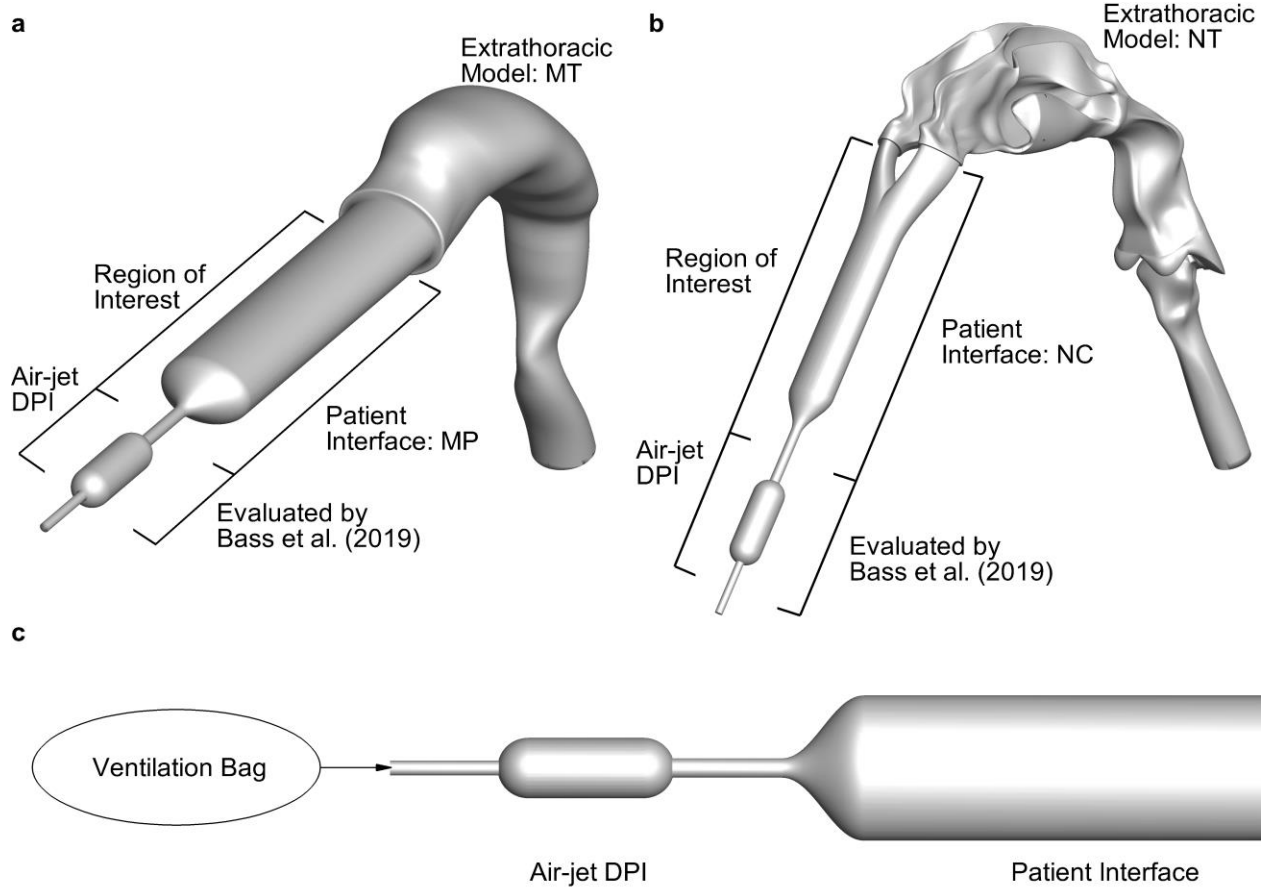
Figure 6.1: Overview of delivery system and extrathoracic models for (a) oral administration via a mouth-piece (MP) through the mouth-throat (MT), (b) nasal administration via a nasal cannula (NC) through the nose-throat (NT), and (c) location of positive-pressure air source (ventilation bag). As noted in the figure, the air-jet DPI was previously evaluated by Bass et al. (2019).
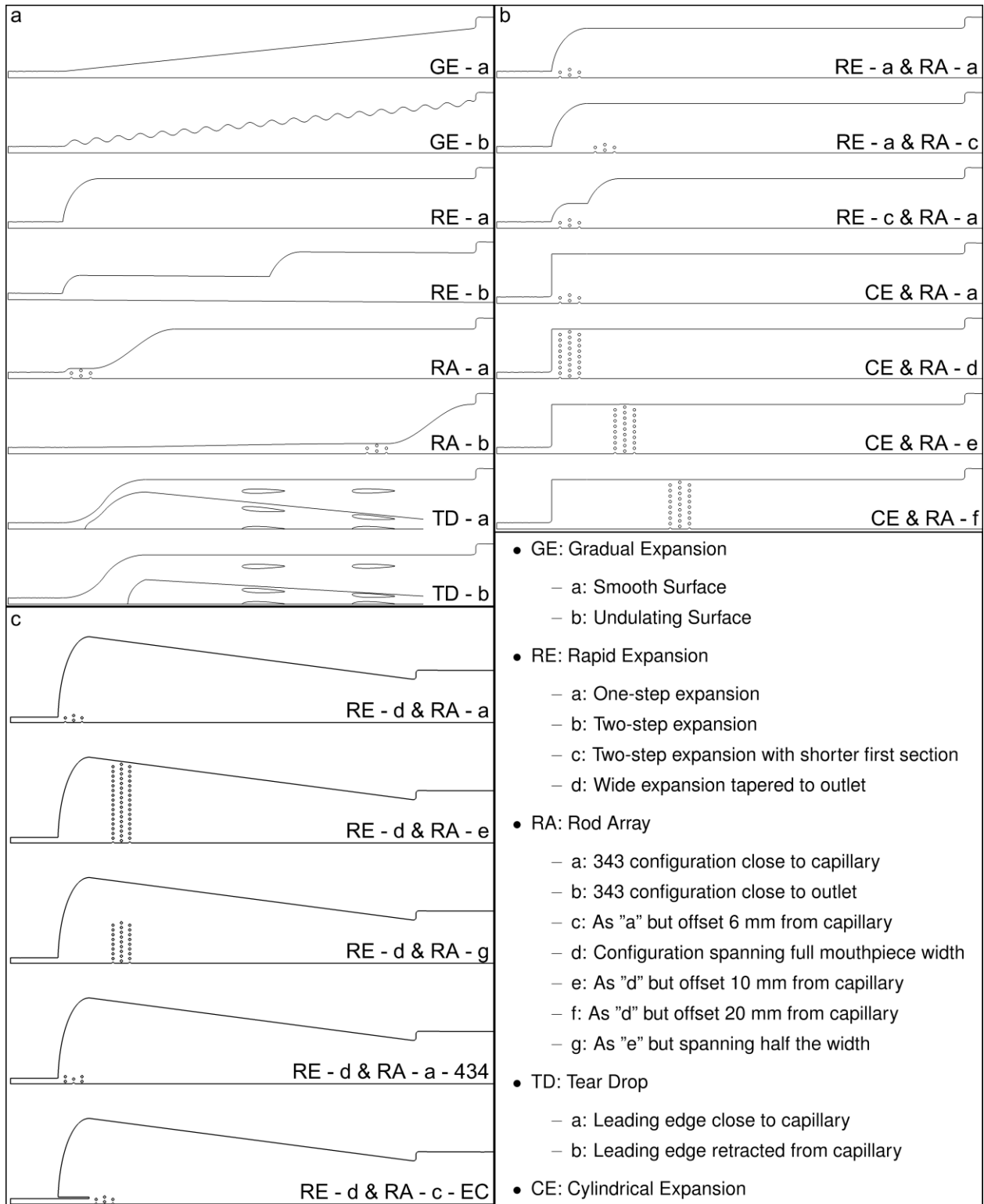
Figure 6.2: Overview of patient interface design concepts for (a) Screening Iteration 1, (b) Screening Iteration 2, and (c) Screening Iteration 3.

266
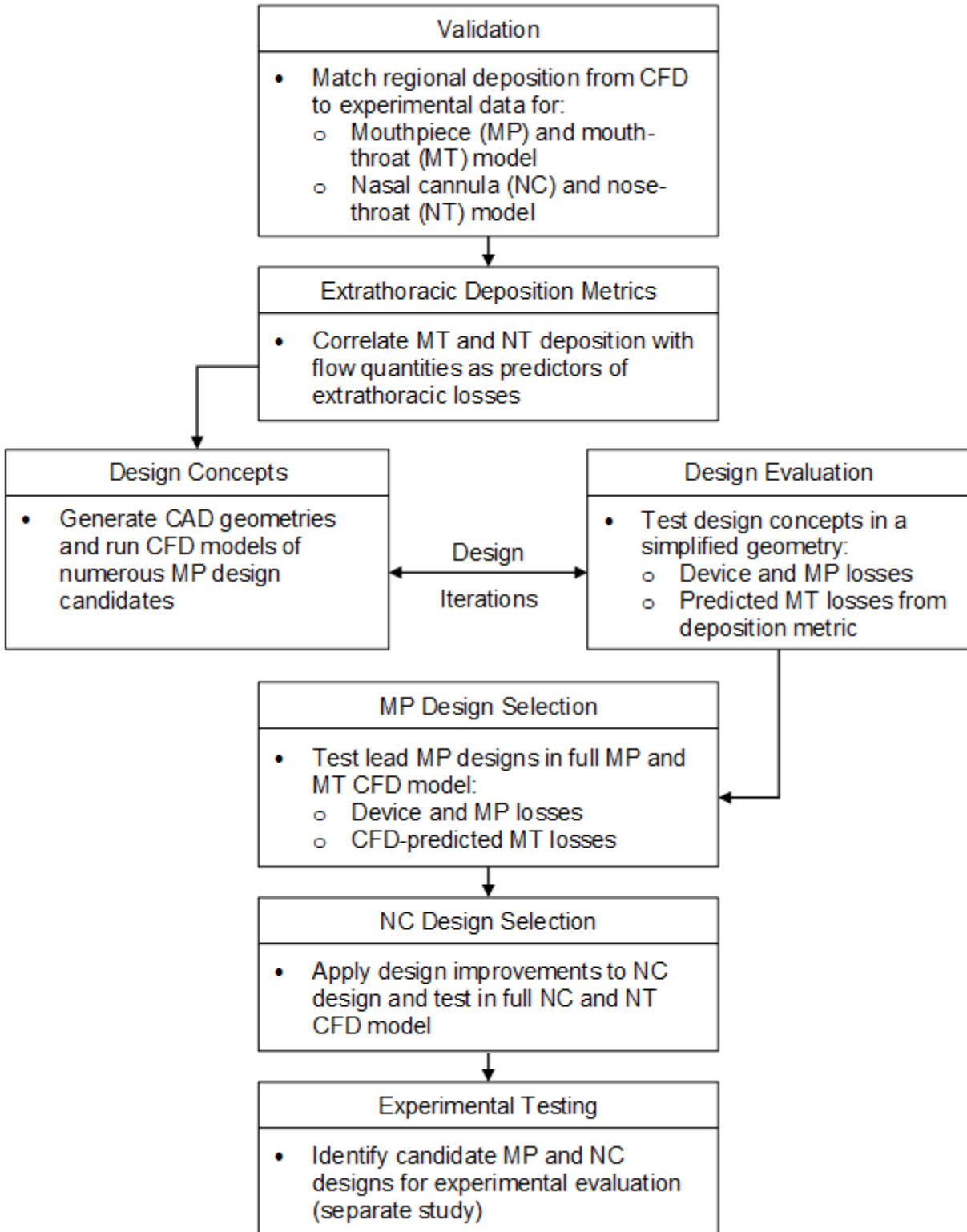
Figure 6.3: Process flow chart to evaluate design concepts with the objective of minimizing losses in the patient interface.
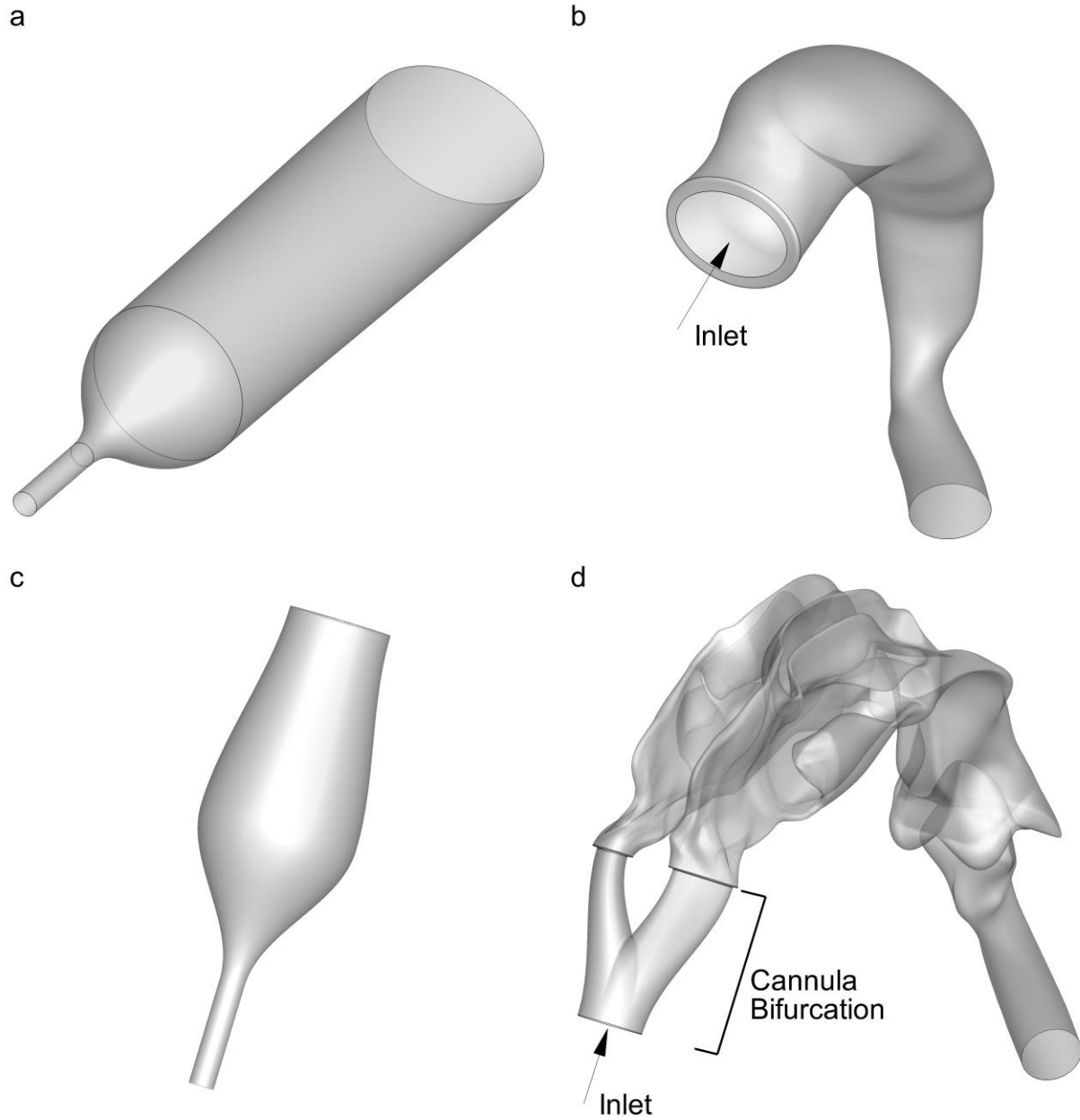
Figure 6.4: Overview of model geometry showing (a) mouthpiece flow pathway, (b) mouth-throat only model (c) nasal cannula flow pathway, and (d) nose-throat and cannula prongs model for evaluation of deposition metrics.
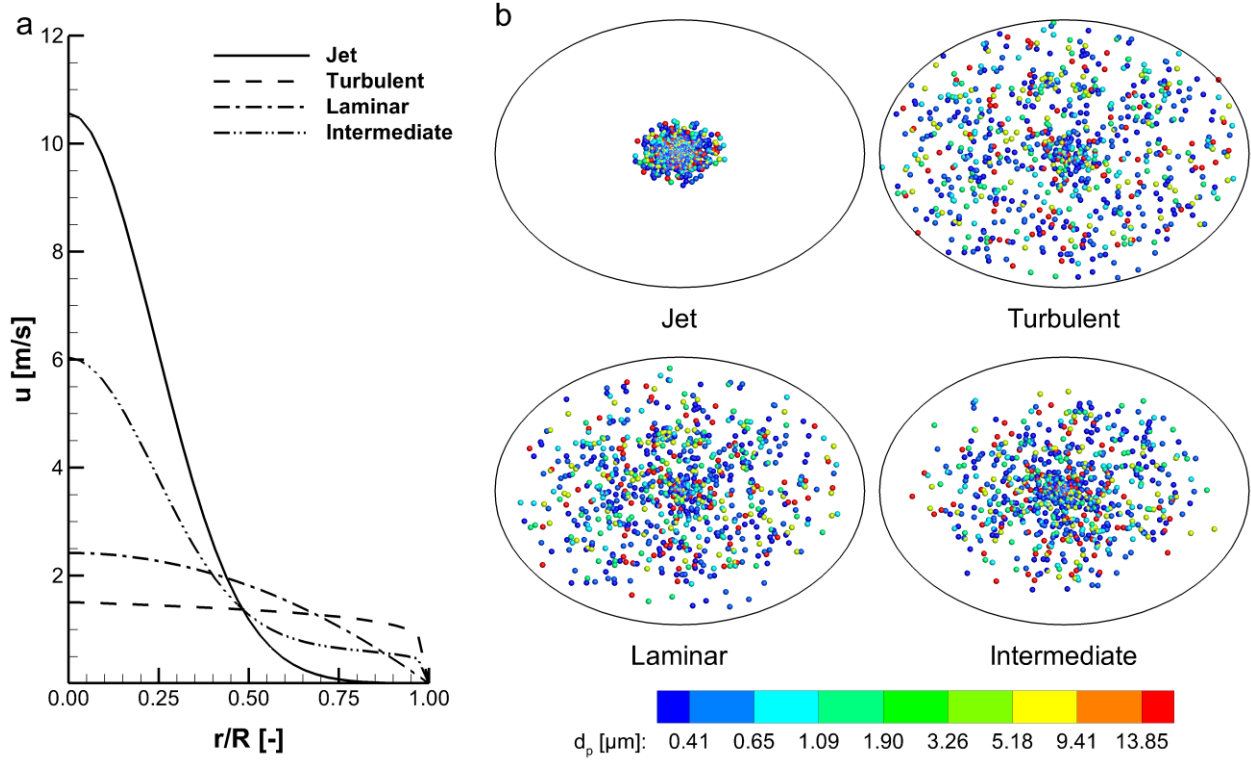
Figure 6.5:   Boundary conditions used to establish extrathoracic deposition metrics in the mouth-throat models showing (a) velocity profiles applied at the inlet boundary and (b) spatial distribution of initial particle locations (nose-throat models used similar boundary conditions).
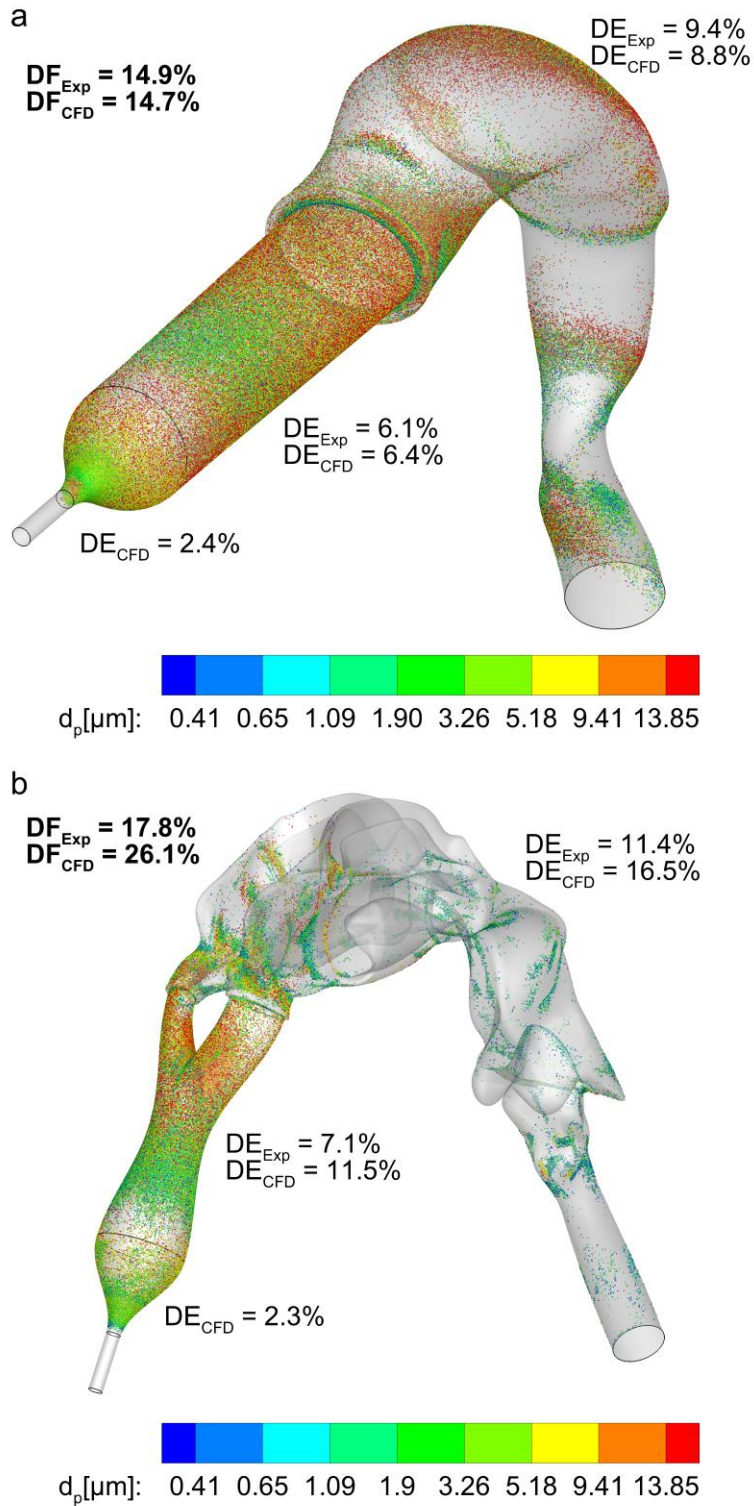
Figure 6.6: Validation of CFD-predicted deposition with experimental data for (a) the mouthpiece and mouth-throat models and (b) the nasal cannula and nose-throat model.
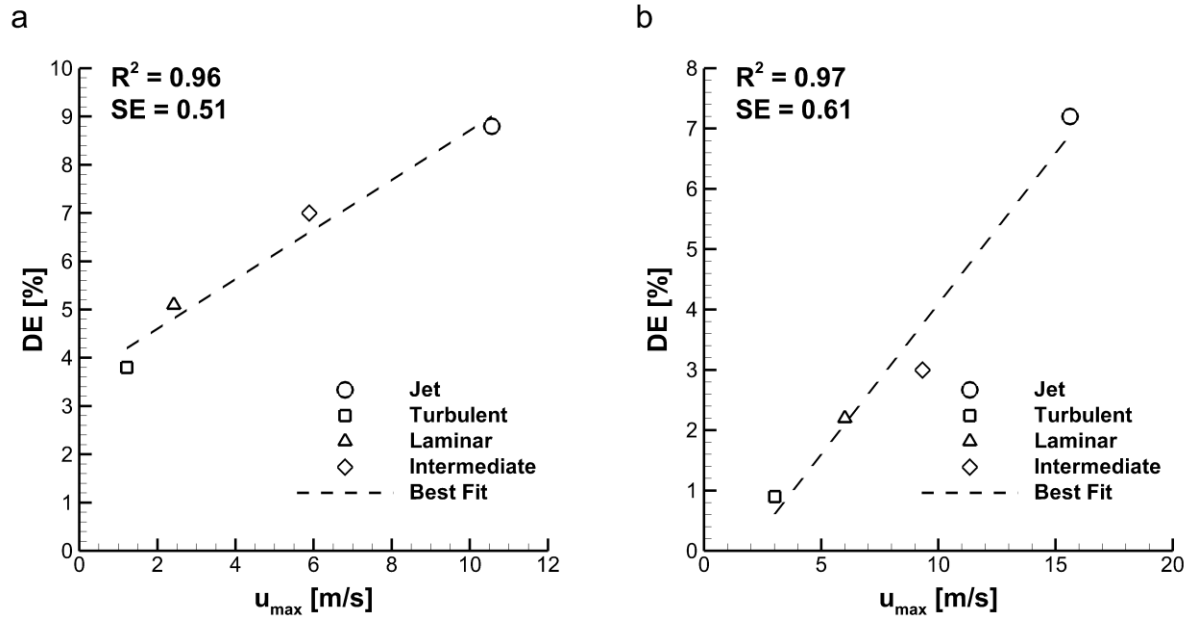
Figure 6.7: Plots showing the correlation between time-average peak velocity at the patient interface outlet (u_{max}) and the deposition efficiency (DE) up to the first impaction point, which is (a) the back of the throat for the mouthpiece and mouth-throat model, and (b) the bifurcation point for the nasal cannula and nose-throat model.
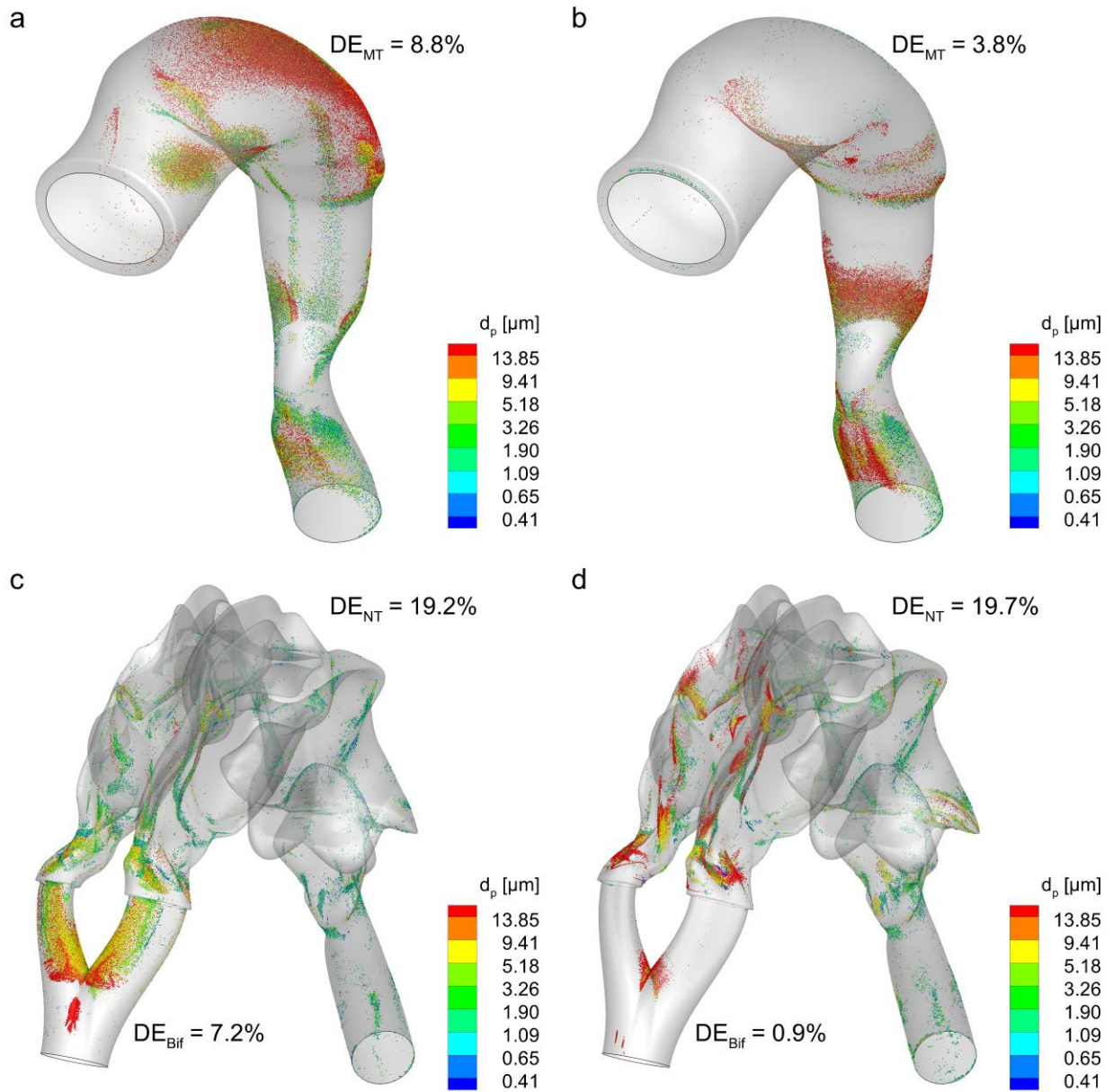
Figure 6.8:   Particle deposition patterns in the (a) mouth-throat (MT) region with the jet inlet velocity profile, (b) MT region with the turbulent inlet velocity profile, (c) nose-throat (NT) and bifurcation (Bif) region with the jet inlet velocity profile, and (d) NT and Bif region with the turbulent inlet velocity profile.
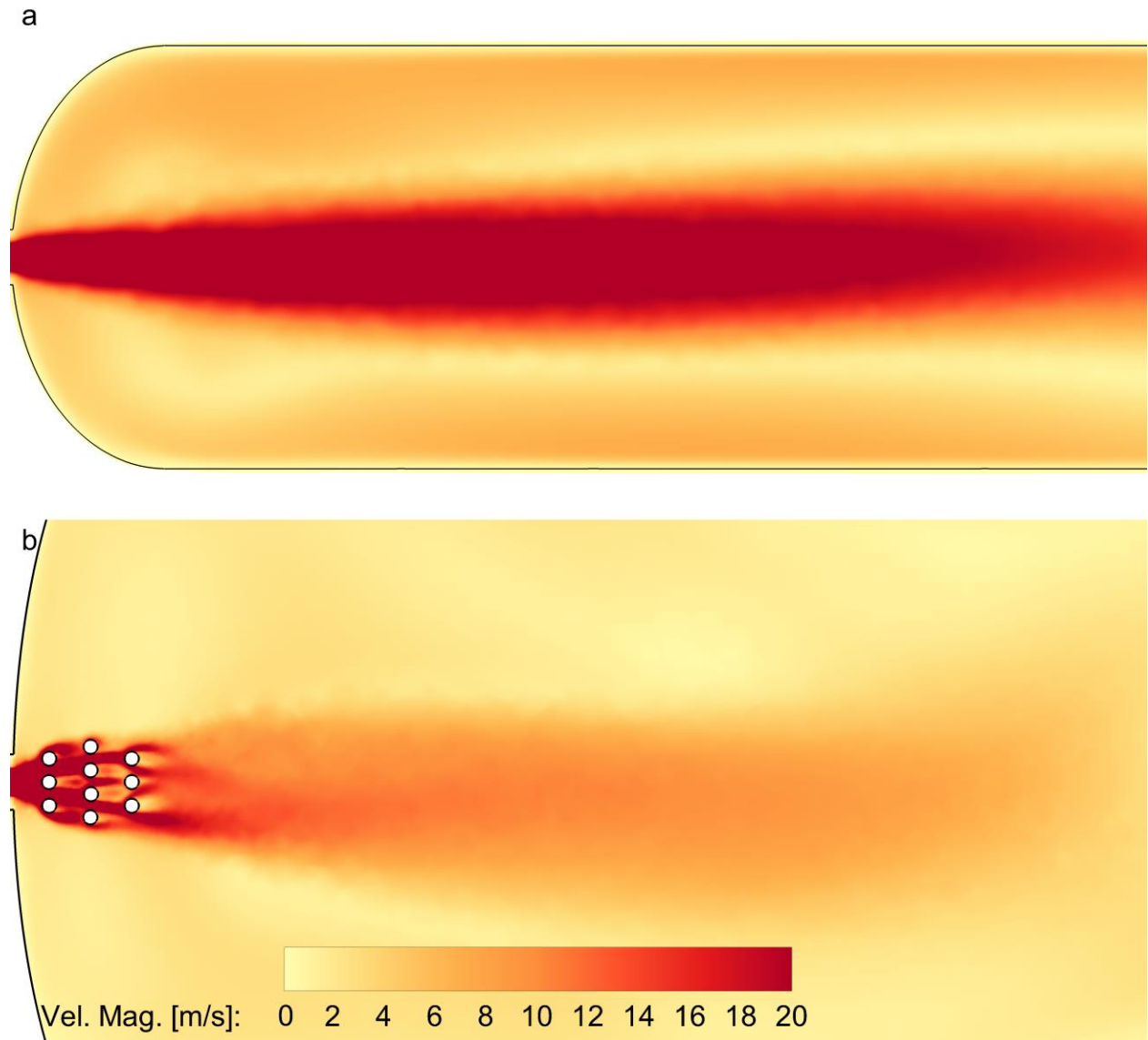
Figure 6.9:   Example of jet diffusion by 3D rod array in the RE-d+RA-a mouth-piece compared to the high velocity inlet jet in the RE-a design. Contours depict nodal values of velocity magnitude (Vel. Mag.) on an axial slice though the mid-plane of the patient interface.
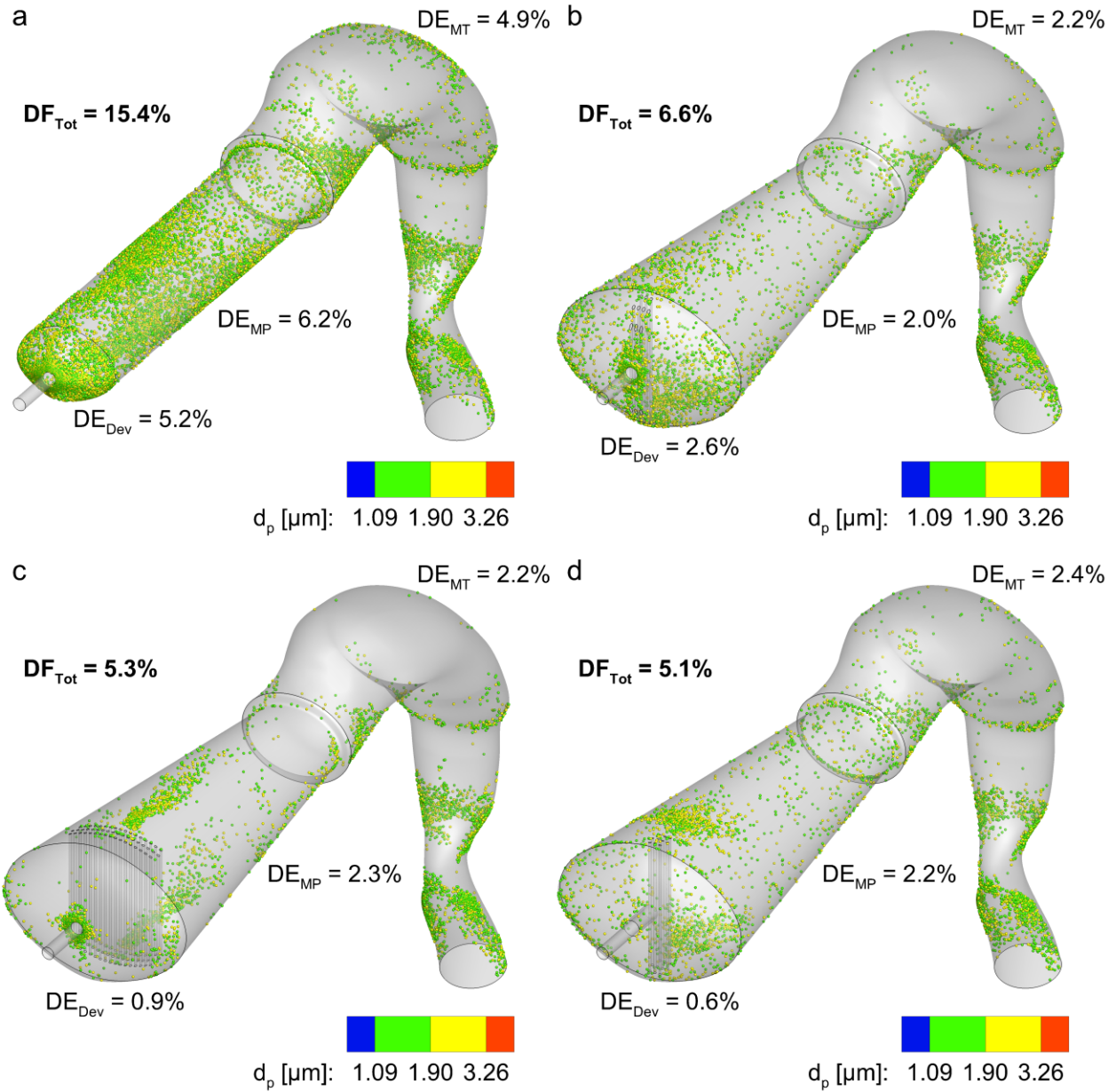
Figure 6.10: Deposition patterns in full mouthpiece & mouth-throat model for the (a) RE-a, (b) RE-d+RA-a, (c) RE-d+RA-g, and (d) RE-d+RA-c-EC design concepts (see Figure 6.2 for a description of the naming convention).

a

DF$_{Tot}$ = 48.7%

DE$_{NT}$ = 27.7%

DE$_{NC}$ = 18.6%

d$_p$ [μm]: 1.09 1.90 3.26

DE$_{Dev}$ = 12.9%

b

DF$_{Tot}$ 26.2%

DE$_{NT}$ = 21.6%

DE$_{NC}$ = 2.9%

d$_p$ [μm]: 1.09 1.90 3.26

DE$_{Dev}$ = 3.0%

c

DF$_{Tot}$ = 26.9%

DE$_{NT}$ = 22.1%

DE$_{NC}$ = 4.7%

d$_p$ [μm]: 1.09 1.90 3.26

DE$_{Dev}$ = 1.6%

d

DF$_{Tot}$ = 24.1%

DE$_{NT}$ = 20.9%

DE$_{NC}$ = 3.3%

d$_p$ [μm]: 1.09 1.90 3.26

DE$_{Dev}$ = 0.8%
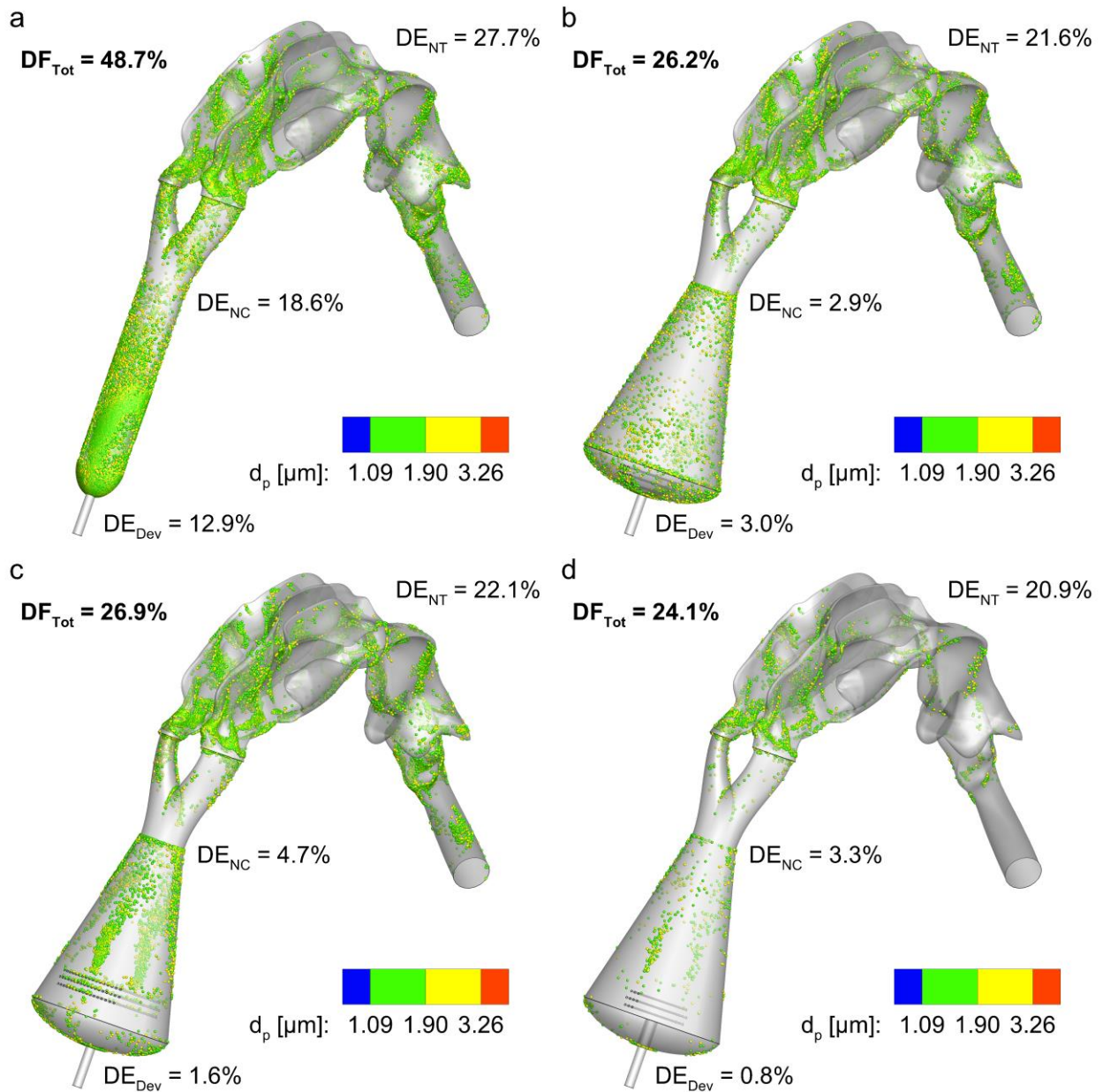
Figure 6.11: Deposition patterns in full nasal cannula & nose-throat model for the (a) RE-a, (b) RE-d+RA-a, (c) RE-d+RA-g, and (d) RE-d+RA-c-EC design concepts (see Figure 6.2 for a description of the naming convention).

275
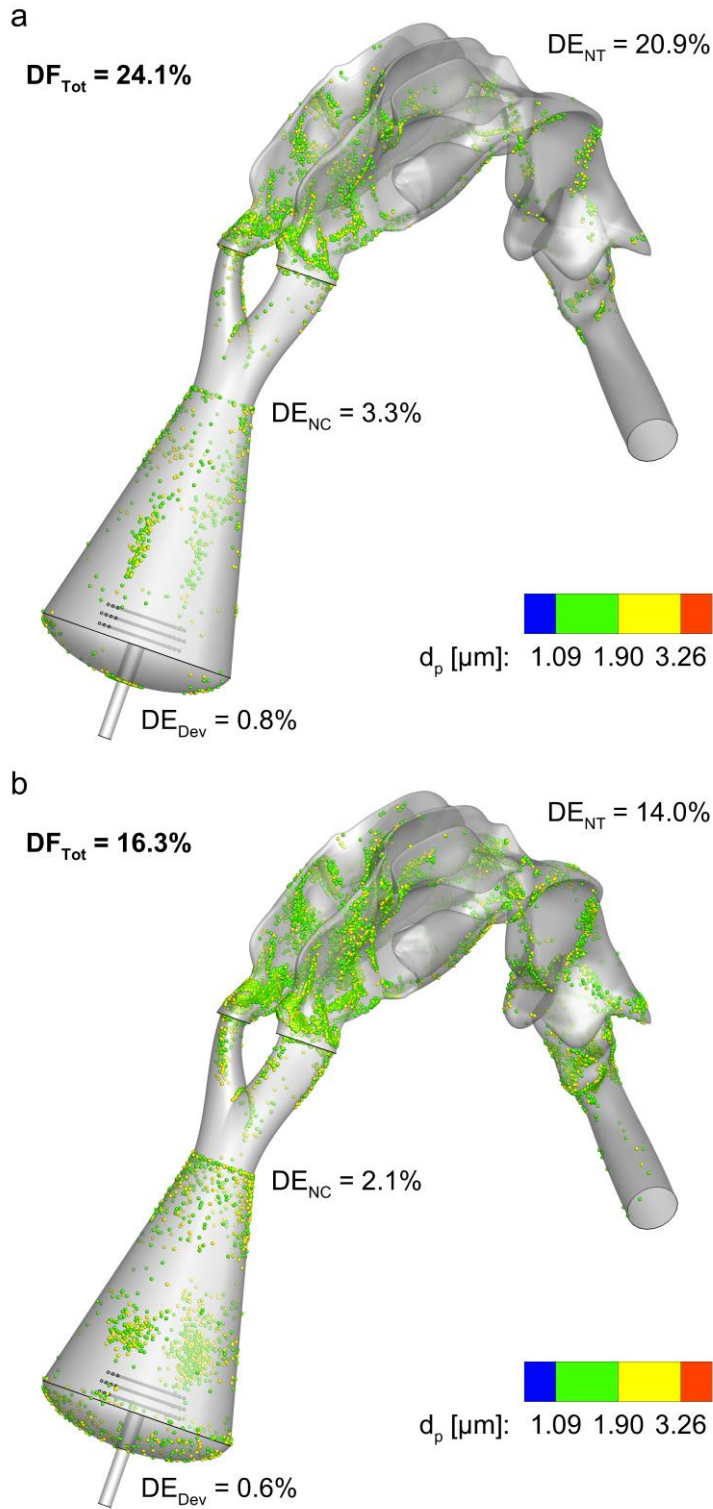
Figure 6.12: Comparison of CFD-predicted deposition for the RE-d+RA-c-EC nasal cannula design operated at (a) 13.3 LPM and (b) 9.9 LPM (25% reduction).

6.7 Tables

Table 6.1:   Summary of experimentally determined patient interface and extrathoracic deposition efficiencies and fractions (based on air-jet DPI emitted dose) from Farkas et al. (2019) for the best-case mouthpiece and nasal cannula devices. Experimental values are given as means with standard deviations shown in parenthesis [n=3].

Region	Mouthpiece [%]	Nasal Cannula [%]
Interface DE	6.1 (0.7)	7.1 (1.7)
ET DE	9.4 (1.6)	11.4 (3.5)
Total DF	14.9 (2.1)	17.8 (4.9)
DE: Deposition efficiency		
DF: Deposition fraction		
ET: Extrathoracic		

Table 6.2: Comparison of peak velocity (Peak Vel.), predicted regional deposition efficiencies (DE) in the device (Dev), mouthpiece (MP), and mouth-throat (MT), and predicted total deposition fraction (DF_{Tot}) between the original mouthpiece and Design Screen 1.

Case	Peak Vel. [m/s]	DE_{Dev} [%]	DE_{MP} [%]	DE_{MT} [%]	DF_{Tot} [%]
Original MP	10.5	2.4	6.4	8.8[a]	16.7
Design Screen 1					
GE-a	4.1	NA[b]	34.4	5.6	38.1
GE-b	4.7	NA[b]	17.0	6.0	21.9
RE-a[c]	5.0	4.4	**1.8**	6.1	**11.8**
RE-b	3.9	14.0	15.9	5.5	31.7
RA-a[d]	2.7	27.7	7.7	**4.9**	36.5
RA-b	19.3	50.5	1.0	13.6	57.6
TD-a	3.7	0.8	57.0	5.4	59.7
TD-b	2.6	0.6	54.7	4.8	57.1

a: Deposition efficiency for the Original MP case is from CFD-predicted particle trajectories, whereas deposition efficiency for all other designs is predicted from peak velocity at the mouthpiece outlet

b: The gradual expansion cases go straight from the device outlet capillary to the mouthpiece, hence there is no device loss

c: The RE-a case gave the best reduction in device and MP losses from Design Screen 1

d: The RA-a case gave the best reduction in MT losses from Design Screen 1

GE: Gradual Expansion
RE: Rapid Expansion
RA: Rod Array
TD: Tear Drop

Table 6.3:   Comparison of peak velocity (Peak Vel.), predicted regional deposition efficiencies (DE) in the device (Dev), mouthpiece (MP), and mouth-throat (MT), and predicted total deposition fraction (DF_{Tot}) among the original mouthpiece, the best cases from Design Screen 1, and Design Screen 2.

Case	Peak Vel. [m/s]	DE_{Dev} [%]	DE_{MP} [%]	DE_{MT} [%]	DF_{Tot} [%]
Original MP	10.5	2.4	6.4	8.8	16.7
Design Screen 1 Best Cases					
RE-a	5.0	4.4	1.8	6.1	11.8
RA-a	2.7	27.7	7.7	4.9	36.5
Design Screen 2					
RE-a+RA-a[a]	2.1	6.0	4.9	4.6	**14.6**
RE-a+RA-c	2.6	1.9	13.2	4.9	19.0
RE-c+RA-a	3.9	22.5	10.6	5.5	34.5
CE+RA-a[a]	2.0	6.8	4.4	4.5	**14.9**
CE+RA-d	3.3	6.6	3.3	5.2	14.4
CE+RA-e[a]	1.8	1.9	7.4	4.4	**13.1**
CE+RA-f	1.7	0.8	9.5	4.4	14.1

a: These cases demonstrated a marked improvement in predicted total deposition fraction over the rod array cases from Design Screen 1, when combined with the rapid expansion or cylindrical geometry, but further improvements are possible

RE: Rapid Expansion
RA: Rod Array
CE: Cylindrical Expansion

Table 6.4: Comparison of peak velocity (Peak Vel.), predicted regional deposition efficiencies (DE) in the device (Dev), mouthpiece (MP), and mouth-throat (MT), and predicted total deposition fraction (DF_{Tot}) among the original mouthpiece, the best cases from Design Screens 1 and 2, and Design Screen 3.

Case	Peak Vel. [m/s]	DE_{Dev} [%]	DE_{MP} [%]	DE_{MT} [%]	DF_{Tot} [%]
Original MP	10.5	2.4	6.4	8.8	16.7
Design Screen 1 and 2 Best Cases					
RE-a[b]	5.0	4.4	1.8	6.1	11.8
RE-a+RA-a	2.1	6.0	4.9	4.6	14.6
CE+RA-a	3.3	6.6	3.3	5.2	14.4
CE+RA-e	1.8	1.9	7.4	4.4	13.1
Design Screen 3					
RE-d+RA-a[a,b]	2.3	2.1	2.2	4.7	**8.7**
RE-d+RA-e[a]	2.4	0.6	2.0	4.8	**7.2**
RE-d+RA-g[a,b]	2.7	0.9	1.7	4.9	**7.4**
RE-d+RA-a-434	3.9	2.9	1.4	5.5	9.6
RE-d+RA-c-EC[a,b]	2.7	0.7	3.0	4.9	**8.4**

a: These cases demonstrate a dramatic improvement in predicted total deposition fraction (<9% combined MP and MT losses) compared to previous design screens

b: Candidate design concepts selected for evaluation with full mouthpiece and mouth-throat CFD model

RE: Rapid Expansion
RA: Rod Array
CE: Cylindrical Expansion
434: 4-3-4 rod array configuration (as opposed to 3-4-3)
EC: Extended capillary from device outlet (inlet to MP)

Chapter 7: Develop CFD Models of Upper Airway Geometries for Pediatric Patients and Evaluate Delivery Efficiency and Aerosol Growth with Comparisons to *In Vitro* Experiments

7.1 Objective

The objective of this study was to develop experimentally validated computational fluid dynamics (CFD) models of the upper airways and growth chambers for 2-3-, 5-6-, and 9-10-year-old patients with Cystic Fibrosis (CF), with a focus on using a nasal cannula for nose-to-lung (N2L) administration. The 5-6-year-old model was experimentally tested and provided *in vitro* data for validation of the CFD model. Results aim to establish whether the hygroscopic properties of the powder formulation and expected residence times through the model are capable of targeting the lower airways beyond Bifurcation 4 (B4+) and maximizing lung retention of the delivered dose.

7.2 Introduction

The primary symptom of CF in the respiratory airways is the dehydration and thickening of mucus due to poor ion transport (Matsui et al., 1998; Tarran et al., 2001). Due to poor mucociliary clearance of this thick mucus (Stoltz et al., 2015), it persists in the patient's airways and provides an ideal habitat for bacterial infections (Boucher, 2007). The most predominant bacteria found in the airways of CF patients is *Pseudomonas aeruginosa* (*Pa*) (Elborn, 2016), which can be treated with inhalation of the antibiotic tobramycin (Ramsey et al., 1999; A. L. Smith, 2002). The bacterial infections cause various forms of damage to the respiratory airways and surfaces, such as inflammation (narrowing of the airways), bronchiectasis (widening of the airways), and mucus plugging (obstructions in the airways) (de Jong et al., 2004). Signs of such damage

are apparent in computed tomography (CT) scans of patients diagnosed with CF at very early stages in their life (Tiddens, Donaldson, Rosenfeld, & Pare, 2010), hence the need for treatment of bacterial infections in pediatric subjects. Our group has recently developed an optimized delivery system for oral and nasal administration of tobramycin to pediatric patients, which consists of a ventilation bag to provide inhalation air, an inline air-jet DPI for efficient aerosolization of the powder, and patient interface (mouthpiece or nasal cannula) for high-efficiency extrathoracic (ET) transmission to the lungs (Bass, Farkas, et al., 2019; Bass & Longest, 2020; Farkas, Bonasera, Bass, Hindle, & Longest, 2020; Farkas et al., 2019).

As a next step in the device development process, the current study explores particle transport through the diseased airways to establish whether the pediatric air-jet DPI system provides effective delivery of the pharmaceutical aerosol through the nose to the lungs. The treatment of all infections with antibiotics requires eradication of the bacterial colonies, otherwise mutated strains of the bacteria may develop that are drug resistant. To ensure eradication of *Pa* with tobramycin, the amount of antibiotic delivered to the airway surface liquid (ASL) must be above the minimum inhibitory concentration (MIC) of 512 mg/L (Bos et al., 2017). Our proposed approach to tobramycin administration in CF-diseased airways is to utilize excipient enhanced growth (EEG) powder formulations to provide uniform dosing and maximize lung retention. EEG aerosols have a small particle size when dry, which is characterized by mass-median aerodynamic diameter (MMAD), that provides highly-efficient penetration into the lower airways. Therefore, the advantage of using EEG aerosols for tobramycin administration is the ability to target deposition in the lower airways where bacterial infection is more

predominant (Tiddens et al., 2010). The hygroscopic excipient in the powder formulation absorbs moisture from the humid respiratory airways, and the dry particles grow to form larger droplets. The larger aerosol size in the lower airways improves lung delivery via an increase in impaction during inhalation and exhalation, as well as increased sedimentation during a breath hold.

The concept of an upper airway and growth chamber model to evaluate EEG aerosol deposition and growth has previously been reported for oral (Longest, Tian, Li, et al., 2012) and nasal (Longest et al., 2015) aerosol administration in adults. An anatomically accurate model of the upper airways, from the ET region to Bifurcation 3 (B3), is used to model aerosol transmission to the lower airways. Thereafter, a cylindrical growth chamber is used to model the aerosol growth as a representation of the humid respiratory airways, with its dimensions selected to give a droplet residence time consistent with the lungs. Previous studies using growth chamber models have shown that they are an effective method for evaluating EEG aerosol growth via a concurrent numerical and experimental approach, with good validation between CFD and *in vitro* deposition and particle size data (Longest et al., 2015; Longest, Tian, Li, et al., 2012). The present study developed new growth chamber models, which included the nose-throat (NT) region through the upper airways (up to B3), to evaluate EEG aerosol deposition and growth in CF-diseased airways of patients aged 2-3, 5-6, and 9-10 years old.

7.3   Methods

Three models were developed to evaluate aerosol transport and growth in a 2-3-, 5-6-, and 9-10-year-old patient. An *in vitro* growth chamber model for a 5-6-year-old

patient (see Figure 7.1) was prototyped and tested with the best-case DPI and nasal cannula from Farkas et al. (2020) (see Figure 7.2) to provide experimental data for CFD model validation. Thereafter, numerical models for all three age groups were developed to evaluate particle deposition and growth in the representative geometries. The geometries used in the *in vitro* and numerical models consists of an upper airway (NT to B3) extracted from CT scans and a growth chamber that was designed to provide an aerosol residence time of approximately two seconds throughout the entire model (see Figure 7.1). Characteristic airway dimensions for the three upper airway models are provided in Table 7.1. Characteristic length scales in the NT region are consistent with nasal deposition studies by Storey-Bishoff et al. (2008) and Golshahi et al. (2011), and dimensions from the trachea were measured directly from CT scans. Measurements beyond the trachea are not reported as the diseased state of the CF airways may not provide a clear comparison between age groups. As expected, characteristic dimensions for older patients are generally larger than the younger patients, which will likely influence aerosol deposition in the upper airways.

Upper Airway and Growth Chamber Geometries

The NT region of the upper airway models were developed by segmentation of CT scans with the Mimics software suite (Materialise, Leuven, Belgium) from patients with healthy airways, as no nasal scans were available for patients diagnosed with CF. This approach was deemed acceptable as the lung disease attributed to CF and *Pa* infections predominantly affects the lower airways (Tiddens et al., 2010). Scans for the NT region of the 2-3-, 5-6-, and 9-10-year-old upper airway models were selected from our database of medically necessary CT scans, which were reviewed for quality and completeness

under an Institutional Review Board protocol. When selecting scans for the study, preference was given to scans that had a slice resolution of 1.0 mm or less and of patients that had heights consistent with average values for the chosen age ranges. For the 2-3-, 5-6-, and 9-10-year-old models, the patient heights were 90 cm, 114 cm, and 144 cm respectively, which are within the 20th and 80th percentiles based on the WHO growth charts (WHO, 2006). The segmentation and CAD model development generally followed the same method as outlined by Bass et al. (2019), with the exception that the latest automated skin surfacing capabilities in SpaceClaim v19.3 were utilized, which reduces the manual effort required to convert STL surfaces to CAD data.

The tracheobronchial (TB) regions of the upper airway model (trachea to B3) were also developed by segmentation of CT scans with Mimics, but the chosen scans were from patients with moderate CF lung damage as scored by the PRAGMA-CF system (Rosenow et al., 2015). The CF CT scans for all three age groups were provided and evaluated for PRAGMA-CF score by Erasmus University Medical Center. For the 2-3-, 5-6-, and 9-10-year-old model, the patient heights were 100 cm, 122 cm, and 131 cm respectively, which are also within the 20th and 80th percentiles based on the WHO growth charts (WHO, 2006) and consistent with the NT scans. After segmentation and CAD model development of the diseased TB regions, the airway was coupled to the NT region of the healthy patient to form the upper airway geometry (NT-B3). The two regions were coupled along the trachea at a point where there was less than a 1.0 mm deviation between the cross-section profiles of the NT and TB regions and preserved the expected tracheal length. A 10 mm coupling region along the length of the trachea (5 mm either side of the coupling point) was then created to define the transition between the NT and

TB regions. Due to the selection of a coupling point where there is minimal difference between two regions and a relatively short coupling section, the effect of artificially joining the healthy NT and diseased TB regions was assumed to be negligible. This assumption will be tested by identifying any abnormal deposition patterns in the coupling region from the CFD results.

The cylindrical growth chamber was designed with insight from preliminary CFD work to provide minimal aerosol loss (<5% deposition) and a residence time of approximately two seconds, which is consistent with the typical particle transport through the lungs. The resulting chamber size for all age groups was a diameter of 101.6 mm (4") and length of 155.0 mm. For the *in vitro* model, the chamber was constructed from a section of clear cast acrylic pipe, sourced from ePlastics (San Diego, CA), and a prototyped lid, base, and outlet pipe.

Experimental Materials and Powder Formulation

Albuterol sulfate (AS) USP was purchased from Spectrum Chemicals (Gardena, CA) and Pearlitol® PF-Mannitol was donated from Roquette Pharma (Lestrem, France). Poloxamer 188 (Leutrol F68) was donated from BASF Corporation (Florham Park, NJ). L-leucine and all other reagents were purchased from Sigma Chemical Co. (St. Louis, MO).

Multiple batches of a spray-dried AS EEG powder formulation were produced based on the optimized method described by Son et al. (Son, Longest, & Hindle, 2013; Son, Longest, Tian, et al., 2013) using a Büchi Nano spray dryer B-90 (Büchi Laboratory-Techniques, Flawil, Switzerland). The AS EEG powder formulation contained a 30:48:20:2% w/w ratio of AS, mannitol, L-leucine, and Poloxamer 188. The AS EEG

powder was used as a surrogate test aerosol in place of tobramycin. It is expected that tobramycin powder formulations with the same hygroscopic properties as AS EEG will perform comparably in regard to targeted lung delivery.

Experimental Methods

The *in vitro* tests of the 5-6-year-old model were conducted under room (22.0°C and 33.5% RH) and humid airway (37.0°C and 99.0% RH) conditions, with the humid conditions controlled in an environment cabinet. In addition, for the humid airway conditions, the model walls were pre-wetted by running humid air (40.0°C and 99.0% RH) through the model before actuating the device in the humid airway experiments. Cooling of the 40°C saturated air in contact with the interior model walls resulted in water vapor condensing onto the walls forming a thin liquid layer. All experimental model components were developed by utilizing the CAD modelling capabilities in SolidWorks 2019 (Dassault Systèmes, Paris, France) and most parts were then rapid prototyped. The exceptions to prototyped parts were the acrylic growth chamber cylinder, as mentioned previously, and the face of the NT region, which was made from cast silicone to create a soft nose. The soft nose was required to accommodate the existing cannula design (which was developed to fit a different NT model) and to provide an air-tight seal around the cannula prongs. The material from which the soft nose is made is also more consistent with the flexible soft tissue of the human nose than rigid 3D printer plastic. The casting process used to make the soft nose was relatively simple, with the cast components developed in SolidWorks 2019 such that the void represents the anterior region of the NT model. The cast was then filled with Dragon Skin^{TM} 20 silicone (Smooth-On, Lower Macungie, PA), left to cure following the product instructions, removed from the cast, and then fixed into

the NT model with epoxy. As an additional precaution against air leaks in the model, all connections between model components included O-rings to ensure air-tight sealing.

The delivery system chosen for experimental testing was the best-case device and nasal cannula combination from Farkas et al. (2020). Details of the pediatric air-jet DPI (see Figure 7.2a) and patient interfaces (see Figure 7.2b) have been discussed extensively in our previous publications related to the development of this delivery system (Bass, Farkas, et al., 2019; Bass & Longest, 2020; Farkas et al., 2020; Farkas et al., 2019). The chosen air-jet DPI operates at an approximate flow rate of 10 LPM (from a positive pressure gas source) and actuation time of 4.5 s (for an inhalation volume of 750 mL for a 5-6-year-old) with inlet and outlet airflow passage (i.e. capillary) diameters of 1.40 mm and 2.39 mm, respectively. The design parameters and operating conditions for the air-jet DPI have previously been shown to give the best aerosolization performance and high-efficiency N2L aerosol transmission (Farkas et al., 2020). The chosen nasal cannula utilizes a 3D rod array to attenuate the high-velocity, highly turbulent air jet that leaves the DPI outlet orifice, which has previously been shown to reduce interface and NT losses (Bass & Longest, 2020).

The device actuation and experimental testing in the present study generally follows the methods presented by our previous *in vitro* development performance evaluation of the pediatric air-jet DPI and patient interfaces (Bass, Farkas, et al., 2019; Farkas et al., 2020). Briefly, the aerosolization chamber is loaded with 10 mg of AS EEG powder and actuated with a 6 kPa positive-pressure air source, using a compressed air line and solenoid valve device, which efficiently aerosolizes the powder. Characterization of the aerosol that leaves the growth chamber was performed using a Next-Generation

Impactor (NGI) and AS drug masses were assayed with high-performance liquid chromatography (HPLC). Preliminary experimental tests of the growth chamber model showed that device actuation time was not sufficient to clear all the aerosol from the growth chamber to the NGI, which lead to low recovered doses as powder remained dispersed in the cylinder and was not assayed. Therefore, a second solenoid valve was utilized that switched between pulling air from the chamber to ambient air, which was controlled by a separate timer from the device actuation and ran for 8 s longer than device actuation. In summary, the testing process was as follows: (i) switch the device solenoid valve to deliver compressed air to the DPI at 10 LPM (see Label 1 in Figure 7.1) and at the same time switch the NGI solenoid valve to pull air through the growth chamber at 45 LPM (see Label 2 in Figure 7.1) allowing make-up air at 35 LPM to be drawn through the top of the growth chamber via one-way valves (see Label 3 in Figure 7.1); (ii) after 4.5 s, the device solenoid valve closes and device actuation stops while the NGI solenoid valve stays open for a total of 12 s, drawing all the aerosol from the chamber and delivering it to the NGI. Using this approach, all recovered doses from experimental runs were greater than 90% (average of 96.5%). The device emitted dose (ED) was defined as the difference between the loaded AS dose and the mass of AS retained in the DPI after actuation, divided by the loaded dose, and expressed as a percentage. The delivery system ED was defined with a similar method, with the combined mass of AS retained in the device and nasal cannula divided by loaded dose. The aerosol MMAD was identified with linear interpolation of a cumulative percentage drug mass vs. cut-off diameter plot from the NGI. The cut-off diameters of each NGI stage were calculated using the formula specified in USP 35 (Chapter 601, Apparatus 5) for the operating flow rate of 45 LPM.

CFD Models

Computational Domain and Spatial Discretization

The computational domain for the 5-6-year-old upper airway and growth chamber replicates the experimental model as closely as possible, with numerical extensions added as needed to ensure fully-developed flow enters the model inlets. As the CFD model in this study neglects the device and patient interface, the inlet to the computational domain begins 5 mm downstream of the nostrils, which is consistent with insertion of the cannula prongs into the soft nose of the *in vitro* model. The inlet boundary is the elliptical cross-section of the cannula prongs, with the surface between the nostrils and prongs defined as walls to represent the air-tight seal between the cannula and soft nose. All other inlet, outlet, and fluid-side wall boundaries are consistent between the computational domain and *in vitro* model. The CFD model geometry was generated by combining the flow path in the upper airway with the internal volume of the growth chamber, and the solid parts of the TB region were subtracted from the air-side volume to include the thickness of the model components in the chamber region. For CFD evaluation of all three age groups, a similar approach was used to generate the 2-3- and 9-10-year-old models, using the same size growth chambers, with all geometries created in SpaceClaim v19.3. Figure 7.3a shows the full geometry, including the upper airway and growth chamber, for the 5-6-year-old CFD model, with Figure 7.3b-d showing only the upper airway geometry for the 2-3-, 5-6-, and 9-10-year-old CFD models, respectively. The cannula prong inlets on all three models were dimensioned to have similar areas, and hence provide similar inlet velocities given a flow rate of 5 LPM, but the major and minor radii of the elliptical prongs differed slightly to accommodate the different nostril

shapes. For the 2-3- and 9-10-year old models, the major and minor radii were 2.5 and 4.5 mm respectively, which gave an average inlet velocity of approximately 2.36 m/s. For the 5-6-year-old model, the major and minor radii were 2.25 and 5.25 mm respectively, which gave an average inlet velocity of 2.25 m/s. As there is only a 0.1 m/s absolute difference in inlet velocity between the models (5.0% relative difference) the effect of changing cannula prongs on NT deposition is expected to be negligible and is a necessary modification to accommodate differing nostril dimensions. Also note that the angular rotation of prongs was different among all three models to fit the specific characteristics of each patient. The effect of these alterations to the cannula design on patient interface deposition is not known at this time.

Spatial discretization of the computational domain was performed by utilizing the meshing capabilities available in FLUENT v19.3 (ANSYS Inc., Canonsburg, PA). An unstructured mesh approach, as opposed to structured hexahedral cells, was used to accurately resolve the complexity of the nasal passage surfaces and the transition from the upper airway to growth chamber regions. Instead of traditional tetrahedral-type cells, polyhedral cells were used to discretize the computational domain, which our group has previously shown to be more computationally efficient and equally as accurate for modeling particle transport through the upper airways (Bass, Boc, et al., 2019). Our previous model development work has also identified that the near-wall (NW) mesh resolution is critical to obtaining a successful experimental validation of the CFD model (Bass & Longest, 2018b). The CFD models in the present study follow our current best practices for polyhedral meshes of the respiratory airways (Bass, Boc, et al., 2019; Bass & Longest, 2018b) with a wall y^+ value of approximately one, five prismatic NW cell layers,

and a layer-to-layer growth ratio of 1.2. As a final step, cell nodes were smoothed in FLUENT v19.3 until the orthogonal quality metric was greater than 0.15, which ensures a high-quality spatial discretization of the computational domain.

Mesh independence of the 5-6-year-old CFD model was established using the Roache method for mesh refinement studies (Roache, 1994) by comparing the volume-average velocity magnitude (v_{mag}) and turbulent kinetic energy (k) between three meshes with increasingly higher degrees of spatial resolution. The three meshes had total cell counts of 1.17, 1.98, and 4.06 million cells, which resulted in normalized grid spacing ratios of 1.51, 1.27, and 1.00 respectively. Comparing the 1.98 and 4.06 million cell meshes, the grid convergence index was less than 1% for both volume-average v_{mag} and k. Using Richardson Extrapolation (Richardson & Gaunt, 1927) to estimate the exact solution of the field quantities and comparing these values to the 1.98 million cell case, the relative error in v_{mag} and k was 0.07% and 0.45%. Therefore, the 1.98 million cell case was chosen for evaluation of the 5-6-year-old model, and its degree of spatial discretization was subsequently applied to the 2-3- and 9-10-year old models. Furthermore, the 1.98 million cell count is consistent with the previous growth chamber study by Longest et al. (2012) which used a total of 1.49 million cells.

Numerical Models and Solver Settings

The Reynolds number at each nostril inlet, given a flow rate of 5 LPM and hydraulic diameter of 6.1 mm (from the elliptical inlet boundary), was approximately 1,000, which suggests laminar flow conditions. However, changes in cross-section throughout the entire domain are known to change local flow conditions and induce turbulence in the respiratory airways (Bass, Boc, et al., 2019). As such, the low-Reynolds number (LRN)

k-ω turbulence model was implemented to model the transitional-to-turbulent flow regime. The LRN k-ω model includes an eddy viscosity damping coefficient that allows it to provide an accurate representation of the flow field in regions of both low and high levels of turbulence. As this study evaluated EEG aerosol growth, both water vapor and air are modeled as components of the continuous phase in the computational domain to account for varying degrees of relative humidity, which required the addition of multi-species and energy transport equations to the standard mass, turbulence, and continuity equations. As the gas phase is composed of both air and water vapor, and temperature is not a constant variable, the incompressible ideal gas law was used to model the fluid density.

Preliminary work on model development showed a jet formed as the flow passed through the constriction of the glottis in the larynx (laryngeal jet), and this jet exhibits transient behavior by oscillating back and forth through the trachea. The laryngeal jet phenomenon is consistent with previous observations by Xi et al. (2008) and has a significant effect on aerosol transport and deposition in the TB region. To capture this phenomenon accurately and achieve a converged solution, a transient formulation of the flow and turbulence transport equations was implemented in the CFD models. A time step of 0.005 s was sufficient to reach convergence within at most 100 iteration per time step and accurately modelled the oscillatory behavior of the laryngeal jet. A negligible difference in flow field and particle deposition results was also observed when decreasing the time step to 0.002 and 0.001 s, so using a time step of 0.005 s was deemed sufficient for all CFD models. The flow field was initialized with quiescent conditions and a water vapor mass fraction that was consistent with either room or humid airway conditions. Monitoring plots of volume-average v_{mag} and k against flow time showed that the

transient start-up plateaued after approximately 0.5 s, so a total simulation time of 1.0 s was used for all CFD models. As an alternative and more computationally efficient method of tracking particles simultaneously with the flow field solution, particle trajectories were calculated at a single representative time step, as opposed to tracking particles throughout the full simulation duration. To ensure particle deposition and residence time was not vastly different between time steps, trajectories were calculated in the 5-6-year-old model every 0.25 s, with the maximum absolute deviation from the mean deposition fraction (DF) being 0.4% and the maximum absolute deviation from the mean residence time being 0.3 s.

FLUENT v19.3 (ANSYS Inc., Canonsburg, PA) was used to obtain solutions for all flow and turbulence equations, and all settings for modeling particle transport in the respiratory airways followed our previously defined best practices (Bass, Boc, et al., 2019; Bass & Longest, 2018b). The spatial discretization of the flow and turbulence transport equations were second-order accurate, the gradient discretization used the Green-Gauss Node-based method, and the SIMPLEC pressure-velocity coupling scheme was used. Further details on the mass, momentum, and turbulence transport equations are available in our previous publications (Longest et al., 2007; Longest et al., 2006). All inlet boundaries used mass flow inlet conditions, with the nostril inlets (see Label 1 in Figure 7.1) each assigned a mass flow that gave a volumetric flow rate of 5 LPM (based on the 10 LPM device flow rate). The two one-way valve inlets (see Label 2 in Figure 7.1) were each assigned a mass flow rate that gave a volumetric flow rate of 17.5 LPM, which totaled a flow rate of 45 LPM through the model outlet to match the NGI operating conditions (see Label 3 in Figure 7.1). Considering the water vapor entering the domain

294

under humid airway conditions, the water vapor mass fraction at the one-way valve inlets was consistent with the 99% RH at 37°C in the environmental chamber. As the device was actuated with compressed air from a wall outlet, the water vapor mass fraction at the nostril inlets was consistent with the 10% RH that is expected from dry wall air. All wall boundaries in the CFD model use the no slip shear condition, the effects of surface roughness on the flow field and particle trajectories were neglected, and the deposit-on-touch particle boundary condition was used to model deposition. As the walls of the *in vitro* model were pre-wetted to be representative of upper airway conditions, the water vapor mass fraction on all model walls was 99% RH at a wall temperature of 37°C.

Particle Transport and Growth

The discrete phase model (DPM) available in FLUENT v19.3 was used to calculate the particle trajectories and deposition through the domain, with the Runge-Kutta scheme selected to integrate the particle equations of motion. All DPM settings followed our previously defined best practices and modeling recommendations (Bass, Boc, et al., 2019; Bass & Longest, 2018b; Longest & Xi, 2007; Walenga & Longest, 2016), which have been validated against experimental deposition data in the upper airways. NW corrections, implemented via FLUENT user-defined functions (UDFs), were applied to correct the over-prediction of micro-particle deposition that is often observed with the LRN k-ω model. These NW corrections have been discussed in detail in our previous studies (Bass, Boc, et al., 2019; Bass & Longest, 2018b; Longest & Xi, 2007) and provide an accurate match between CFD and experimental deposition data. The effect of two-way coupling between the flow field and particles, which is where the particle trajectories and growth influence the continuous phase and *vice versa*, was evaluated as a possible

295

improvement to matching numerical and experimental growth results. This is in contrast to one-way coupling where only the flow field influences the particle trajectories and growth. For two-way coupling, changes to water vapor mass fractions in the continuous phase, based on mass transfer in and out of the discrete phase, is implemented via a UDF and was previously described by Longest and Hindle (2011). Preliminary work showed that a monodisperse aerosol, as opposed to using a polydisperse size distribution, was capable of providing the expected aerosol growth and minimized computational expense. When evaluating two-way particle tracking, reducing processing times is an important consideration due to the additional computational requirements. The initial particle diameter entering the nostrils is based on the 1.53 μm MMAD for the best-case device and nasal cannula combination from Farkas et al. (2020). To ensure particle convergence, a total of 10,000 particles were introduced to the domain, with 5,000 particles at each nostril inlet.

The current study implemented an enhancement to the NW correction UDFs regarding the threshold, below which, the damping of the wall-normal velocity is applied to model particle-wall hydrodynamic interactions. Previous versions of the NW correction UDFs used a critical wall-normal distance between the particle and wall (called the NW limit), and the wall-normal velocity was damped in the region below this value, with CFD models using a typical NW limit value of 1-2 μm (Bass, Boc, et al., 2019; Bass & Longest, 2018b). A drawback to this approach in the current study is that there is a vast difference between the average velocity in the upper airways and growth chamber, so a single NW limit value was not able to achieve adequate model validation for both regions. Therefore, a local Stokes number was implemented to define the criterion for damping the wall-

296

normal velocity as a non-dimensionalized approach. The local Stokes number (Stk_l) was defined as:

$$\text{Stk}_l = \frac{v_p \rho_p d_p^2 C_c}{18 \mu_f h_p} \tag{7.3.1}$$

where: v_p is the particle velocity magnitude, ρ_p is the particle density, d_p is the particle diameter, C_c is the Cunningham slip correction factor, μ_f is the fluid viscosity, and h_p is the wall-normal distance between the particle and wall. With this implementation of the NW correction UDFs, a critical Stk_l of 15 was used to determine whether the wall-normal velocity is damped (as opposed to the NW limit), which gave the best validation with experimental deposition data throughout the model geometry.

As a dry particle absorbs water from the humid airways it becomes a droplet, with this condensation (as well as evaporation) of water implemented in FLUENT v19.3 via a UDF. Longest and Xi (2008) originally reported the heat and mass transfer model for multicomponent hygroscopic aerosols in the respiratory airways that was used in the current study. These aerosol growth UDFs have been successfully validated against experimental data in a simplified coiled tube geometry (Longest & Hindle, 2012), adult growth chamber models (Longest et al., 2015; Longest, Tian, Li, et al., 2012), and for noninvasive ventilation high flow therapy (Golshahi et al., 2013). The mass flux between the droplet and humid ambient air is dependent on the mass fraction of water vapor on the surface of the droplet ($Y_{v,s}$), which is given as:

$$Y_{v,s} = \frac{P_{v,s} S}{\rho_f R_v T_d} \tag{7.3.2}$$

where: S is the water activity coefficient, $P_{v,s}$ is the water vapor saturation pressure, ρ_f is the fluid density, R_v is water vapor gas constant, and T_d is the droplet temperature. In

Equation (7.3.2), the water vapor saturation pressure ($P_{v,s}$) is a function of the droplet temperature, which is calculated in the growth UDFs with the Antoine equation and includes the influence of the Kelvin effect, as follows:

$$P_{v,s} = \exp\left(\frac{23.196 - 3816.44}{T_d - 46.13}\right) \times \exp\left(\frac{4\sigma_d}{d_d\rho_d R_v T_d}\right) \tag{7.3.3}$$

where: σ_d is the droplet surface tension, d_d is the droplet diameter, and ρ_d is the droplet density. In Equation (7.3.3), the droplet surface tension is a function of the droplet temperature, which is given by:

$$\sigma_d = 0.0761 - 1.55E\text{-}4(T_d - 273) \tag{7.3.4}$$

In Equation (7.3.2), the water activity coefficient (S) is given by:

$$S = \left(1 + \frac{i_{AS}\chi_{AS} + i_{MN}\chi_{MN} + i_L\chi_L}{\chi_w}\right)^{-1} \tag{7.3.5}$$

where: i represents the component van't Hoff factors, χ represents the component mole fraction, and the subscripts AS, MN, and L are the Albuterol Sulfate, Mannitol, and I-Leucine formulation components, respectively. The growth UDFs calculate the mass flux (Δm_w) to or from the droplet from condensation and evaporation as:

$$\Delta m_w = \rho_f h_m (Y_{v,s} - Y_{v,f}) \tag{7.3.6}$$

where: h_m is the mass transfer coefficient and $Y_{v,f}$ is the mass fraction of water vapor in the ambient air. In Equation (7.3.6), the mass transfer coefficient (h_m) is given as:

$$h_m = \text{Sh}\frac{D}{d_d} \tag{7.3.7}$$

where: Sh is the Sherwood number and D is the mass diffusivity. Further details on the specifics of the particle growth UDFs with regard to growth chamber models were

described by Longest et al. (2012), and the material and hygroscopic properties for the drug and the excipients were presented by Longest and Hindle (2011).

7.4   Results

Experimental Aerosol Deposition and Growth

Table 7.2 summarizes the aerosol deposition and growth results from experimental testing of the 5-6-year-old model under room (22.0°C and 33.5% RH) and airway (37.0°C and 99.0% RH) conditions. The mean (standard deviation (SD)) delivery system ED (exiting the cannula and based on the device loaded dose) was 80.1% (3.6%) and 79.4% (2.8%) for room and airway conditions respectively, which is consistent with the previous experimental testing of the same device and nasal cannula combination by Farkas et al. (2020) (reported as 79.5% (2.6%)). N2L aerosol transmission was very good and provided high-efficiency delivery to the lower airways (B4+), with mean (SD) NT-B3 deposition losses of 4.2% (0.9%) and 5.3% (2.3) for room and airway conditions, respectively. Comparing upper airway losses between the room and airway results shows EEG aerosol growth in the humid conditions does not affect impaction deposition in the NT and TB regions, and is hence capable of targeting the lower airways, as there is no statistical significance between the room and airway NT-B3 DFs (p-value = 0.25). *In vitro* losses in the growth chamber were below the acceptable limit (<5%) under both the room and airway conditions with mean (SD) DFs of 3.7% (2.1%) and 0.9% (0.6%), respectively. There was a significant increase in growth chamber losses under room conditions compared to the humid experimental test (p-value = 0.03), which may be attributed to increased static charge on the cast acrylic cylinder when humidity is relatively low.

The aerosol MMAD at the growth chamber outlet under room conditions is significantly larger (p-value = 0.002) than the aerosol size at the cannula prong outlet reported by Farkas et al. (2020), with mean (SD) MMADs of 1.70 (0.05) µm and 1.53 (0.03) µm respectively. This result is consistent with observations from the growth chamber study from Longest et al. (2012). At this time, it is unclear whether a small amount of hygroscopic growth occurs in the *in vitro* model under room conditions, or whether deposition associated with Brownian diffusion and turbulent dispersion increases the aerosol MMAD at the growth chamber outlet. Comparing aerosol growth between the room and airway conditions, the MMAD increased from 1.70 µm to 3.49 µm (with an absolute difference of 1.49 µm MMAD or growth ratio of 1.9) due to humidity in the respiratory airways, which is expected to provide targeted drug delivery to the lower airways.

CFD Model Validation

The validation of CFD-predicted aerosol deposition and growth with experimental data is illustrated in Figure 7.4. Figure 7.4a shows deposition results in the computational domain under room conditions, with DFs based on the ED from the delivery system (as opposed to loaded dose), due to the fact that the CFD model does not include the device or patient interface. Numerical deposition predictions in the NT-B3 model and growth chamber regions match the *in vitro* data well and are within the experimental SD, which indicates successful validation of the particle tracking models. CFD predictions of depositional losses in the growth chamber are somewhat lower than the experimental results, but as mentioned previously, it is suspected that static charge on the acrylic cylinder walls increased losses in this region. The CFD models do not include the effect

of static charge on wall boundaries, and hence this behavior was not accounted for in the numerical deposition results. As stated in the Methods, a 10 mm coupling region between the healthy NT and CF-diseased TB regions was required in the model geometry. Deposition patterns in the trachea, where the coupling region is located, do not show any signs of abnormal deposition, which suggests the steps taken to connect the NT and TB regions do not adversely affect interpretation of the results. Due to the relatively small amount of hygroscopic particle growth that occurs under room conditions, aerosol MMADs are not compared between experiments and CFD results in Figure 7.4a.

Figure 7.4b compares aerosol deposition and growth between experimental and numerical data under humid airway conditions, with one-way coupling between the continuous and discrete phase. As with the results from room conditions, CFD-prediction of DFs in the NT-B3 model and growth chamber regions are well validated against *in vitro* data and fall within the experimental SDs. A small decrease in airway model deposition fraction was observed for humid airway conditions, which is surprising considering that aerosol size increase should increase deposition by impaction. However, this small decrease can be attributed to the random nature of both the turbulent dispersion model and anisotropic NW turbulence corrections, and may also stem from small variations in the flow fields for each case. That said, both CFD models are well validated and fall within the experimental SDs for aerosol deposition, so the CFD predictions are considered an accurate representation of particle transport. There was also no statistical significance between NT-B3 losses when comparing experimental results under room and airway conditions, so the DF increase that was observed during *in vitro* testing cannot be attributed only to the presence of humidity. Looking at losses in the growth chamber, static

charge on the cylinder walls is expected to be lower under humid conditions, and this supports the decrease in deposition losses in this region that is seen in Figure 7.4b. The CFD-predicted deposition on the growth chamber walls also shows a closer match to experimental results in Figure 7.4b, which reinforces the suggestion that growth chamber losses under room conditions were due to static charge on the cylinder walls. The CFD-predicted MMAD at the growth chamber outlet compares well to the *in vitro* data, which indicates successful validation of the one-way coupled particle transport models and evaporation/condensation UDFs.

Comparisons between the one-way and two-way coupled particle tracking methods for aerosol deposition and growth are provided in Table 7.3. This shows there is little difference between the two methods in the current study, with a maximum absolute difference between two-way and one-way particle tracking for NT-B3 DF, Chamber DF, and outlet MMAD of 0.1%, 0.7%, and 0.06 μm respectively. For two-way coupling, results are presented for both 10 and 20 coupled cycles between the continuous and discrete phase, which shows that doubling the number of coupled cycles does not influence aerosol deposition and growth. Two-way coupled particle tracking consumes water vapor (and reduces the RH) from the continuous phase as the particles grow under humid conditions, but the relatively large volume of the growth chamber region means a large amount of humid air is available, which is the most likely reason why there is little apparent difference between one-way and two-way coupled particle tracking in the current study. When considering particle paths through narrow airway bifurcations with less volume, the effect of using with one-way or two-coupled particle tracking may be more pronounced.

As the CFD model is well validated against experimental results using one-way particle tracking (see Figure 7.4), this method is used throughout the remainder of this study.

Flow Field Characteristics

Figure 7.5 shows plots of velocity magnitude and relative humidity to illustrate the flow field characteristics in the computational domain. Figure 7.5a presents a contour plot of velocity magnitude on a plane that cuts through the left nostril, nasal passage, trachea, and growth chamber. The figure demonstrates the wide range of velocity magnitudes in the CFD model; for example, the velocity magnitudes at Point A and B were 8.55 m/s and 0.16 m/s respectively. This justifies the implementation of a local Stokes number to determine the upper limit of the NW region, below which, wall-normal velocity is damped to model particle-wall hydrodynamic interactions. The inset in Figure 7.5a shows a close-up view of flow through the larynx and clearly illustrates the laryngeal jet phenomena. Similarly, Figure 7.5c shows the three-dimensional nature of the laryngeal jet with an iso-surface of 7.0 m/s velocity magnitude through the trachea.

Figure 7.5b shows contours of relative humidity on the same plane as Figure 7.5a, with the inset providing a close-up view of the nostrils and anterior nose. This illustrates the introduction of the dry actuation air (at 10% RH) to the computational domain, which is delivered from the cannula prong outlets in the experimental model. By the time the flow reaches the nasopharynx region, observations from the CFD model show the dry air has mixed with the humid air and RH values are greater than approximately 90%. Conditions in the growth chamber are close to 99% RH, which facilitates aerosol growth and provides an accurate representation of the respiratory airways. Figure 7.5d shows an

303

iso-surface of 80% RH in the nasal passage and further illustrates mixing of dry and humid air in the anterior region of the nose.

Residence Time and Maximum Particle Growth

Figure 7.6 plots the particle diameter (as MMAD) vs. residence time for the 5-6-year-old CFD model. The points represent the diameter and time for each individual particle that was tracked through the domain, at the time that they either deposited or exited the mixing chamber, up to a maximum time of 5.0 s. The red dotted line shows a logistic best-fit curve that represents the average particle diameter vs. residence time profile, which is given by:

$$d_p = \frac{2.67}{0.75 + \exp(-4.5t)}$$
(7.4.1)

where: d_p is the particle diameter and t is the particle residence time. This shows that the MMAD begins to plateau around 1.2 s and levels off completely by a residence time of 2.0 s. As $t \to \infty$ in Equation (7.4.1), the particle diameter (d_p) approaches an MMAD of 3.56 µm. From this, the t_{90} is defined as the residence time used in Equation (7.4.1) that gives an MMAD that is 90% of 3.56 µm, which for this case is 0.55 s. Therefore, a residence time of approximately 2.0 s is more than sufficient to maximize aerosol growth and target drug delivery in the lower airways.

Comparison of Deposition and Growth between Age Groups

CFD predicted particle trajectories (colored by MMAD) and regional DFs are presented in Figure 7.7. All three models show that the particle MMADs were less than approximately 2.5 µm when the aerosol leaves the upper airways (NT-B3) and enters the growth chamber. This suggests the hygroscopic properties of the powder formulation are capable of targeting drug delivery to the lower airways (B4+). This claim was further

supported with CFD predictions of relatively low aerosol deposition in the NT-B3 region for all age groups. The MMADs at the outlet of the growth chamber for the 2-3- (Figure 7.7a) and 9-10-year-old (Figure 7.7c) models were 3.40 µm and 3.47 µm respectively, which is consistent with the 3.38 µm MMAD from the 5-6-year-old model (Figure 7.4b and Figure 7.7b). As stated above, a residence time of approximately 0.55 s was required to reach 90% of the average final particle size for the 5-6-year-old model. Similar expectations can be applied to the 2-3- and 9-10-year-old age groups, based on the consistency in CFD predictions of aerosol growth between all three models. The relatively large increase in aerosol size (absolute increase of 1.49 µm MMAD or a growth ratio of 1.9) suggests the EEG powder formulation is capable of targeting the lower airways. The larger particle diameters in the lower airways are expected to reduce exhalation losses with an increase in particle momentum and impaction, and improve lung retention with an increase in sedimentation deposition (if a breath hold maneuver is employed).

As mentioned previously, the delivery system and powder formulation provide high-efficiency N2L transmission in the 5-6-year-old model with a NT-B3 DF of 4.8%, as shown by both Figure 7.4b and Figure 7.7b. For the 2-3-year-old model in Figure 7.7a, the NT-B3 losses are higher than the 5-6-year-old with a CFD-predicted DF of 10.9%. This increase in upper airway losses can be attributed to the smaller airway dimensions in the younger patient (see Table 7.1), which leads to an increase in impaction deposition. For the 9-10-year-old model in Figure 7.7c, the NT-B3 losses are also higher than the 5-6-year-old with a CFD-predicted DF of 7.0%. In this case, the increased losses are most likely due to the increase in length of the upper airways, which leads to longer residence times and more hygroscopic growth in the NT-B3 region. Looking at the particle

trajectories in Figure 7.7c, the MMADs in the 9-10-year-old model are approximately 2.5 µm around the glottis, whereas the MMADs in a similar region for the 2-3- and 5-6-year-old models is less than approximately 1.75 µm. The increased particle size in the upper airways for the 9-10-year-old caused more impaction losses and accounts for the small increase in NT-B3 DFs. Despite the 2-3- and 9-10-year-old models having slightly higher deposition in the NT-B3 region than the 5-6-year-old model, upper airway losses were relatively low for all three cases and expected drug delivery to the lower airways (B4+) was high. Upper airway losses may be improved by designing air-jet DPIs specifically for the 2-3 and 9-10-year-old age groups.

7.5 Discussion

This study meets the objective by using a concurrent numerical and experimental approach to demonstrate EEG powder formulations are capable of targeting the lower airways (B4+) with N2L transmission through the diseased airways of pediatric patients with CF. Upper airway losses (NT-B3) for the 2-3-, 5-6-, and 9-10-year-old age groups were 10.9%, 4.8%, and 7.0%, respectively. Furthermore, the experimental results in Table 7.2 show upper airway penetration fractions of approximately 70%, which is a vast improvement to lung doses in pediatric patients compared to commercial devices. For example, Below et al. (2013) reported that the Novolizer and Easyhaler provide a lung dose (with respect to nominal dose) of 5% and 22%, respectively, on the tracheal filter of a 4-5-year-old *in vitro* model. For the Cyclohaler, HandiHaler, and Spinhaler, Linder et al. (2014) reported lung delivery efficiencies of 9% to 11%. The validated CFD models showed the aerosol MMAD is expected to grow to at least 3.3 µm in the lower airways after a residence time of approximately two seconds. As aerosol MMADs greater than 2.5

306

μm are expected to be retained in the lungs (Longest et al., 2015), this demonstrates EEG powder formulations are capable of maximizing lung dose in the diseased airways. Both N2L transmission and lung retention may be improved further by designing devices and powder formulations that are specific to each age group. Results in Figure 7.7 showed differences in NT-B3 losses between the three models, which are attributed to differences in airway dimensions between patients at different ages (see Table 7.1).

As a secondary outcome of this study, a locally-defined Stokes number (see Equation (2.3.1)) was implemented for the first time to define the NW region where wall-normal velocities are damped to model particle-wall hydrodynamic interactions. This approach led to successful validation of the CFD model by matching experimental particle deposition data in both the upper airways and growth chamber regions. The implementation of particle condensation and growth, as described by Equations (7.3.2) to (7.3.7), was also successfully validated by matching the experimental characterization of the aerosol MMAD at the growth chamber outlet.

A primary limitation of the current study for evaluating tobramycin delivery to CF-diseased airways is the use of AS EEG powder as a surrogate test aerosol. At this time, the hygroscopic properties of tobramycin, particularly the van't Hoff factor, have not been experimentally determined, and as such tobramycin EEG powder formulations cannot be evaluated with CFD models. Despite this limitation to the current study, inferences on the ability for the delivery system to provide highly-efficient N2L transmission are still valid, providing future tobramycin EEG powder formulation have similar hygroscopic capabilities as the AS EEG aerosol. Other limitations include the use of a growth chamber as a representation of particle growth in the lung pathways, modifications to the cannula

prongs specific to each patient, and a lack of evaluation regarding interpatient variability. The growth chamber was designed to provide a residence time of two seconds, which is consistent with transport through the airways, but particle trajectories through lung bifurcations are vastly different and may have an influence on aerosol growth. As such, evaluation of EEG aerosol transport and growth through complete airways of CF-diseased lungs is required, which may be modelled using the stochastic individual pathway methodology (Longest et al., 2015; Longest & Hindle, 2009a; Longest et al., 2007; Longest, Tian, Delvadia, et al., 2012; Longest, Tian, Walenga, et al., 2012; Longest & Vinchurkar, 2007b; Tian et al., 2011; Walenga & Longest, 2016). Modifying the cannula prong dimensions and angular rotation for the 2-3- and 9-10-year-old age groups may influence upstream losses in the patient interface. If device development of age-specific devices is conducted, the effect of modifying the cannula design can be tested at the same time. Finally, the current study evaluated a single upper airway model for each of the three age groups, but interpatient variability is known to be significant for nasal deposition of aerosols (Garcia, Tewksbury, Wong, & Kimbell, 2009; Golshahi, Noga, & Finlay, 2012; Golshahi et al., 2011; Storey-Bishoff et al., 2008) and should be taken into consideration.

Future work should intend to address the limitations of the current study that are outlined above, including the evaluation of cannula modifications and expectations for interpatient variability. The most important consideration for future work is to identify the hygroscopic properties of tobramycin and conduct CFD-based evaluation of tobramycin EEG aerosol transport through complete airway models. Identification of optimal powder formulations is required to maximize lung delivery and retention, which can be tested by

changing the fractions and types of hygroscopic excipients. Two-way coupled particle tracking should also be reconsidered in complete airway models, as the reduced volume of airway bifurcations compared to the growth chamber may cause a greater decrease in RH values in the continuous phase as the particles absorb moisture. Also, the effect of two-way coupled particle tracking is expected increase in significance as the aerosol grows beyond 3 μm (Longest & Hindle, 2010, 2012), which is true for the current powder formulation. Beyond numerical and *in vitro* testing of the air-jet DPI and 3D rod array interface, *in vivo* evaluation of tobramycin delivery to the lower airways is required. Additional validation of the locally-defined Stokes number and its implementation in the NW correction UDFs is required to determine whether it is a worthwhile enhancement for a variety of geometries and applications. Finally, future experimental work that uses growth chamber models should endeavor to minimize static charge on the cast acrylic cylinder to reduce chamber losses and provide better comparisons between the *in vitro* and CFD results.

In conclusion, three growth chamber models were developed that represent the diseased upper airways of pediatric patients diagnosed with CF in the age ranges of 2-3, 5-6, and 9-10 years old. The CFD models successfully validated aerosol deposition and growth through the computational domain against experimental data via the implementation of NW corrections and aerosol condensation and growth models. Results show that the chosen air-jet DPI and nasal cannula delivery system was capable of providing highly-efficient N2L aerosol delivery to the lower airways (B4+), with NT-B3 losses of 10.9%, 4.8%, and 7.0% for the 2-3-, 5-6-, and 9-10-year-old models respectively. Lung retention of the delivered aerosol is also expected to be high, as the

aerosol grows to an MMAD of approximately 3.4 µm in all three cases after a residence

time of approximately two seconds.

7.6   Figures
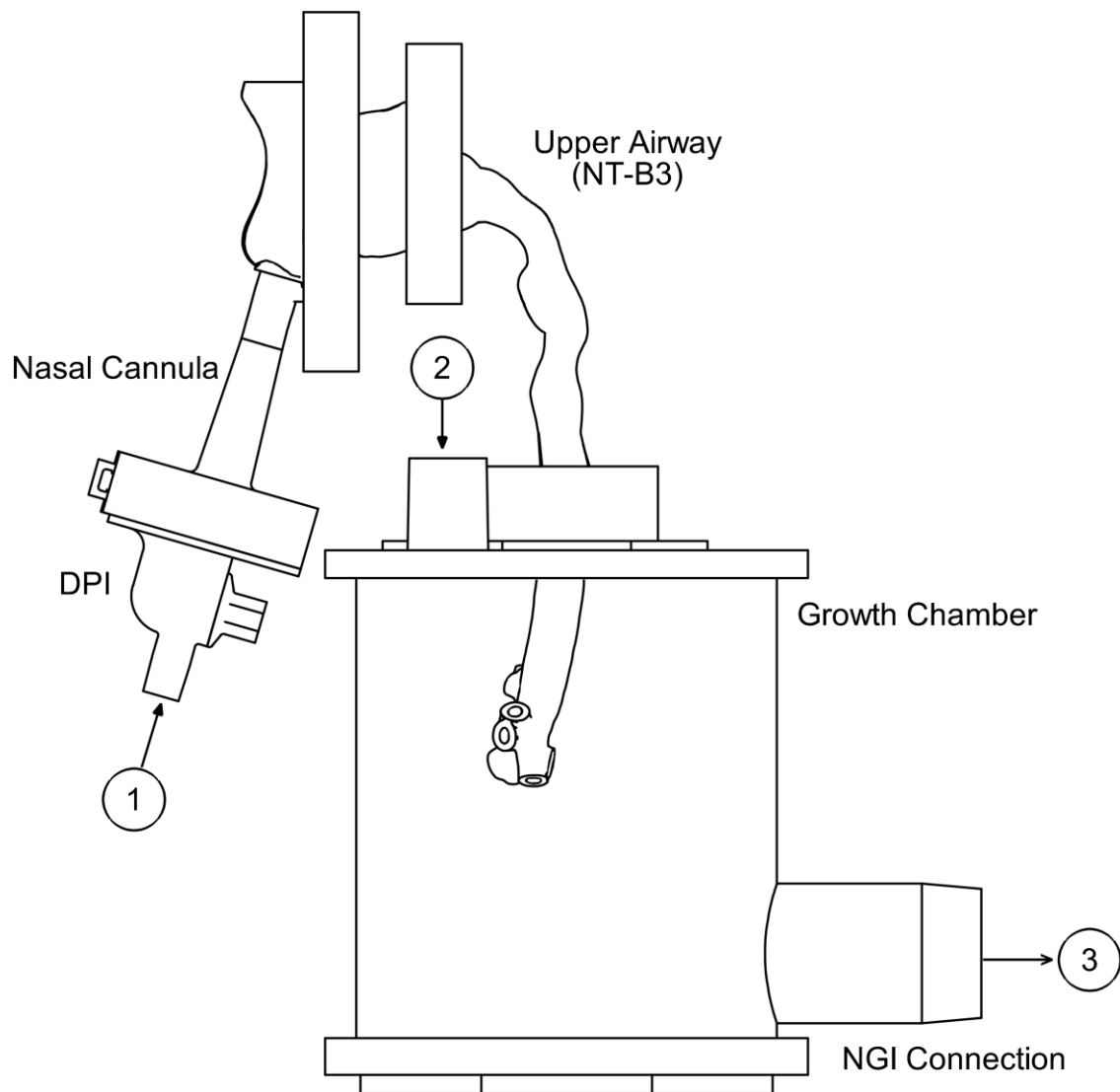
Figure 7.1:   Schematic of the experimental model showing the device (Air-jet DPI), patient interface (Nasal Cannula), *in vitro* model (Upper Airway), and two-second residence time chamber (Growth Chamber). Air flow in and out of the model is labelled (1) 10 LPM actuation air into the device, (2) 35 LPM make-up air through two one-way valves on the top of the chamber, and (3) 45 LPM to the NGI.
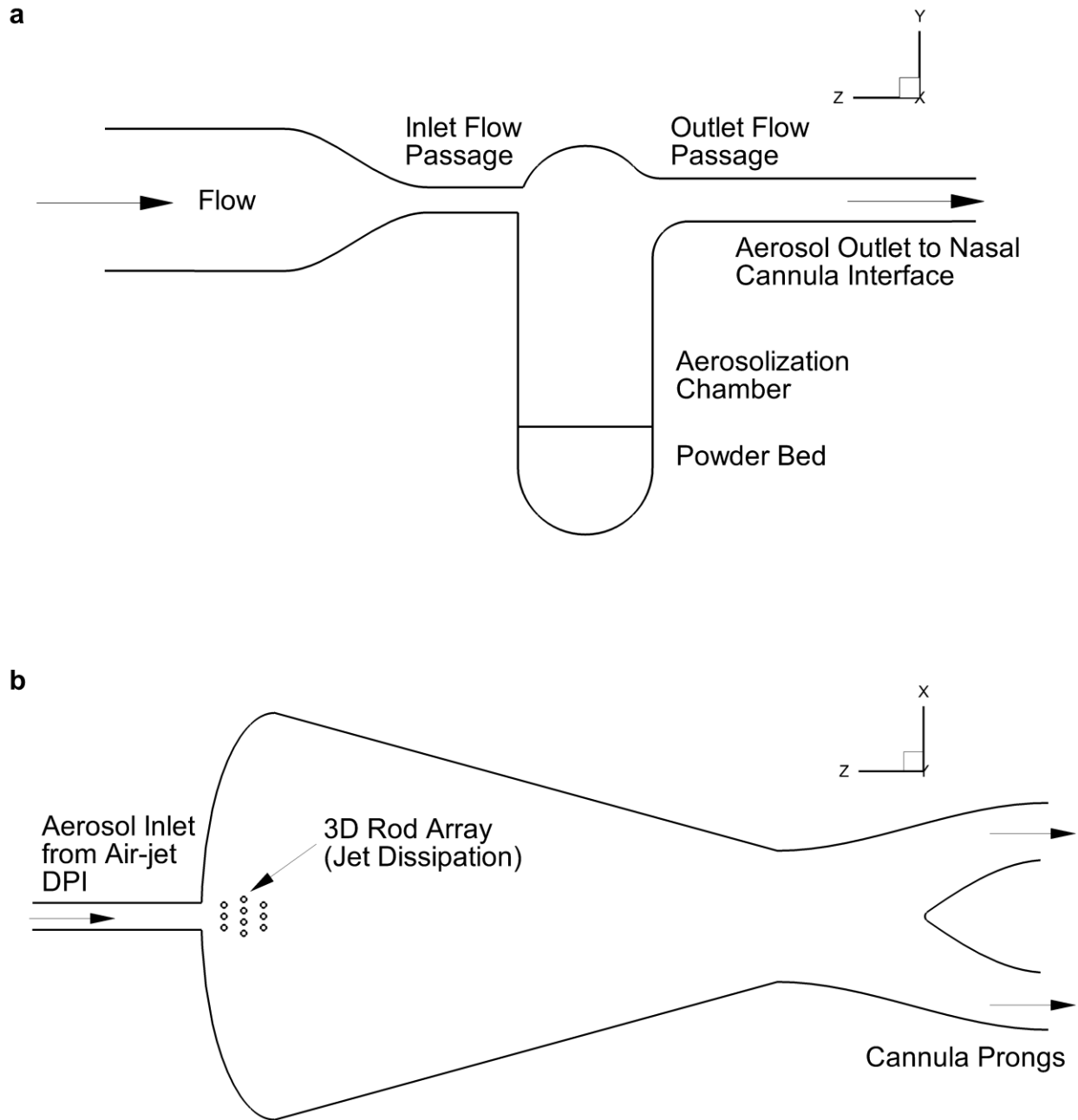
Figure 7.2: Overview of flow pathways for the best-case nose-to-lung delivery system from Farkas et al. (2020) showing (a) the air-jet dry powder inhaler with inlet and outlet flow passages and powder aerosolization chamber and (b) the 3D rod array nasal cannula. Note that the air-jet DPI and cannula interface are included in the *in vitro* portion of the study but not in the CFD models.
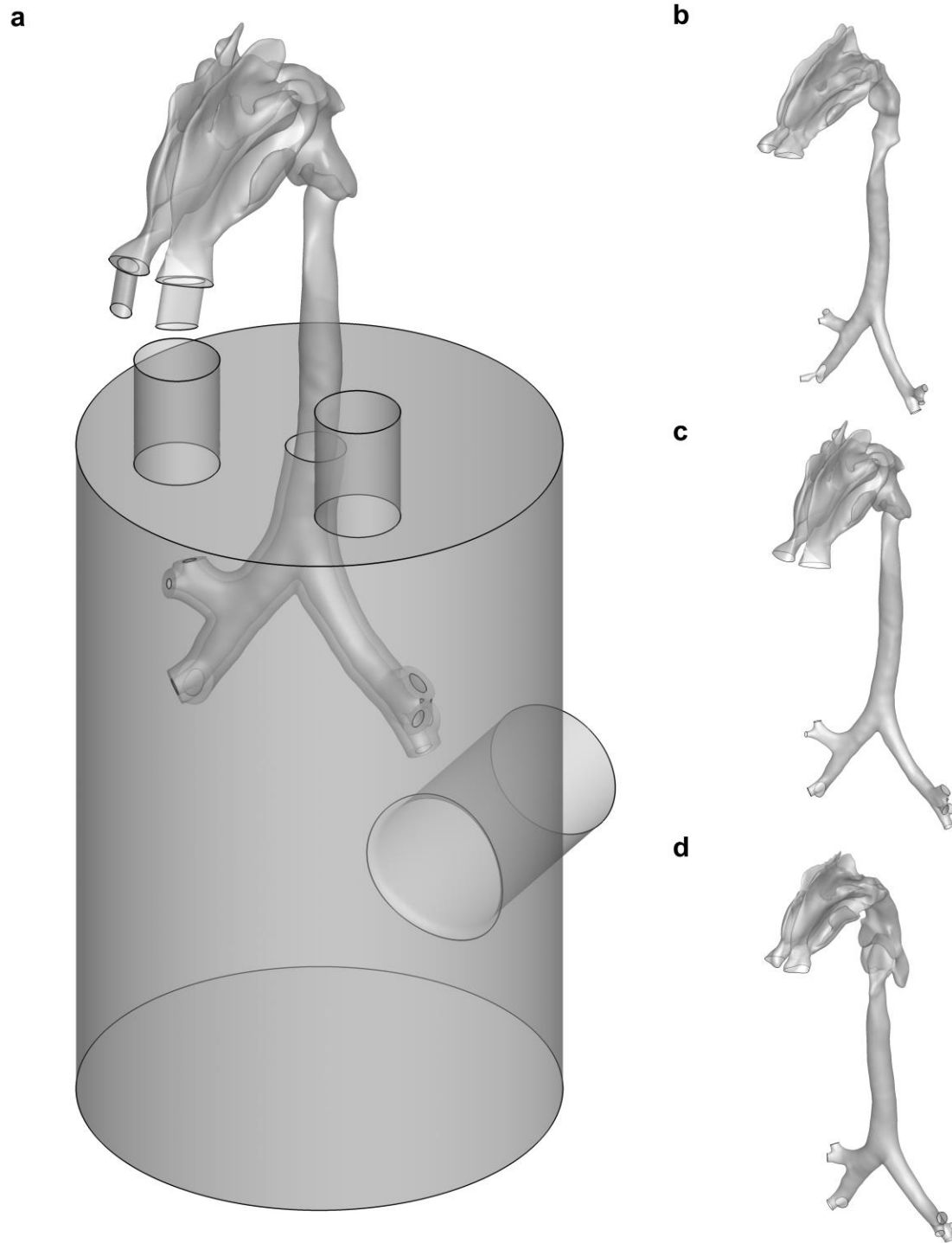
Figure 7.3:   Summary of computational domains showing (a) the full CFD model of the nose-throat, tracheobronchial region, and growth chamber for the 5-6-year-old child, (b) the nose-throat to B3 (NT-B3) for the 2-3-year-old child, (c) the NT-B3 for the 5-6-year-old child, and (d) the NT-B3 for the 9-10-year-old child.
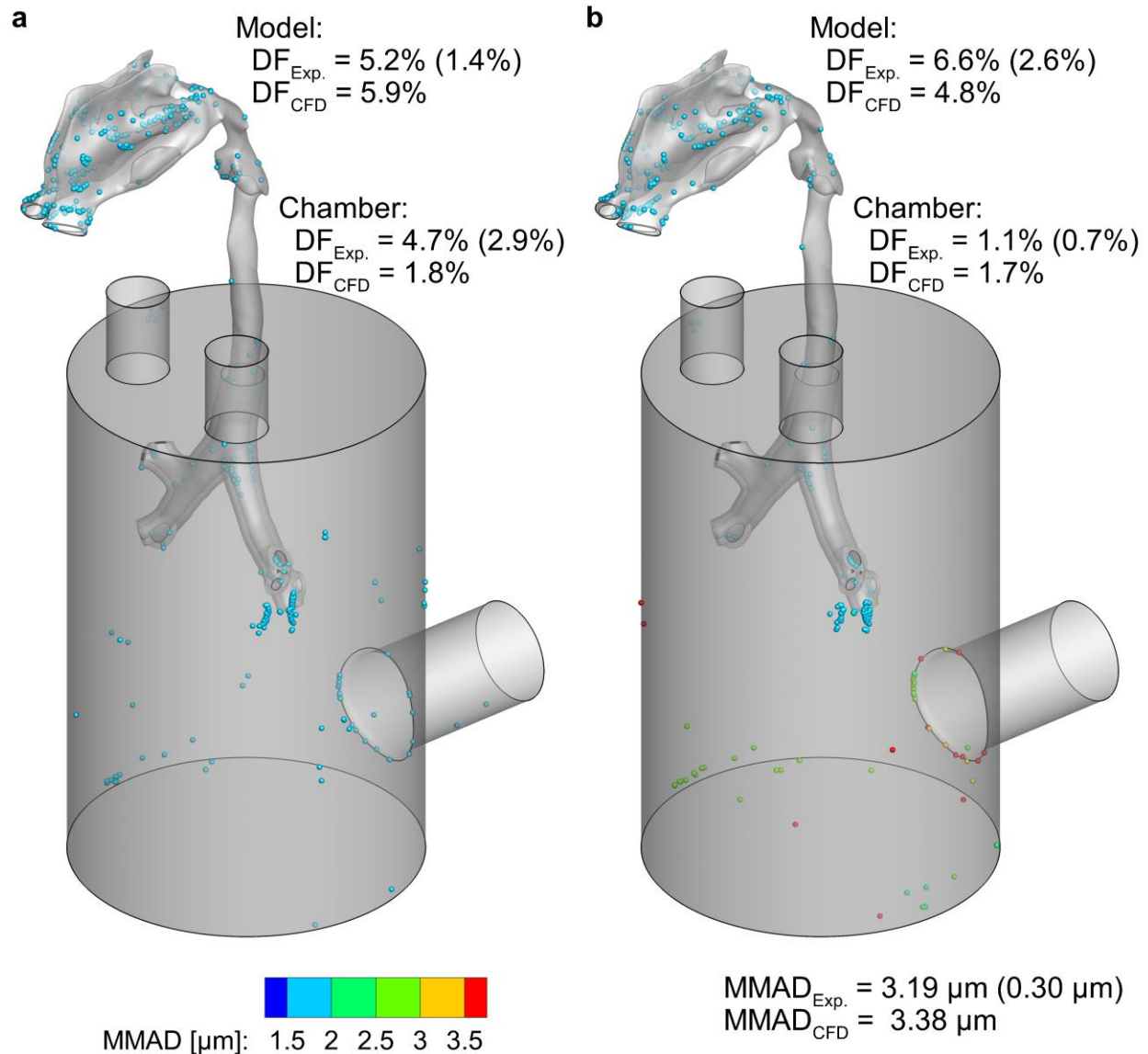
Figure 7.4: Validation of the numerical models showing (a) comparison of deposition fractions (DF) in the airway and chamber regions between the CFD and *in vitro* experimental (Exp.) results under room (i.e. no particle growth) conditions (22.0 °C and 33.5% RH) and (b) comparison of regional DF and particle mass-median aerodynamic diameter (MMAD) at the model outlet between the CFD and experimental results under upper airway conditions (37°C and 99%RH). Note that DFs here are given based on system emitted dose, instead of loaded dose, as the CFD models do not include the delivery system.
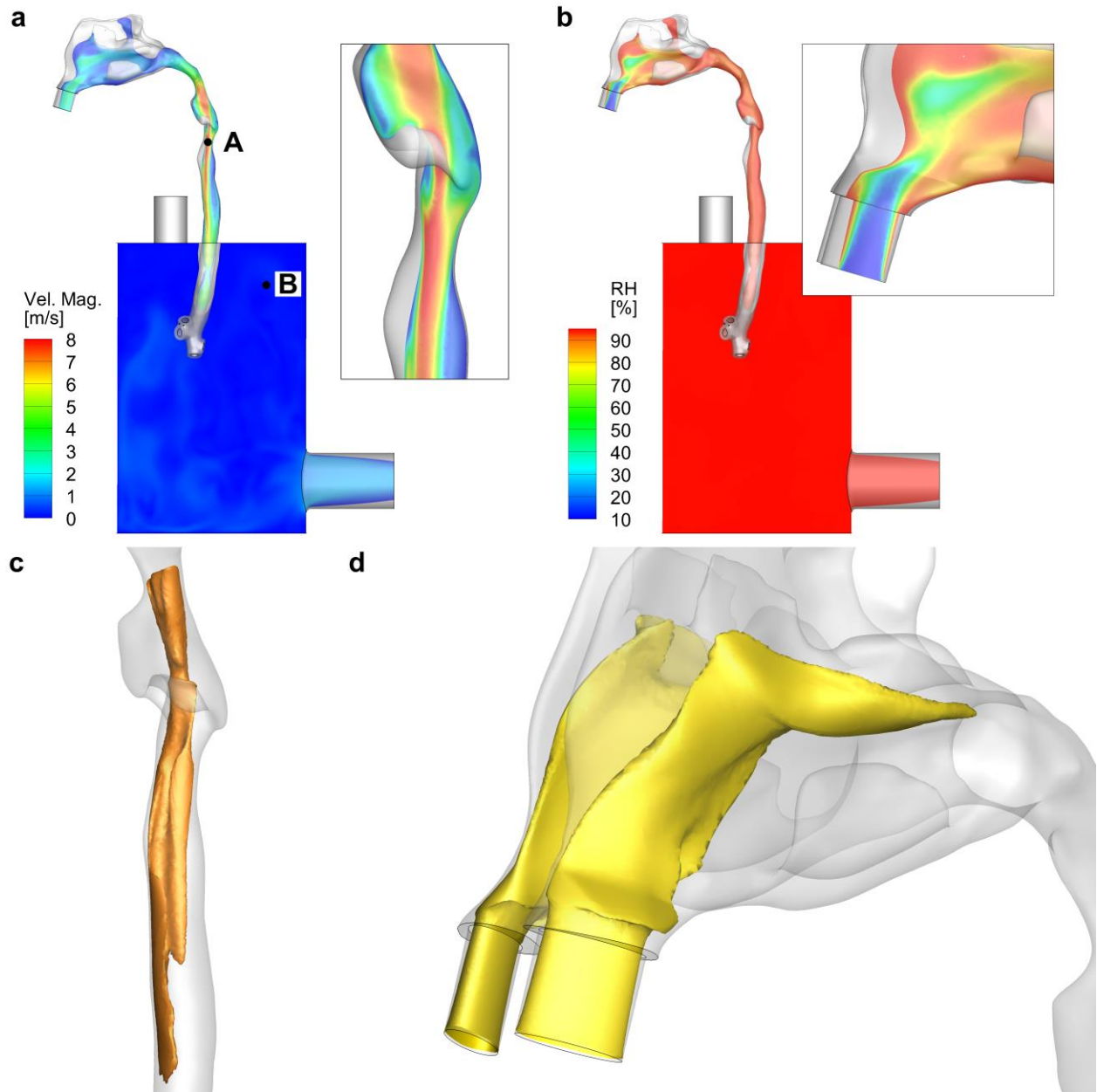
Figure 7.5: Summary of flow field characteristics in the 5-6-year-old model showing (a) contours of velocity magnitude (Vel. Mag.) with a close-up view of the laryngeal jet, (b) contours of relative humidity (RH) with a close-up view of the dry wall air (used to actuate the device) entering the *in vitro* model, (c) iso-surface of 7 m/s velocity magnitude depicting the 3D nature of the laryngeal jet, and (d) iso-surface of 80% RH in the nasal cavity.
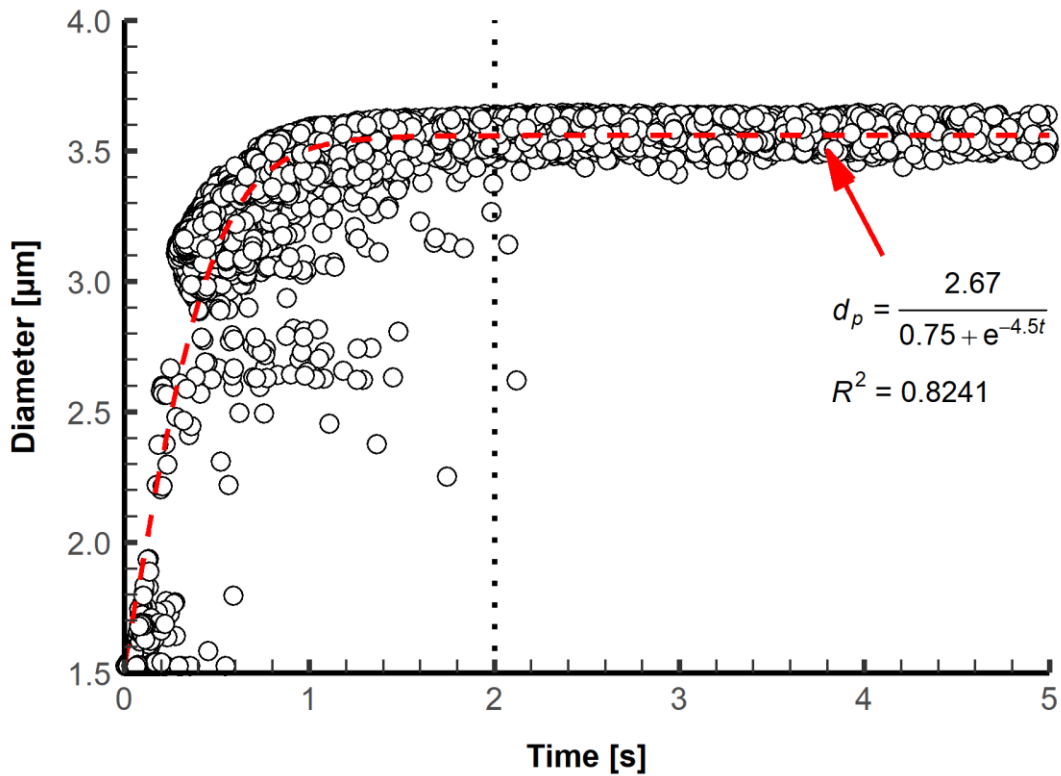
Figure 7.6: Plot of particle diameter vs. residence time, with each individual point representing the values for a single particle at the time it deposited or exited the computational domain. The red dashed line shows the best-fit curve and the dotted line marks the average chamber residence time, which shows a two-second residence time is sufficient to maximize particle growth.

The equation shown in the figure:

$$d_p = \frac{2.67}{0.75 + e^{-4.5t}}$$

$$R^2 = 0.8241$$
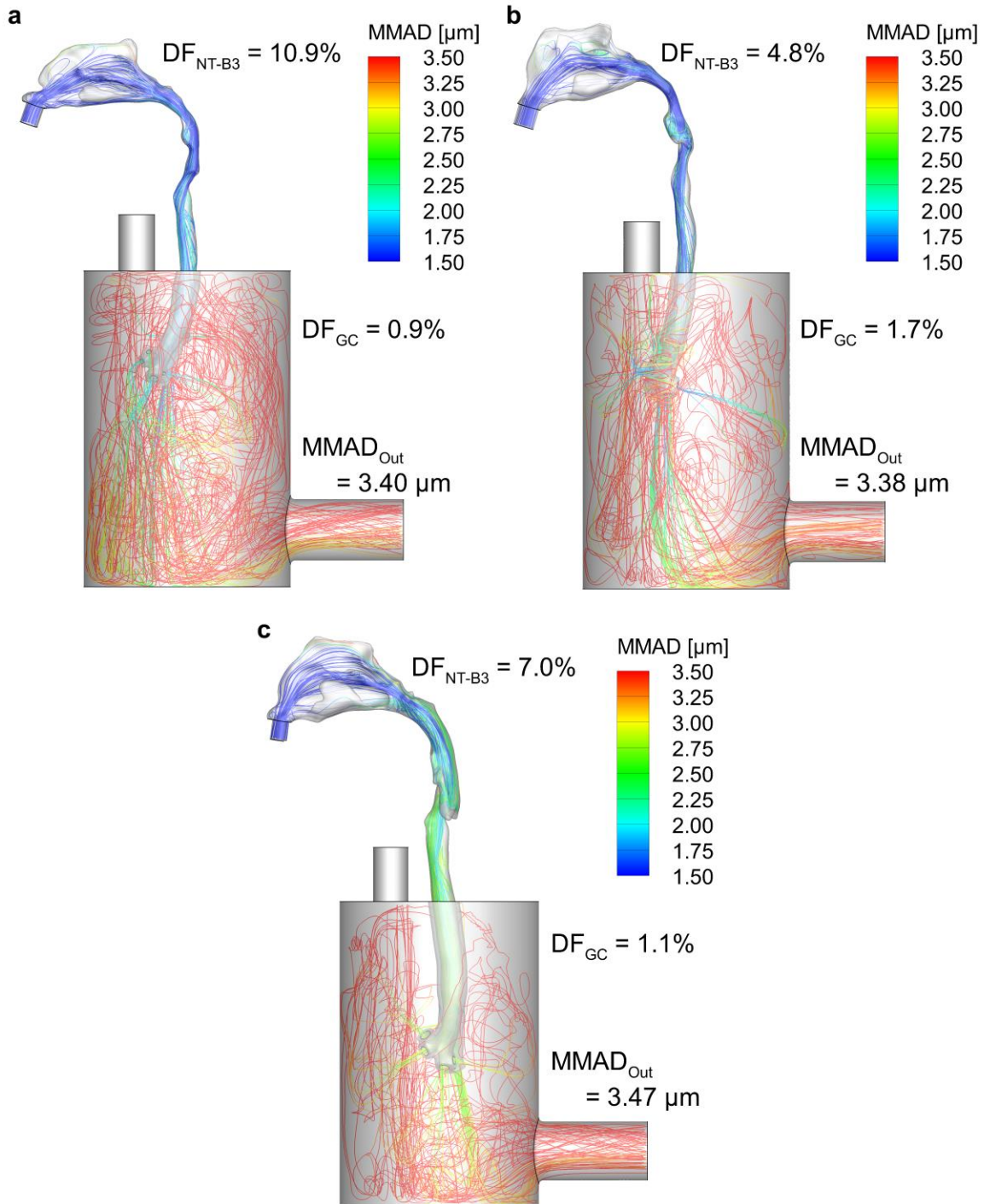
Figure 7.7: Examples of CFD-predicted particle trajectories and growth through the domain for the (a) 2-3-year-old, (b) 5-6-year-old, and (c) 9-10-year-old models, with annotations of nose-throat to Bifurcation 3 deposition fraction (DF_{NT-B3}), growth chamber deposition fraction (DF_{GC}), and outlet mass-median aerodynamic diameter ($MMAD_{Out}$).

7.7   Tables

Table 7.1:   Characteristic dimensions for the 2-3-, 5-6-, and 9-10-year-old upper airway

models.

Dimension	2-3-year-old	5-6-year-old	9-10-year-old
V [mm^3]	18,411	24,186	41,323
A_s [mm^2]	13,742	16,202	23,060
V/A_s [mm]	1.34	1.49	1.79
L_{CP} [mm]	124.4	126.4	128.5
$\sqrt{V/L_{CP}}$ [mm]	12.2	13.8	17.9
$D_{h,G}$ [mm]	5.7	6.7	6.8
L_T [mm]	64.6	75.3	97.7

V: NT-B3 volume
A_s: NT-B3 surface area
L_{CP}:   Central path length from nostrils to glottis
$D_{h,G}$:   Hydraulic diameter of the glottis
L_T: Length of trachea from glottis to carinal ridge

Table 7.2:   Summary of aerosol deposition and growth from experimental testing under room and humid airway conditions. Deposition fractions are defined based on device loaded dose. Experimental values are given as means with standard deviations shown in parenthesis [n=3].

	Room Conditions (22.0°C and 33.5% RH)	**Airway Conditions (37.0°C and 99.0% RH)**
Aerosol Deposition		
Device DF [%]	13.3 (2.1)	13.8 (3.1)
Cannula DF [%]	6.6 (1.5)	6.9 (0.5)
System ED [%]	80.1 (3.6)	79.4 (2.8)
NT-B3 DF [%]	4.2 (0.9)	5.3 (2.3)
Chamber DF [%]	3.7 (2.1)	0.9 (0.6)
Model PF [%]	70.6 (5.0)	70.1 (1.4)
Aerosol Growth		
MMAD [μm]	1.70 (0.05)	3.19 (0.30)
RH: Relative humidity		
DF: Deposition fraction		
ED: Emitted dose		
NT-B3: Nose-throat to Bifurcation 3		
PF: Penetration fraction		
MMAD: Mass-median aerodynamic diameter		

Table 7.3: Comparison of aerosol deposition and growth between the one-way and two-way coupled particle tracking methods. Deposition fractions are based on delivery system emitted dose.

	One-way Coupling	Two-way Coupling 10 Cycles	Two-way Coupling 20 Cycles
Aerosol Deposition			
NT-B3 DF [%]	4.8	4.7	4.8
Chamber DF [%]	1.7	1.2	1.0
Aerosol Growth			
MMAD [µm]	3.38	3.39	3.32
NT-B3:	Nose-throat to Bifurcation 3		
DF:	Deposition fraction		
MMAD:	Mass-median aerodynamic diameter		

Chapter 8: Extend and Develop CFD Lung Models to Predict Regional Lung Deposition and Tobramycin ASL Concentrations in Healthy and CF Complete-airway Lung Models

8.1   Objective

The objective of this study was to develop a high-efficiency aerosol delivery strategy for nose-to-lung (N2L) administration of tobramycin antibiotics to children with Cystic Fibrosis (CF) using a complete-airway computational fluid dynamics (CFD) model. The basis of the strategy is excipient enhanced growth (EEG) delivery where a small particle aerosol is initially formed and increases in size through the respiratory airways. Ideal conditions for antibiotic aerosol delivery included: (i) airway surface liquid (ASL) concentrations of tobramycin greater than the minimum inhibitory concentration (MIC) of 512 mg/L; (ii) uniform drug delivery throughout the tracheobronchial (TB) airways; and (iii) high concentrations of tobramycin in the small TB airways (which often have occlusions and trapped air). Specifically, this study aimed to: (i) determine tobramycin concentration in the ASL for N2L aerosol delivery in a 5-6-year-old complete airway model for static and EEG aerosol administration; (ii) determine the effect of CF-diseased airways on aerosol delivery for static and EEG aerosols; and (iii) determine the extent to which EEG powder formulations can overcome the challenges associated with the delivery of aerosols to partially occluded airways.

8.2   Introduction

Bacterial lung infections in patients that are diagnosed with CF can be treated by oral prophylactic antibiotics (Elborn, 2016; Hoiby, 2011), but administration of inhaled tobramycin is the preferred method as it treats *Pseudomonas aeruginosa* (*Pa*) infections

directly in the airways (Proesmans, Vermeulen, Boulanger, Verhaegen, & De Boeck, 2013; Ratjen, Munck, Kho, Angyalosi, & Grp, 2010; Taccetti et al., 2012). *Pa* is the most predominant bacteria found in the lungs of CF patients (Elborn, 2016), and early treatment in pediatric patients can prevent the development of chronic infections during childhood (Hoiby, 2011). In a series of publications, our group has developed a high-efficiency delivery system (Bass, Farkas, et al., 2019; Bass & Longest, 2020; Farkas et al., 2020; Farkas et al., 2019) for N2L administration of tobramycin EEG powder formulations to children. Most recently, the best-case air-jet dry powder inhaler (DPI) and nasal cannula system from Farkas et al. (2020) demonstrated excellent aerosolization and delivery performance, with a 1.53 μm mass-median aerodynamic diameter (MMAD) and 79.5% emitted dose (ED) from the cannula prong outlets. This delivery system is operated at a flow rate of approximately 10 LPM, which combined with an inhalation volume of 750 mL, gives an actuation time of approximately 4.5 s. The small aerosol size and hygroscopic growth of the powder formulation is expected to maximize nasal transmission and target delivery to the lower airways. Concurrent numerical and experimental evaluation in a growth chamber model of a 5-6-year-old CF patient (Chapter 7) showed low upper airway losses (6.6%) and an outlet MMAD of 3.19 μm after a residence time of approximately 2.0 s.

This study builds upon the previous work in this series by evaluating EEG aerosol transport and delivery in an anatomically-accurate, complete-airway, CFD model. The growth chamber model provides a good representation of typical aerosol residence times through the lungs, but particle trajectories through airway bifurcations are expected to be very different. Our group has developed and used stochastic individual pathway (SIP)

models for a number of studies on pharmaceutical aerosol delivery in the complete-airway CFD models. This method has been successfully validated against both *in vitro* (Longest, Tian, Delvadia, et al., 2012; Longest, Tian, Walenga, et al., 2012; Tian et al., 2011) and *in vivo* (Longest et al., 2015; Tian et al., 2015; Walenga & Longest, 2016) data sets. The current study advances SIP modeling capabilities by applying the method to pediatric patients and including the effects of CF-related airway disease on airway anatomy.

Previous work has also used albuterol sulphate (AS) EEG powder formulations as a surrogate test aerosol, as the hygroscopic properties of tobramycin were not established. The water activity characteristics for tobramycin were identified by supplemental work for this study, following a similar method as Longest and Hindle (2011), which allowed for CFD-based evaluation of tobramycin EEG powder formulations through complete-airway models. The EEG method uses an initially small aerosol size, with the particles growing in size and becoming droplets due to hygroscopic excipients that absorb moisture from the humid airways. The chosen hygroscopic excipient in this case was mannitol, which has the added benefit of improving transport though the ASL (Geller & Rubin, 2009). This study provides a proof of concept for the administration of tobramycin EEG aerosol to the diseased airways of pediatric CF patients. EEG delivery strategies are capable of navigating the natural filtration of the extrathoracic (ET) region and targeting delivery to specific airways. Lung retention can also be improved, with the larger final particle size increasing sedimentation (breath-hold) and impaction (exhalation) deposition in the lower airways. These advantages are well suited to the challenges associated with treating bacterial infection in diseased airways, as antibiotics require uniform dosing and high drug concentrations at the site of infection.

8.3   Methods

SIP Airways

The SIP methodology for complete airway modeling has been utilized in numerous studies by our group and has shown successful validation against both *in vitro* (Longest, Tian, Delvadia, et al., 2012; Longest, Tian, Walenga, et al., 2012; Tian et al., 2011) and *in vivo* (Longest et al., 2015; Walenga & Longest, 2016) data. The current study follows the most recent methodology and best practices for SIP models from Tian et al. (2015) who validated pharmaceutical aerosol deposition against *in vivo*, 2D gamma scintigraphy results. Briefly, the airways of the lungs are split into three regions that are modeled individually with CFD: (i) the upper airways consisting of the nose-throat to Bifurcation 3 (NT-B3); (ii) the middle airways (B4-B7); and (iii) the lower airways (B8-B15). Alveolar models are also available for evaluation of aerosol transport beyond B15 (Khajeh-Hosseini-Dalasm & Longest, 2015). Separating the airways into distinct regions allows for the application of the required CFD models to account for differences in flow conditions throughout the lungs. The upper airway geometry is extracted from computed tomography (CT) scans to ensure that it is anatomically accurate and specific to the chosen patient population (e.g. adults, pediatrics, and disease states). The small diameters of the middle and lower airways make it difficult to extract them from CT scans, so idealized, physically realistic bifurcation units are used for the geometry from B4-B15 (Heistracher & Hofmann, 1995). Previous work has shown that following pathways through the lower-left lobe provides a representative average of deposition in the entire lung (Longest, Tian, Delvadia, et al., 2012), so the same approach is applied in the current study as a basis for comparison between aerosol delivery strategies. However, future studies are planned

that intend to compare lobar differences between healthy and CF-diseased airways. The current study assumes a breath-hold maneuver is performed by the patient after aerosol administration, and as such all particles that leave B15 are assumed to deposit in the alveoli by sedimentation deposition. Therefore, a numerical alveolar-level aerosol transport and deposition model was not required.

The SIP models in previous work have focused on aerosol transport through adult airways. As the current study is specific to healthy and CF-diseased pediatric airways, modifications to the models must be made to account for the differences in airway dimensions and disease characteristics. For the upper airways, the NT-B3 region is extracted from CT scans of a healthy and a CF-diagnosed 5-6-year-old child. For the B4-B7 and B8-B15 regions, the SIP geometries must first be scaled to appropriate dimensions. The scale factor was selected such that the B4 inlet diameter matched the hydraulic diameter of the B3 outlets into the lower-left lobe from the upper airway CT scans. A hydraulic diameter was used as the CT scan geometry had non-circular outlets. For the healthy and CF-diseased airways the measured diameters were 4.4 mm and 3.8 mm, respectively, which is consistent with the 4.4 mm diameter from the ICRP model (1994) and the 4.6 mm diameter (standard error of 0.37 mm) from Phalen et al. (1985) of an average 5-year-old. It is also expected that the diseased airways would generally have smaller diameters due to mucus accumulation and inflammation (de Jong et al., 2004), as well as CF patients generally being underdeveloped compared to their peers (Stalvey et al., 2017). This approach to scaling the SIP geometries was previously validated against well-known algebraic and empirical correlations for an infant complete airway model (Bass & Longest, 2018a). Due to the absence of relevant *in vitro* and *in vivo* data,

the current study also validates the 5-6-year-old SIP models against the ICRP (1994), Rudolf (1990), and Finlay (2001) algebraic correlations of deposition fraction. Specifically, the Finlay correlation combines an analytical approximation for sedimentation (Heyder & Gebhart, 1977) and an empirical impaction probability (Chan & Lippmann, 1980). To account for hygroscopic growth in the correlations, the particle size in distal regions of each model is taken as the average particle size from upstream outlets of the CFD results. For example, the particle size entering the B4 region in the correlations is taken as the average MMAD of the aerosol that leaves the upper airway CFD model (NT-B3).

As a disease and in combination with bacterial infections, CF is associated with several types of damage to the airways, including inflammation (airway narrowing), bronchiectasis (airway widening), and mucus accumulation (airway obstructions) (de Jong et al., 2004). Instances of these forms of airway damage were observed in CF-diagnosed patients at very early ages (Tiddens et al., 2010), with examples from CT scans of a 5-6-year-old patient shown in Figure 8.1a. Label A in Figure 8.1a shows an example of axisymmetric mucus plugging on a daughter branch of a bifurcation, Label B shows an example of asymmetric mucus accumulation in the bifurcation, and Label C shows an example of bronchiectasis. To provide an accurate representation of the diseased airways, modifications were added to the B4-B7 and B8-15 SIP regions to account for CF-related airway damage. Figure 8.1b shows axisymmetric mucus plugging on the daughter branch of B4, Figure 8.1c shows asymmetric mucus accumulation in the bifurcation region of B5, Figure 8.1d shows axisymmetric bronchiectasis on the daughter branch of B6, and Figure 8.1e shows asymmetric mucus accumulation on the daughter branch of B7 (not shown in CT scan example). These four forms of lung damage were

selected as they were both representative of observations in CF-diseased airways and could be added to the structured block meshing of the SIP models. More complex forms of airway damage would require an unstructured meshing approach for the SIP bifurcations, which has not currently been validated. Measurements from CT scans of a patient with moderate CF disease, as scored by PRAGMA-CF (Rosenow et al., 2015), showed an average 30% change in cross section (narrowing or widening) in areas of airway damage, up to an approximate maximum of 60% to 70%. As such, these same localized percent reductions or increases in airway dimensions were included in the diseased SIP models (as shown in Figure 8.1b-e) to be consistent with observations from the CT scans.

In summary, four SIP models were evaluated in the current study as a basis for comparison between healthy patients and varying degrees of CF disease states, namely: the (i) Healthy; (ii) CF Scaled; (iii) CF Moderate; and (iv) CF Severe models. For the Healthy model, the upper airways (NT-B3) were extracted from separate head and chest CT scans taken from a single patient on the same day. The CT scans were medically necessary, yet unrelated to airway disease, and confirmed to be free of airway abnormalities by a pediatric otolaryngologist. The B4-B7 and B8-B15 regions of the Healthy model were scaled versions (to a B4 inlet diameter of 4.4 mm) of the adult SIP geometries through the lower-left lobe, as described above. For the three CF models, the upper airways used the same nose-throat (NT) region as the Healthy model, as CT scans of the nasal cavity for CF patients are typically not conducted to minimize radiation exposure. The trachea to B3 region was extracted from CT scans of a patient with moderate CF disease, which were provided by Erasmus Medical Centre (Dr. Harm

Tiddens), and coupled to the healthy NT region. This CF upper airway geometry is the same as the 5-6-year-old model used in the growth chamber study (Chapter 7). For the B4-B7 and B8-B15 regions, three examples of each region were developed to account for varying degrees of disease state. The CF Scaled model uses scaled versions (to a B4 inlet diameter of 3.8 mm) of the adult SIP geometries through the lower-left lobe. The CF Moderate model starts with the CF Scaled geometry and adds one form of airway damage (from Figure 8.1b-e) to each bifurcation with a 30% change in cross section. Forms of airway damage added to each bifurcation were randomly selected. Similarly, the CF Severe model also starts with the CF Scaled geometry, but adds one instance of axisymmetric mucus plugging (Figure 8.1b), asymmetric mucus accumulation (Figure 8.1c), and axisymmetric bronchiectasis (Figure 8.1d) to each bifurcation (resulting in three forms of damage per bifurcation) with a 60% change in cross section. Comparisons between the Healthy and CF models are given in Figure 8.2, with Figure 8.2a showing the NT-B3, B4-B7, and B8-B15 regions for the Healthy model, and Figure 8.2b showing the same three regions for the CF Moderate model. Comparing between the three CF models, Figure 8.3a and b show the B4-B7 and B8-B15 regions for the CF Scaled model, Figure 8.3c and d show the same two regions of the CF Moderate model, and Figure 8.3e and f show the extreme case in the CF Severe model.

One final consideration for applying SIP models to CF-diseased pediatric airways is lobar ventilation and its influence on flow distribution at each of the outlets in the upper airway CFD models. For the original SIP models, lobar ventilation fractions were sourced from Horsfield et al. (1971), Asgharian and Price (2006), and Yin et al. (2010), which were measured from healthy adults. However, lobar differences in disease severity is known

to exist in the lungs of CF patients (Bos et al., 2017; Bos et al., 2015), which affects lobar ventilation fractions. In the current study, lobar ventilation fractions were measured directly from inhalation and exhalation CT scans of a 5-6-year-old with moderate CF disease (the same patient as the upper airway models). Lung lobes were semi-automatically segmented from the inhalation and exhalation scans using the Chest Imaging Platform module (Estepar et al., 2015) available in the open-source 3D Slicer CT segmentation software (Kikinis, Pieper, & Vosburgh, 2014). The ratio of inhalation to exhalation volume for each lobe was then used to determine the lobar ventilation fractions specific to the selected patient. Figure 2.1 shows the segmentation of each lung lobe at inhalation and exhalation, and Table 7.1 summarizes the ventilation fractions for the healthy (based on the adult SIP models) and diseased models.

CFD Models

Computational Domain and Spatial Discretization

The geometry for the computational domain of both the Healthy and CF upper airway models was generated with a similar method to the growth chamber study (Chapter 7). Briefly, CT scans of the nasal cavity and tracheobronchial airways were segmented with the Mimics software suite (Materialise, Leuven, Belgium). The triangular STL surfaces of the NT-B3 regions were then converted to CAD surfaces by utilizing the automated skin surfacing capabilities in SpaceClaim v19.3 (ANSYS Inc., Canonsburg, PA), and prepared for mesh generation. Spatial discretization of the computational domain was performed with the polyhedral meshing capabilities available in FLUENT v19.3 (ANSYS Inc., Canonsburg, PA) to accurately resolve the complexity of the nasal cavity geometry. The spatial resolution of the mesh matched the grid independent,

validated results from the growth chamber study (Chapter 7). The near-wall mesh resolution follows our best practices of five prismatic layers and an area-averaged wall y^+ value of approximately one (Bass, Boc, et al., 2019; Bass & Longest, 2018b). Numerical extensions were added to each of the upper airway B3 outlets to prevent reversed flow and aid in convergence of the transport equations. As the physically realistic bifurcations of the B4-B7 and B8-B15 regions lend themselves to blocked topologies, a structured hexahedral mesh can be applied to resolve the spatial discretization, which improves solution convergence, model accuracy, and computation times. The spatial resolution of the B4-B7 and B8-B15 regions matches the models used in the *in vivo* validations described by Tian et al. (2015). When adding examples of airway damage to the middle and lower airways for the CF Moderate and CF Severe models, care was taken to maintain the blocking structure and spatial resolution of the SIP models.

Numerical Models and Solver Settings

The numerical models and solver settings for the upper airway flow fields generally followed the SIP best practices outlined by Tian et al. (2015). Despite an inlet Reynolds number of approximately 1,000 (flow rate of 5 LPM and hydraulic diameter of 6.1 mm), low-Reynolds number (LRN) k-ω turbulence was used to model the transitional-to-turbulent flow regime, as the glottis in the laryngeal region is known to induce turbulence (Bass, Boc, et al., 2019; Xi et al., 2008; J. X. Xi et al., 2012). A transient form of the transport equations was also employed to model the oscillatory behavior of the laryngeal jet (Xi et al., 2008), which is also consistent with the SIP modeling recommendations presented by Tian et al. (2015). Plots of deposition fraction vs. flow time were monitored and aerosol deposition was observed to plateau at approximately 0.5 s, so flow solutions

were terminated after 1.0 s flow time instead of modeling the full 4.5 s actuation time. In contrast to the upper airways, the CFD set-up for the middle and lower airways employs laminar flow models and a steady-state formulation of the transport equations. Observations from CFD models have previously shown that turbulent flow can extend from the laryngeal jet through B4 (Xi et al., 2008), but validation work in the SIP models have shown the best match to *in vivo* data with laminar conditions in the B4-B7 and B8-B15 regions (Longest et al., 2015; Tian et al., 2015; Walenga & Longest, 2016). For context, in the Healthy model, the Reynolds number is approximately 500 at the B4 inlet and approximately 100 at the B8 inlet.

Beyond considerations specific to SIP models, the remaining solver settings followed our previously defined best practices for respiratory aerosol transport (Bass, Boc, et al., 2019; Bass & Longest, 2018b). FLUENT v19.3 (ANSYS Inc., Canonsburg, PA) was used to obtain solutions for all flow and turbulence equation. The spatial discretization of the flow and turbulence transport equations were second-order accurate, the gradient discretization used the Green-Gauss Node-based method, and the SIMPLEC pressure-velocity coupling scheme was used. As the current study evaluates hygroscopic aerosol growth, the continuous phase in the flow field was composed of air and water vapor to model the relative humidity (RH) of the fluid. The multi-species and energy models were activated, and the incompressible ideal gas law was used to model fluid density.

In this study, the pediatric air-jet DPI was operated in nose-to-lung aerosol delivery mode, in which the nasal cannula interface is inserted into the nostrils forming an airtight seal. The simulation began at the nostril interface. As the device was operated at a flow

331

rate of 10 LPM, the mass flow inlet boundary condition was applied at the nostrils with a mass flow rate selected that provided a volumetric flow rate of 5 LPM through each nostril. The water vapor mass fraction at the nostril inlets was consistent with the 10% RH that is expected from dry wall air, which is passed through the air-jet DPI and nasal cannula, and the temperature was set to ambient conditions (20°C). The outlet boundaries in the upper airway models were set to the outflow condition at approximately the lobar bronchi, where a fraction of the total outlet mass flow rate is applied to each boundary, with the fractions defined for the Healthy and CF models as shown in Table 7.1. Downstream of the upper airways, in the B4-B7 and B8-B15 regions, the inlet boundaries used velocity inlet boundary conditions with a parabolic spatial profile (due to laminar flow) that matched the volume flow rate from the upstream bifurcation outlet. The water vapor mass fractions at the inlet to the middle and lower airways were taken as the area-weighted average value from the upstream outlet, which was close to 99% RH in all cases as the dry wall air had completely mixed with the humid airway by the end of the upper airways. Outlet boundaries used outflow fractions that assume 50% of the flow goes through each bifurcation outlet, which is consistent with the assumptions from Tian et al. (2015). The wall boundaries in all models used the no-slip shear condition, and effects of surface roughness were neglected as airway surfaces are expected to be smooth at the microscopic level. In addition, the water vapor mass fraction on all wall boundaries was set to 99% RH as the airway surfaces are expected to be moist.

Particle Transport and Growth

The discrete phase model (DPM) available in FLUENT v19.3 was used to calculate the particle trajectories and deposition through the domain, with all DPM settings following

our previously defined best practices and modeling recommendations (Bass, Boc, et al., 2019; Bass & Longest, 2018b). In the upper airways, where the k-ω turbulence model is applied, near-wall corrections were implemented (Longest & Xi, 2007) to account for the over-prediction of aerosol deposition associated with the k-ω model. As the middle and lower airways were modeled with laminar flow conditions the near-wall corrections were not applicable and not required. At the inlet to the upper airway models, particles were introduced in to the domain with a monodisperse size distribution, which is an acceptable assumption based on findings from Tian et al. (2015). Using a polydisperse size distribution would provide a more accurate representation of the aerosol, but would be more computationally expensive in the transient model. In the B4-B7 and B8-B15 regions, the particles were introduced with a polydisperse distribution that matched the aerosol size at the upstream outlet and accounted for variability in particle growth through the upper airways. To ensure particle convergence, a total of 90,000 particles were introduced into each SIP region, which is consistent with the recommendations from Tian et al. (2015).

The growth of the EEG aerosol is implemented in the CFD models with the evaporation and condensation UDF that was described in Chapter 7 and originally presented by Longest and Xi (2008). Previous work has utilized AS EEG powder formulation as a surrogate test aerosol for tobramycin, as the hygroscopic properties for tobramycin were not available. In the current study, the hygroscopic properties for tobramycin were established by the VCU School of Pharmacy, which allowed for tobramycin EEG formulations and its growth characteristics to be modeled with CFD for the first time. The material and hydroscopic properties for tobramycin used in this study

were a molecular weight of 467.5 g/mol, density of 990.0 kg/m^3, saturated mole fraction of 0.037, and van't Hoff factor of 2.46. The true density was measured by gas pycnometer AccuPyc II 1340 (Micromeritics) and the water activity (saturated mole fraction and van't Hoff factor) was measured with a method consistent with Longest and Hindle (2011). The chosen tobramycin EEG powder formulation in this study contained a 60:20:20% w/w ratio of tobramycin, mannitol, and L-leucine, which resulted in a particle density of 1117.2 kg/m^3.

In summary, four initial aerosol cases were modeled to demonstrate a comparison between delivery strategies and provide a proof of concept for tobramycin EEG aerosol administration to CF-diseased airways, namely: (i) Base EEG; (ii) Min Static; (iii) Max Static; and (iv) Optimal EEG. The Base EEG case includes aerosol growth based on the tobramycin EEG powder formulation stated above, and an initial monodisperse geometric particle diameter of 1.45 µm, which is consistent with the 1.53 µm aerosol MMAD from the chosen delivery system (Farkas et al., 2020). The Min Static case does not include aerosol growth and uses an initial geometric particle diameter of 1.45 µm (ρ = 1117.2 kg/m^3) to evaluate how hygroscopic growth influences drug delivery by drawing comparisons with the Base EEG case. Similarly, the Max Static case also does not include hygroscopic growth, but uses an initial geometric particle diameter of 3.31 µm (3.50 µm MMAD) to evaluate how a small or large aerosol size penetrates the upper airways. The three initial aerosol cases stated above all assumed a nominal value of 75 mg of tobramycin entered the upper airways, which was used to determine ASL concentrations throughout the airways. Based on the current fraction of tobramycin loaded into EEG particles, this would require a 125 mg mass of delivered powder. In

contrast, the Optimal EEG case uses a monodisperse aerosol with a geometric particle diameter of 1.45 µm that represents 50 mg of tobramycin, and a second monodisperse aerosol with a geometric particle diameter of 1.80 µm (aerodynamic diameter of 1.91 µm) that represents 25 mg of tobramycin, which both included hygroscopic growth. This case demonstrates how delivery strategies can be optimized to achieve regional deposition targets, such as the uniform distribution and lower thresholds associated with inhaled antibiotics. If a polydisperse aerosol were employed, the Optimal EEG case could be described as a bi-modal distribution, with the first peak (smaller aerosol) used to target distal airways and the second peak (larger aerosol) used to target intermediate regions. The selection of the Optimal EEG tobramycin mass distribution and particle sizes was based on analysis of the CFD results, but is included here for clarity in the Methods section.

ASL Volumes

To determine whether the delivered tobramycin provided uniform concentrations and was above the MIC, regional ASL volumes in the lung bifurcations and alveoli were required. The airway surface area was measured from the SIP models and combined with estimations of ASL thickness to determine the regional ASL volume, which can be used with the deposited mass and bifurcation counts to establish regional tobramycin concentrations (mg/L). The method for calculating regional tobramycin concentration in the ASL is given as:

$$c_R = \frac{\sum_{i=1}^{N} \text{DF}_i m_{in}}{\sum_{i=1}^{N} V_i} \tag{8.3.1}$$

where: c_R is the concentration in region R, DF_i is the CFD-predicted DF in the bifurcation, m_{in} is the mass that enters region R, and V_i is the ASL volume in the bifurcation. Previous

studies of aerosol delivery to CF-diseased airways have assumed a uniform ASL thickness throughout the airways (Bos et al., 2017; Bos et al., 2015), with minimum (Tarran et al., 2005) and maximum (Tarran, Button, & Boucher, 2006) thicknesses of 3 μm and 7 μm, and also evaluated an average thickness of 5 μm. These uniform ASL thicknesses were specific to CF-disease lungs, but the literature shows that ASL thickness varies between bifurcation levels (Hasan & Lange, 2007; ICRP, 1994; Patton, 1996).

In the extrathoracic (ET), bronchial (BB), and bronchiolar (bb) regions, the ICRP model (1994) reports the thickness of the mucus and cilia layers (which combined give the ASL thickness) as 15 μm, 11 μm, and 6 μm, respectively. More recently, Hasan and Lange (2007) presented a mass conservation model for estimating ASL thickness ($h_{ASL,k}$) based on mucus production and clearance rates:

$$h_{M,k} = r_k - \sqrt{r_k^2 - \frac{\sum_{i=k}^{N} p_i}{2^k \pi v_k}} \tag{8.3.2}$$

$$r_k = \frac{d_k}{2} - h_{C,k} \tag{8.3.3}$$

$$h_{ASL,k} = h_{C,k} + h_{M,k} \tag{8.3.4}$$

where: k is the generation number, h_M is the mucus layer thickness, r_k is the radius of the airway up to the mucus layer, p_i is the mucus production rate, v_k is the mucus clearance rate, d_k is the generation diameter, and $h_{C,k}$ is the height of the cilia layer. The cilia height was determined from experimental measurements by Serafini and Michaelson (1977) and the bifurcation-level mucus production distribution was sourced from material measured from rhesus monkeys by Plopper et al. (1989). Mucus clearance rates are known to have both interpatient and intrapatient (from day-to-day) variability (Hasan &

Lange, 2007; Lange, Hancock, Samuel, & Finlay, 2001). Typical fast and slow clearance rates in the trachea for healthy nonsmoking adults (Wanner, Salathe, & O'Riordan, 1996) are 15 mm/min and 5 mm/min, respectively, with Yeates et al. (1976) reporting no difference in clearance rates for CF-diseased lungs. Clearance rates in distal lung regions are scaled from the tracheal value and data sourced from Stahlhofen (1980). For mucus production, Finlay et al. (2000) reported a pediatric (4-years-old) rate of 2.8 mL/day based on body-weight scaling from adult values, with Oberwaldner et al. (Oberwaldner, Evans, & Zach, 1986; Oberwaldner, Theissl, Rucker, & Zach, 1991) reporting that production rates can be up to four times higher in CF-diseased airways. In the alveolar-interstitial region (AI), the ASL is predominantly surfactant with Weibel (1963) and Macklin (1955) reporting thicknesses of 0.068 μm and 0.2 μm, respectively. This was combined with the AI surface area from the ICRP model (1994), scaled to pediatric dimensions, and gave the ASL volume distal to B15.

In summary, three ASL volume cases were evaluated in the current study to provide a range of tobramycin concentration predictions, namely: the (i) ICRP ASL, (ii) Min ASL, and (iii) Max ASL volumes. In the ET, BB, and bb regions, the ICRP ASL volume is simply based on the regional thicknesses reported by the ICRP model (1994). The Min ASL volume in the NT-B15 regions is based on the mass conservation model (Hasan & Lange, 2007) and uses fast clearance (trachea: 15 mm/min) and low mucus production (2.8 mL/day for a healthy pediatric) as input to the model, which provides the minimum estimation of ASL volume. Similarly, the Max ASL volume also uses the mass conservation model, but uses slow clearance (trachea: 5 mm/min) and increased mucus production (11.2 mL/day, or four times higher than a healthy pediatric), which provides

the maximum estimation of ASL volume. In the upper airway CFD models, distinctions are not made between bifurcation levels, so an area-average ASL thickness from B1-B3 is combined with its surface area to determine the ASL volume in this region. As the mass conservation model only includes bifurcation-level mucus production distribution from B1 through B14, the ASL thickness for B15 was assumed to be the same as B14. The results present regional tobramycin concentrations as an ensemble of multiple bifurcations, so the effect of this assumption is assumed to be negligible. Similarly, the mass conservation model does not include the ET region, so the thickness for the Min and Mas ASL cases were scaled from the ICRP model based on total ASL volumes. In the AI region, the Min ASL volume uses the 0.068 µm thickness from Weibel (1963), the Max ASL volume uses the 0.2 µm thickness from Macklin (1955), and the ICRP ASL volume uses the average of these two values (0.134 µm). For the three cases detailed above, Table 8.2 summarizes the bifurcation-level ASL thicknesses and volumes, and Table 8.3 summarizes the regional total ASL volumes used in calculation of tobramycin concentrations.

8.4   Results

CFD Model Validation and Upper Airway Deposition

Figure 8.5 shows regional deposition fractions and patterns in the upper airways (NT-B3) for the Healthy (Figure 8.5a) and CF Moderate (Figure 8.5b) models. The total DF shown in Figure 8.5b is compared against the *in vitro* data from the 5-6-year-old growth chamber model (Chapter 7). Note that both the CFD and experimental results in Figure 8.5 use an AS EEG powder formulation, but validate aerosol deposition, not growth. The initial AS EEG aerosol size from the growth chamber study was a geometric

diameter of 1.29 µm (1.53 µm MMAD with ρ = 1399.7 kg/m^3), which is consistent with the MMAD of the tobramycin EEG aerosol that is evaluated in subsequent sections, and little aerosol growth is expected in the ET region. This demonstrates validation of the upper airway CFD model as the numerical prediction of aerosol deposition is within the standard deviation of experimental replicates. Surprisingly, total and regional deposition fractions in the Healthy model are higher than the CF Moderate model (absolute difference of 2.4%), though the difference between the two models is relatively small considering the experimental standard deviation (2.6%). The variation in deposition between the two models can be attributed to interpatient variability. Inspection of the TB anatomy in Figure 8.5 shows that the B1 branching angle is noticeably larger in the Healthy geometry, which would suggest an increase in impaction deposition, and there is clearly more deposition on the carinal ridge in the first bifurcation. CF-related airway damage would presumably lead to increased deposition losses in the CF Moderate model, but disease is known to be more predominant in the lower airways (Tiddens et al., 2010), so differences in the upper airways are expected to be small.

Table 8.4 compares regional deposition in the bronchial (Trachea to B8) and bronchiolar (B9-B15) regions between the Healthy SIP models and the ICRP (1994), Rudolf (1990), and Finlay (2001) models. The aerosol size entering the bronchial region (from the outlet of B3) was an MMAD of 1.67 µm, and the size entering the bronchiolar region (from the outlet of B7) was an MMAD of 2.23 µm. The CFD results compare well with the ICRP and Rudolf correlations, with the algebraic Finlay model suggesting slightly higher deposition in these regions. These results are consistent with conclusions from Bass and Longest (2018a), which used a similar method for validating the numerical SIP

model results. It is noted that aerosol growth was accounted for in the correlations by using the average aerosol size in distal regions from upstream regions. This validation of the SIP models ensures that CFD-predictions of deposited drug mass provide accurate regional ASL concentrations.

Particle Trajectories and Aerosol Growth

Figure 8.6 illustrates particle trajectories and growth through the three regions of the Healthy (Figure 8.6a) and CF Moderate (Figure 8.6b) models for the Base EEG aerosol case. Note that particle trajectories extend beyond the computation domain due to the addition of numerical extensions. In both models, the particle MMAD leaving the upper airways is less than approximately 2.0 μm, which provides good N2L aerosol transmission. In distal regions (B4-B15) of the healthy and CF-diseased lungs, the tobramycin EEG powder formulation grows larger than 2.5 μm due to hygroscopic absorption of moisture from the humid airways. This aerosol size increase would lead to increased sedimentation deposition (with a breath hold) and impaction deposition (upon exhalation), and helps to target lung regions where CF-related bacterial infections are more predominant. The growth characteristics of the tobramycin EEG powder formulation in the current study (60:20:20% w/w ratio of tobramycin:mannitol:L-leucine) is consistent with the AS EEG powder that has been used as a surrogate test aerosol in Chapter 7 and previous publications (Bass, Farkas, et al., 2019; Bass & Longest, 2020; Farkas et al., 2020; Farkas et al., 2019).

Airway Surface Liquid Concentrations

Table 8.5 summarizes CFD-predicted regional deposition fractions (similar to Figure 8.5), which were combined with the assumed 75 mg of tobramycin (leaving the

340

nasal cannula) and ASL volumes (see Table 8.2) to determine regional drug concentrations. Figure 8.7 plots the tobramycin concentrations in the ASL for all four SIP models and the ICRP (Figure 8.7a), Min (Figure 8.7b), and Max (Figure 8.7c) ASL volumes for the Base EEG aerosol. The solid and dashed lines on these plots indicate the MIC (512 mg/L) and double the MIC for reference. Table 8.6 summarizes regional tobramycin concentrations relative to the MIC for the Base EEG aerosol and compares between all SIP models and ASL volumes. This shows that the Base EEG delivery strategy, with 75 mg of tobramycin emitted from the delivery system, is consistently capable of delivering tobramycin ASL concentrations that are well above the MIC for all SIP models and ASL volumes considered. The worst-case regional delivery is the B4-B7 region of the Healthy SIP model with Max ASL volume that had a CFD-predicted concentration of 2.5 x MIC. Recall that the dimensions of the Healthy SIP model were larger than all CF-diseased models, due to different scaling factors, which decreases the Stokes number and suggest less impaction deposition. This justifies the lower tobramycin ASL concentrations that the CFD models predicted in the Healthy SIP model, as less drug mass is deposited. In the CF SIP models, the worst-case regional delivery is the B4-B7 region of the CF Scaled model with Max ASL volumes that had a CFD-predicted concentration of 2.9 X MIC. Interestingly, the models with increased states of disease progression (CF Moderate and CF Severe) had higher concentrations, as the forms of lung damage added to the geometry increased potential impaction deposition sites. Though the minimum delivered concentrations are above the MIC targets of this study, regional uniformity of tobramycin in the ASL can be improved with an optimal EEG delivery strategy.

341

Figure 8.8 and Table 8.7 present the tobramycin concentrations for all SIP models and ASL volumes considered for the Min Static aerosol. As with the Base EEG case, the small aerosol size of the Min Static aerosol is capable of penetrating the upper airways beyond B3. However, as there is no hygroscopic growth, the aerosol is also able to navigate the filtration of the lower airways and shows relatively low levels of deposition in the B4-B7 and B8-B15 regions. Therefore, delivered tobramycin concentrations in the ASL for the lower airways is low for all cases considered. Minimum concentrations were predicted to be only just above the MIC for the B8-B15 region of the Healthy SIP model with Max ASL volume (1.0 x MIC), with similar results for the B8-B15 regions of the CF SIP models with Max ASL volume (1.2-1.6 x MIC). Figure 8.9 and Table 8.8 present the tobramycin concentrations for all SIP models and ASL volumes considered for the Max Static aerosol. In this case, concentrations are consistently high and well above the MIC due to a large amount of deposited drug mass from the larger aerosol size (minimum concentrations of 3.1 and 4.8 x MIC for the Healthy and CF SIP models, respectively). However, as there is poor N2L transmission due to the increased particle size, CFD predictions show up to a 10-fold difference in regional concentrations (4.8-45.9 x MIC in the NT and B4-B7 regions of CF Scaled with Max ASL) and exhibit poor dose uniformity throughout the airways.

Figure 8.10 and Table 8.9 present the tobramycin concentrations for all SIP models and ASL volumes considered for the Optimal EEG aerosol. Recall that the Optimal EEG aerosol used 50 mg of 1.45 μm and 25 mg of 1.80 μm particles (geometric particle diameters). For the three CF SIP models, the Optimal EEG case reduced variability in regional concentrations and is consistently well above the MIC (minimum of 5.8 x MIC in

the B4-B7 region of CF Scaled with Max ASL). Table 8.10 compares the ratios of maximum to minimum concentrations in all SIP models, ASL volumes, and aerosol cases. For the CF-diseased models with EEG aerosols, variability (expressed as the ratio of maximum to minimum ASL concentration) is reduced from a range of 2.4- to 5.2-fold (Base EEG) to a range of 1.7- to 4.3-fold (Optimal EEG). For the Healthy SIP model, variability in tobramycin concentration is also reduced with the Optimal EEG aerosol, but it is not as low as the CF-diseased models. As the delivery system is intended to administer antibiotics to pediatric patients with CF, the variability in the Healthy model is not considered a negative outcome. However, this does raise questions on interpatient variability and its influence on establishing an optimal delivery strategy.

8.5   Discussion

This study meets the objective by providing a proof of concept for tobramycin EEG aerosol administration to treat bacterial lung infections in pediatric patients diagnosed with CF. Validated CFD predictions demonstrated that the EEG delivery strategy was consistently capable of delivering tobramycin to the ASL that was above the MIC for all cases considered, with the minimum CF-diseased concentration being 2.8 and 5.8 x MIC for the Base and Optimal EEG aerosol, respectively. The Optimal EEG aerosol was capable of reducing regional concentration variability to an approximate four-fold difference between maximum and minimum CFD-predicted values. Furthermore, the validated numerical models predicted high tobramycin ASL concentrations in the lower airways (B8-B15), where bacterial infections are more predominant (Tiddens et al., 2010), with a minimum concentration of 7.5 x MIC in the CF Moderate SIP model with Max ASL volume. This study assumed a nominal value of 75 mg of tobramycin entering the upper

airways from the delivery system, which combined with the 79.5% device ED (Farkas et al., 2020) and 60% mass fraction in the EEG formulation, suggests a loaded dose of approximately 160 mg of powder. This is high considering the device is designed to hold 100 mg of powder (Farkas et al., 2020), but the high-efficiency delivery of tobramycin to the ASL means that less powder would still ensure concentrations above the MIC. For example, a loaded dose of 100 mg of powder (60 mg of the drug) leads to 47.7 mg of tobramycin entering the upper airway, which gives a worst-case ASL concentration of 3.7 x MIC for the Optimal EEG aerosol. Alternatively, different EEG powder formulations that increase the mass fraction of drug relative to excipients may be considered, as the water activity characteristics show that tobramycin has good hygroscopic properties.

As a secondary outcome, this study directly compared a range of static and EEG aerosol delivery strategies and demonstrates the advantages of powder formulations that utilize hygroscopic growth. The Min Static aerosol was capable of navigating the filtration of the ET region, but the small aerosol size in the lower airways lead to low tobramycin ASL concentrations. This becomes more of an issue when considering drug delivery and lung retention during a breath-hold or upon patient exhalation. The Max Static aerosol provided high regional ASL concentrations, but variability between regions was poor due to increased upper airway losses. Only the EEG aerosol cases were able to provide good N2L transmission, and meet the MIC and regional variability targets that are associated with the administration of inhaled antibiotics. This study also compared the delivery of inhaled tobramycin between healthy patients and varying degrees of CF disease states. The smaller dimensions of the CF-diseased airways and addition of various forms of lung damage increase the likelihood of impaction deposition throughout the SIP models, which

leads to an increase in predictions of tobramycin concentrations from the numerical models. This is promising for treatment methods with inhaled antibiotics, as the regions with increased lung damage are also likely to have the most bacterial infections, which is where the drug is required. The increase in CFD-predicted tobramycin delivery in the CF models is most apparent in the middle airways (B4-B7) due to the increased flow velocities in this region compared to the lower airways (B8-B15).

Interpatient variability in delivered tobramycin concentrations was apparent when drawing comparisons between the Healthy and CF models. Differences in upper airway anatomy lead to differences in CFD-predicted losses in the NT-B3 region, which in turn affected the amount of drug that was delivered to the middle and lower airways. Interpatient variability has been well established for infant, pediatric, and adult populations in the ET region (Garcia et al., 2009; Golshahi et al., 2012; Golshahi et al., 2011; Storey-Bishoff et al., 2008), and it is reasonable to expect the same in regard to deposition in distal diseased (Bos et al., 2015) airways. Establishing an ideal EEG delivery strategy that is applicable to the entire patient population is difficult, as an optimal aerosol for one patient may not meet delivery targets for others. One approach may be to define low, medium and high deposition models for the ET region and distal airways that are representative of the chosen patient population, which is similar to the method described by Rani et al. (2020). Predictions of delivered tobramycin concentrations are also inherently dependent on the estimations of regional ASL volumes, which also exhibit interpatient and intrapatient variability (Hasan & Lange, 2007; Lange et al., 2001). Regarding MIC targets, results should focus on predicted aerosol delivery to ASL thicknesses that provide estimations of maximum ASL volumes, as the concentration

exhibits the worst-case scenario. The mass conservation model (Hasan & Lange, 2007) gives increased fidelity over the ICRP model (ICRP, 1994) as it provides bifurcation-level estimations of ASL thickness in the airways. However, as with all models, it is only as accurate as the assumptions and inputs allow. The cilia thickness was estimated from data measured from adults (Serafini & Michaelson, 1977) and the bifurcation-level mucus production distribution from rhesus monkeys (Plopper et al., 1989), both of which may need to be redefined for pediatric patients with CF. Furthermore, lobar and regional variability in mucus production, especially for diseased airways, has a direct effect on CFD predictions of regional variability in delivered tobramycin concentrations. Finally, the ASL volumes in this study do not account for the mucus accumulation and plugging that is typically observed in CF-diseased airways. Measurements from CT scans showed up a to 70% reduction in airway cross sections, equating to mucus accumulations that are approximately 1 mm thick, which is three orders of magnitude larger than the calculated ASL thicknesses. The sites of mucus accumulations are expected to be highly infected with bacteria, so adequate delivery of tobramycin is important in these regions.

Beyond the variability in deposition predictions and ASL volumes, limitations in the current study primarily include assumptions made in the numerical models and validation of the CFD predictions. In the middle and lower airway SIP geometries, a parabolic velocity profile was applied at the inlet that matched the upstream outlet volumetric flow rate. This assumption was made as the non-circular shape and polyhedral mesh topology in the upper airways does not permit one-to-one matching of cell centroids and velocities between regions, which is recommended by the *in vivo* validation of Tian et al. (2015). The parabolic profile assumption is reasonable, given the laminar flow conditions, but the

curvature of airway bifurcations is known to skew the velocity profile at the outlet (Longest & Oldham, 2008). An improved approach would be to map the non-circular spatial distribution to the circular SIP model inlet and use inverse-distance weighted interpolation between the velocities at the polyhedral and hexahedral face centroids. The CFD models also assumed that the MMAD of the tobramycin EEG aerosol that is emitted from the delivery system was the same as the experimental data from Farkas et al. (2020), which used an AS EEG powder formulation as a surrogate test aerosol. As the particle density differs between the tobramycin and AS EEG powder formulations (1117.2 kg/m^3 and 1339.72 kg/m^3, respectively), it is reasonable to expect different MMADs for the same device, if the physical particle diameter is the same between the two from the spray drying process. The differences in powder dispersion characteristics between tobramycin and AS EEG formulations are also not established, which may also affect the aerosol size leaving the DPI. Finally, the outlet ventilation fractions in the upper airway models were based on lobar volumes extracted from inhalation and exhalation CT scans, and assumed that all lobes inflated at the same rate. However, in CF-diseased lungs, it is known that that the inflation of each lobe is time dependent (L. J. Smith et al., 2018). That is, the inflation of a particular lobe may be delayed in relation to the onset of inhalation, and the rate of inflation for each lobe varies. This can influence how much tobramycin is delivered to each lung lobe based on the timing of inflation and aerosol delivery. For example, for a 4.5 s device actuation time, aerosol may hypothetically only be emitted from the delivery system for approximately 2.0 s. If one of the lung lobes only begins inflating after a 1.0 s delay, it would receive much less of the inhaled antibiotic than the other four lobes.

With regard to CFD model validation, the current study matched deposition in the upper airway CF model with the experimental data (both with the same AS powder formulation) from the growth chamber study (Chapter 7). The healthy B4-B7 and B8-B15 SIP models were validated against algebraic and empirical correlations (W. H. Finlay, 2001; ICRP, 1994; Rudolf et al., 1990). Ideally, the predictions of aerosol deposition in all CFD models would be validated directly against *in vitro* or *in vivo* data. Ethical concerns limit the availability of *in vivo* datasets for pediatric patients with CF, especially with radio-labelling, due to the amount of medically necessary CT scans that CF patients may require during their life. SIP models have been validated against *in vitro* data by a number of previous studies (Longest, Tian, Delvadia, et al., 2012; Longest, Tian, Walenga, et al., 2012; Tian et al., 2011), and similar methods could be applied to the CF SIP models that were developed by the current study. The difficulty with experimental testing of diseased pediatric models is whether current 3D printing capabilities can accurately produce physical models with small airway dimensions. Similarly, the current study does not directly validate the CFD-predicted growth of the tobramycin EEG powder formation against experimental data. Previous work (Chapter 7) successfully validated the particle condensation and evaporation models for AS EEG powder formulations, and the tobramycin hygroscopic properties were experimentally determined based on the same methods (Longest & Hindle, 2011), so the numerical results are expected to be accurate. However, the CFD models for tobramycin EEG growth should also be validated against *in vitro* data from a growth chamber model to increase confidence in the numerical predictions.

As this is the first study of its kind to evaluate tobramycin EEG powder formulations in SIP models of CF-diseased airways, the scope for future work is extensive. As mentioned in the Methods section, the current study followed pathways through the lower-left lobe as this has previously been shown to be representative of the ensemble average deposition in the entire lung (Longest, Tian, Delvadia, et al., 2012). Future studies are planned that will compare lobar and regional variability in aerosol deposition, which is known to be an issue in CF-diseased lungs (Bos et al., 2017; Bos et al., 2015), as some lobes are generally more damaged than others. Future work also intends to expand the range of pediatric populations considered by evaluating both a 2-3- and 9-10-year-old model. Establishing whether the CF-diseased SIP models provide an accurate representation of aerosol transport and deposition in the diseased airways is also required. One approach may be to extract anatomically accurate, diseased bifurcations from CT scans and compare them to the CF Moderate and Severe bifurcations. Adjustments can then be made to the SIP models to improve the match to diseased airway results. Previous work (Bos et al., 2017; Bos et al., 2015) has shown that CF diseased airways can be extracted from CT scans up to approximately B6, so assumptions would still need to be made about the lower airways. This approach would also need to establish how unstructured meshes, required for modeling the complex geometry of diseased airways from CT scans, compare with structured hexahedral meshes in airway bifurcations.

Beyond expanding and improving the computational domain, the detail and potential accuracy of the numerical models can also be explored in future work. The use of polydisperse aerosols, as opposed to the monodisperse aerosol in this study, provides

349

a more realistic representation of the aerosol that enters the domain and may influence drug delivery to the lower airways. Two-way coupling between the continuous (fluid) and discrete (particles) phase is also a more accurate, yet computationally expensive, method of modeling aerosol growth, which has previously provided a better match to experimental data (Longest & Hindle, 2012). Laminar flow was assumed in the middle and lower airways based on the *in vivo* SIP model validation by Tian et al. (2015), but the k-ω model may be considered in future work as constrictions in the diseased airway may induce turbulence. In stenosed tubes, which are similar to the CF-diseased airway constrictions, previous work has shown that a 50-75% area reduction at Reynolds numbers of 400-1100 can induce turbulent flow (Ahmed & Giddens, 1983a, 1983b; Ghalichi et al., 1998). Alveolar models (Khajeh-Hosseini-Dalasm & Longest, 2015) may also be used to establish the breath-hold duration required to maximize sedimentation deposition. The current delivery system requires an actuation time of approximately 4.5 s, so an extended breath-hold period may not be feasible, but if the powder empties early in the delivery cycle, it also may not be necessary. Related to actuation time, device flow rates may be considered as part of delivery strategy optimization, in addition to bi-modal size distributions, to target regions of the lungs and reduce regional variability. However, compromises will need to be made, as the aerosolization performance of the air-jet DPI is also influenced by the flow rate through the device (Bass, Farkas, et al., 2019).

In conclusion, this study provides a proof of concept for high-efficiency EEG aerosol administration to treat bacterial infection in CF-diseased airways and meet the dosing requirements of inhaled tobramycin antibiotics. This is the first such study to apply numerical models for the evaluation of tobramycin EEG powder formulations in complete-

airway, diseased, pediatric SIP models. An optimal EEG aerosol was identified that met the delivery targets associated with tobramycin administration, with ASL concentrations above the MIC, minimal regional variability, and high concentrations in the lower airways. Comparisons were made between static and EEG particles that demonstrated the advantages of administering aerosols that utilize hygroscopic growth. Furthermore, comparisons were made between models that represent healthy patients and varying degrees of CF disease states. Future work is planned that intends to expand upon this initial study and further evaluate the use of EEG aerosols in pediatric CF patients.

8.6 Figures
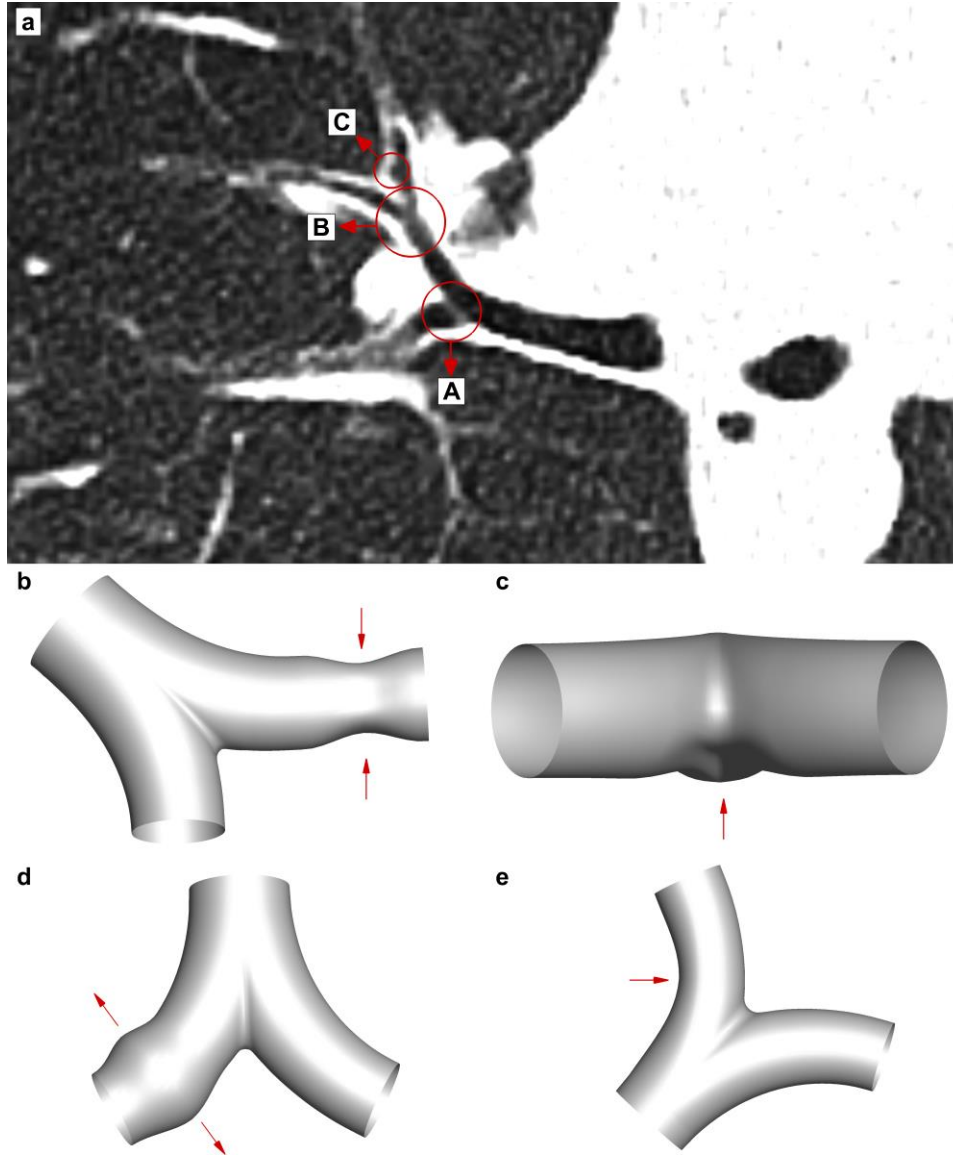
Figure 8.1: Examples of CF-related lung damage in (a) CT scans, with Label A showing axisymmetric mucus plugging on a daughter branch, Label B showing asymmetric mucus plugging in the bifurcation region, and Label C showing localized widening of a daughter branch (bronchiectasis); and examples of lung damage implemented in the SIP geometry with (b) axisymmetric mucus plugging, (c) asymmetric mucus accumulation in the bifurcation region, (d) axisymmetric bronchiectasis, and (d) asymmetric mucus accumulation in the daughter branch (not shown in CT scan).
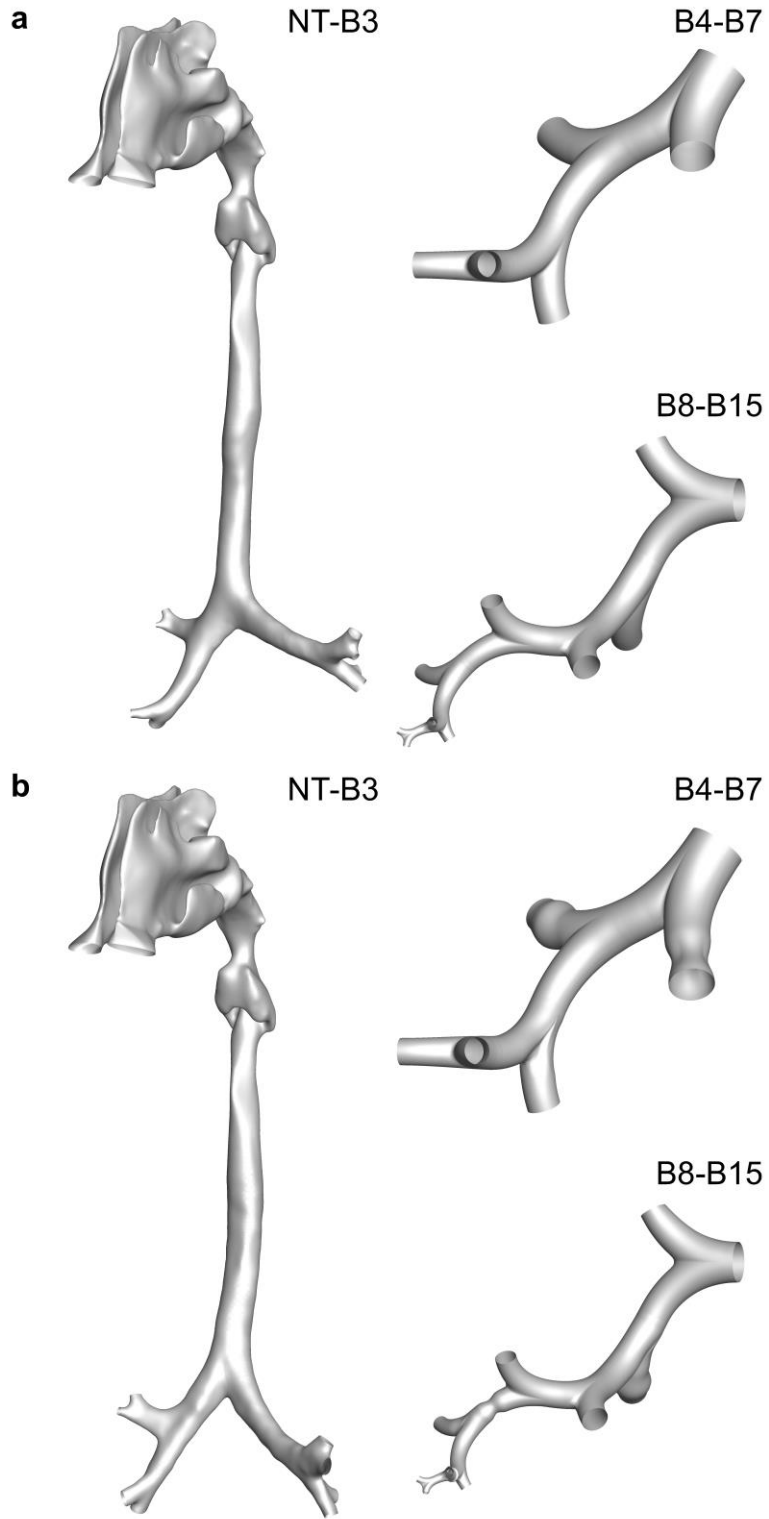
Figure 8.2:   Overview of CFD SIP model geometries showing the (a) Healthy and (b) CF

Moderate 5-6-year-old models.
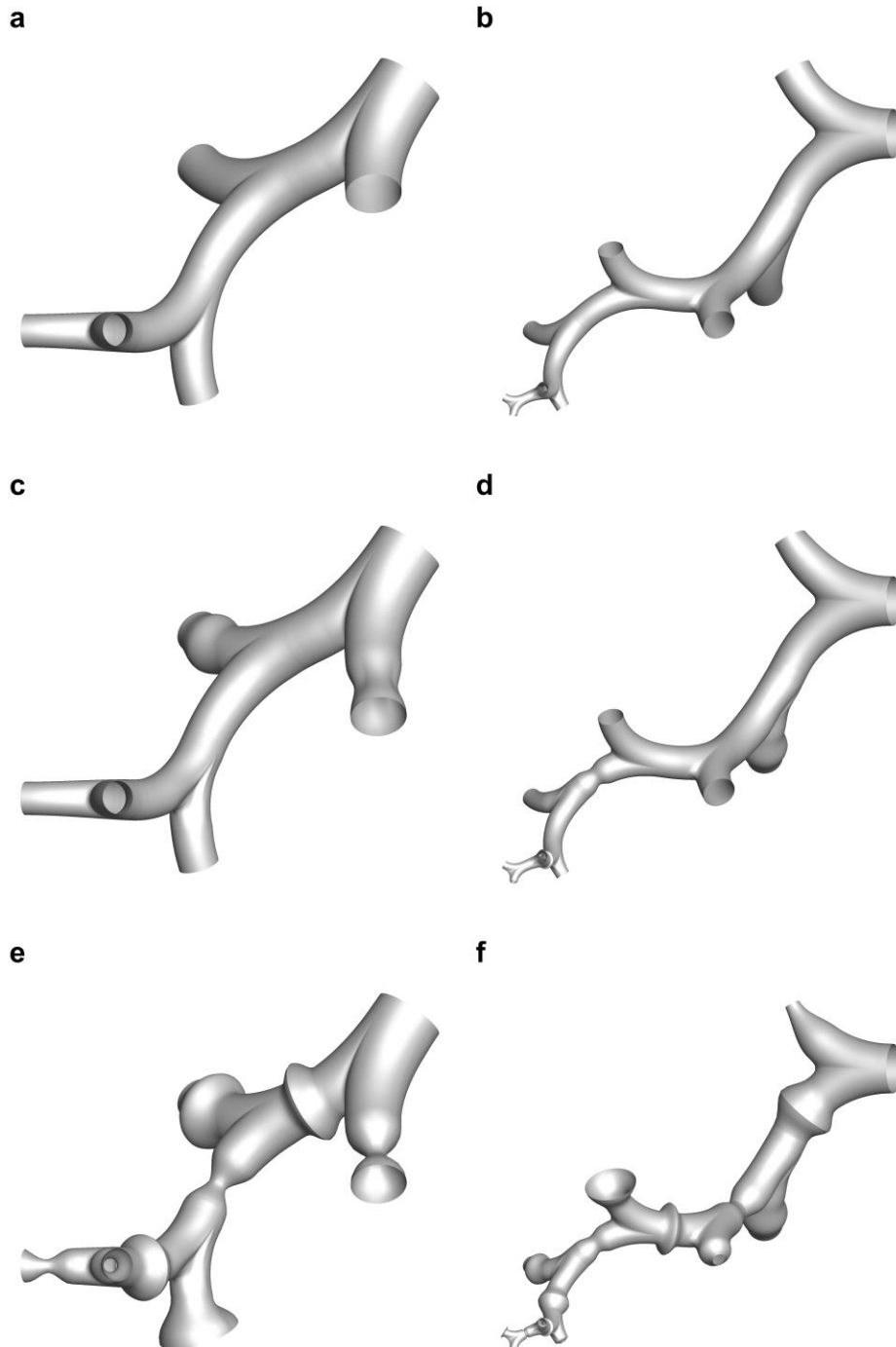
Figure 8.3: Overview of the lower airway SIP geometries for the three CF-diseased models showing the (a) CF Scaled B4-B7, (b) CF Scaled B8-B15, (c) CF Moderate B4-B7 (d) CF Moderate B8-B15, (e) CF Severe B4-B7, and (f) CF Severe B8-B15 SIP models.
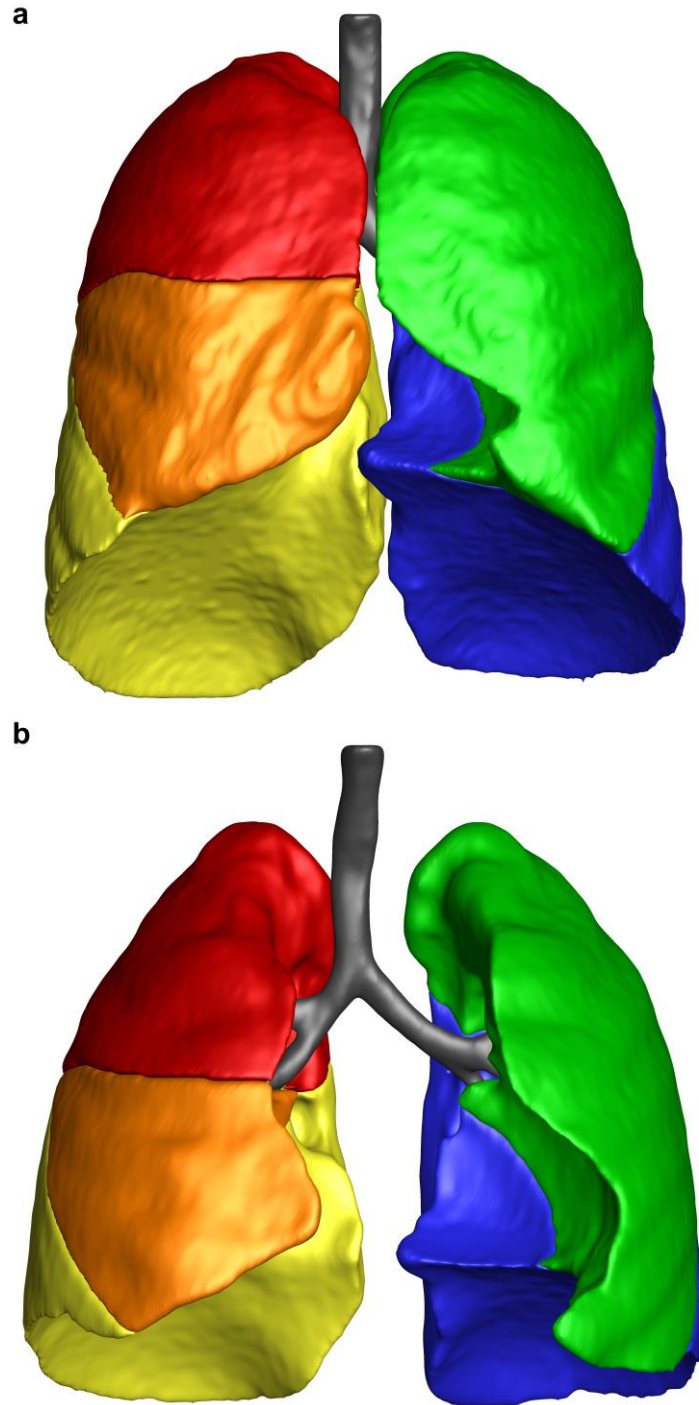
Figure 8.4:   Comparison of extracted lobes from CT scans at (a) inhalation and (b) exhalation. Lobes are colored as: green – left upper; blue – left lower; red – right upper; orange – right middle; and yellow – right lower.
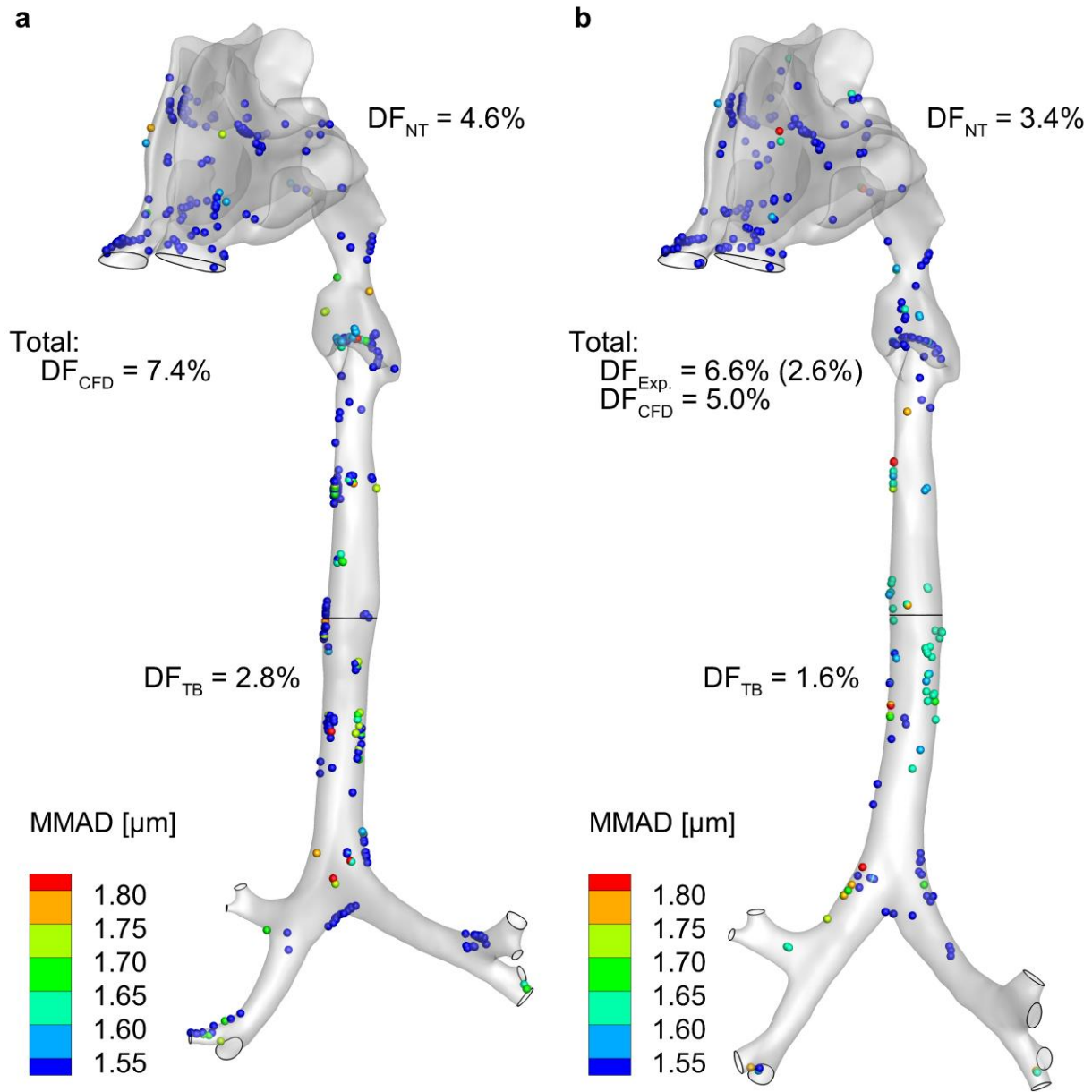
Figure 8.5: Deposition patterns in the NT-B3 region for the (a) Healthy and (b) CF Moderate models. Note that validation of the CF-diseased model is compared against the experimental deposition data from the 5-6-year-old CF growth chamber model in Chapter 7.
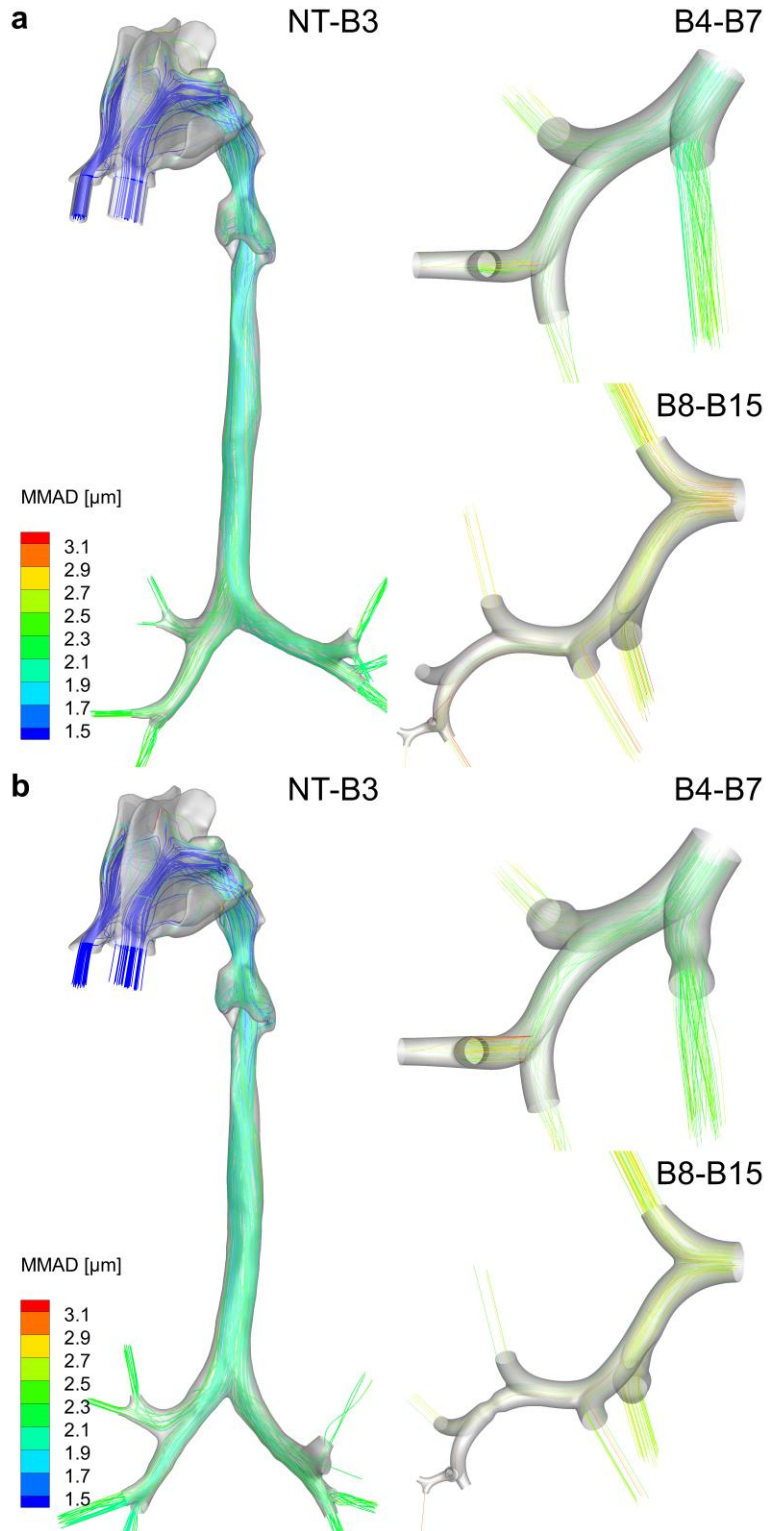
Figure 8.6: Particle trajectories and growth through the CFD regions, with the Base EEG aerosol, for the (a) Healthy and (b) CF Moderate SIP models.
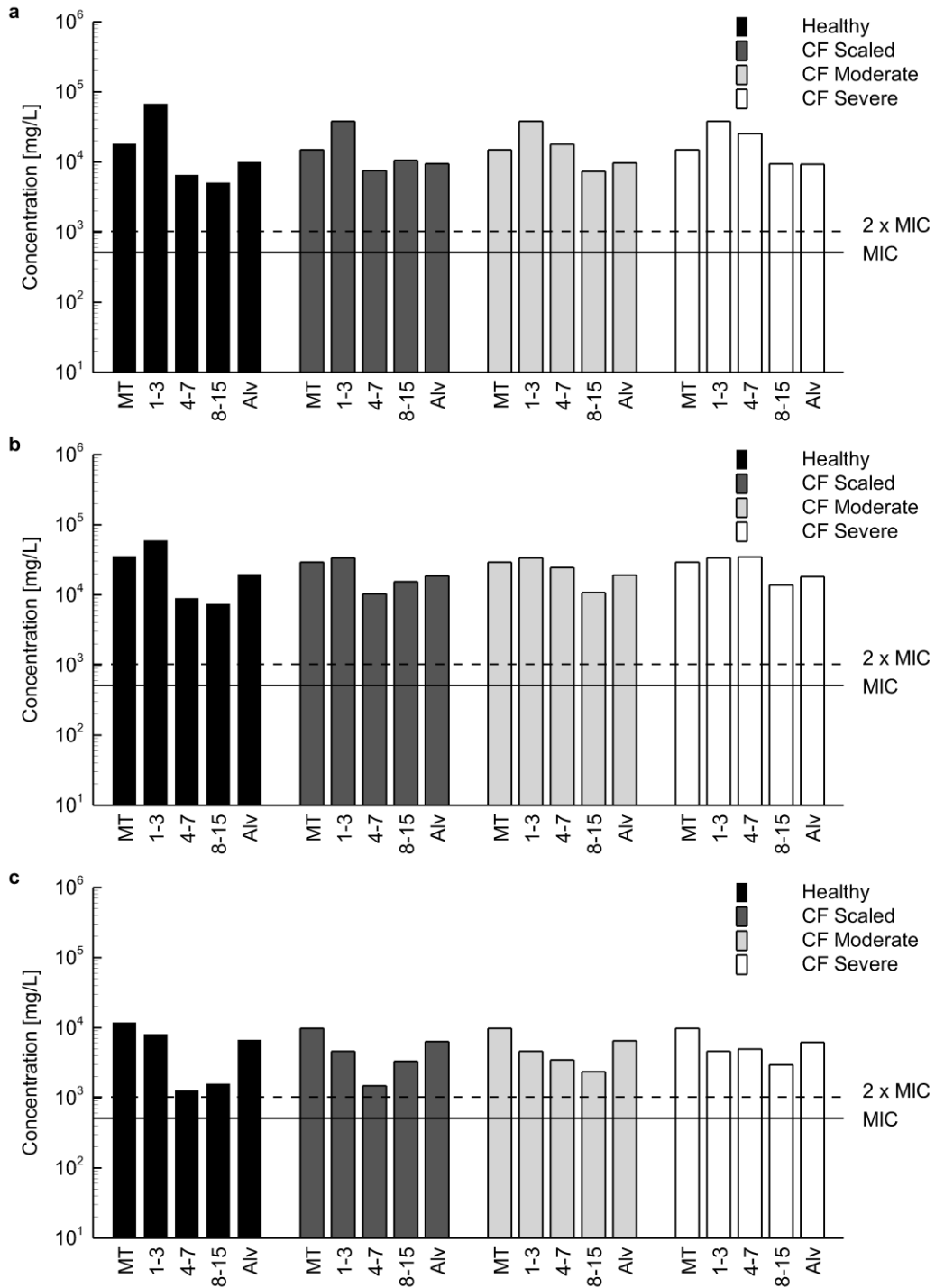
Figure 8.7: Regional tobramycin concentrations in the airway surface liquid (ASL) between the Healthy, CF Scaled, CF Moderate, and CF Severe models for the Base EEG aerosol, with respect to the (a) ICRP, (b) Min, and (c) Max ASL volumes.
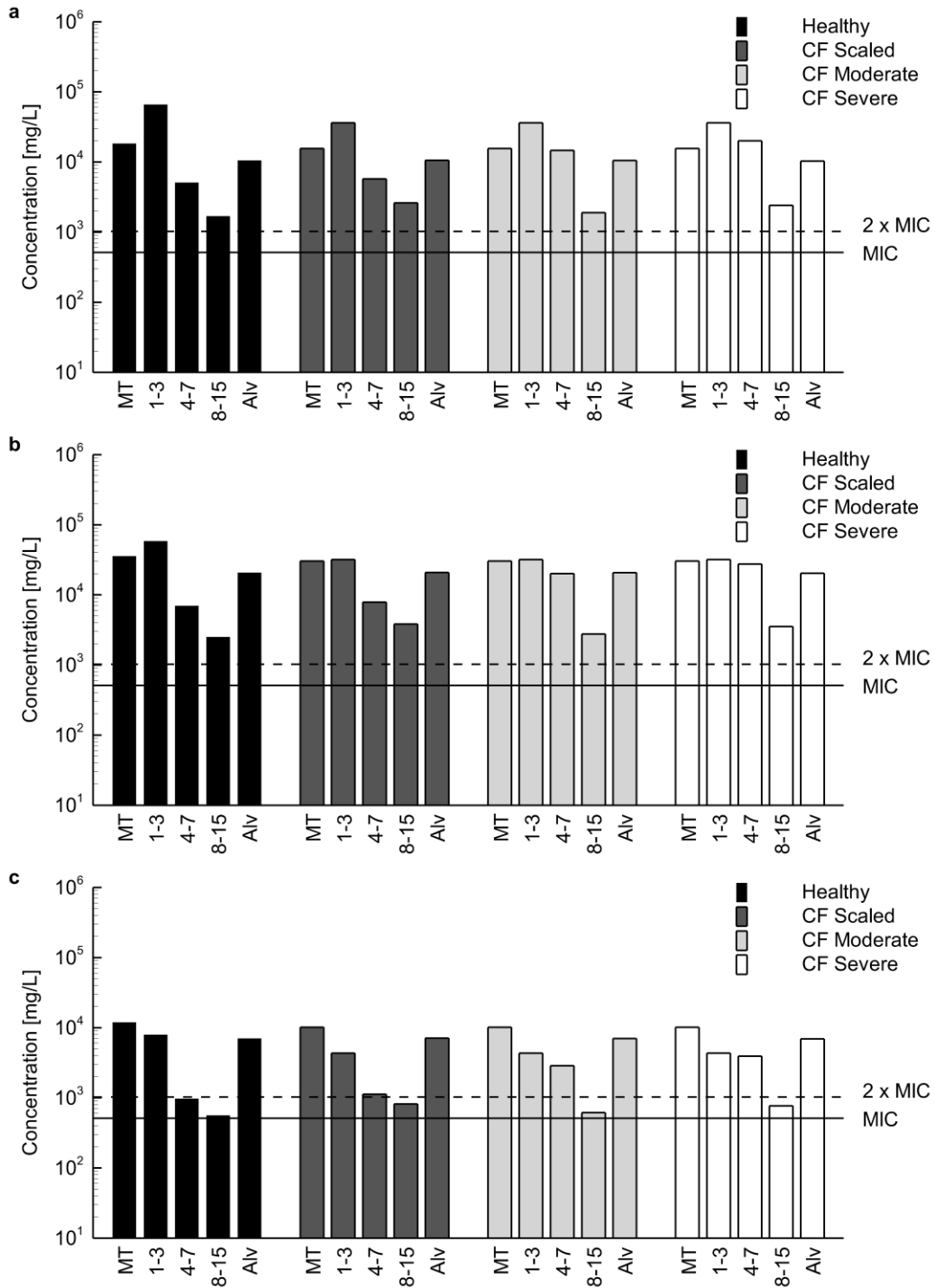
Figure 8.8: Regional tobramycin concentrations in the airway surface liquid (ASL) between the Healthy, CF Scaled, CF Moderate, and CF Severe models for the Min Static aerosol, with respect to the (a) ICRP, (b) Min, and (c) Max ASL volumes.
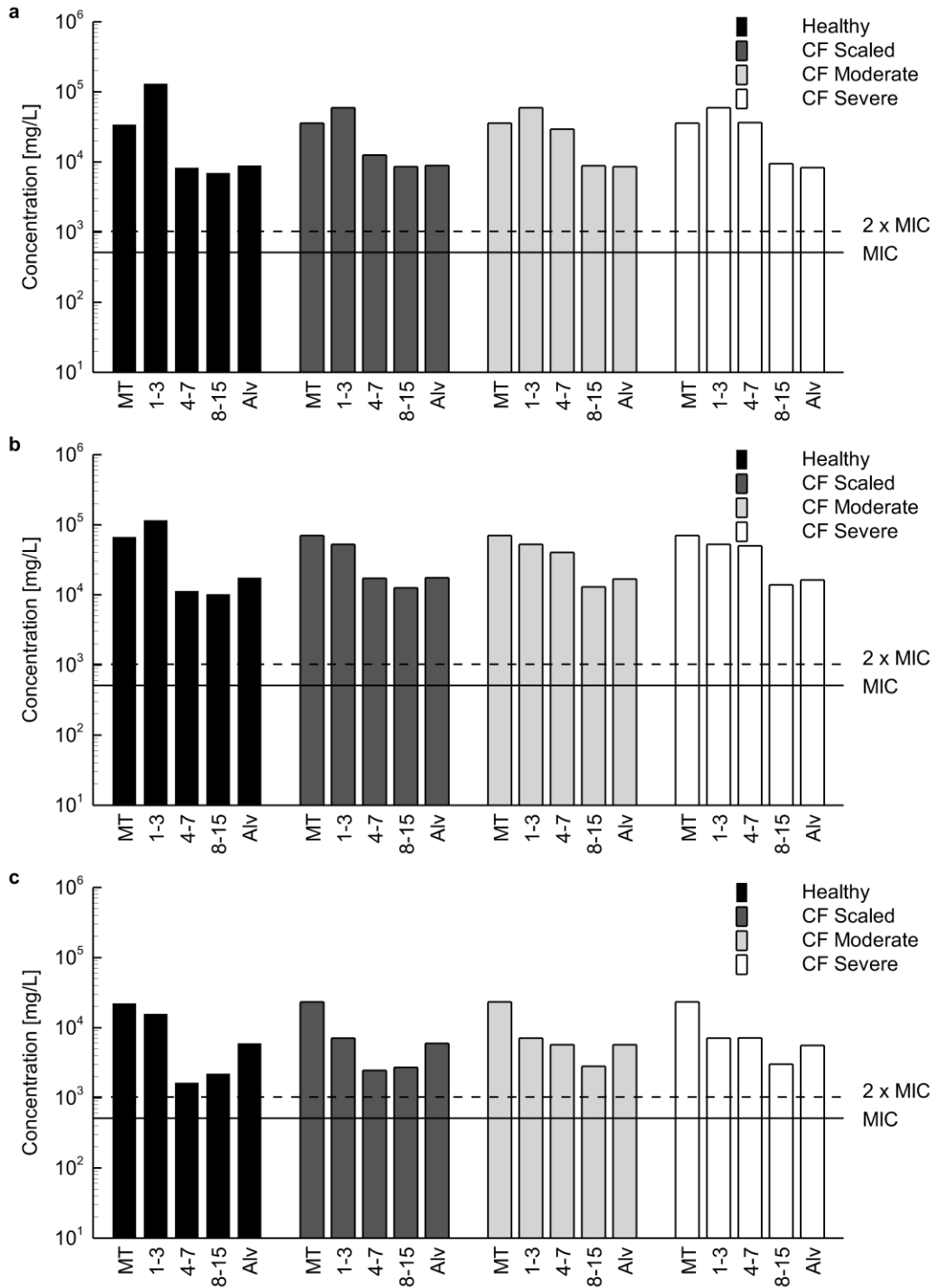
Figure 8.9: Regional tobramycin concentrations in the airway surface liquid (ASL) between the Healthy, CF Scaled, CF Moderate, and CF Severe models for the Max Static aerosol, with respect to the (a) ICRP, (b) Min, and (c) Max ASL volumes.
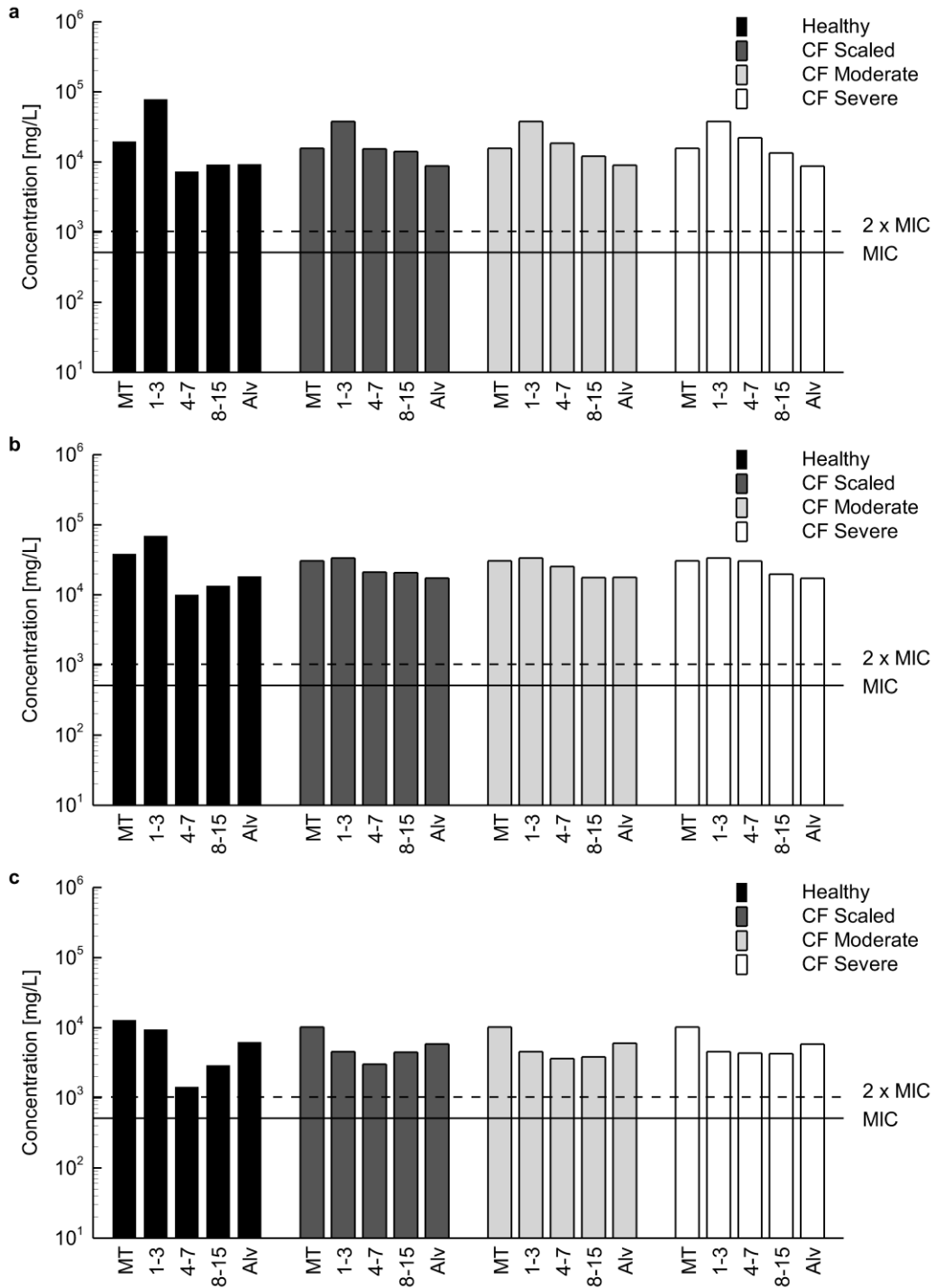
Figure 8.10: Regional tobramycin concentrations in the airway surface liquid (ASL) between the Healthy, CF Scaled, CF Moderate, and CF Severe models for the Optimal EEG aerosol, with respect to the (a) ICRP, (b) Min, and (c) Max ASL volumes.

8.7   Tables

Table 8.1:   Comparison of lobar ventilation fractions between healthy and CF-diseased lungs.

Lobe	Healthy[a]	CF Diseased
Left Upper	14%	16%
Left Lower	7%	7%
Right Upper	33%	28%
Right Middle	15%	21%
Right Lower	31%	28%
a: Ventilation fractions consistent with the Adult SIP model (Tian et al., 2015)		

Table 8.2:   Summary of bifurcation-level surface area, airway surface liquid thickness, and volume for the ICRP, Min, and Max ASL volumes. Values are given for a single bifurcation, that is, not summed over the number of a given bifurcation found in the lungs.

Region	A_s [cm^2]	ICRP h [µm]	V [µL]	Min h [µm]	V [µL]	Max h [µm]	V [µL]
B4	1.47	11.00	1.62	10.19	1.50	76.67	11.27
B5	1.43	11.00	1.57	9.60	1.37	72.80	10.40
B6	0.99	11.00	1.09	8.20	0.82	58.42	5.81
B7	0.81	11.00	0.90	6.74	0.55	42.84	3.49
B8	0.47	11.00	0.51	5.85	0.27	33.82	1.58
B9	0.42	6.00	0.25	5.31	0.22	28.94	1.22
B10	0.23	6.00	0.14	4.95	0.11	26.15	0.59
B11	0.20	6.00	0.12	4.67	0.10	24.05	0.49
B12	0.15	6.00	0.092	4.39	0.067	21.74	0.33
B13	0.040	6.00	0.024	4.23	0.017	20.66	0.084
B14	0.025	6.00	0.015	3.44	0.0083	10.13	0.025
B15	0.016	6.00	0.010	3.44	0.0053	10.13	0.016

A_s: Surface area
h: Airway surface liquid thickness
V: Airway surface liquid volume
BX: Bifurcation number X

Table 8.3:   Summary of regional airway surface liquid volumes for the ICRP, Min, and

Max ASL volumes. Values for each region include summation over the number of a given

bifurcation found in the lungs.

Region	V_{ICRP} [mL]	V_{Min} [mL]	V_{Max} [mL]
NT	0.19	0.10	0.29
B1-B3	0.03	0.04	0.27
B4-B7	0.13	0.10	0.67
B8-B15	0.89	0.61	2.81
Alv	6.41	3.25	9.56
Total	7.65	4.09	13.60

V_{ICRP}: ICRP ASL Volume
V_{Min}: Min ASL Volume
V_{Max}: Max ASL Volume
NT: Nose-throat region
BX: Bifurcation number X
Alv: Alveolar region

Table 8.4: Comparison of regional deposition in the Healthy SIP model to algebraic and empirical correlations.

Region	CFD SIP	MMAD [μm]	ICRP[a]	Rudolf[b]	Finlay[c]
BB (T-B8)	2.25%	1.67	2.17%	1.58%	5.12%
Bb (B9-B15)	4.74%	2.23	3.56%	5.91%	10.86%

a: Sourced from (ICRP, 1994)
b: Sourced from (Rudolf et al., 1990)
c: Sourced from (W. H. Finlay, 2001)

BB: Bronchial region
bb: Bronchiolar region

Table 8.5: Summary of regional deposition fractions (DF) for all SIP models and all aerosol cases.

Region	Healthy DF [%]	CF Scaled DF [%]	CF Moderate DF [%]	CF Severe DF [%]
Base EEG				
NT	4.6	3.8	3.8	3.8
1-3	2.7	1.5	1.5	1.5
4-7	1.2	1.4	3.3	4.6
8-15	6.6	13.4	9.6	12.4
Min Static				
NT	4.6	3.9	3.9	3.9
1-3	2.6	1.4	1.4	1.4
4-7	0.9	1.1	2.7	3.7
8-15	2.2	3.3	2.4	3.1
Max Static				
NT	8.6	9.1	9.1	9.1
1-3	5.2	2.4	2.4	2.4
4-7	1.7	2.5	5.8	7.1
8-15	9.8	11.8	12.6	13.7
Optimal EEG				
NT	5.0	4.0	4.0	4.0
1-3	3.1	1.5	1.5	1.5
4-7	1.4	2.8	3.4	4.1
8-15	12.1	18.3	15.7	17.6

Table 8.6:   Summary of regional tobramycin concentrations in the airway surface liquid (ASL), compared to the minimum inhibitory concentration (MIC), for all SIP models, all ASL volumes, and the Base EEG case.

Region	Healthy [x MIC mg/L]	CF Scaled [x MIC mg/L]	CF Moderate [x MIC mg/L]	CF Severe [x MIC mg/L]
ICRP ASL Volume				
NT	35.5	29.2	29.2	29.2
1-3	131.7	74.4	74.4	74.4
4-7	12.8	14.7	35.0	49.5
8-15	9.9	20.6	14.4	18.4
Alveolar	19.5	18.5	18.9	18.1
Min ASL Volume				
NT	67.5	55.5	55.5	55.5
1-3	98.8	55.8	55.8	55.8
4-7	16.6	19.1	45.5	64.4
8-15	14.4	30.1	21.0	26.8
Alveolar	38.5	36.5	37.3	35.7
Max ASL Volume				
NT	23.3	19.1	19.1	19.1
1-3	14.6	8.3	8.3	8.3
4-7	2.5	2.9	6.8	9.6
8-15	3.1	6.5	4.6	5.8
Alveolar	13.1	12.4	12.7	12.1

Table 8.7:   Summary of regional tobramycin concentrations in the airway surface liquid (ASL), compared to the minimum inhibitory concentration (MIC), for all SIP models, all ASL volumes, and the Min Static case.

Region	Healthy [x MIC mg/L]	CF Scaled [x MIC mg/L]	CF Moderate [x MIC mg/L]	CF Severe [x MIC mg/L]
ICRP ASL Volume				
NT	35.7	30.4	30.4	30.4
1-3	129.0	70.6	70.6	70.6
4-7	9.9	11.2	28.7	39.2
8-15	3.3	5.1	3.7	4.7
Alveolar	20.5	20.7	20.5	20.2
Min ASL Volume				
NT	67.8	57.8	57.8	57.8
1-3	96.8	53.0	53.0	53.0
4-7	12.9	14.6	37.3	51.0
8-15	4.8	7.4	5.4	6.9
Alveolar	40.4	40.8	40.4	39.8
Max ASL Volume				
NT	23.4	19.9	19.9	19.9
1-3	14.3	7.8	7.8	7.8
4-7	1.9	2.2	5.6	7.6
8-15	1.0	1.6	1.2	1.5
Alveolar	13.7	13.9	13.7	13.5

Table 8.8: Summary of regional tobramycin concentrations in the airway surface liquid (ASL), compared to the minimum inhibitory concentration (MIC), for all SIP models, all ASL volumes, and the Max Static case.

Region	Healthy [x MIC mg/L]	CF Scaled [x MIC mg/L]	CF Moderate [x MIC mg/L]	CF Severe [x MIC mg/L]
ICRP ASL Volume				
NT	66.6	70.0	70.0	70.0
1-3	255.4	115.6	115.6	115.6
4-7	16.1	24.6	57.4	71.2
8-15	13.6	16.8	17.3	18.5
Alveolar	17.4	17.4	16.7	16.2
Min ASL Volume				
NT	126.5	133.0	133.0	133.0
1-3	191.6	86.7	86.7	86.7
4-7	20.9	32.0	74.6	92.6
8-15	19.8	24.5	25.2	27.0
Alveolar	34.3	34.3	32.9	32.0
Max ASL Volume				
NT	43.6	45.9	45.9	45.9
1-3	28.4	12.8	12.8	12.8
4-7	3.1	4.8	11.1	13.8
8-15	4.3	5.3	5.5	5.9
Alveolar	11.7	11.7	11.2	10.9

Table 8.9:   Summary of regional tobramycin concentrations in the airway surface liquid (ASL), compared to the minimum inhibitory concentration (MIC), for all SIP models, all ASL volumes, and the Optimal EEG case.

Region	Healthy [x MIC mg/L]	CF Scaled [x MIC mg/L]	CF Moderate [x MIC mg/L]	CF Severe [x MIC mg/L]
ICRP ASL Volume				
NT	38.3	30.6	30.6	30.6
1-3	152.8	74.0	74.0	74.0
4-7	14.2	30.0	36.1	43.2
8-15	18.0	27.6	23.6	26.3
Alveolar	18.2	17.1	17.6	17.1
Min ASL Volume				
NT	72.8	58.1	58.1	58.1
1-3	114.6	55.5	55.5	55.5
4-7	18.5	39.0	46.9	56.2
8-15	26.3	40.3	34.4	38.4
Alveolar	35.9	33.7	34.7	33.7
Max ASL Volume				
NT	25.1	20.0	20.0	20.0
1-3	17.0	8.2	8.2	8.2
4-7	2.8	5.8	7.0	8.4
8-15	5.7	8.7	7.5	8.3
Alveolar	12.2	11.5	11.8	11.5

Table 8.10: Ratios of maximum to minimum regional concentration, demonstrating deposition variability, for all SIP models, all ASL volumes, and all initial aerosol cases.

Region	Base EEG	Min Static	Max Static	Optimal EEG
Healthy				
ICRP ASL Volume	13.3	39.1	18.8	10.8
Min ASL Volume	6.8	20.1	9.7	6.2
Max ASL Volume	9.4	22.4	14.0	9.1
CF Scaled				
ICRP ASL Volume	5.1	13.8	6.9	4.3
Min ASL Volume	2.9	7.8	5.4	1.7
Max ASL Volume	6.7	12.3	9.6	3.4
CF Moderate				
ICRP ASL Volume	5.2	19.1	6.9	4.2
Min ASL Volume	2.7	10.7	5.3	1.7
Max ASL Volume	4.2	17.0	8.4	2.9
CF Severe				
ICRP ASL Volume	4.1	15.0	7.1	4.3
Min ASL Volume	2.4	8.4	4.9	1.7
Max ASL Volume	3.3	13.4	7.8	2.4

Chapter 9: Conclusions and Future Work

9.1 Objective 1: Accurate CFD Simulations of Aerosol Delivery in Infants and Children

The packed bed lung model study (Chapter 2) sought a complete-airway *in vitro* model with aerosol deposition characteristics similar to *in vivo* conditions in an infant, which meets the requirements of Task 1.1. This study concluded that *in vitro* packed bed lung models are capable of matching total aerosol deposition in the lungs of an infant. However, comparisons between sphere layers and bifurcation regions of a CFD SIP model showed a marked difference in regional deposition patterns and particle residence times. This means that packed bed models are not well suited for comparisons with regional *in vivo* data, where gamma scintigraphy characterizes deposition in central and peripheral regions. The fundamental issue was that the geometry of the voids in a packed bed model are too far removed from lung bifurcations, such that particle trajectories and deposition patterns were very different. The positive outcome from this study was that the CFD-based infant SIP model matched algebraic and empirical correlations with regard to deposition profiles across the micro-particle size range.

The 90° bend study (Chapter 3) established recommended meshing and solution guidelines for modeling aerosol transport and deposition with the LRN k-ω model, which meets the requirements of Task 1.2. This study demonstrated the successful validation of the numerical models against experimental data across a range of Reynolds numbers and micro-particle sizes. The primary benefit of these recommendations is an increase in model accuracy and consistency, as well as streamlining the CFD mesh and model development process. Furthermore, the results from the two-equation k-ω model, with

near-wall corrections, provided comparable accuracy to the more complex LES model. LES models are more computationally expensive, so utilizing the more efficient k-ω model has benefits when running transient studies or more advance particle tracking methods.

The 6-month-old nose-to-lung study (Chapter 4) validated the CFD meshing and solution guidelines in a nasal cavity model, which meets the requirements of Task 1.3. The nasal cavity model had more complex geometry features and flow field conditions than the characteristic 90° bend, which extended the applicability of the aforementioned CFD recommendations. Numerical results compared well with experimental data for nasal administration of EEG aerosols to infants. As a secondary outcome, this study also demonstrated the capabilities of EEG aerosols for navigating the natural filtration of the extrathoracic airways in infant patients, which maximizes available lung dose. Furthermore, evaluation of the CFD results identified deposition hotspots in the nasal cannula and nostril regions, which should be the focus of further effort to reduce depositional losses. A final outcome of this study was an anatomically-accurate infant nose-to-lung model, extracted from CT scans, which will be useful for future studies on pharmaceutical aerosol delivery to infants.

9.2   Objective 2: Quantitative Analysis and Design of High Efficiency Pediatric DPIs

The tobramycin DPI study (Chapter 5) detailed the optimization process for improving the aerosolization performance of a positive-pressure pediatric DPI, which meets the requirements of Task 2.1. This study developed dispersion parameters and correlations that were predictive of the aerosol MMAD and emitted dose from the DPI outlets. *A priori* validation of the best-case design candidates was successful, whereby

experimental results confirmed the performance improvements from CFD predictions, with no subsequent changes to the numerical models. Furthermore, results showed how changes to design parameters affected turbulent kinetic energy and flow rate (by changes to flow resistance), which were key factors in the dispersion parameter correlations. The best-case design candidates improved aerosolization performance over the initial device by reducing aerosol MMAD from 1.69 µm to 1.55 µm and increasing emitted dose from 86.0% to 92.3%, while maintaining a constant pressure drop across the device.

The patient interface study (Chapter 6) presented design improvements to pediatric mouthpieces and nasal cannulas that minimized delivery system and extrathoracic losses, thus maximizing available lung dose, which meets the requirements of Task 2.2. The aerosolization performance of the air-jet DPI (from Task 2.1) requires small diameter capillaries, which lead to a highly-turbulent, high velocity jet entering the patient interface and extrathoracic region. This jet increases aerosol loss in these regions through turbulent dispersion and inertial impaction, so a design was sought that was capable of effectively diffusing the air jet. This study followed several design iterations, which concluded that the addition of a 3D rod array and widening the geometry near the device outlet capillary gave the best reduction in losses. Three mouthpiece design concepts were presented with CFD predictions of a three-fold reduction in total interface and extrathoracic loss over the original design (from 16.7% to 5.1%). The nasal cannula design concepts were not as efficient, as the design concepts were not as effective at reducing losses in the nose-throat region. However, a 25% reduction in device flow rate (from 13.3 to 9.9 LPM) reduced delivery system and extrathoracic losses from 24.1% to 16.3%. This reduction in device flow rate is not expected to have a negative impaction on

374

the DPI aerosolization performance (Bass, Farkas, et al., 2019). Furthermore, this study presented correlations that were predictive of extrathoracic deposition based on the maximum value of the velocity profile that leaves the patient interface. This showed that for a constant flow rate, the downstream deposition was vastly different if the velocity had a high peak velocity (jet-like profile) compared with a low peak velocity (blunt turbulent profile). This has implications for extrathoracic loss correlations that utilize the impaction parameter (Qd_a), as this traditional metric does not capture the characteristics of the velocity profile that enters the mouth-throat or nose-throat regions.

9.3   Objective 3: CFD Predictions of EEG Aerosol Antibiotic Delivery to Children with Cystic Fibrosis

The growth chamber study (Chapter 7) developed three experimental and CFD models (2-3-, 5-6-, and 9-10-year-olds) for evaluating upper airway deposition and EEG aerosol size increase through the lungs of CF pediatric patients, which meets the requirements of Task 3.1 and 3.2. This study demonstrated concurrent numerical and experimental analysis of EEG aerosol delivery, with good validation of the CFD results against *in vitro* deposition and growth data. Results showed administration of EEG aerosols with the best-case delivery system gave low upper airway losses, with approximately 11%, 5%, and 7% deposition for the 2-3-, 5-6-, and 9-10-year-old models, respectively, at a constant device actuation flow rate of 10 LPM. This is a marked improvement over evaluation of commercial devices and delivery strategies in the literature, with the best available case being 22% lung dose (78% loss) from the Easyhaler (Below et al., 2013). The growth chamber was designed to provide a particle residence time of approximately 2.0 s, which is consistent with typical particle trajectories through

the lungs, resulting in final aerosol MMAD of approximately 3.3 µm due to hygroscopic growth. The larger aerosol size in distal regions of the lungs is expected to maximize lung retention of the delivered drug via increased sedimentation (during a breath-hold maneuver) and impaction (upon exhalation) deposition. This study also presented an enhancement to the near-wall corrections by implementing a local particle Stokes number to determine when particle-wall hydrodynamic interactions are modeled. The new method provided a non-dimensional approach and allowed the near-wall corrections to work independently of local flow conditions.

The CF SIP study (Chapter 8) developed complete-airway CFD models of diseased pediatric patients to predict regional tobramycin concentrations delivered to the airway surface liquid, which meets the requirements of Task 3.3. This study provided a proof of concept for EEG aerosol administration to treat bacterial infections in the diseased airways of CF patients. Treatment of infection with antibiotics requires the drug dose to be above a minimum lower threshold and a uniform distribution through all lung regions. For both EEG aerosol cases considered, the delivered tobramycin concentration within the airway surface liquid was consistently above the minimum inhibitory concentration (MIC), which is 512 mg/L, within all lung regions. For the CF-diseased models, the minimum predicted concentration in all lung regions was 2.9 x MIC for the base EEG aerosol and 5.8 x MIC for the optimal case. The optimal case also reduced regional variability to an approximate four-fold difference between maximum and minimum concentrations. Furthermore, the CFD models predicted high tobramycin concentrations in the lower airways, where CF-related airway damage is most predominant, with a minimum value of 7.5 x MIC in the B8-B15 region. As a secondary

outcome, this study also compared the advantages of EEG powder formulations compared to static aerosols (no hygroscopic growth) in regard to nasal transmission and targeted drug delivery. Finally, this study evaluated delivery to airways with varying degrees of disease state and considered the influence of interpatient variability on optimal delivery strategies.

9.4   Contributions to Science

From the studies detailed in this dissertation, the contributions to the fields of CFD methods development, respiratory device design, and aerosol delivery strategy development are summarized below.

Task 1.1: Evaluate Deposition Realism of In Vitro Packed-Bed Breathing Infant Lung Model (BIL)

- Thorough assessment of packed bed lung models and their use for *in vitro* evaluation of pharmaceutical aerosol delivery, showing they are representative of total, but not regional, deposition fractions
- Complete-airway CFD SIP model of microparticle particle tracking and deposition in a neonate

Task 1.2: Recommendations for Simulation of Microparticle Transport and Deposition Using Two-Equation Turbulence Models

- A set of CFD meshing and solution guidelines for modeling microparticle trajectories through respiratory airways, which were validated against experimental data in a characteristic 90° bend geometry
- Enhancement to near-wall corrections that interpolate flow quantities at the particle location, from nodal values, with an inverse-distance weighted method

- Established that the k-ω turbulence model, with near-wall corrections, is capable of matching *in vitro* data with comparable accuracy to the more computationally-expensive LES model

Task 1.3: Validating CFD Predictions of N2L Aerosol Delivery in a 6-Month-Old Infant Airway Model

- Experimental and CFD models for nasal administration of pharmaceutical aerosols to a 6-month-old infant

- Further validation of k-ω turbulence and the aforementioned guidelines in the complex flow field of the nasal cavity

Task 2.1: CFD Optimization of an Inline DPI for EEG Tobramycin Formulations

- Pediatric air-jet DPI designs that maximize aerosolization performance by optimization of inlet and outlet capillary diameters

- Dispersion parameters that are predictive of the device aerosol size and emitted dose from CFD flow field quantities

Task 2.2: Develop DPI Patient Interfaces for Improved Aerosol Delivery to Children

- Patient interface design concepts that minimize delivery system and extrathoracic losses by utilizing a 3D rod array for flow intensity attenuation

- Deposition correlations that are predictive of extrathoracic losses from characteristics of the flow field at the interface outlet

Task 3.1: Develop In Vitro Upper Airway Geometries of CF Patients in Age Ranges of 2-3, 5-6, And 9-10 Years

- Three rapid-prototyped growth chamber models for the given age ranges and moderate disease state that will be utilized in future tobramycin EEG aerosol studies

Task 3.2: Develop CFD Models of Upper Airway Geometries for Pediatric Patients and Evaluate Delivery Efficiency and Aerosol Growth with Comparisons to In Vitro Experiments

- Concurrent numerical and experimental evaluation of hygroscopic aerosol growth through CF-diseased pediatric upper airways

- Enhancement to near-wall corrections that implement a localized particle Stokes number as a non-dimensional method of identifying when particle-wall hydrodynamic interactions take effect

Task 3.3: Extend and Develop CFD Lung Models to Predict Regional Lung Deposition and Tobramycin ASL Concentrations in Healthy and CF Complete-Airway Lung Models

- Proof of concept for administration of tobramycin EEG aerosols to treat bacterial infections in pediatric CF patients

- Development of complete-airway pediatric SIP models that include forms of airway damage that are associated with CF and bacterial infection

9.5 Future Work

Considering CFD methods development for respiratory drug delivery, future work should focus on exploring new meshing technologies and modeling capabilities as they

become available in commercial software. Polyhedral cell topologies are a relatively recent advancement in volume discretization methods, which have been shown to provide computationally-efficient, accurate, and validated results (Bass, Boc, et al., 2019; Bass & Longest, 2020). Unstructured meshing approaches, such as polyhedral cells, are invaluable when developing the computational domain for complex geometries, as the surface and volume discretization can conform to irregular surfaces. Considering diseased airways where structured meshes may not be feasible, polyhedral cells will be useful for resolving flow fields and particle trajectories in the complex domain. Commercial CFD software is also regularly updated, and advancements in modeling and solver capabilities may be implemented to reduce the computational overhead and increase the solution and post-processing detail. For example, physical details of the secondary breakup mechanism in air-jet DPIs and through 3D rod arrays is not well understood at this time. Discrete element methods or other advanced Lagrangian tracking models may be able to provide more insight into this phenomenon. For diseased airways, the complete-airway SIP models can be developed further to provide a more realistic and validated representation of aerosol transport in the airways of pediatric CF patients. Further enhancements can also be made to the near-wall corrections to make them suitable to a wider range of applications and reduce the amount of parameter tuning that is required to match *in vitro* and *in vivo* data sets.

For delivery system improvements, future work should explore the influence of more design factors on DPI aerosolization performance. This dissertation evaluated changes to the inlet and outlet capillary diameters, but the size and shape of the aerosolization chamber can be optimized, as well as flow orifice positioning and actuation

flow rates. Similar optimization studies can be conducted on the 3D rod array patient interfaces that explore the effects of rod array configuration and placement on delivery system and extrathoracic losses. Other design changes may be required to maximize system performance in different pediatric age ranges, such as younger (2-3-year-old) and older (9-10-year-old) patients. Furthermore, it would be interesting to test the aerosol dispersion parameters and extrathoracic loss correlations on a wider range of air-jet DPI design concepts and different patient populations. Finally, as mentioned above, greater insight in to the secondary break-up mechanisms, as the powder is aerosolized and passes through the rod array, is required.

Regarding delivery strategy development, future work should expand the assessment of EEG aerosols in complete-airway CFD models by evaluating lobar variability in delivered tobramycin and consider the 2-3- and 9-10-year-old age groups. Interpatient variability and its effect on establishing optimized delivery strategies should be considered, as well as the use of different cannula sizes (to meet the needs of the entire patient population) and how they influence delivery system and extrathoracic losses. Direct validation of the numerical models for aerosol deposition and growth of tobramycin EEG powder formulations is required. In addition, the optimal EEG delivery strategy can be explored further by testing the influence of powder formulation (mass fractions of drug and excipients), bi-modal aerosol size distributions, and delivery flow rates. Finally, advanced CFD modeling capabilities can be implemented, such as polydisperse aerosols and two-way coupled tracking, to improve the accuracy and detail in results obtained from numerical models.

List of References

Ahmed, S. A., & Giddens, D. P. (1983a). Flow Disturbance Measurements through a Constricted Tube at Moderate Reynolds-Numbers. *Journal of Biomechanics, 16*(12), 955-963. doi:Doi 10.1016/0021-9290(83)90096-9

Ahmed, S. A., & Giddens, D. P. (1983b). Velocity-Measurements in Steady Flow through Axisymmetric Stenoses at Moderate Reynolds-Numbers. *Journal of Biomechanics, 16*(7), 505-&. doi:Doi 10.1016/0021-9290(83)90065-9

Ahmed, S. A., & Giddens, D. P. (1984). Pulsatile Poststenotic Flow Studies with Laser Doppler Anemometry. *Journal of Biomechanics, 17*(9), 695-&. doi:Doi 10.1016/0021-9290(84)90123-4

Amirav, I. (2011). Aerosol therapy in infants & Toddlers- Challenges and Solutions. *Allergy, Asthma and Immunology: From Genes to Clinical Application: Proceedings of the Iv World Asthma and Copd Forum and Xvi International Congress on Rehabilitation in Medicine and Immunorehabilitation*, 105-120.

Amirav, I., Balanov, I., Gorenberg, M., Luder, A. S., Newhouse, M. T., & Groshar, D. (2002). beta-agonist aerosol distribution in respiratory syncytial virus bronchiolitis in infants. *Journal of Nuclear Medicine, 43*(4), 487-491.

Amirav, I., Borojeni, A. A. T., Halamish, A., Newhouse, M. T., & Golshahi, L. (2015). Nasal Versus Oral Aerosol Delivery to the "Lungs" in Infants and Toddlers. *Pediatric Pulmonology, 50*(3), 276-283. doi:10.1002/ppul.22999

Amirav, I., & Newhouse, M. T. (2001). Aerosol therapy with valved holding chambers in young children: Importance of the facemask seal. *Pediatrics, 108*(2), 389-394. doi:DOI 10.1542/peds.108.2.389

Andersen, D. H. (1938). Cystic fibrosis of the pancreas and its relation to celiac disease: A clinical and pathologic study. *American Journal of Diseases of Children, 56*(2), 344-399. doi:10.1001/archpedi.1938.01980140114013

Anderson, W. K., & Bonhaus, D. L. (1994). An Implicit Upwind Algorithm for Computing Turbulent Flows on Unstructured Grids. *Computers & Fluids, 23*(1), 1-21. doi:Doi 10.1016/0045-7930(94)90023-X

ANSYS. (2012). *ANSYS FLUENT Theory Guide* (14.5 ed.). Canonsburg, PA: ANSYS.

ANSYS. (2017). *ANSYS FLUENT User Guide* (18.2 ed.). Canonsburg, PA: ANSYS.

Ariane, M., Sommerfeld, M., & Alexiadis, A. (2018). Wall collision and drug-carrier detachment in dry powder inhalers: Using DEM to devise a sub-scale model for CFD calculations. *Powder Technology, 334*, 65-75.

Asgharian, B., & Price, O. T. (2006). Airflow distribution in the human lung and its influence on particle deposition. *Inhalation Toxicology, 18*, 795-801.

Awadalla, M., Miyawaki, S., Abou Alaiwa, M. H., Adam, R. J., Bouzek, D. C., Michalski, A. S., . . . Stoltz, D. A. (2014). Early Airway Structural Changes in Cystic Fibrosis Pigs as a Determinant of Particle Distribution and Deposition. *Annals of Biomedical Engineering, 42*(4), 915-927. doi:10.1007/s10439-013-0955-7

Ball, C. G., Uddin, M., & Pollard, A. (2008). High resolution turbulence modelling of airflow in an idealised human extra-thoracic airway. *Computers & Fluids, 37*(8), 943-964. doi:10.1016/j.compfluid.2007.07.021

Bass, K., Boc, S., Hindle, M., Dodson, K., & Longest, P. W. (2019). High-Efficiency Nose-to-Lung Aerosol Delivery in an Infant: Development of a Validated

Computational Fluid Dynamics Method. *Journal of Aerosol Medicine and Pulmonary Drug Delivery, DOI: 10.1089/jamp.2018.1490*.

Bass, K., Farkas, D., & Longest, P. W. (2019). Optimizing Aerosolization Using Computational Fluid Dynamics in a Pediatric Air-Jet Dry Powder Inhaler. *AAPS PharmSciTech, 20*(8). doi:doi.org/10.1208/s12249-019-1535-4

Bass, K., & Longest, P. W. (2018a). Development of an infant complete-airway in vitro model for evaluating aerosol deposition. *Medical Engineering & Physics, 58*, 47-55. doi:doi.org/10.1016/j.medengphy.2018.05.002

Bass, K., & Longest, P. W. (2018b). Recommendations for simulating microparticle deposition at conditions similar to the upper airways with two-equation turbulence models. *Journal of Aerosol Science, 119*, 31-50. doi:10.1016/j.jaerosci.2018.02.007

Bass, K., & Longest, P. W. (2020). Development of Dry Powder Inhaler Patient Interfaces for Improved Aerosol Delivery to Children. *AAPS PharmSciTech, In review*.

Behara, S. R. B., Farkas, D. R., Hindle, M., & Longest, P. W. (2014). Development of a high efficiency dry powder inhaler: effects of capsule chamber design and inhaler surface modifications. *Pharmaceutical Research, 31*, 360-372.

Behara, S. R. B., Longest, P. W., Farkas, D. R., & Hindle, M. (2014a). Development and Comparison of New High-Efficiency Dry Powder Inhalers for Carrier-Free Formulations. *Journal of Pharmaceutical Sciences, 103*(2), 465-477. doi:10.1002/jps.23775

Behara, S. R. B., Longest, P. W., Farkas, D. R., & Hindle, M. (2014b). Development of high efficiency ventilation bag actuated dry powder inhalers. *International Journal of Pharmaceutics, 465*, 52-62.

Below, A., Bickmann, D., & Breitkreutz, J. (2013). Assessing the performance of two dry powder inhalers in preschool children using an idealized pediatric upper airway model. *International Journal of Pharmaceutics, 444*(1-2), 169-174.

Bhattacharjee, S., & Grosshandler, W. (1988). *The formation of a wall jet near a high temperature wall under microgravity environment.* Paper presented at the ASME 1988 National Heat Transfer Conference, Volume 1.

Blasius, H. (1913). Das Ähnlichkeitsgesetz bei Reibungsvorgängen in Flüssigkeiten. *Forsch. Arb. Ing.-Wes.*

Bos, A. C., Mouton, J. W., van Westreenen, M., Andrinopoulou, E. R., Janssens, H. M., & Tiddens, H. A. W. M. (2017). Patient-specific modelling of regional tobramycin concentration levels in airways of patients with cystic fibrosis: can we dose once daily? *Journal of Antimicrobial Chemotherapy, 72*(12), 3435-3442. doi:10.1093/jac/dkx293

Bos, A. C., van Holsbeke, C., de Backer, J. W., van Westreenen, M., Janssens, H. M., Vos, W. G., & Tiddens, H. (2015). Patient-Specific Modeling of Regional Antibiotic Concentration Levels in Airways of Patients with Cystic Fibrosis: Are We Dosing High Enough? *Plos One, 10*(3), 20. doi:10.1371/journal.pone.0118454

Boucher, R. C. (2007). Cystic fibrosis: a disease of vulnerability to airway surface dehydration. *Trends in Molecular Medicine, 13*(6), 231-240.

Brand, P., Selzer, T., Tuch, T., Schulz, A., & Heyder, J. (1994). Accuracy and resolution power of aerosol-derived airway morphometry in a simple lung model. *Experimental Lung Research, 20*(3), 185-205.

Breuer, M., Baytekin, H. T., & Matida, E. A. (2006). Prediction of aerosol deposition in 90º bends using LES and an efficient Lagrangian tracking method. *Journal of Aerosol Science, 37*, 1407-1428.

Burgel, P. R., Bellis, G., Olesen, H. V., Viviani, L., Zolin, A., Blasi, F., . . . Care, E. E. T. F. P. (2015). Future trends in cystic fibrosis demography in 34 European countries. *European Respiratory Journal, 46*(1), 133-141. doi:10.1183/09031936.00196314

Byron, P. R., Hindle, M., Lange, C. F., Longest, P. W., McRobbie, D., Oldham, M. J., . . . Finlay, W. H. (2010). In vivo-in vitro correlations: predicting pulmonary drug deposition from pharmaceutical aerosols. *Journal of Aerosol Medicine and Pulmonary Drug Delivery, 23*(S2), S-59-S-69.

Carrigy, N. B., Ruzycki, C. A., Golshahi, L., & Finlay, W. H. (2014). Pediatric In Vitro and In Silico Models of Deposition via Oral and Nasal Inhalation. *Journal of Aerosol Medicine and Pulmonary Drug Delivery, 27*(3), 149-169. doi:10.1089/jamp.2013.1075

Chan, T. L., & Lippmann, M. (1980). Experimental measurements and empirical modeling of the regional deposition of inhaled particles in humans. *American Industrial Hygiene Association Journal, 41*(6), 399-408.

Chen, X., Zhong, W., Zhou, X., Jin, B., & Sun, B. (2012). CFD–DEM simulation of particle transport and deposition in pulmonary airway. *Powder Technology, 228*, 309-318. doi:doi.org/10.1016/j.powtec.2012.05.041

Chen, X. B., Lee, H. P., Chong, V. F. H., & Wang, D. Y. (2009). Assessment of Septal Deviation Effects on Nasal Air Flow: A Computational Fluid Dynamics Model. *Laryngoscope, 119*(9), 1730-1736. doi:10.1002/lary.20585

Cheng, S. H., Gregory, R. J., Marshall, J., Paul, S., Souza, D. W., White, G. A., . . . Smith, A. E. (1990). Defective Intracellular-Transport and Processing of Cftr Is the Molecular-Basis of Most Cystic-Fibrosis. *Cell, 63*(4), 827-834. doi:Doi 10.1016/0092-8674(90)90148-8

Chua, H. L., Collis, G. G., Newbury, A. M., Chan, K., Bower, G. D., Sly, P. D., & Lesouef, P. N. (1994). The influence of age on aerosol deposition in children with cystic-fibrosis. *European Respiratory Journal, 7*(12), 2185-2191.

Clark, A. R., McKenna, C., & MacLoughlin, R. (2018). *Aerosol Delivery in Term and Preterm Infants: The Final Frontier.* Paper presented at the Respiratory Drug Delivery 2018.

Coates, M. S., Chan, H.-K., Fletcher, D. F., & Chiou, H. (2007). Influence of mouthpiece geometry on the aerosol delivery performance of a dry powder inhalation. *Pharmaceutical Research, 24*(8), 1450-1456.

Coates, M. S., Chan, H.-K., Fletcher, D. F., & Raper, J. A. (2005). Influence of air flow on the performance of a dry powder inhaler using computational and experimental analyses. *Pharmaceutical Research, 22*(9), 1445-1453.

Coates, M. S., Chan, H.-K., Fletcher, D. F., & Raper, J. A. (2006). Effect of design on the performance of a dry powder inhaler using computational fluid dynamics. Part 2: Air inlet size. *Journal of Pharmaceutical Sciences, 95*(6), 1382-1392.

Coates, M. S., Fletcher, D. F., Chan, H.-K., & Raper, J. A. (2004). Effect of design on the performance of a dry powder inhaler using computational fluid dynamics. Part 1: Grid structure and mouthpiece length. *Journal of Pharmaceutical Sciences, 93*(11), 2863-2876.

Coates, M. S., Fletcher, D. F., Chan, H.-K., & Raper, J. A. (2005). The role of capusle on the performance of a dry powder inhaler using computational and experimental analyses. *Pharmaceutical Research, 22*(6), 923-932.

Crowe, C. T., Troutt, T. R., & Chung, J. N. (1996). Numerical models for two-phase turbulent flows. *Annual Review of Fluid Mechanics, 28*, 11-43.

D'Ottavio, T., & Goren, S. L. (1982). Aerosol capture in granular beds in the impaction dominated regime. *Aerosol Science and Technology, 2*(2), 91-108.

Dalhoff, A. (2014). Pharmacokinetics and Pharmacodynamics of Aerosolized Antibacterial Agents in Chronically Infected Cystic Fibrosis Patients. *Clinical Microbiology Reviews, 27*(4), 753-782. doi:10.1128/Cmr.00022-14

de Jong, P. A., Nakano, Y., Lequin, M. H., Mayo, J. R., Woods, R., Pare, P. D., & Tiddens, H. A. W. M. (2004). Progressive damage on high resolution computed tomography despite stable lung function in cystic fibrosis. *European Respiratory Journal, 23*(1), 93-97. doi:10.1183/09031936.03.00006603

DeHaan, W. H., & Finlay, W. H. (2004). Predicting extrathoracic deposition from dry powder inhalers. *Journal of Aerosol Science, 35*, 309-331.

Delvadia, R., Longest, P. W., & Byron, P. R. (2012). In vitro tests for aerosol deposition. I. Scaling a physical model of the upper airways to predict drug deposition variation in normal humans. *Journal of Aerosol Medicine, 25*(1), 32-40.

Delvadia, R. R., Hindle, M., Longest, P. W., & Byron, P. R. (2013). In vitro tests for aerosol deposition II: IVIVCs for different dry powder inhalers in normal adults. *Journal of Aerosol Medicine and Pulmonary Drug Delivery, 26*(3), 138-144.

Delvadia, R. R., Longest, P. W., Hindle, M., & Byron, P. R. (2013). In Vitro Tests for Aerosol Deposition. III: Effect of Inhaler insertion angle on aerosol deposition. *Journal of Aerosol Medicine and Pulmonary Drug Delivery, 26*(3), 145-156.

Delvadia, R. R., Wei, X. Y., Longest, P. W., Venitz, J., & Byron, P. R. (2016). In Vitro Tests for Aerosol Deposition. IV: Simulating Variations in Human Breath Profiles for Realistic DPI Testing. *Journal of Aerosol Medicine and Pulmonary Drug Delivery, 29*(2), 196-206. doi:10.1089/jamp.2015.1215

Dhapare, S., Spence, B., Boc, S., Wei, X., Bass, K., Longest, P. W., & Hindle, M. (2018). *Breath-synchronized Delivery of Aerosols to Infants Using a Very Low Volume Mixer-heater.* Paper presented at the Respiratory Drug Delivery 2018.

Donlan, R. M. (2002). Biofilms: Microbial life on surfaces. *Emerging Infectious Diseases, 8*(9), 881-890. doi:DOI 10.3201/eid0809.020063

Dunnill, M. S. (1962). Postnatal growth of the lung. *Thorax, 17*(4), 329-333.

El Taoum, K. K., Xi, J. X., Kim, J., & Berlinski, A. (2015). In Vitro Evaluation of Aerosols Delivered via the Nasal Route. *Respiratory Care, 60*(7), 1015-1025. doi:10.4187/respcare.03606

Elborn, J. S. (2016). Cystic fibrosis. *Lancet, 388*(10059), 2519-2531. doi:10.1016/s0140-6736(16)00576-6

Estepar, R. S., Ross, J. C., Harmouche, R., Onieva, J., Diaz, A. A., & Washko, G. R. (2015). Chest Imaging Platform: An Open-Source Library And Workstation For

Quantitative Chest Imaging. *American Journal of Respiratory and Critical Care Medicine, 191*.

Everard, M. L. (2003). Inhalation therapy for infants. *Advanced Drug Delivery Reviews, 55*(7), 869-878. doi:doi.org/10.1016/S0169-409X(03)00082-6

Farkas, D., Bonasera, S., Bass, K., Hindle, M., & Longest, P. W. (2020). Advancement of a Positive-Pressure Dry Powder Inhaler for Children: Use of a Vertical Aerosolization Chamber and Three-Dimensional Rod Array Interface. *Pharmaceutical Research, In review*.

Farkas, D., Hindle, M., Bass, K., & Longest, P. W. (2019). Development of an Inline Dry Powder Inhaler for Oral or Trans-Nasal Aerosol Administration to Children. *Journal of Aerosol Medicine and Pulmonary Drug Delivery, In review*.

Farkas, D., Hindle, M., & Longest, P. W. (2018a). Application of an inline dry powder inhaler to deliver high dose pharmaceutical aerosols during low flow nasal cannula therapy. *International Journal of Pharmaceutics, 546*(1-2), 1-9. doi:10.1016/j.ijpharm.2018.05.011

Farkas, D., Hindle, M., & Longest, P. W. (2018b). Efficient Nose-to-Lung Aerosol Delivery with an Inline DPI Requiring Low Actuation Air Volume. *Pharmaceutical Research, 35*(10). doi:UNSP 194

10.1007/s11095-018-2473-7

Finlay, W. H. (2001). *The mechanics of inhaled pharmaceutical aerosols: An introduction*. San Diego: Academic Press.

Finlay, W. H., Lange, C. F., King, M., & Speert, D. P. (2000). Lung delivery of aerosolized dextran. *American Journal of Respiratory and Critical Care Medicine, 161*(1), 91-97. doi:DOI 10.1164/ajrccm.161.1.9812094

Finlay, W. H., & Martin, A. R. (2008). Recent advances in predictive understanding of respiratory tract deposition. *Journal of Aerosol Medicine and Pulmonary Drug Delivery, 21*(2), 189-206.

Fok, T. F., Monkman, S., Dolovich, M., Gray, S., Coates, G., Paes, B., . . . Kirpalani, H. (1996). Efficiency of aerosol medication delivery from a metered dose inhaler versus jet nebulizer in infants with bronchopulmonary dysplasia. *Pediatric Pulmonology, 21*(5), 301-309.

Frank-Ito, D. O., Wofford, M., Schroeter, J. D., & Kimbell, J. S. (2016). Influence of Mesh Density on Airflow and Particle Deposition in Sinonasal Airway Modeling. *Journal of Aerosol Medicine and Pulmonary Drug Delivery, 29*(1), 46-56. doi:10.1089/jamp.2014.1188

Garcia, G. J. M., Tewksbury, E. W., Wong, B. A., & Kimbell, J. S. (2009). Interindividual Variability in Nasal Filtration as a Function of Nasal Cavity Geometry. *Journal of Aerosol Medicine and Pulmonary Drug Delivery, 22*(2), 139-155. doi:10.1089/jamp.2008.0713

Gebhart, J., & Heyder, J. (1985). Removal of aerosol-particles from stationary air within porous-media. *Journal of Aerosol Science, 16*(2), 175-187.

Gebhart, J., Roth, C., & Stahlhofen, W. (1973). Filtration properties of glass bead media for aerosol particles in the 0.1-2 um size range. *Journal of Aerosol Science, 4*(5), 355-371.

Geller, D. E., & Rubin, B. K. (2009). Respiratory care and cystic fibrosis. *Respiratory Care, 54*(6), 796-800.

Ghalichi, F., Deng, X., Champlain, A. D., Douville, Y., King, M., & Guidoin, R. (1998). Low Reynolds number turbulence modeling of blood flow in arterial stenoses. *Biorheology, 35*(4&5), 281-294.

Golshahi, L., Finlay, W. H., Olfert, J. S., Thompson, R. B., & Noga, M. L. (2010). Deposition of inhaled ultrafine aerosols in replicas of nasal airways of infants. *Aerosol Science and Technology, 44*(9), 741-752.

Golshahi, L., Noga, M. L., & Finlay, W. H. (2012). Deposition of inhaled micrometer-sized particles in oropharyngeal airway replicas of children at constant flow rates. *Journal of Aerosol Science, 49*, 21-31. doi:10.1016/j.jaerosci.2012.03.001

Golshahi, L., Noga, M. L., Thompson, R. B., & Finlay, W. H. (2011). In vitro deposition measurement of inhaled micrometer-sized particles in extrathoracic airways of children and adolescents during nose breathing. *Journal of Aerosol Science, 42*(7), 474-488. doi:10.1016/j.jaerosci.2011.04.002

Golshahi, L., Tian, G., Azimi, M., Son, Y. J., Walenga, R., Longest, P. W., & Hindle, M. (2013). The Use of Condensational Growth Methods for Efficient Drug Delivery to the Lungs during Noninvasive Ventilation High Flow Therapy. *Pharmaceutical Research, 30*(11), 2917-2930. doi:10.1007/s11095-013-1123-3

Hansen, C. R., Pressler, T., & Hoiby, N. (2008). Early aggressive eradication therapy for intermittent Pseudomonas aeruginosa airway colonization in cystic fibrosis patients: 15 years experience. *Journal of Cystic Fibrosis, 7*(6), 523-530. doi:10.1016/j.jcf.2008.06.009

Hansen, S. K., Rau, M. H., Johansen, H. K., Ciofu, O., Jelsbak, L., Yang, L., . . . Molin, S. (2012). Evolution and diversification of Pseudomonas aeruginosa in the paranasal sinuses of cystic fibrosis children have implications for chronic lung infection. *Isme Journal, 6*(1), 31-45. doi:10.1038/ismej.2011.83

Hasan, M. A., & Lange, C. F. (2007). Estimating in vivo airway surface liquid concentration in trials of inhaled antibiotics. *Journal of Aerosol Medicine-Deposition Clearance and Effects in the Lung, 20*(3), 282-293. doi:10.1089/jam.2007.0603

Heistracher, T., & Hofmann, W. (1995). Physiologically realistic models of bronchial airway bifurcations. *Journal of Aerosol Science, 26*(3), 497-509.

Herring, M. J., Putney, L. F., Wyatt, G., Finkbeiner, W. E., & Hyde, D. M. (2014). Growth of alveoli during postnatal development in humans based on stereological estimation. *American Journal of Physiology-Lung Cellular and Molecular Physiology, 307*(4), L338-L344.

Heyder, J., & Gebhart, J. (1977). Gravitational deposition of particles from laminar aerosol flow through inclined circular tubes. *Journal of Aerosol Science, 8*(4), 289-295.

Hindle, M., & Longest, P. W. (2012). Condensational growth of combination drug-excipient submicrometer particles for targeted high efficiency pulmonary delivery: Evaluation of formulation and delivery device. *Journal of Pharmacy and Pharmacology, 64*(9), 1254-1263. doi:DOI: 10.1111/j.2042-7158.2012.01476.x

Hindle, M., & Longest, P. W. (2013). Quantitative analysis and design of a spray aerosol inhaler. Part 2: Improvements in mouthpiece performance. *Journal of Aerosol Medicine and Pulmonary Drug Delivery, 26*(5), 237-247.

Hislop, A. A., Wigglesworth, J. S., & Desai, R. (1986). Alveolar development in the human-fetus and infant. *Early Human Development, 13*(1), 1-11.

Hjelmfelt, A. T., & Mockros, L. F. (1966). Motion of Discrete Particles in a Turbulent Fluid. *Applied Scientific Research, 16*(2), 149-+. doi:Doi 10.1007/Bf00384062

Hoiby, N. (2011). Recent advances in the treatment of Pseudomonas aeruginosa infections in cystic fibrosis. *BMC Medicine, 9*, 32.

Holbrook, L. T. (2015). *Generation and delivery of charged aerosols to infant airways.* (Ph. D dissertation), Virginia Commonwealth University, Richmond, VA.

Holbrook, L. T., & Longest, P. W. (2013). Validating CFD predictions of highly localized aerosol deposition in airway models: In vitro data and effects of surface properties. *Journal of Aerosol Science, 59*, 6-21.

Horsfield, K., Dart, G., Olson, D. E., & Cumming, G. (1971). Models of the human bronchial tree. *Journal of Applied Physiology, 31*, 207-217.

ICRP. (1994). *Human respiratory tract model for radiological protection*. Oxford: Pergamon.

Janssens, H. M., De Jongste, J. C., Fokkens, W. J., Robben, S. G. F., Wouters, K., & Tiddens, H. A. W. M. (2001). The Sophia Anatomical Infant Nose-Throat (SAINT) model: A valuable tool to study aerosol deposition in infants. *Journal of Aerosol Medicine-Deposition Clearance and Effects in the Lung, 14*(4), 433-441. doi:Doi 10.1089/08942680152744640

Javaheri, E., Golshahi, L., & Finlay, W. H. (2013). An idealized geometry that mimics average infant nasal airway deposition. *Journal of Aerosol Science, 55*, 137-148.

Jayaraju, S. T., Bronus, M., Verbanck, S., & Lacor, C. (2007). Fluid flow and particle deposition analysis in a realistic extrathoracic airway model using unstructured grids. *Journal of Aerosol Science, 38*, 494-508.

Jayaraju, S. T., Brouns, M., Lacor, C., Belkassem, B., & Verbanck, S. (2008). Large eddy and detached eddy simulations of fluid flow and particle deposition in a human mouth-throat. *Aerosol Science, 39*, 862-875.

Jin, H. H., Fan, J. R., Zeng, M. J., & Cen, K. F. (2007). Large eddy simulation of inhaled particle deposition within the human upper respiratory tract. *Aerosol Science, 38*, 257-268.

Khajeh-Hosseini-Dalasm, N., & Longest, P. W. (2015). Deposition of particles in the alveolar airways: Inhalation and breath-hold with pharmaceutical aerosols. *Journal of Aerosol Science, 79*, 15-30.

Kikinis, R., Pieper, S. D., & Vosburgh, K. G. (2014). 3D Slicer: A Platform for Subject-Specific Image Analysis, Visualization, and Clinical Support. In J. F. (Ed.), *Intraoperative Imaging and Image-Guided Therapy.* New York, NY: Springer.

Kleinstreuer, C., & Zhang, Z. (2003). Laminar-to-turbulent fluid-particle flows in a human airway model. *International Journal Of Multiphase Flow, 29*(2), 271-289.

Lambert, A. R., O'Shaughnessy, P. T., Tawhai, M. H., Hoffman, E. A., & Lin, C.-L. (2011). Regional deposition of particles in an image-based airway model: Large-eddy simulation and left-right lung ventilation asymmetry. *Aerosol Science and Technology, 45*, 11-25.

Lange, C. F., Hancock, R. E. W., Samuel, J., & Finlay, W. H. (2001). In vitro aerosol delivery and regional airway surface liquid concentration of a liposomal cationic

peptide. *Journal of Pharmaceutical Sciences, 90*(10), 1647-1657. doi:DOI 10.1002/jps.1115

Langston, C., Kida, K., Reed, M., & Thurlbeck, W. M. (1984). Human-lung growth in late gestation and in the neonate. *American Review of Respiratory Disease, 129*(4), 607-613.

Laube, B. L., Sharpless, G., Shermer, C., Sullivan, V., & Powell, K. (2012). Deposition of dry powder generated by solovent in Sophia Anatomical infant nose-throat (SAINT) model. *Aerosol Science and Technology, 46*, 514-520.

Lee, K. W., & Gieseke, J. A. (1979). Collection of aerosol particles by packed beds. *Environmental Science & Technology, 13*(4), 466-470.

Lee, S. L., & Durst, F. (1982). On the Motion of Particles in Turbulent Duct Flows. *International Journal Of Multiphase Flow, 8*(2), 125-146. doi:Doi 10.1016/0301-9322(82)90013-1

Lexmond, A. J., Hagedoorn, P., Frijlink, H. W., Rottier, B. L., & de Boer, A. H. (2017). Prerequisites for a dry powder inhaler for children with cystic fibrosis. *Plos One, 12*(8), e0183130.

Lexmond, A. J., Kruizinga, T. J., Hagedoorn, P., Rottier, B. L., Frijlink, H. W., & De Boer, A. H. (2014). Effect of inhaler design variables on paediatric use of dry powder inhalers. *Plos One, 9*(6), e99304.

Lin, C. L., Tawhai, M. H., McLennan, G., & Hoffman, E. A. (2007). Characteristics of the turbulent laryngeal jet and its effect on airflow in the human intra-thoracic airways. *Respiratory Physiology and Neurobiology, 157*, 295-309.

Lin, H. L., Harwood, R. J., Fink, J. B., Goodfellow, L. T., & Ari, A. (2015). In Vitro Comparison of Aerosol Delivery Using Different Face Masks and Flow Rates With a High-Flow Humidity System. *Respiratory Care, 60*(9), 1215-1219. doi:10.4187/respcare.03595

Lindert, S., Below, A., & Breitkreutz, J. (2014). Performance of dry powder inhalers with single dosed capsules in preschool children and adults using improved upper airway models. *Pharmaceutics, 6*, 36-51.

Linnane, B., Kearse, L., O'Connell, N. H., Fenton, J., Kiernan, M. G., & Dunne, C. P. (2015). A case of failed eradication of cystic fibrosis-related sinus colonisation by Pseudomonas aeruginosa. *Bmc Pulmonary Medicine, 15*. doi:ARTN 114 10.1186/s12890-015-0113-0

Longest, P. W., Azimi, M., Golshahi, L., & Hindle, M. (2014). Improving aerosol drug delivery during invasive mechanical ventilation with redesigned components. *Respiratory Care, 59*(5), 686-698.

Longest, P. W., Azimi, M., & Hindle, M. (2014). Optimal delivery of aerosols to infants during mechanical ventilation. *Journal of Aerosol Medicine and Pulmonary Drug Delivery, 27*(5), 371-385.

Longest, P. W., & Farkas, D. (2018). Development of a new inhaler for high-efficiency dispersion of spray-dried powders using computational fluid dynamics (CFD) modeling. *The AAPS Journal, DOI: 10.1208/s12248-018-0281-y.*

Longest, P. W., Farkas, D., Bass, K., & Hindle, M. (2019). Use of Computational Fluid Dynamics (CFD) Dispersion Parameters in the Development of a New DPI Actuated with Low Air Volumes. *Pharmaceutical Research, 36*(8).

Longest, P. W., Golshahi, L., Behara, S. R. B., Tian, G., Farkas, D. R., & Hindle, M. (2015). Efficient Nose-to-Lung (N2L) Aerosol Delivery with a Dry Powder Inhaler. *Journal of Aerosol Medicine and Pulmonary Drug Delivery, 28*(3), 189-201. doi:10.1089/jamp.2014.1158

Longest, P. W., & Hindle, M. (2009a). Evaluation of the Respimat Soft Mist inhaler using a concurrent CFD and in vitro approach. *Journal of Aerosol Medicine and Pulmonary Drug Delivery, 22*(2), 99-112.

Longest, P. W., & Hindle, M. (2009b). Excipient enhanced growth (EEG) of nanoparticle aerosols to enable improved pulmonary targeting and retention. *Provisional Patent Application*.

Longest, P. W., & Hindle, M. (2009c). Quantitative Analysis and Design of a Spray Aerosol Inhaler. Part 1: Effects of Dilution Air Inlets and Flow Paths. *Journal of Aerosol Medicine and Pulmonary Drug Delivery, 22*(3), 271-283. doi:10.1089/jamp.2008.0739

Longest, P. W., & Hindle, M. (2010). CFD simulations of enhanced condensational growth (ECG) applied to respiratory drug delivery with comparisons to in vitro data. *Journal of Aerosol Science, 41*(8), 805-820. doi:10.1016/j.jaerosci.2010.04.006

Longest, P. W., & Hindle, M. (2011). Numerical Model to Characterize the Size Increase of Combination Drug and Hygroscopic Excipient Nanoparticle Aerosols. *Aerosol Science and Technology, 45*(7), 884-899. doi:10.1080/02786826.2011.566592

Longest, P. W., & Hindle, M. (2012). Condensational Growth of Combination Drug-Excipient Submicrometer Particles for Targeted High Efficiency Pulmonary Delivery: Comparison of CFD Predictions with Experimental Results. *Pharmaceutical Research, 29*(3), 707-721. doi:10.1007/s11095-011-0596-1

Longest, P. W., Hindle, M., & Das Choudhuri, S. (2009). Effects of generation time on spray aerosol transport and deposition in models of the mouth-throat geometry. *Journal of Aerosol Medicine and Pulmonary Drug Delivery, 22*(3), 67-84.

Longest, P. W., Hindle, M., Das Choudhuri, S., & Byron, P. R. (2007). Numerical simulations of capillary aerosol generation: CFD model development and comparisons with experimental data. *Aerosol Science and Technology, 41*(10), 952-973.

Longest, P. W., Hindle, M., Das Choudhuri, S., & Xi, J. (2008). Comparison of ambient and spray aerosol deposition in a standard induction port and more realistic mouth-throat geometry. *Journal of Aerosol Science, 39*(7), 572-591.

Longest, P. W., & Holbrook, L. T. (2012). In silico models of aerosol delivery to the respiratory tract - Development and applications. *Advanced Drug Delivery Reviews, 64*, 296-311.

Longest, P. W., Kleinstreuer, C., & Buchanan, J. R. (2004). Efficient computation of micro-particle dynamics including wall effects. *Computers & Fluids, 33*(4), 577-601.

Longest, P. W., & Oldham, M. J. (2008). Numerical and experimental deposition of fine respiratory aerosols: Development of a two-phase drift flux model with near-wall velocity corrections. *Aerosol Science, 39*, 48-70.

Longest, P. W., Son, Y.-J., Holbrook, L. T., & Hindle, M. (2013). Aerodynamic factors responsible for the deaggregation of carrier-free drug powders to form

micrometer and submicrometer aerosols. *Pharmaceutical Research, 30*, 1608-1627. doi:DOI: 10.1007/s11095-013-1001-z

Longest, P. W., Tian, G., Delvadia, R., & Hindle, M. (2012). Development of a stochastic individual path (SIP) model for predicting the deposition of pharmaceutical aerosols: Effects of turbulence, polydisperse aerosol size, and evaluation of multiple lung lobes. *Aerosol Science and Technology, 46*(12), 1271-1285.

Longest, P. W., Tian, G., Li, X., Son, Y. J., & Hindle, M. (2012). Performance of Combination Drug and Hygroscopic Excipient Submicrometer Particles from a Softmist Inhaler in a Characteristic Model of the Airways. *Annals of Biomedical Engineering, 40*(12), 2596-2610. doi:10.1007/s10439-012-0616-2

Longest, P. W., Tian, G., Walenga, R. L., & Hindle, M. (2012). Comparing MDI and DPI aerosol deposition using in vitro experiments and a new stochastic individual path (SIP) model of the conducting airways. *Pharmaceutical Research, 29*(6), 1670-1688.

Longest, P. W., & Vinchurkar, S. (2007a). Effects of mesh style and grid convergence on particle deposition in bifurcating airway models with comparisons to experimental data. *Medical Engineering and Physics, 29*(3), 350-366.

Longest, P. W., & Vinchurkar, S. (2007b). Validating CFD predictions of respiratory aerosol deposition: Effects of upstream transition and turbulence. *Journal of Biomechanics, 40*(2), 305-316.

Longest, P. W., Vinchurkar, S., & Martonen, T. B. (2006). Transport and deposition of respiratory aerosols in models of childhood asthma. *Journal of Aerosol Science, 37*, 1234-1257.

Longest, P. W., Walenga, R. L., Son, Y. J., & Hindle, M. (2013). High-Efficiency Generation and Delivery of Aerosols Through Nasal Cannula During Noninvasive Ventilation. *Journal of Aerosol Medicine and Pulmonary Drug Delivery, 26*(5), 266-279. doi:10.1089/jamp.2012.1006

Longest, P. W., & Xi, J. X. (2007). Effectiveness of direct Lagrangian tracking models for simulating nanoparticle deposition in the upper airways. *Aerosol Science and Technology, 41*(4), 380-397. doi:10.1080/02786820701203223

Longest, P. W., & Xi, J. X. (2008). Condensational growth may contribute to the enhanced deposition of cigarette smoke particles in the upper respiratory tract. *Aerosol Science and Technology, 42*(8), 579-602. doi:10.1080/02786820802232964

Lotfi, A., Simmons, A., & Barber, T. (2016). Evaluation of Different Meshing Techniques for the Case of a Stented Artery. *Journal of Biomechanical Engineering-Transactions of the Asme, 138*(3).

Macklin, C. C. (1955). Pulmonary sumps, dust accumulations, alveolar fluid and lymph vessels. *Acta Anat (Basel), 23*(1), 1-33. doi:10.1159/000140979

Mallol, J., Rattray, S., Walker, G., Cook, D., & Robertson, C. F. (1996). Aerosol deposition in infants with cystic fibrosis. *Pediatric Pulmonology, 21*(5), 276-281.

Martonen, T. B., Musante, C. J., Segal, R. A., Schroeter, J. D., Hwang, D., Dolovich, M. A., . . . Fleming, J. S. (2000). Lung Models: Strengths and Limitations. *Respiratory Care, 45*(6), 712-736.

Matida, E. A., Finlay, W. H., Breuer, M., & Lange, C. F. (2006). Improving prediction of aerosol deposition in an idealized mouth using large-eddy simulation. *Journal of Aerosol Medicine, 19*(3), 290-300.

Matida, E. A., Finlay, W. H., & Grgic, L. B. (2004). Improved numerical simulation of aerosol deposition in an idealized mouth-throat. *Journal of Aerosol Science, 35*, 1-19.

Matsui, H., Grubb, B. R., Tarran, R., Randell, S. H., Gatzy, J. T., Davis, C. W., & Boucher, R. C. (1998). Evidence for periciliary liquid layer depletion, not abnormal ion composition, in the pathogenesis of cystic fibrosis airways disease. *Cell, 95*(7), 1005-1015. doi:Doi 10.1016/S0092-8674(00)81724-9

Mayell, S. J., Munck, A., Craig, J. V., Sermet, I., Brownlee, K. G., Schwarz, M. J., . . . Soc, E. C. F. (2009). A European consensus for the evaluation and management of infants with an equivocal diagnosis following newborn screening for cystic fibrosis. *Journal of Cystic Fibrosis, 8*(1), 71-78. doi:10.1016/j.jcf.2008.09.005

Minocchieri, S., Burren, J. M., Bachmann, M. A., Stern, G., Wildhaber, J., Buob, S., . . . Nelle, M. (2008). Development of the premature infant nose throat-model (PrINT-Model) - An upper airway replica of a premature neonate for the study of aerosol delivery. *Pediatric research, 64*(2), 141-146.

Moller, M. E., Alanin, M. C., Gronhoj, C., Aanaes, K., Hoiby, N., & von Buchwald, C. (2017). Sinus bacteriology in patients with cystic fibrosis or primary ciliary dyskinesia: A systematic review. *American Journal of Rhinology & Allergy, 31*(5), 293-298. doi:10.2500/ajra.2017.31.4461

Nield, D. A., & Bejan, A. (1999). *Convetion in Porous Media* (2nd ed.). New York: Springer.

Oberwaldner, B., Evans, J. C., & Zach, M. S. (1986). Forced Expirations against a Variable Resistance - a New Chest Physiotherapy Method in Cystic-Fibrosis. *Pediatric Pulmonology, 2*(6), 358-367. doi:DOI 10.1002/ppul.1950020608

Oberwaldner, B., Theissl, B., Rucker, A., & Zach, M. S. (1991). Chest Physiotherapy in Hospitalized-Patients with Cystic-Fibrosis - a Study of Lung-Function Effects and Sputum Production. *European Respiratory Journal, 4*(2), 152-158.

Ochs, M., Nyengaard, J. R., Jung, A., Knudsen, L., Voigt, M., Wahlers, T., . . . Gundersen, H. J. r. G. (2004). The number of alveoli in the human lung. *American Journal of Respiratory and Critical Care Medicine, 169*(1), 120-124.

Patton, J. S. (1996). Mechanisms of macromolecule absorption by the lungs. *Advanced Drug Delivery Reviews, 19*(1), 3-36. doi:Doi 10.1016/0169-409x(95)00113-L

Peric, M. (2004). Flow simulation using control volumes of arbitrary polyhedral shape. *ERCOFTAC Bulletin, 62*.

Phalen, R. F., Oldham, M. J., Beaucage, C. B., Crocker, T. T., & Mortensen, J. D. (1985). Postnatal enlargement of human tracheo-bronchial airways and implications for particle deposition. *Anatomical Record, 212*(4), 368-380.

Plopper, C. G., Heidsiek, J. G., Weir, A. J., George, J. A., & Hyde, D. M. (1989). Tracheobronchial epithelium in the adult rhesus monkey: a quantitative histochemical and ultrastructural study. *Am J Anat, 184*(1), 31-40. doi:10.1002/aja.1001840104

Proesmans, M., Vermeulen, F., Boulanger, L., Verhaegen, J., & De Boeck, K. (2013). Comparison of two treatment regimens for eradication of Pseudomonas

aeruginosa infection in children with cystic fibrosis. *Journal of Cystic Fibrosis, 12*(1), 29-34. doi:10.1016/j.jcf.2012.06.001

Pui, D. Y. H., Romay-Novas, F., & Liu, B. Y. H. (1987). Experimental study of particle depositon in bends of circular cross section. *Aerosol Science and Technology, 7*, 301-315.

Ramsey, B. W., Pepe, M. S., Quan, J. M., Otto, K. L., Montgomery, A. B., Williams-Warren, J., . . . Grp, C. F. I. T. S. (1999). Intermittent administration of inhaled tobramycin in patients with cystic fibrosis. *New England Journal of Medicine, 340*(1), 23-30. doi:Doi 10.1056/Nejm199901073400104

Rani, W. K., Bass, K., Strickler, S. C., Dodson, K., & Longest, P. W. (2020). Sets of Characteristic Infant Nasal Models for Testing Nose-to-Lung Pharmaceutical Aerosol Delivery. *Journal of Aerosol Medicine and Pulmonary Drug Delivery, In preparation*.

Ratjen, F., Munck, A., Kho, P., Angyalosi, G., & Grp, E. S. (2010). Treatment of early Pseudomonas aeruginosa infection in patients with cystic fibrosis: the ELITE trial. *Thorax, 65*(4), 286-291. doi:10.1136/thx.2009.121657

Registry, C. F. F. P. (2016). *2016 Annual Data Report*. Retrieved from Bethesda, Maryland:

Reminiac, F., Vecellio, L., Mac Loughlin, R., Le Pennec, D., Cabrera, M., Vourc'h, N. H., . . . Ehrmann, S. (2017). Nasal High Flow Nebulization in Infants and Toddlers: An In Vitro and In Vivo Scintigraphic Study. *Pediatric Pulmonology, 52*(3), 337-344. doi:10.1002/ppul.23509

Richardson, L. F., & Gaunt, J. A. (1927). The deferred approach to the limit. Part I. Single lattice. Part II. Interpenetrating lattices. *Philosophical Transactions of the Royal Society of London Series a-Containing Papers of a Mathematical or Physical Character, 226*, 299-361. doi:DOI 10.1098/rsta.1927.0008

Roache, P. J. (1994). Perspective: A Method for Uniform Reporting of Grid Refinement Studies. *Journal of Fluids Engineering-Transactions of the Asme, 116*(3), 405-413. doi:Doi 10.1115/1.2910291

Rosati, J. A., Leith, D., & Kim, C. S. (2003). Monodisperse and polydisperse aerosol deposition in a packed bed. *Aerosol Science and Technology, 37*(6), 528-535.

Rosenow, T., Oudraad, M. C. J., Murray, C. P., Turkovic, L., Kuo, W., de Bruijne, M., . . . Surveillance, A. R. E. (2015). PRAGMA-CF A Quantitative Structural Lung Disease Computed Tomography Outcome in Young Children with Cystic Fibrosis. *American Journal of Respiratory and Critical Care Medicine, 191*(10), 1158-1165. doi:10.1164/rccm.201501-0061OC

Rosenthal, F. S., Blanchard, J. D., & Anderson, P. J. (1992). Aerosol bolus dispersion and convective mixing in human and dog lungs and physical models. *Journal of Applied Physiology, 73*(3), 862-873.

Rudolf, G., Kobrich, R., & Stahlhofen, W. (1990). Modeling and algebraic formulation of regional aerosol deposition in man. *Journal of Aerosol Science, 21*, S403-S406.

Rygg, A., & Longest, P. W. (2016). Absorption and Clearance of Pharmaceutical Aerosols in the Human Nose: Development of a CFD Model. *Journal of Aerosol Medicine and Pulmonary Drug Delivery, 29*(5), 416-431. doi:10.1089/jamp.2015.1252

Ryval, J., Straatman, A. G., & Steinman, D. A. (2004). Two-equation turbulence modeling of pulsatile flow in a stenosed tube. *Journal of Biomechanical Engineering-Transactions of the Asme, 126*(5), 625-635. doi:10.1115/1.1798055

Saini, D., Yurteri, C. U., Grable, N., Sims, R. A., & Mazumder, M. K. (2002). Drug delivery studies on electrostatically charged dry powder inhaler aerosols using a glass bead lung model. *Conference Record of the 2002 Ieee Industry Applications Conference, Vols 1-4*, 2451-2453.

Salmon, B., Wilson, N. M., & Silverman, M. (1990). How much aerosol reaches the lungs of wheezy infants and toddlers? *Archives of Disease in Childhood, 65*(4), 401-403.

Schlichting, H. (1987). *Boundary-Layer Theory*.

Schroeter, J. D., Musante, C. J., Hwang, D. M., Burton, R., Guilmette, R., & Martonen, T. B. (2001). Hygroscopic growth and deposition of inhaled secondary cigarette smoke in human nasal pathways. *Aerosol Science and Technology, 34*(1), 137-143.

Serafini, S. M., & Michaelson, E. D. (1977). Length and distribution of cilia in human and canine airways. *Bull Eur Physiopathol Respir, 13*(4), 551-559.

Shepard, D. (1968). *A two-dimensional interpolation function for irregularly-spaced data*. Paper presented at the Proceedings of the 1968 23rd ACM national conference.

Shur, J., Lee, S. L., Adams, W., Lionberger, R., Tibbatts, J., & Price, R. (2012). Effect of device design on the in vitro performance and comparability for capsule-based dry powder inhalers. *The AAPS Journal, 14*(4), 667-676.

Smith, A. L. (2002). Inhaled antibiotic therapy: What drug? What dose? What regimen? What formulation? *Journal of Cystic Fibrosis, 1*(Suppl 2), 189-193.

Smith, L. J., Collier, G. J., Marshall, H., Hughes, P. J. C., Biancardi, A. M., Wildman, M., . . . Wild, J. M. (2018). Patterns of regional lung physiology in cystic fibrosis using ventilation magnetic resonance imaging and multiple-breath washout. *European Respiratory Journal, 52*(5). doi:Artn 1800821

10.1183/13993003.00821-2018

Somayaji, R., & Parkins, M. D. (2015). Tobramycin inhalation powder: an efficient and efficacious therapy for the treatment of Pseudomonas aeruginosa infection in cystic fibrosis. *Therapeutic delivery, 6*(2), 121-137. doi:10.4155/tde.14.94

Sommerfeld, M. (1990). Particle Dispersion in Turbulent-Flow - the Effect of Particle-Size Distribution. *Particle & Particle Systems Characterization, 7*(4), 209-220. doi:DOI 10.1002/ppsc.19900070135

Son, Y. J., Longest, P. W., & Hindle, M. (2012). Aerosolization characteristics of dry powder inhaler formulations for the enhanced excipient growth application: Effect of spray drying conditions. *Respiratory Drug Delivery 2012, 3*, 899-902.

Son, Y. J., Longest, P. W., & Hindle, M. (2013). Aerosolization characteristics of dry powder inhaler formulations for the excipient enhanced growth (EEG) application: Effect of spray drying process conditions on aerosol performance. *International Journal of Pharmaceutics, 443*(1), 137-145. doi:doi.org/10.1016/j.ijpharm.2013.01.003

Son, Y. J., Longest, P. W., Tian, G., & Hindle, M. (2013). Evaluation and modification of commercial dry powder inhalers for the aerosolization of a submicrometer

excipient enhanced growth (EEG) formulation. *European Journal of Pharmaceutical Sciences, 49*(3), 390-399. doi:10.1016/j.ejps.2013.04.011

Sosnowski, M., Krzywanski, J., & Gnatowska, R. (2017). Polyhedral meshing as an innovative approach to computational domain discretization of a cyclone in a fluidized bed CLC unit. *Energy and Fuels 2016, 14*.

Spalding, D. B. (1961). A Single Formula for the "Law of the Wall". *Journal of Applied Mechanics, 28*(3), 455-458. doi:10.1115/1.3641728

Stahlhofen, W. (1980). Experimental-Determination of the Regional Deposition of Aerosol-Particles in the Human Respiratory-Tract. *American Industrial Hygiene Association Journal, 41*(6), 385-398. doi:Doi 10.1080/15298668091424933

Stalvey, M. S., Pace, J., Niknian, M., Higgins, M. N., Tarn, V., Davis, J., . . . Rowe, S. M. (2017). Growth in Prepubertal Children With Cystic Fibrosis Treated With Ivacaftor. *Pediatrics, 139*(2). doi:ARTN e20162522

10.1542/peds.2016-2522

Stapleton, K. W., Guentsch, E., Hoskinson, M. K., & Finlay, W. H. (2000). On the suitability of k-epsilon turbulence modeling for aerosol deposition in the mouth and throat: A comparison with experiment. *Journal of Aerosol Science, 31*(6), 739-749.

Stoltz, D. A., Meyerholz, D. K., & Welsh, M. J. (2015). Origins of Cystic Fibrosis Lung Disease. *New England Journal of Medicine, 372*(4), 351-362. doi:10.1056/NEJMra1300109

Storey-Bishoff, J., Noga, M., & Finlay, W. H. (2008). Deposition of micrometer-sized aerosol particles in infant nasal airway replicas. *Journal of Aerosol Science, 39*(12), 1055-1065. doi:10.1016/j.jaerosci.2008.07.011

Subramaniam, R. P., Richardson, R. B., Morgan, K. T., Kimbell, J. S., & Guilmette, R. A. (1998). Computational fluid dynamics simulations of inspiratory airflow in the human nose and nasopharynx. *Inhalation Toxicology, 10*(5), 473-502.

Sunbul, F. S., Fink, J. B., Harwood, R., Sheard, M. M., Zimmerman, R. D., & Ari, A. (2015). Comparison of HFNC, bubble CPAP and SiPAP on aerosol delivery in neonates: An in-vitro study. *Pediatric Pulmonology, 50*(11), 1099-1106. doi:10.1002/ppul.23123

Taccetti, G., Bianchini, E., Cariani, L., Buzzetti, R., Costantini, D., Trevisan, F., . . . Eradicati, I. G. P. A. (2012). Early antibiotic treatment for Pseudomonas aeruginosa eradication in patients with cystic fibrosis: a randomised multicentre study comparing two different protocols. *Thorax, 67*(10), 853-859. doi:10.1136/thoraxjnl-2011-200832

Tarran, R., Button, B., & Boucher, R. C. (2006). Regulation of normal and cystic fibrosis airway surface liquid volume by phasic shear stress. *Annual Review of Physiology, 68*, 543-561. doi:10.1146/annurev.physiol.68.072304.112754

Tarran, R., Button, B., Picher, M., Paradiso, A. M., Ribeiro, C. M., Lazarowski, E. R., . . . Boucher, R. C. (2005). Normal and cystic fibrosis airway surface liquid homeostasis - The effects of phasic shear stress and viral infections. *Journal of Biological Chemistry, 280*(42), 35751-35759. doi:10.1074/jbc.M505832200

Tarran, R., Grubb, B. R., Parsons, D., Picher, M., Hirsh, A. J., Davis, C. W., & Boucher, R. C. (2001). The CF salt controversy: In vivo observations and therapeutic

approaches. *Molecular Cell, 8*(1), 149-158. doi:Doi 10.1016/S1097-2765(01)00286-6

Tavernini, S., Church, T. K., Lewis, D. A., Noga, M., Martin, A. R., & Finlay, W. H. (2018). Deposition of micrometer-sized aerosol particles in neonatal nasal airway replicas. *Aerosol Science and Technology, 52*(4), 407-419.

Tennekes, H., & Lumley, J. L. (1972). *A First Course in Turbulence.* Cambridge: MIT Press.

Thurlbeck, W. M. (1982). Postnatal human-lung growth. *Thorax, 37*(8), 564-571.

Tian, G., Hindle, M., Lee, S., & Longest, P. W. (2015). Validating CFD predictions of pharmaceutical aerosol deposition with in vivo data. *Pharmaceutical Research, 32*, 3170-3187.

Tian, G., Hindle, M., & Longest, P. W. (2014). Targeted lung delivery of nasally administered aerosols. *Aerosol Science and Technology, 48*(4), 434-449.

Tian, G., Longest, P. W., Li, X., & Hindle, M. (2013). Targeting aerosol deposition to and within the lung airways using excipient enhanced growth. *Journal of Aerosol Medicine and Pulmonary Drug Delivery, 26*(5), 248-265.

Tian, G., Longest, P. W., Su, G., Walenga, R. L., & Hindle, M. (2011). Development of a stochastic individual path (SIP) model for predicting the tracheobronchial deposition of pharmaceutical aerosols: Effects of transient inhalation and sampling the airways. *Journal of Aerosol Science, 42*(11), 781-799.

Tiddens, H. A. W. M., Donaldson, S. H., Rosenfeld, M., & Pare, P. D. (2010). Cystic Fibrosis Lung Disease Starts in the Small Airways: Can We Treat It More Effectively? *Pediatric Pulmonology, 45*(2), 107-117. doi:10.1002/ppul.21154

Tong, Z., Zhong, W., Yu, A., Chan, H.-K., & Yang, R. (2016). CFD–DEM investigation of the effect of agglomerate–agglomerate collision on dry powder aerosolisation. *Journal of Aerosol Science, 92*, 109-121. doi:doi.org/10.1016/j.jaerosci.2015.11.005

Vaish, M., Kleinstreuer, C., Kolanjiyil, A. V., Saini, N., & Pillalamarri, N. R. (2016). Laminar/turbulent airflow and microsphere deposition in a patient-specific airway geometry using an open-source solver. *International Journal of Biomedical Engineering and Technology, 22*(2), 145-161. doi:10.1504/Ijbet.2016.079145

van Ertbruggen, C., Corieri, P., Theunissen, R., Riethmuller, M. L., & Darquenne, C. (2008). Validation of CFD predictions of flow in a 3D alveolated bend with experimental data. *Journal of Biomechanics, 41*(2), 399-405. doi:10.1016/j.jbiomech.2007.08.013

Varghese, S. S., & Frankel, S. H. (2003). Numerical modeling of pulsatile turbulent flow in stenotic vessels. *Journal of Biomechanical Engineering-Transactions of the Asme, 125*(4), 445-460. doi:10.1115/1.1589774

Verbanck, S., Ghorbaniasl, G., Biddiscombe, M. F., Dragojlovic, D., Ricks, N., Lacor, C., . . . Underwood, S. R. (2016). Inhaled aerosol distribution in human airways: A scintigraphy-guided study in a 3D printed model. *Journal of Aerosol Medicine and Pulmonary Drug Delivery, 29*(6), 525-533.

Vinchurkar, S., & Longest, P. W. (2008). Evaluation of hexahedral, prismatic and hybrid mesh styles for simulating respiratory aerosol dynamics. *Computers and Fluids, 37*(3), 317-331.

Walenga, R. L., & Longest, P. W. (2016). Current Inhalers deliver very small doses to the lower tracheobronchial airways: Assessment of healthy and constricted lungs. *J Pharm Sci, 105*, 147-159.

Walenga, R. L., Tian, G., Hindle, M., Yelverton, J., Dodson, K., & Longest, P. W. (2014). Variability in nose-to-lung aerosol delivery. *Journal of Aerosol Science, 78*, 11-29.

Walenga, R. L., Tian, G., & Longest, P. W. (2013). Development of characteristic upper tracheobronchial airway models for testing pharmaceutical aerosol delivery. *Journal of Biomechanical Engineering, 135*(9), 091010-091010-091018.

Walsh, B. K., & DiBlasi, R. M. (2010). Mechanical ventilation of the neonate and pediatric patient. In B. K. Walsh, M. P. Czervinske, & R. M. DiBlasi (Eds.), *Perinatal and Pediatric Respiratory Care* (pp. 325-347). St. Louis: Saunders Elsevier.

Wang, Y., & James, P. W. (1999). On the effect of anisotropy on the turbulent dispersion and deposition of small particles. *International Journal Of Multiphase Flow, 22*, 551-558.

Wanner, A., Salathe, M., & O'Riordan, T. G. (1996). Mucociliary clearance in the airways. *Am J Respir Crit Care Med, 154*(6 Pt 1), 1868-1902. doi:10.1164/ajrccm.154.6.8970383

Wei, X., Hindle, M., Kaviratna, A., Huynh, B. K., Delvadia, R. R., Sandell, D., & Byron, P. R. (2018). In Vitro Tests for Aerosol Deposition. VI: Realistic Testing with Different Mouth–Throat Models and In Vitro—In Vivo Correlations for a Dry Powder Inhaler, Metered Dose Inhaler, and Soft Mist Inhaler. *Journal of Aerosol Medicine and Pulmonary Drug Delivery*.

Weibel, E. R. (1963). *Morphometry of the human lung*. New York,: Academic Press.

White, F. M. (1991). *Viscous fluid flow* (2nd ed.). New York: McGraw-Hill.

White, F. M. (2006). *Viscous fluid flow* (3rd ed.). New York, NY: McGraw-Hill Higher Education.

WHO. (2006). WHO Child Growth Standards: Length/height-for-age, weight-for-age, weight-for-length, weight-for-height and body mass index-for-age: Methods and development. Geneva: World Health Organization.

Wilcox, D. C. (1998). *Turbulence Modeling for CFD, 2nd Ed.* California: DCW Industries, Inc.

Wong, W., Fletcher, D. F., Traini, D., Chan, H. K., & Young, P. M. (2012). The use of computational approaches in inhaler development. *Advanced Drug Delivery Reviews, 64*(4), 312-322.

Xi, Longest, P. W., & Martonen, T. B. (2008). Effects of the laryngeal jet on nano-and microparticle transport and deposition in an approximate model of the upper tracheobronchial airways. *Journal of Applied Physiology, 104*(6), 1761-1777.

Xi, J., & Longest, P. W. (2007). Transport and deposition of micro-aerosols in realistic and simplified models of the oral airway. *Annals of Biomedical Engineering, 35*(4), 560-581.

Xi, J. X., Berlinski, A., Zhou, Y., Greenberg, B., & Ou, X. W. (2012). Breathing Resistance and Ultrafine Particle Deposition in Nasal-Laryngeal Airways of a Newborn, an Infant, a Child, and an Adult. *Annals of Biomedical Engineering, 40*(12), 2579-2595. doi:10.1007/s10439-012-0603-7

Yang, J., Wu, C.-Y., & Adams, M. (2014). Three-dimensional DEM–CFD analysis of air-flow-induced detachment of API particles from carrier particles in dry powder inhalers. *Acta Pharmaceutica Sinica B, 4*(1), 52-59. doi:doi.org/10.1016/j.apsb.2013.11.003

Yeates, D. B., Sturgess, J. M., Kahn, S. R., Levison, H., & Aspin, N. (1976). Mucociliary transport in trachea of patients with cystic fibrosis. *Arch Dis Child, 51*(1), 28-33. doi:10.1136/adc.51.1.28

Yeh, H. C., & Schum, G. M. (1980). Models of human-lung airways and their application to inhaled particle deposition. *Bulletin of Mathematical Biology, 42*(3), 461-480.

Yin, Y., Choi, J., Hoffman, E. A., Tawhai, M. H., & Lin, C.-L. (2010). Simulation of pulmonary air flow with a subject-specific boundary condition. *Journal of Biomechanics, 43*, 2159-2163.

Zhang, Y., Finlay, W. H., & Matida, E. A. (2004). Particle deposition measurements and numerical simulation in a highly idealized mouth-throat. *Journal of Aerosol Science, 35*(7), 789-803. doi:10.1016/j.jaerosci.2003.12.006

Zhang, Y., Gilbertson, K., & Finlay, W. H. (2007). In vivo-in vitro comparison of deposition in three mouth-throat models with Qvar and Turbuhaler inhalers. *Journal of Aerosol Medicine, 20*(3), 227-235.

Zhang, Z., & Kleinstreuer, C. (2003). Low-Reynolds-number turbulent flows in locally constricted conduits: A comparison study. *AIAA Journal, 41*(5), 831-840.

Zhang, Z., & Kleinstreuer, C. (2011). Laminar-to-turbulent fluid-nanoparticle dynamics simulations: Model comparisons and nanoparticle-deposition applications. *International Journal for Numerical Methods in Biomedical Engineering, 27*(12), 1930-1950. doi:10.1002/cnm.1447

Vita

KARL BASS

1200 Semmes Avenue, #416, Richmond, VA, 23224

(804) 334 1465, karlbass36@gmail.com

Education

- **Doctor of Philosophy in Mechanical and Nuclear Engineering** (2020)

  Virginia Commonwealth University, Richmond, VA, USA

- **Bachelor of Engineering in Motorsport Engineering** (2009)

  University of West England, Bristol, UK

Journal Articles

Bass, K., Farkas, D. F., & Longest, P. W. (2019). Optimizing Aerosolization using Computational Fluid Dynamics in a Pediatric Air-jet Dry Powder Inhaler. *AAPS PharmSciTech*, 20:329. DOI: https://doi.org/10.1208/s12249-019-1535-4

Farkas, D. F., Hindle, M., Bonasera S., Bass, K., & Longest, P. W. (2019). Development of an Inline Dry Powder Inhaler for Oral or Trans-Nasal Aerosol Administration to Children. *Journal of Aerosol Medicine and Pulmonary Drug Delivery*. (Advance online). DOI: https://doi.org/10.1089/jamp.2019.1540

Longest, P. W., Farkas, D. F., Bass K., & Hindle, M. (2019). Use of Computational Fluid Dynamics (CFD) Dispersion Parameters in the Development of a New DPI Actuated with Low Air Volumes. *Pharmaceutical Research*, *36*(8). DOI: https://doi.org/10.1007/s11095-019-2644-1

Bass, K., & Longest, P. W. (2019). High Efficiency Nose-to-Lung (N2L) Aerosol Delivery in an Infant: Development of a Validated CFD Method. *Journal of Aerosol Medicine and Pulmonary Drug Delivery, 32, 132-148*. DOI: https://doi.org/10.1089/jamp.2018.1490

Longest, P. W., Bass K., El-Achwah, A., Dutta, R., Rani, V., Thomas, M. L., & Hindle, M. (2018). Use of Computational Fluid Dynamics Deposition Modeling in Respiratory Drug Delivery. *Expert Opinion on Drug Delivery, 16, 7-26*. DOI: https://doi.org/10.1080/17425247.2019.1551875

Bass, K., & Longest, P. W. (2018). Development of an Infant Complete-airway In Vitro Model for Evaluating Aerosol Deposition. *Medical Engineering & Physics, 58, 47-55.* DOI: https://doi.org/10.1016/j.medengphy.2018.05.002

Bass, K., & Longest, P. W. (2018). Recommendations for Simulating Microparticle Deposition at Conditions Similar to the Upper Airways with Two-equation Turbulence Models. *Journal of Aerosol Science, 119, 31-50.* DOI: https://doi.org/10.1016/j.jaerosci.2018.02.007

In Press

Bass, K. & Longest, P. W. (2020). Development of DPI Patient Interfaces for Improved Aerosol Delivery to Children. *AAPS PharmSciTech*

Conference Proceedings

Conference Abstracts and Presentations (Presenting authors are noted with an asterisk)

Bass*, K. & Longest, P. W. (2020). A New Approach to Reduce Interface and Extrathoracic Depositional Losses with Pediatric Dry Powder Inhalers. *Respiratory Drug Delivery 2020* (April 2020), Palm Desert, CA. (Poster and peer-reviewed abstract).

Longest*, P. W., Farkas, D. F., Bass, K., Howe, C., Boc, S., Mommin, M., Dhapre, S., Hassan, A., Bonasera, S., & Hindle, M. (2020). Reviving Positive Pressure DPIs for Efficient and Reproducible Aerosol Delivery to Infants and Children. *Respiratory Drug Delivery 2020* (April 2020), Palm Desert, CA. (Podium presentation and peer-reviewed abstract).

Farkas, D. F., Bass, K., Bonasera, S., Hindle, M. & Longest*, P. W. (2020). Development of a Positive Pressure Air-Jet DPI for Pediatric Subjects. *Respiratory Drug Delivery 2020* (April 2020), Palm Desert, CA. (Poster and peer-reviewed abstract).

Bass*, K., Boc, S., Hindle, M., Dodson, K., & Longest, P. W. (2018). Validating CFD Predictions of Small Particle Aerosol Deposition in an Infant Nasal Airway Model. 2018 International Aerosol Conference (September 2018), St. Louis, MO. (Podium presentation and peer-reviewed abstract).

Dhapre*, S., Spence, B., Boc, S., Wei, X., Bass, K., Longest, P. W., & Hindle, M. (2018). Breath-synchronized Delivery of Aerosols to Infants Using a Very Low Volume Mixer-heater. *Respiratory Drug Delivery 2018* (April 2018), Tucson, AZ. (Poster and peer-reviewed abstract).

Bass*, K., & Longest, P. W. (2017). Recommendations for Reducing CFD Model Variability and Matching Experimental Data When Simulating Microparticle Deposition with Two-Equation Turbulence Models. *36th AAAR Annual Conference* (October 2017), Raleigh, NC. (Podium presentation and peer-reviewed abstract).

Boc*, S., Spence, B., Bass, K., Longest, P. W., & Hindle, M. (2017). Improved Nose-to-Lung (N2L) Aerosol Delivery in an in Vitro Infant Airway Model. *21st International Congress of the International Society for Aerosols in Medicine* (June 2017), Santa Fe, NM, *Journal of Aerosol Medicine and Pulmonary Drug Delivery*, 30(3), 32-33. (Poster and peer-reviewed abstract).

Bass, K., Boc, S., Hindle, M., & Longest*, P. W. (2017). High Efficiency Nose-to-Lung (N2L) Aerosol Delivery in an Infant: Development of a Validated CFD Method. *21st International Congress of the International Society for Aerosols in Medicine* (June 2017), Santa Fe, NM, *Journal of Aerosol Medicine and Pulmonary Drug Delivery*, 30(3), 8-8. (Poster and peer-reviewed abstract).

Boc, S., Spence, B., Bass, K., Longest, P. W., & Hindle*, M. (2017). High-Efficiency Delivery of Aerosols via an Infant Nasal Cannula. *Respiratory Drug Delivery 2017* (April 2017), Antibes, France. (Poster and peer-reviewed abstract).

Holbrook, L. T., Bass, K., Hindle, M., & Longest*, P. W. (2015). Development of a Realistic Ventilated Infant Lung Model for Assessing the Delivery Efficiency and Effectiveness of Aerosolized Surfactants. 2015 BMES Annual Meeting (October 2015), Tampa, FL. (Podium presentation and peer-reviewed abstract).